micromachines

Special Issue Reprint

Emerging Micro Manufacturing Technologies and Applications, 2nd Edition

Edited by
Nikolaos Tapoglou

mdpi.com/journal/micromachines

MDPI

Emerging Micro Manufacturing Technologies and Applications, 2nd Edition

Emerging Micro Manufacturing Technologies and Applications, 2nd Edition

Guest Editor

Nikolaos Tapoglou

MDPI

Basel • Beijing • Wuhan • Barcelona • Belgrade • Novi Sad • Cluj • Manchester

Guest Editor
Nikolaos Tapoglou
Department of Industrial
Engineering and Management
International Hellenic
University
Thessaloniki
Greece

Editorial Office
MDPI AG
Grosspeteranlage 5
4052 Basel, Switzerland

This is a reprint of the Special Issue, published open access by the journal *Micromachines* (ISSN 2072-666X), freely accessible at: https://www.mdpi.com/journal/micromachines/special_issues/0H2SCECNI4.

For citation purposes, cite each article independently as indicated on the article page online and as indicated below:

Lastname, A.A.; Lastname, B.B. Article Title. *Journal Name* **Year**, *Volume Number*, Page Range.

ISBN 978-3-7258-5187-4 (Hbk)
ISBN 978-3-7258-5188-1 (PDF)
https://doi.org/10.3390/books978-3-7258-5188-1

Contents

About the Editor

Nikolaos Tapoglou

Nikolaos Tapoglou is an Assistant Professor in the Department of Industrial Engineering and Management of the International Hellenic University, Thessaloniki, Greece (IHU). His research interests include additive manufacturing processes, gears and gear manufacturing, as well as CAD/CAM/CAE systems. He specializes in AM processes for manufacturing of metal components both with DED and PBF processes, he is an expert in the development of CAD based simulation models and systems. He has co-authored over 45 journal and conference publications and has worked on more than 40 research projects with a total budget exceeding EUR 5M.

Preface

In recent years, manufacturing at the microscale has gained a lot of traction owing to the drive towards lightweighting, electrification, and sustainability. Industrial sectors that have shown increasing interest in micromachining include medical, space, aerospace, automotive and consumer electronics. The micromanufacturing industry is a multi-billion-dollar industry with an annual growth rate of approximately 5%.

Research in academia has focused on the experimental investigation of micromachining processes such as micro milling, micro turning, and micro grinding. In addition, numerical and finite element models have been developed to predict the performance of micromachined parts. Over the last few years, a series of manufacturing processes have emerged in the macro-manufacturing sector that have shown great potential in the improvement of said processes; however, their use on a microscale has not been thoroughly modeled and understood. Moreover, multiple manufacturing processes are being developed for the needs of microelectronic and mechanical components and systems.

Therefore, this Issue showcases recent advances in novel and emerging manufacturing technologies and applications at the microscale.

Nikolaos Tapoglou
Guest Editor

micromachines

MDPI

Editorial

Editorial for the Special Issue on Emerging Micro Manufacturing Technologies and Applications, 2nd Edition

Nikolaos Tapoglou [1,2]

[1] Industrial Engineering and Management Department, International Hellenic University, 57001 Thessaloniki, Greece; ntapoglou@ihu.gr
[2] Laboratory of Machine Elements and Machine Design, School of Mechanical Engineering, Aristotle University of Thessaloniki, 54124 Thessaloniki, Greece

Manufacturing micro-components has become a key area of interest for research, owing to the growing demand for miniaturized components and assemblies, and a series of applications across multiple industrial sectors. The drive towards miniaturization is especially critical in industrial sectors like medical, consumer electronics, optics, and general engineering. These sectors drive the development of processes that can deliver components with sub-micron accuracy and flawless surface quality. Manufacturing processes like additive manufacturing, drawing, and electrochemical machining have been adapted to meet the requirements of microscale production, whilst on the other hand, processes like electrochemical deposition and electroforming have been developed with micromachining in mind. Research in the field, as in most manufacturing fields, has focused on the development of robust processes and simulation models that can lead to the optimization of micro manufacturing processes [1,2]. Building upon the success of the first edition of the *Emerging Micro Manufacturing Technologies and Applications* Special Issue [3], this second edition will continue to explore recent advances in the field. This issue features eight original research papers covering topics including micro-electronic device manufacturing, surface property modification, and additive manufacturing.

In particular, Liu et al. (Contribution 1) investigated the finishing process of the internal surface of cobalt chromium cardiovascular stents. Their research introduced a novel method for producing highly spherical Al_2O_3 magnetic abrasive particles that were used as an abrasive medium in the investigation. A dedicated experimental rig was produced for the magnetic abrasive finishing of long ultra-fine cardiovascular stents. Investigations were conducted on the influence of process parameters on the final stent quality. After processing, the inner surface roughness (Ra) of the tubes was reduced significantly from 0.337 μm to 0.09 μm, achieving a removal thickness of 5.106 μm.

Li et al. (Contribution 2) proposed a wire anode scanning electroforming method, which was used to improve the thickness uniformity of the electroformed metal layers. This process was based on a reciprocating paddle incorporating an ultra-fine inert wire anode. Numerical simulations allowed for the investigation of the process parameters and their effect on the deposited material characteristics. The experimental findings showcased an improvement in thickness uniformity by 15.5% on single-scale components and 11.4% on multi-scale component arrays, when compared to traditional electroforming.

Zuo et al. (Contribution 3) introduced a novel ultraviolet lithography-assisted sintering method for the fabrication of convex glass microlens arrays. The method involved the solidification of micropillar arrays of quartz glass using UV lithography, followed by

debinding and sintering into the final shape. The fabrication method successfully demonstrated the manufacturing of lenses with diameters of 30, 40, 50, and 60 μm; MLAs with average focal lengths of 122, 151, 175, and 201 μm were used.

Cao et al. (Contribution 4) performed an experimental investigation into the drawing of single-crystal copper wires. They focused on the effect of drawing and annealing process parameters on the mechanical and electrical properties of the material whilst also taking into consideration the microstructure of the material. Experiments included multi-pass drawing with varying single-pass deformations and drawing speeds, followed by annealing at different temperatures and rates. The results showed that a 14% single-pass deformation led to optimal overall wire performance, increased tensile strength, and reduced resistivity. Drawing at 500 m/min increased tensile strength further. Optimal annealing temperatures were found to be 350–400 °C.

Yang et al. (Contribution 5) focused their investigation on a novel periodically reducing current (PRC) over-growth electroforming (EF) process. The process was used for fabricating ultra-narrow precision slits with widths of less than 10 μm. As part of their work, numerical simulations were coupled with experimental investigations. Numerical simulations revealed that the PRC mode significantly improved the cathode current density distribution and ion concentration within the narrowing slit. Experimental validation demonstrated that PRC over-growth EF can reliably achieve slits with a width of 5 ± 0.1 μm and a surface roughness of less than 62.8 nm.

Li et al. (Contribution 6) investigated the feasibility of fabricating microgroove structures on Zr-based metallic glass (MG) using jet electrochemical machining (jet-ECM) with sodium nitrate ($NaNO_3$) electrolytes. The experimental investigation showed that Zr-based MG exhibits passivation, transpassivation, and re-passivation behaviors in NaNO3 solution. Based on the investigation, an applied voltage of 25 V, a nozzle travel rate of 100 μm/s, and a $NaNO_3$ electrolyte concentration of 10 wt% yielded the optimal results in terms of accuracy and surface quality.

Zhang et al. (Contribution 7) proposed a periodically lifting necked entrance through the mask electroforming process. The goal of the investigation was the cost-effective fabrication of high aspect ratio micro- and mesoscale metallic components. Coupling simulation and experimental trials, the researchers demonstrated that an appropriate necked entrance size significantly improved the flow field and current density uniformity.

Finally, Huang et al. (Contribution 8) developed a scalable DLP additive manufacturing method to simultaneously print large and small features with high local shape accuracy. The method achieved minimum printing resolutions of 101 μm (at 20.5 cm) and 157 μm (at 30.5 cm). When compared to traditional DLP, the proposed method offered an improved accuracy of small features, reducing both roundness and straightness errors.

Acknowledgments: The guest editor would like to thank the authors for submitting their excellent contributions to this Special Issue. Furthermore, the present Special Issue would not have been possible without the expert reviewers that carefully evaluated the manuscripts and provided helpful comments and suggestions for improvements. A special thank you goes to the editors and the MDPI team for their outstanding management of this Special Issue.

Conflicts of Interest: The author declares no conflicts of interest.

List of Contributions:

1. Liu, G.; Zhao, Y.; Li, Z.; Yu, H.; Cao, C.; Meng, J.; Zhang, H.; Zhao, C. Investigation of Spherical Al_2O_3 Magnetic Abrasive Prepared by Novel Method for Finishing of the Inner Surface of Cobalt–Chromium Alloy Cardiovascular Stents Tube. *Micromachines* **2023**, *14*, 621. https://doi.org/10.3390/mi14030621.

2. Li, S.; Ming, P.; Zhang, J.; Zhang, Y.; Yan, L. Concurrently Fabricating Precision Meso- and Microscale Cross-Scale Arrayed Metal Features and Components by Using Wire-Anode Scanning Electroforming Technique. *Micromachines* **2023**, *14*, 979. https://doi.org/10.3390/mi14050979.
3. Zuo, F.; Ma, S.; Zhao, W.; Yang, C.; Li, Z.; Zhang, C.; Bai, J. An Ultraviolet-Lithography-Assisted Sintering Method for Glass Microlens Array Fabrication. *Micromachines* **2023**, *14*, 2055. https://doi.org/10.3390/mi14112055.
4. Cao, J.; Wu, X.; Su, C.; Jia, H.; Sun, Y. Processing and Properties of Single-Crystal Copper Wire. *Micromachines* **2023**, *14*, 2080. https://doi.org/10.3390/mi14112080.
5. Yang, X.; Zhang, X.; Ming, P.; Li, Y.; Wang, W.; Zhang, Y.; Li, Z.; Li, L.; Xiao, Y.; Guo, X.; et al. Fabricating Ultra-Narrow Precision Slit Structures with Periodically Reducing Current Over-Growth Electroforming. *Micromachines* **2024**, *15*, 76. https://doi.org/10.3390/mi15010076.
6. Li, D.; Ming, P.; Niu, S.; Yang, G.; Cheng, K. Fabricating Precise and Smooth Microgroove Structures on Zr-Based Metallic Glass Using Jet-ECM. *Micromachines* **2024**, *15*, 497. https://doi.org/10.3390/mi15040497.
7. Zhang, Y.; Ming, P.; Zhang, X.; Li, X.; Li, L.; Yang, Z. Jet Electroforming of High-Aspect-Ratio Microcomponents by Periodically Lifting a Necked-Entrance Through-Mask. *Micromachines* **2024**, *15*, 753. https://doi.org/10.3390/mi15060753.
8. Huang, J.; Cai, J.; Huangfu, C.; Li, S.; Chen, G.; Yun, H.; Xiao, J. A Scalable Digital Light Processing 3D Printing Method. *Micromachines* **2024**, *15*, 1298. https://doi.org/10.3390/mi15111298.

References

1. Basile, V.; Modica, F.; Rebaioli, L.; Surace, R.; Fassi, I. Process Chains for Micro-Manufacturing: Modeling and Case Studies. *J. Manuf. Mater. Process* **2023**, *7*, 215. [CrossRef]
2. Li, X.; Ming, P.; Ao, S.; Wang, W. Review of additive electrochemical micro-manufacturing technology. *Int. J. Mach. Tools Manuf.* **2022**, *173*, 103848. [CrossRef]
3. Tapoglou, N. Editorial for the Special Issue on Emerging Micro Manufacturing Technologies and Applications. *Micromachines* **2023**, *14*, 1248. [CrossRef] [PubMed]

micromachines

MDPI

Article

Investigation of Spherical Al_2O_3 Magnetic Abrasive Prepared by Novel Method for Finishing of the Inner Surface of Cobalt–Chromium Alloy Cardiovascular Stents Tube

Guangxin Liu, Yugang Zhao *, Zhihao Li, Hanlin Yu, Chen Cao, Jianbing Meng , Haiyun Zhang * and Chuang Zhao

School of Mechanical Engineering, Shandong University of Technology, Zibo 255049, China
* Correspondence: zygsdut@126.com (Y.Z.); zhy@sdut.edu.cn (H.Z.)

Abstract: In this investigation, spherical Al_2O_3 magnetic abrasive particles (MAPs) were used to polish the inner surface of ultra-fine long cobalt–chromium alloy cardiovascular stent tubes. The magnetic abrasives were prepared by combining plasma molten metal powder and hard abrasives, and the magnetic abrasives prepared by this new method are characterized by high sphericity, narrow particle size distribution range, long life, and good economic value. Firstly, the spherical Al_2O_3 magnetic abrasives were prepared by the new method; secondly, the polishing machine for the inner surface of the ultra-fine long cardiovascular stent tubes was developed; finally, the influence laws of spindle speed, magnetic pole speed, MAP filling quantities, the magnetic pole gap on the surface roughness (Ra), and the removal thickness (RT) of tubes were investigated. The results showed that the prepared Al_2O_3 magnetic abrasives were spherical in shape, and their superficial layer was tightly bound with Al_2O_3 hard abrasives with sharp cutting; the use of spherical Al_2O_3 magnetic abrasives could achieve the polishing of the inner surface of ultra-fine cobalt–chromium alloy cardiovascular bracket tubes, and after processing, the inner surface roughness (Ra) of the tubes decreased from 0.337 μm to 0.09 μm and had an RT of 5.106 μm.

Keywords: spherical Al_2O_3 magnetic abrasive; cobalt–chromium alloy; cardiovascular stent tubes; plasma molten metal powder; magnetic abrasive finishing

1. Introduction

Cardiovascular diseases (CVDs), the most prevalent diseases affecting human health, cause more than 18 million deaths annually [1–3]. Cardiovascular stenting techniques have become an important tool in the treatment of CVDs because of their unique immediate patency and minimally invasive nature [4–6]. The cobalt–chromium (Co–Cr) alloy vascular stent is a medical implant with good mechanical properties, high resistance to wear and tear, and high biocompatibility that is safe and reliable and has obvious clinical benefits [7–9]. However, the production process of drawing produces defects such as pits and bumps on the internal surface of cardiovascular stents, which bring high internal surface roughness to the stent tubing, limiting the stable flow of blood, and the detachment of the defective layer can also cause harm to the patient with the implant. Medical implants must have low roughness and, therefore, require the polishing of cobalt–chromium alloy cardiovascular stent tubing [10]. The inner wall of the tubing is polished and the defect layer is removed at the same time. Currently, the polishing of the inner wall of vascular stent tubing is mainly performed chemically [11–13]. However, the results of chemical polishing are not satisfactory, with new defects such as pitting and bulging, due to difficulties in the introduction of chemical reagents into ultra-slender vascular stent tubing and the difficulty in controlling them [14]. After chemical polishing, these defects will continue to exist in the processed vascular stent, which is extremely harmful to the majority of patients undergoing vascular stenting procedures, causing blood disorders, vascular inflammation, and secondary blockage of blood vessels. At the same time, improper disposal of the waste

solution after chemical polishing can also cause environmental pollution, which is not in line with the concept of green development.

Magnetic abrasive finishing (MAF), a process that employs the magnetic attraction of a composite powder containing hard abrasives and ferromagnetic metals to polish the surface of the workpiece, is adaptive and highly efficient [15,16]. MAF can not only finish flat surfaces [17,18], internal and external cylindrical surfaces [19–21], and curved surfaces [22,23], but also deburr a machined surface [24,25]. Currently, MAF has been extensively studied in highly sophisticated industries such as healthcare, communication technology, aerospace, and the military [26–32]. MAF has now been applied to polish the inner walls of tubes [33–36]; however, few studies have emerged using magnetic abrasives to polish the inner walls of ultra-fine cobalt–chromium alloy cardiovascular stent tubes. This is due to the irregular shape of existing magnetic abrasives, which not only makes loading into ultra-fine long cardiovascular stent tubing difficult, but also makes the depth of cut of the machined surface inconsistent, limiting the improvement of surface quality. At the same time, the low grinding life of existing magnetic abrasives seriously affects the grinding and polishing efficiency, further limiting the application of magnetic particle grinding in cardiovascular stent tubing polishing. The lack of processing equipment specifically designed for defect removal and inner wall polishing of ultra-long cardiovascular stent tubing is another factor limiting the application of MAF in ultra-long vascular stent tubing polishing. Magnetic abrasives (MAPs), as key components of MAF [15,16], are mainly prepared by the bonding method [37], mechanical mixing method [38,39], atomization fast-setting method [40,41], in situ alloy hardening method [42], hot press sintering method [43], plasma spraying method [44–46], and electroless plating method [47]. The bonding method [37] uses a special binder, hard abrasive powder, and iron matrix powder mixed in a certain ratio, and the prepared magnetic abrasive is obtained after curing, crushing, and screening. The low cost and simple process are the characteristics of this preparation method; however, the curing and crushing process leads to irregularity of the prepared magnetic abrasives, which limits its introduction into ultra-fine long cardiovascular support tubes. The addition of hard abrasives that are easily dislodged significantly reduces the grinding life and greatly reduces the efficiency of grinding and polishing the inner wall of the tubing. The mechanical mixing method [38,39], a simple preparation method, results in a magnetic abrasive made by mixing a certain percentage of lipid, hard abrasive powder, and ferromagnetic powder in proportion to each other. Through this, method it is simpler to prepare magnetic abrasives, but in the grinding and polishing process, the ferromagnetic powder and hard abrasives are easily decomposed due to the joint action of centrifugal force and magnetic force, and the ideal polishing effect cannot be achieved. The atomization rapid coagulation method [40,41] results in a magnetic abrasive prepared by using aerosolized powder-making equipment combined with high-speed spraying of hard abrasive, which is rapidly solidified by gas cooling (or water cooling). The magnetic abrasives prepared by this method have outstanding features such as high grinding capacity and long life. However, this method is based on the preparation of powder by the atomization method, and the prepared magnetic abrasives have a normal particle size distribution, which is consistent with the particle size distribution of metal powders prepared by the atomization method [48]. The magnetic abrasives prepared by the atomization fast coagulation method have less than half of the particle size in the effective range, low yield, and serious material waste, and are not economical. The economic value is low when using high-priced diamond or CBN powder as hard abrasives, which is not in line with the green development concept. The in situ alloy hardening method [42] is a magnetic abrasive preparation method that generates a hardened layer on the surface of carbon-based iron powder through a chemical reaction. The magnetic abrasives prepared by this method are spherical in shape, but no sharp cutting edge exists and the abrasive performance is very low, which makes it difficult to remove and polish the defect layer of ultra-long cardiovascular stent tubes. The hot-press sintering method [43] was used to produce magnetic abrasives by crushing a mixture of sintered iron matrix powder and

hard abrasives. The magnetic abrasives prepared by this method have the disadvantages of difficult comminution and irregular shape, which make them difficult to introduce into the interior of ultra-fine cobalt–chromium alloy cardiovascular stent tubing. The plasma spraying method [44–46] was used to prepare regular spherical magnetic abrasives by using high-temperature melting and spheroidization of the plasma torch. The hard abrasive phase of the magnetic abrasives prepared by this method is severely passivated or even detached due to high temperature, with low bond strength and greatly reduced grinding life. The electroless composite plating method [48] is to add ferromagnetic powder and diamond hard abrasive to the chemical solution, so that diamond abrasive grains and plated metal are co-deposited on the ferromagnetic powder substrate to produce magnetic abrasives. The magnetic abrasives prepared by this method have irregular morphology and low abrasive performance. The magnetic abrasives prepared by the above-described magnetic abrasive preparation methods all show limitations for finishing ultra-long cardiovascular stent tubes.

The magnetic abrasives prepared by the combination method of plasma molten metal powder and hard abrasives have the characteristics of high sphericity, controllable particle size (the particle size of the prepared magnetic abrasives is controlled by adjusting the particle size of the iron matrix in the raw material), long life, and good economic value. The preparation method not only solves the problems of low bonding strength between metal matrix and hard abrasive, short service life, and poor grinding performance, which cannot be overcome in the traditional plasma fused magnetic abrasive preparation method, but also solves the key technical problems of uneven particle size and low yield of magnetic abrasive prepared by the traditional aerosolized magnetic abrasive method, and has the advantages of both, reduces the preparation cost, and improves the preparation quality. It is convenient to introduce ultra-fine and long cobalt–chromium alloy cardiovascular stent tubing for processing, and solves the problem of processing tools used for polishing the inner wall of ultra-fine and ultra-long cobalt–chromium alloy cardiovascular stent tubing. In this study, an ultra-fine and ultra-long cardiovascular stent tubing inner wall polishing machine was also developed to solve the problem of the lack of special processing equipment for defect layer removal and magnetic particle grinding inner wall polishing of ultra-fine and long cardiovascular stent tubing.

In the current work, we have investigated the removal of defective layers from the inner walls of cardiovascular stents using magnetic particle finishing, and the magnetic abrasives used were obtained by atomization [49,50]. As reviewed earlier, the disadvantage of the atomization method when preparing magnetic abrasives from expensive hard abrasives such as CBN and PCD is that there is serious waste, and the available grain size does not exceed 50%. The new method for the preparation of magnetic abrasives proposed in this paper has the characteristics of the atomization method, where hard abrasives are firmly bonded to the iron substrate, and is also able to improve the particle size distribution problem. The focus of this paper is the removal and polishing of defective layers on the inner wall of cardiovascular stent tubing using the new method of magnetic abrasive preparation.

2. Preparation Principle and Procedure of Al_2O_3 Magnetic Abrasive

The schematic diagram of the equipment for preparing spherical Al_2O_3 magnetic abrasive by combining plasma molten metal powder and hard abrasive is shown in Figure 1. The equipment consists of a plasma generator, drum wheel type precision powder mixing device, abrasive spray tray, magnetic abrasive synthesis condensation chamber, gas station and pipeline, power supply and air supply system, vacuum dust removal system, and so on. The principle of preparing spherical Al_2O_3 magnetic abrasive is as follows: the spherical iron matrix with particle size within a certain range (e.g., 106~120 μm) is mixed with low-pressure inert gas through the drum wheel type precision powder mixer and delivered to the stable plasma torch for heating, and the spherical iron matrix is heated to form micro-droplets moving down along the plasma torch; meanwhile, the Al_2O_3 hard

abrasive is mixed with high-pressure plasma torch through the drum wheel type precision powder mixer. At the same time, Al_2O_3 hard abrasive is mixed with high-pressure inert gas by the drum wheel type precision powder mixer feeder and accelerated by the Laval type abrasive annular slit spray disc. The Al_2O_3 hard abrasive particles reach a very high velocity and shoot into the falling metal micro-droplets like bullets, which only overcome the surface tension of the metal droplets to enter the inside instead of breaking the metal droplets, thus avoiding the generation of even smaller metal droplets and ensuring the prepared magnetic abrasive with narrow particle size distribution range. Finally, the Al_2O_3 hard abrasive particles are bonded to the superficial layer of metal particles by rapid condensation (condensation speed up to 10^5 K/s) to form a high-performance spherical Al_2O_3 magnetic abrasive.

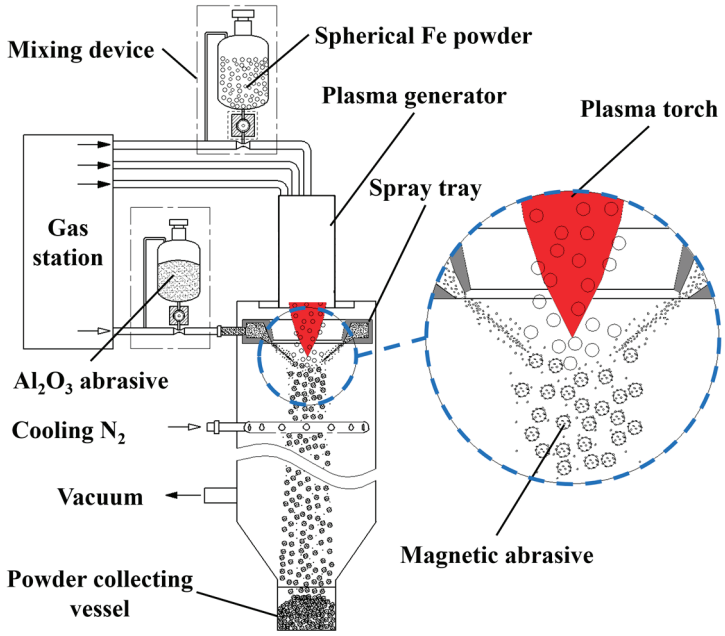

Figure 1. Schematic diagram of combining plasma molten metal powder with sprayed abrasive powder.

The steps of preparing Al_2O_3 spherical magnetic abrasive by combining plasma molten metal powder and jet hard powder are as follows: make preparations before magnetic abrasive preparation, place the raw materials in the drum and wheel precision powder mixer, turn on the power of vacuum dust removal system for dust extraction, turn on the power supply and water supply system for power supply, cooling water, and cooling gas, and establish a stable plasma torch for magnetic abrasive preparation. After the preparation, turn off the power supply and air supply system; when the temperature of the abrasive collector is lowered to the same temperature as the room temperature, take off the abrasive collector and obtain the magnetic abrasive, unbound metal powder, and Al_2O_3 hard abrasive after sieving, and store them in an airtight container after separation; finally, turn off the power supply of the vacuum and dust removal system.

Table 1 shows the process parameters of the spherical Al_2O_3 magnetic abrasive prepared by the combination of plasma molten metal powder and hard abrasives, Figure 2 shows the spray tray structure parameters diagram, and Figure 3 shows the SEM image of the spherical Al_2O_3 magnetic abrasive prepared by the new method introduced in this paper. From the figure, it can be seen that the spherical Al_2O_3 magnetic abrasive prepared under the process parameters listed in Table 1 has the remarkable advantages of spherical appearance, dense bonding of hard abrasives to the superficial layer of the iron matrix, sharp and exposed cutting edges, and firm bonding, etc. These advantages indicate that the magnetic abrasive has a high grinding capacity. The above advantages of

the prepared Al_2O_3 magnetic abrasive are due to the high-speed flight of the Al_2O_3 hard abrasive during the preparation of the magnetic abrasive, which does not pass through the high-temperature region (over 2730°C high temperature region), and the very short heating time, so that the cutting edge of the Al_2O_3 hard abrasive after the formation of the magnetic abrasive is not blunted by the heat and maintains its original sharpness. The high-speed Al_2O_3 hard abrasive only overcomes the surface tension of the metal microdroplets and enters the inside of the microdroplets without breaking the metal microdroplets, thus avoiding the formation of small-size magnetic abrasives and, thus, the size of the prepared magnetic abrasives is effectively controlled.

Table 1. Preparation of raw materials and preparation parameters.

Raw Materials	Preparation Parameters
Spherical ferromagnetic metal powder (composition 99.9% Fe, particle size: 106~120 μm); alumina hard abrasive (d50 = 14 μm)	Ring seam nozzle (nozzle cone angle 65°, nozzle annular seam diameter 3.5 mm, nozzle bore diameter 46 mm, inlet pressure of nozzle 0.5 MPa); distance between nozzle and plasma generator 70 mm; I = 700 A, Ar = 1000 L/h, H_2 = 200 L/h, iron powder 40 g/min, Al_2O_3 powder 240 g/min, equipment power 25.34 kW

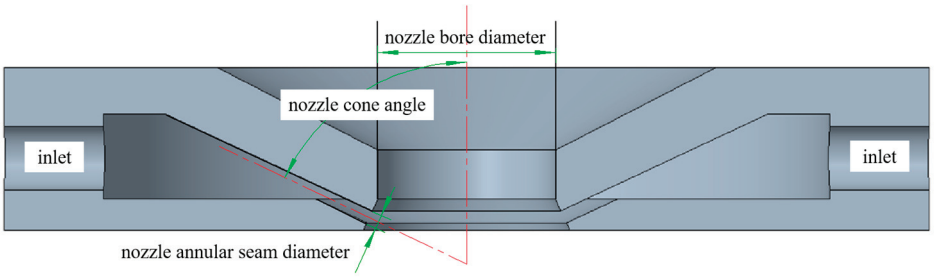

Figure 2. Spray tray structure parameters diagram.

Figure 3. SEM image of spherical Al_2O_3 magnetic abrasive.

3. Experiment

3.1. Processing Equipment and Principles

Figure 4 shows the self-developed polishing machine for magnetic particle finishing processing on the inner wall surface of ultra-slender vascular stent tubes, and the per-

formance parameters of this equipment are shown in Table 2. The polishing machine is composed of a numerical control system developed based on the windows system and a mechanical part, where the mechanical part includes a pedestal, synchronous belt, AC servo motor, magnetic device, and other components. Figure 5 shows a principle diagram of magnetic particle finishing on the inner wall of ultra-slender cardiovascular stent tubes. The working principle of this polishing machine is that the servo motors at both ends of the polishing machine drive the tube rotation, while the magnetic device, through the magnetization of the internal magnetic abrasive to form a magnetic abrasive brush on the inner wall of the tube, produces a small pressure, and the magnetic abrasive brush inside the tube is attracted by the magnetic pole to perform reciprocal movement in the process. In the process of movement, from the servo motors at both ends with the same speed but opposite directions, the magnetic pole attracts the magnetic abrasices. In this process, the tube rotation direction remains unchanged and the magnetic pole device moves reciprocally, which makes the single grain hard abrasive form spatial spiral lines crossing each other on the inner surface of the tube, and the defective layer on the inner wall of the tube will be squeezed by the magnetic abrasive and micro removal, so as to remove and polish the defective layer on the inner surface of the tube. The magnetic pole used has a rectangular groove, and the direction is perpendicular to the tube to improve the polishing efficiency.

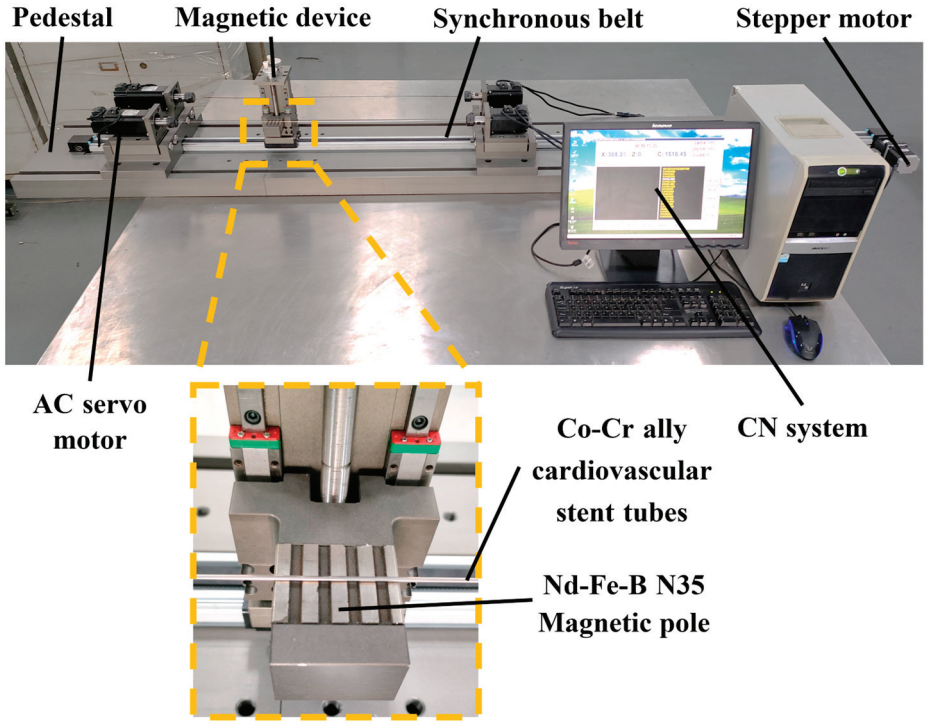

Figure 4. Ultra-slender cardiovascular stent tube inner wall magnetic particle finishing machine.

The steps of magnetic abrasive finishing of ultra-long cardiovascular support tubes are: (1) fill the tube with magnetic abrasive and cutting fluid proportionally and seal both ends; (2) clamp the tube through the precision chuck to ensure no loosening; (3) adjust the tensioning device for tightening; (4) prepare the CNC program for polishing; (5) after polishing is completed, remove the seal, rinse the tube with anhydrous ethanol, and then air-dry and store in a dry place.

Table 2. Equipment performance parameters.

Parameter	Value
Spindle speed (rpm)	≤2000
Machining tube diameter (mm)	0.3–3
Machining tube length (mm)	100–2000
Magnetic pole speed (mm/min)	≤1000

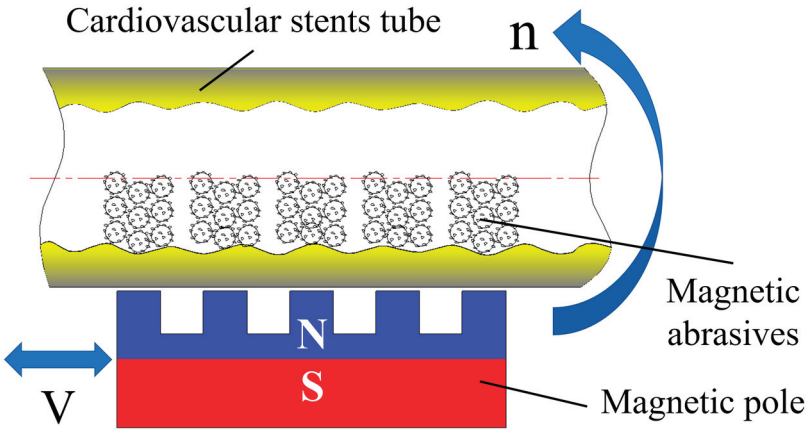

Figure 5. Principle diagram of magnetic particle finishing on the inner wall of ultra-slender cardiovascular stents tube.

3.2. Force Analysis

As shown in Figure 6, a single magnetic abrasive is subjected to two forces inside the cardiovascular support tube: F_x along the isomagnetic potential and F_y along the magnetic force line, and their combined force is F_m, pointing towards the inner wall surface, where F_m causes the magnetic abrasive to make a small indentation depth h against the inner wall surface. The magnetic poles remain in a non-contact mode with the magnetic abrasive inside the tube throughout the process.

$$F_x = \left(\frac{4\pi d^3}{3}\right)\chi H\frac{\partial H}{\partial x} \tag{1}$$

$$F_y = \left(\frac{4\pi d^3}{3}\right)\chi H\frac{\partial H}{\partial y} \tag{2}$$

where: χ—the magnetization rate of spherical Al_2O_3 magnetic abrasives;

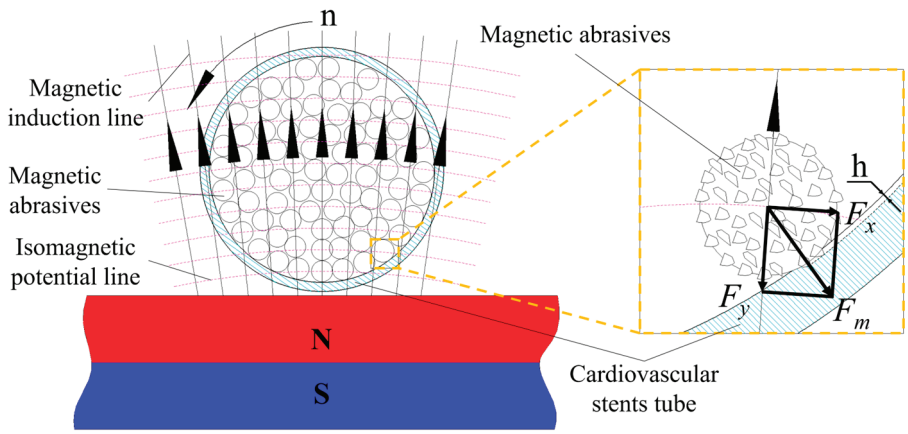

Figure 6. Force diagram of a single magnetic abrasive in a cardiovascular stents tube.

d—the diameter of the spherical Al_2O_3 magnetic abrasive (mm);
H—the magnetic field strength at the location being processed (A/m);
$\frac{\partial H}{\partial x}$—the rate of change of the magnetic field along the direction of the magnetic lines of force;
$\frac{\partial H}{\partial y}$—the rate of change of the magnetic field along the magnetic isotope.

3.3. Experimental Materials

The ultra-slender cobalt–chromium alloy cardiovascular stent tube samples used for the test were produced by the drawing process, with lengths of 1.8–2.0 m, an outer diameter of 1.8 mm, and an inner diameter of 1.6 mm, shown as Figure 7. The elemental content of the material is listed in Table 3, and the mechanical properties are listed in Table 4.

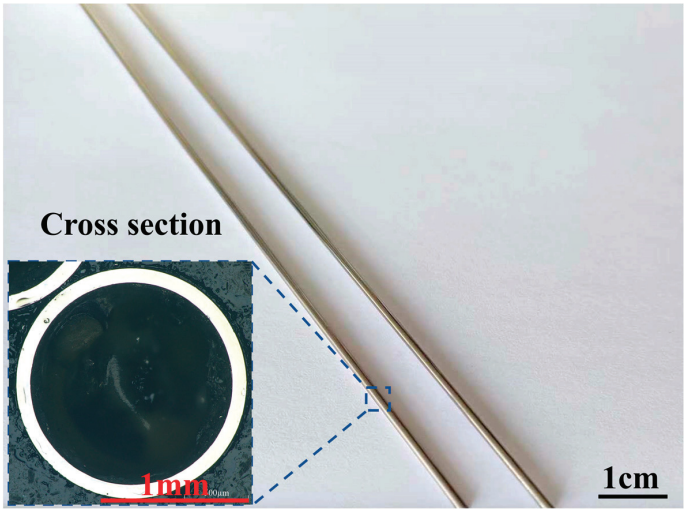

Figure 7. Ultra-slender cobalt–chromium alloy cardiovascular stent tubes.

Table 3. Composition of Co–Cr cardiovascular stent tubes.

Element	Co	Cr	W	C	Ni	Mn	O
w/%	47–49	19–20	11–12	≤10	≤9	≤2	≤2

Table 4. Mechanical properties of cobalt–chromium alloy cardiovascular stent tubes.

Performance Indicators	Density ($g \cdot cm^3$)	Modulus of Elasticity (GPa)	Tensile Strength (MPa)	Yield Strength	Elongation (%)
Value	9.2	243	820–1200	420–600	35–55

3.4. Finishing Experiments

The effects of spindle speed, magnetic pole speed, MAP filling quantities, magnetic pole gap on the surface roughness (Ra), and removal thickness (RT) of the tube inner wall were investigated. The effective length of each machined tube specimen was 0.5 m. The inside wall roughness (Ra) of the machined tube specimens was measured at 5 mm intervals for each process parameter using DSX1000 Digital Microscopes (OLYMPUS, Tokyo, Japan). The sampling length L was 0.25 mm, and the evaluation length Ln was 5 L. Five measurements were taken to eliminate measurement errors. The tube wall removal thickness (RT) was measured by cutting, inlaying, polishing, and etching under DSX1000 Digital Microscopes, and each section was measured 5 times to eliminate measurement errors, and the average value was calculated as the final value. The experimental parameters shown as Table 5.

Table 5. Experimental parameters.

Process Parameters	Values
Finishing time (h)	4
Al_2O_3 MAP particle size (μm)	125~150
Cutting fluid	$V_{Anti\text{-}rust\ emulsified\ oil}$:$V_{Deionized\ water}$ = 1:20
Spindle speed (rpm)	100, 300, 500, 700, 900
Magnetic pole speed (mm/min)	50, 100, 150, 200, 250
MAP loading quantities (g)	0.05, 0.10, 0.15, 0.20, 0.25
Magnetic pole gap (mm)	0.5, 1.0, 1.5, 2.0, 2.5

4. Results and Discussions

4.1. The Effect of Spindle Speed on Ra and RT of Tube Inner Wall

The fixed process parameters are magnetic pole speed: 50 mm/min, MAP filling quantities: 0.15 g, and magnetic pole gap: 0.5 mm. The effect of spindle speed on the Ra and RT values of the inner wall of the tube is shown in Figure 8. In the experimental parameters, the Ra value showed a decreasing trend when the spindle speed increased from 100 rpm to 300 rpm, the lowest Ra value was 0.9 μm at 300 rpm, and the Ra value continued to increase to 263 μm as the spindle speed increased beyond 300 rpm, which occurred at 900 rpm. This was due to the fact that once the spindle speed was not at the optimal speed, the magnetic abrasive brush inside the tube was disturbed and the machining accuracy was reduced. The highest value of RT for the inner wall was 5.186 μm at 100 rpm, which tended to decrease as the spindle speed continued to increase. This is due to the fact that the magnetic abrasive brush inside the tube is affected by the spindle speed, and the lower the spindle speed is in the test range, the more stable the magnetic abrasive brush is, which makes the material removal rate increase.

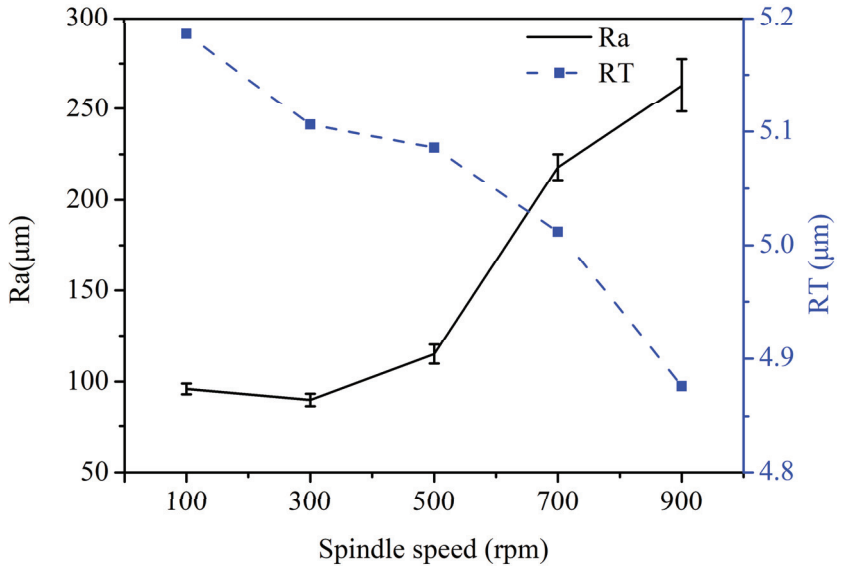

Figure 8. Graph of the effect of spindle speed on Ra and RT values.

4.2. The Effect of Magnetic Pole Speed on Ra and RT of Tube Inner Wall

The fixed process parameters are spindle speed: 300 rpm, MAP filling quantities: 0.15 g, and magnetic pole gap: 0.5 mm. Figure 9 is a graph of the effect of magnetic pole speed on Ra and RT values. It can be seen that Ra and RT values show different trends with increasing pole speed; Ra value increases with increasing magnetic pole speed, while RT value decreases with increasing magnetic pole speed. The extreme values of both occur at a magnetic pole speed of 50 mm/min. This is due to the fact that during machining, when other process parameters are certain, the smaller the magnetic pole speed is, the denser the "spacing" of the formed trajectory and the denser the trajectory lines on the unit machining

area are, and the cumulative number of machining per unit machining surface increases, thus improving the machining efficiency and machining accuracy. In contrast, the larger the speed of magnetic pole movement, the larger the "spacing" of the formed trajectory is, the sparser the trajectory lines per unit machining area are, and the cumulative number of machining per unit machining area decreases, thus reducing the machining efficiency and machining accuracy.

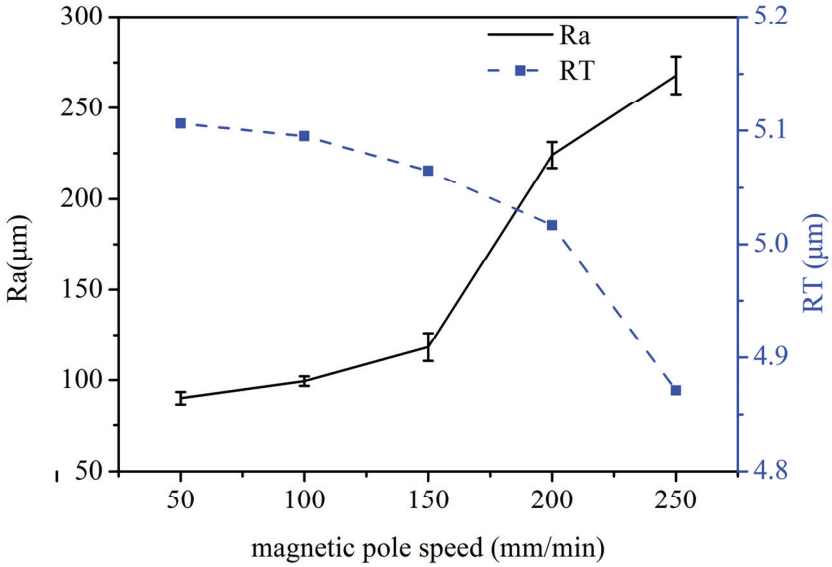

Figure 9. Graph of the effect of magnetic pole speed on Ra and RT values.

4.3. The Effect of MAP Filling Quantities on Ra and RT of Tube Inner Wall

The fixed process parameters are spindle speed: 300 rpm, magnetic pole speed: 50 mm/min, and magnetic pole gap: 0.5 mm. Figure 10 shows the graph of the effect of MAP loading quantities on Ra and RT values of the tube inner wall. It can be seen from the graph that with the increase in MAP filling quantities, the Ra value shows a trend of first a sharp decline, then a slow rise, and then a decline. The lowest value of Ra corresponds to the MAP filling quantities of 0.15 g. With the increase in MAP filling quantities of the inner wall, the RT value shows a rising trend that is first sharp and then slow. The MAPs filling quantities of 0.25 g can reach the maximum RT value of 5.2 μm. This is because when the MAP filling quantities in the tube are too large, the thickness of the magnetic abrasive brush becomes large, so the elasticity of the magnetic abrasive brush becomes poor, and MAPs can not flip the cycle, reducing the service life and processing efficiency. When the MAPs filling quantities are small, only a magnetic abrasive brush with low finishing efficiency can be formed, which does not have high finishing performance, while the MAPs filling quantities being moderate results in high finishing performance. The moderate MAP filling quantities have high processing performance, which can remove the defective layer of the inner wall of the tube and polish effectively. From the experimental results, it can be found that the right MAP filling quantities can reach high processing efficiency, while too much MAP filling will cause waste and too little MAP filling will make the processing efficiency lower.

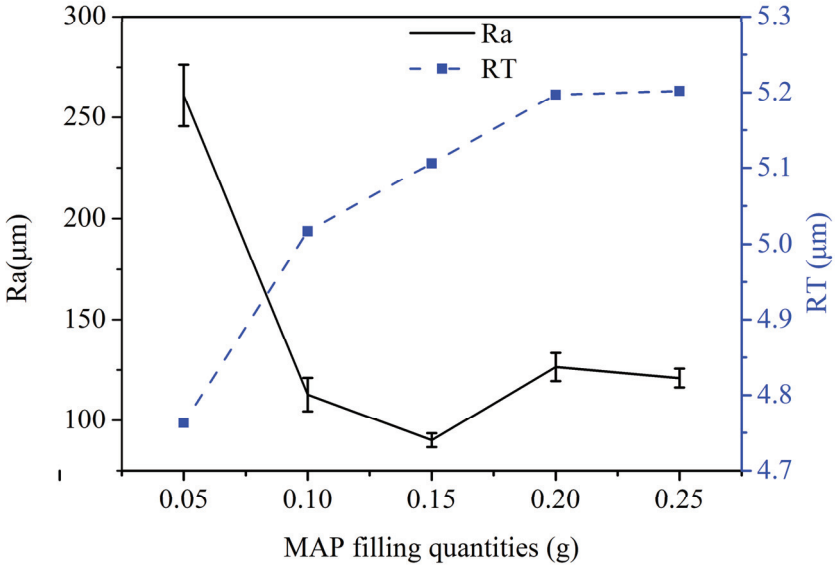

Figure 10. Graph of the effect of MAP filling quantities on Ra and RT values of tube inner wall.

4.4. The Effect of Magnetic Pole Gap on Ra and RT of Tube Inner Wall

The fixed process parameters are spindle speed: 300 rpm, magnetic pole speed: 50 mm/min, and MAP filling quantities: 0.15 g. The effect of the magnetic pole gap on the Ra and RT values of the inner wall of the tube is shown in Figure 11. It can be seen from the figure that as the magnetic pole gap increases, the Ra value increases and the RT value decreases. This is due to the fact that smaller pole distance has denser magnetic lines of force and higher magnetic induction strength, which attracts magnetic abrasives more strongly, resulting in harder magnetic abrasive brushes and higher cutting forces, leading to reduced inner wall surface roughness and increased material removal. As the magnetic pole distance continues to increase, the magnetic lines of force diverge and the stiffness of the magnetic abrasive brush decreases, preventing effective material removal and surface roughness reduction.

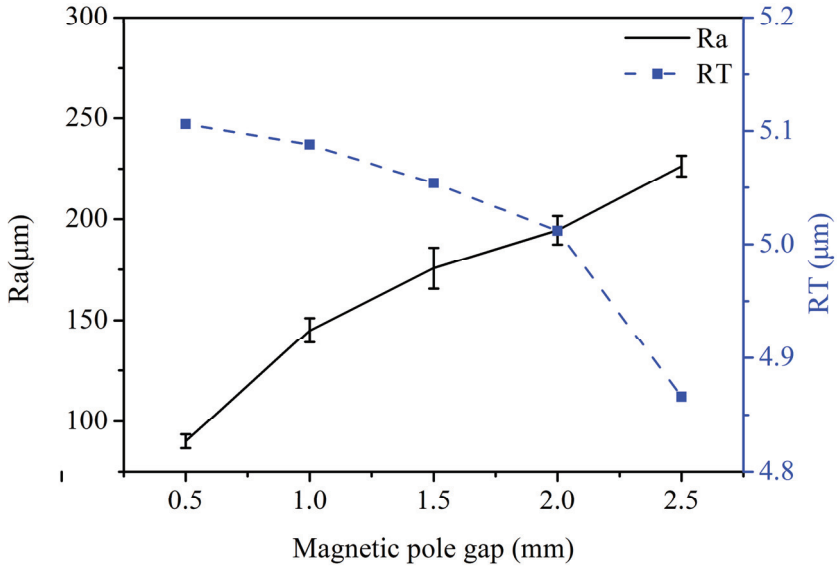

Figure 11. Graph of the effect of magnetic pole gap on Ra and RT of tube inner wall.

Figure 12 shows the SEM images after a processing time of 4 h with spherical Al_2O_3 magnetic abrasive, where the magnetic abrasive filling is 0.15 g, the spindle speed is 300 r/min, the magnetic abrasive particle size range is 125~150 μm, and slotted magnetic

poles are used. After processing with the above parameters, the surface roughness of the inner wall of the tube was reduced from 0.337 μm to Ra = 0.09 μm. Figure 11 shows that the defect layer on the inner wall of the tube was effectively removed after processing, defects such as pits and bumps disappeared, and the surface became smooth. This indicates that the spherical Al_2O_3 magnetic abrasive prepared by a new method combining plasma molten metal powder and hard abrasives can remove the defects on the inner wall of cardiovascular stent tubes due to the manufacturing process with excellent finishing effect.

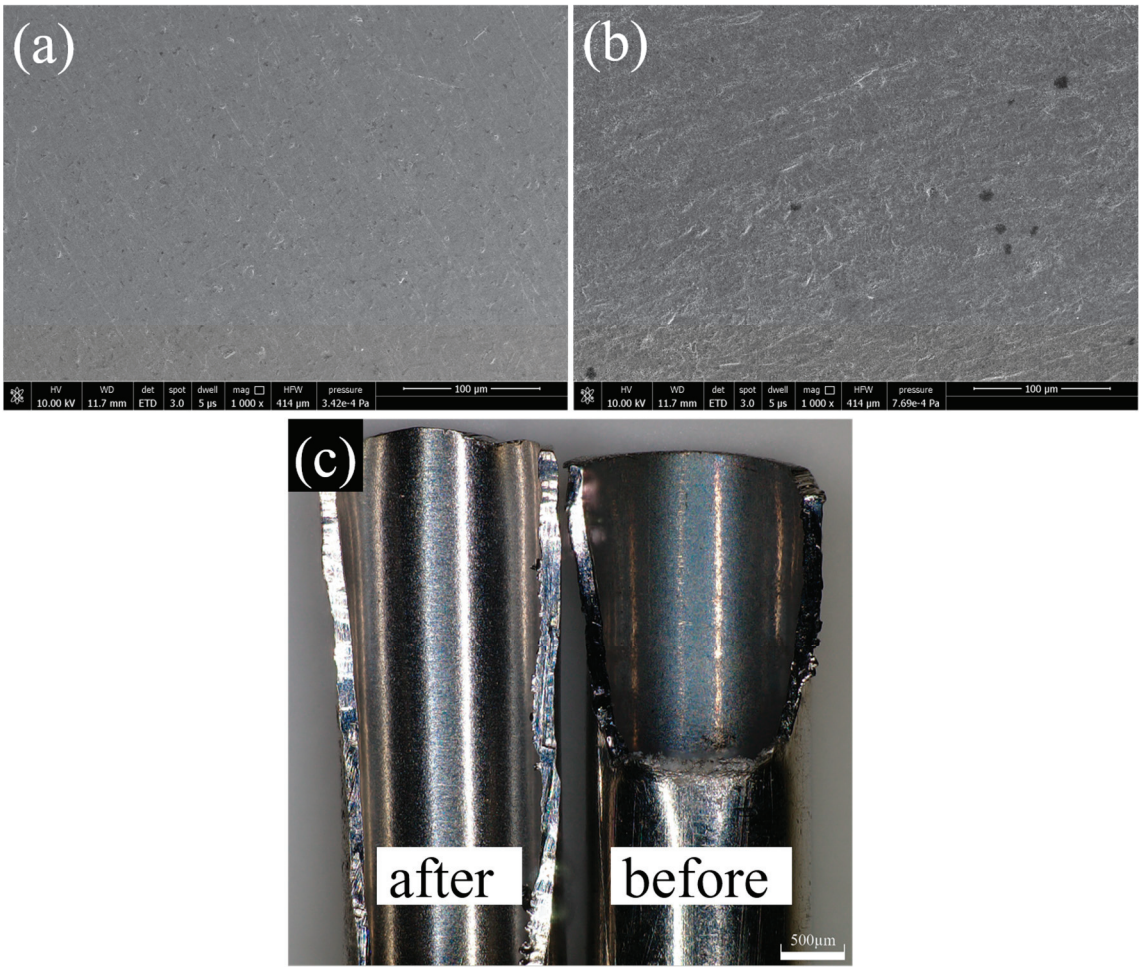

Figure 12. (**a**) SEM image of tube inner wall surface after finishing (Ra = 0.09 μm); (**b**) SEM image of tube inner wall surface before finishing (Ra = 0.337 μm); (**c**) comparison image of after and before finishing.

5. Conclusions

In this investigation, spherical Al_2O_3 magnetic abrasives were prepared by a combined plasma molten metal powder and hard abrasives method, which has potential finishing performance and is expected to overcome the problem of removing and polishing the defect layer on the inner wall of ultra-slender cardiovascular stent tubing. The test results obtained by grinding and polishing the inner surface of cobalt–chromium alloy cardiovascular stent tubing with it led to the following conclusions.

(1) A new method, a combination of plasma molten metal powder and hard abrasives, was used to successfully prepare Al_2O_3 magnetic abrasives with high sphericity, controllable particle size, long life and good economic value that are well suited for the removal and polishing of defect layers on the inner surface of ultra-fine and ultra-long cobalt–chromium alloy cardiovascular stents.

(2) CNC processing equipment specifically applied to magnetic abrasives for removing defect layers and polishing the inner wall of ultra-fine and long cardiovascular stent tubing was developed.

(3) This paper uses spherical Al_2O_3 magnetic abrasive to finish the inner wall of ultra-fine long cobalt–chromium alloy cardiovascular stent tubing, which can remove surface defects such as bumps and pits generated during the production process.

(4) The effects of spindle speed, magnetic pole speed, MAP filling quantities, and magnetic pole gap on the Ra and RT values of the tube inner wall surface were investigated by single-factor testing, resulting in a reduction in surface roughness (RA) from 0.337 μm to 0.09 μm and RT of 5.106 μm.

Author Contributions: The method was conceived by Y.Z., the experiments were designed by G.L. and performed by Z.L., H.Y., C.C., J.M., H.Z. and C.Z. All the authors took part in the paper. All authors have read and agreed to the published version of the manuscript.

Funding: The authors would like to acknowledge all of the support received from the National Natural Science Foundation of China (No. 51875328) and the Natural Science Foundation of Shandong Province (No. ZR2019MEE013).

Institutional Review Board Statement: Not applicable.

Informed Consent Statement: Not applicable.

Data Availability Statement: Not applicable.

Conflicts of Interest: The authors declare that they have no known competing financial interests or personal relationships that could have appeared to influence the work reported in this paper.

References

1. Qiu, H.; Tu, Q.; Gao, P.; Li, X.; Maitz, M.F.; Xiong, K.; Huang, N.; Yang, Z. Phenolic-amine chemistry mediated synergistic modification with polyphenols and thrombin inhibitor for combating the thrombosis and inflammation of cardiovascular stents. *Biomaterials* **2021**, *269*, 120626. [CrossRef]
2. Oikonomou, E.K.; Antoniades, C. The role of adipose tissue in cardiovascular health and disease. *Nat. Rev. Cardiol.* **2019**, *16*, 83–99. [CrossRef] [PubMed]
3. Zhao, D.; Ding, S.X.; Karimi, H.R.; Li, Y.; Wang, Y. On robust Kalman filter for two-dimensional uncertain linear discrete time-varying systems: A least squares method. *Automatica* **2019**, *99*, 203–212. [CrossRef]
4. Yang, L.; Wu, H.; Lu, L.; He, Q.; Xi, B.; Yu, H.; Luo, R.; Wang, Y.; Zhang, X. A tailored extracellular matrix (ECM)—Mimetic coating for cardiovascular stents by stepwise assembly of hyaluronic acid and recombinant human type III collagen. *Biomaterials* **2021**, *276*, 121055. [CrossRef] [PubMed]
5. Cockerill, I.; See, C.; Young, M.; Wang, Y.; Zhu, D. Designing better cardiovascular stent materials: A learning curve. *Adv. Funct. Mater.* **2021**, *31*, 2005361. [CrossRef]
6. Lyu, N.; Du, Z.; Qiu, H.; Gao, P.; Yang, Z. Mimicking the nitric oxide-releasing and glycocalyx functions of endothelium on vascular stent surfaces. *Adv. Sci.* **2020**, *7*, 2002330. [CrossRef]
7. Kapnisis, K.; Constantinides, G.; Georgiou, H.; Cristea, D.; Gabor, C.; Munteanu, D.; Brott, B.; Anderson, P.; Lemons, J.; Anayiotos, A. Multi-scale mechanical investigation of stainless steel and cobalt–chromium stents. *J. Mech. Behav. Biomed. Mater.* **2014**, *40*, 240–251. [CrossRef]
8. O'Brien, B.; Zafar, H.; Ibrahim, A.; Zafar, J.; Sharif, F. Coronary Stent Materials and Coatings: A Technology and Performance Update. *Ann. Biomed. Eng.* **2016**, *44*, 523–535. [CrossRef] [PubMed]
9. Hanawa, T. Materials for metallic stents. *J. Artif. Organs* **2009**, *12*, 73–79. [CrossRef]
10. Finazzi, V.; Demir, A.G.; Biffi, C.A.; Migliavacca, F.; Petrini, L.; Previtali, B. Design and functional testing of a novel balloon-expandable cardiovascular stent in CoCr alloy produced by selective laser melting. *J. Manuf. Process.* **2020**, *55*, 161–173. [CrossRef]
11. Simka, W.; Kaczmarek, M.; Baron-Wiecheć, A.; Nawrat, G.; Marciniak, J.; Żak, J. Electropolishing and passivation of NiTi shape memory alloy. *Electrochimica. Acta* **2010**, *7*, 2437–2441. [CrossRef]
12. Van Hooreweder, B.; Lietaert, K.; Neirinck, B.; Lippiatt, N.; Wevers, M. CoCr F75 scaffolds produced by additive manufacturing: Influence of chemical etching on powder removal and mechanical performance. *J. Mech. Behav. Biomed. Mater.* **2017**, *70*, 60–67. [CrossRef] [PubMed]
13. Zhao, H.; Humbeeck, J.V.; Sohier, J.; De Scheerder, I. Electrochemical polishing of 316L stainless steel slotted tube coronary stents. *J. Mater. Sci. Mater. Med.* **2002**, *13*, 911–916. [CrossRef]

14. Yamaguchi, H.; Kang, J.; Hashimoto, F. Metastable austenitic stainless steel tool for magnetic abrasive finishing. *CIRP Ann.* **2011**, *60*, 339–342. [CrossRef]
15. Zhang, G.-X.; Zhao, Y.-G.; Zhao, D.-B.; Yin, F.S.; Zhao, Z.D. Preparation of white alumina spherical composite magnetic abrasive by gas atomization and rapid solidification. *Scr. Mater.* **2011**, *5*, 416–419. [CrossRef]
16. Qian, C.; Fan, Z.; Tian, Y.; Liu, Y.; Han, J.; Wang, J. A review on magnetic abrasive finishing. *Int. J. Adv. Manuf. Technol.* **2021**, *112*, 619–634. [CrossRef]
17. Zou, Y.; Xie, H.; Dong, C.; Wu, J. Study on complex micro surface finishing of alumina ceramic by the magnetic abrasive finishing process using alternating magnetic field. *Int. J. Adv. Manuf. Technol.* **2018**, *97*, 2193–2202. [CrossRef]
18. Fan, Z.; Tian, Y.; Liu, Z.; Shi, C.; Zhao, Y. Investigation of a novel finishing tool in magnetic field assisted finishing for titanium alloy Ti-6Al-4V. *J. Manuf. Process.* **2019**, *43*, 74–82. [CrossRef]
19. Yun, H.; Han, B.; Chen, Y.; Liao, M. Internal finishing process of alumina ceramic tubes by ultrasonic-assisted magnetic abrasive finishing. *Int. J. Adv. Manuf. Technol.* **2016**, *85*, 727–734. [CrossRef]
20. Zhang, J.; Hu, J.; Wang, H.; Kumar, A.S.; Chaudhari, A. A novel magnetically driven polishing technique for internal surface finishing. *Precis. Eng.* **2018**, *54*, 222–232. [CrossRef]
21. Zhang, J.; Wang, H.; Kumar, A.S.; Jin, M. Experimental and theoretical study of internal finishing by a novel magnetically driven polishing tool. *Int. J. Mach. Tools Manuf.* **2020**, *153*, 103552. [CrossRef]
22. Wang, C.; Cheung, C.F.; Ho, L.T.; Yung, K.L.; Kong, L. A novel magnetic field-assisted mass polishing of freeform surfaces. *J. Mater. Process. Technol.* **2020**, *279*, 116552. [CrossRef]
23. Yamaguchi, H.; Srivastava, A.K.; Tan, M.A.; Riveros, R.E.; Hashimoto, F. Magnetic abrasive finishing of cutting tools for machining of titanium alloys. *CIRP Ann.* **2012**, *61*, 311–314. [CrossRef]
24. Guo, J.; Liu, K.; Wang, Z.; Tnay, G.L. Magnetic field-assisted finishing of a mold insert with curved microstructures for injection molding of microfluidic chips. *Tribol. Int.* **2017**, *114*, 306–314. [CrossRef]
25. Ko, S.; Baron, Y.M.; Park, J. Micro deburring for precision parts using magnetic abrasive finishing method. *J. Mater. Process. Technol.* **2007**, *187–188*, 19–25. [CrossRef]
26. Singh, G.; Kumar, H.; Kansal, H.K.; Srivastava, A. Effects of Chemically assisted Magnetic Abrasive Finishing Process Parameters on Material Removal of Inconel 625 tubes. *Procedia Manuf.* **2020**, *48*, 466–473. [CrossRef]
27. Kajal, S.; Jain, V.K.; Ramkumar, J.; Nagdeve, L. Experimental and theoretical investigations into internal magnetic abrasive finishing of a revolver barrel. *Int. J. Adv. Manuf. Tech.* **2019**, *100*, 1106–1107. [CrossRef]
28. Singh, P.; Singh, L.; Singh, S. Manufacturing and performance analysis of mechanically alloyed magnetic abrasives for magneto abrasive flow finishing. *J. Manuf. Process.* **2020**, *50*, 161–169. [CrossRef]
29. Guo, J.; Feng, W.; Jong, H.J.H.; Suzuki, H.; Kang, R. Finishing of rectangular microfeatures by localized vibration-assisted magnetic abrasive polishing method. *J. Manuf. Process.* **2020**, *49*, 204–213. [CrossRef]
30. Wu, P.-Y.; Yamaguchi, H. Material Removal Mechanism of Additively Manufactured Components Finished using Magnetic Abrasive Finishing. *Procedia Manuf.* **2018**, *26*, 394–402. [CrossRef]
31. Yao, C.; Zhang, W.; Li, K.; Xu, X.; Li, H. Study on the formation mechanism of the magnetic abrasive particle layer on the surface of saw wire in magnetic induction-free abrasive wire sawing. *Powder Technol.* **2018**, *327*, 163–169. [CrossRef]
32. Singh, R.K.; Singh, D.; Gangwar, S. Advances in magnetic abrasive finishing for futuristic requirements—A review. *Mater. Today Proc.* **2018**, *5*, 20455–20463. [CrossRef]
33. Yamaguchi, H.; Shinmura, T.; Sekine, M. Uniform internal finishing of SUS304 stainless steel bent tube using a magnetic abrasive finishing process. *J. Manuf. Sci. Eng.* **2005**, *127*, 605–611. [CrossRef]
34. Wang, Y.; Hu, D. Study on the inner surface finishing of tubing by magnetic abrasive finishing. *Int. J. Mach. Tools Manuf.* **2005**, *45*, 43–49. [CrossRef]
35. Srivastava, A.; Kumar, H.; Singh, S. Investigations into internal surface finishing of titanium (Grade 2) tube with extended magnetic tool. *Sci. Direct Procedia Manuf.* **2018**, *26*, 181–189. [CrossRef]
36. Ihara, I.; Nakano, E.; McLamore, E.; Schueller, J.K.; Toyoda, K.; Umetsu, K.; Yamaguchi, H. Cleanability of milk deposits on inner stainless steel tubing surfaces prepared by magnetic abrasive finishing. *Eng. Agric. Env. Food* **2016**, *10*, 63–68. [CrossRef]
37. Ahn, B.W.; Lee, S.H. Run-to-run process control of magnetic abrasive finishing using bonded abrasive particles. *Proc. Inst. Mech. Eng. B J. Eng. Manuf.* **2012**, *226*, 1963–1975. [CrossRef]
38. Chen, Y.; Song, Q.H.; Wang, X. Study on the characteristics of simply mixed the magnetic abrasive particles. *Adv. Mater. Res.* **2007**, *24–25*, 133–138. [CrossRef]
39. Fan, Z.; Tian, Y.; Zhou, Q.; Shi, C. Enhanced magnetic abrasive finishing of Ti–6Al–4V using shear thickening fluids additives. *Precis. Eng.* **2020**, *64*, 300–306. [CrossRef]
40. Gao, Y.; Zhao, Y.; Zhang, G. Preparation of Al2O3 magnetic abrasives by gas-solid two-phase double-stage atomization and rapid solidification. *Mater. Lett.* **2018**, *215*, 300–304. [CrossRef]
41. Gao, Y.; Zhao, Y.; Zhang, G.; Yin, F.; Zhao, G.; Guo, H. Preparation and characterization of spherical diamond magnetic abrasive powder by atomization process. *Diam. Relat. Mater.* **2020**, *102*, 107658. [CrossRef]
42. Li, W.; Li, J.; Cheng, B.; Zhang, X.; Song, Q.; Wang, Y.; Zhang, T.; Seniuts, U.; Belotsrkovsky, M. Achieving in-situ alloy-hardening core-shell structured carbonyl iron powders for magnetic abrasive finishing. *Mater. Des.* **2021**, *212*, 110198. [CrossRef]

43. Liao, G.B.; Zhang, M.M.; Li, Y.J.; Liu, Z.Q.; Chen, Y. Preparation of magnetic abrasive by sintering method finishing by sintering method. *Key Eng. Mater.* **2011**, *487*, 273–277. [CrossRef]
44. Yamaguchi, H.; Hanada, K. Development of spherical magnetic abrasive made by plasma spray. *J. Manuf. Sci. Eng.* **2008**, *130*, 0311071–0311079. [CrossRef]
45. Hanada, K.; Yamaguchi, H.; Zhou, H. New spherical magnetic abrasives with carried diamond particles for internal finishing of capillary tubes. *Diam. Relat. Mater.* **2008**, *17*, 1434–1437. [CrossRef]
46. Hanada, K.; Yamaguchi, H. Development of spherical iron-based composite powder with carried alumina abrasive grains by plasma spray. *Adv. Mater. Res.* **2009**, *75*, 43–46. [CrossRef]
47. Yang, B.; Lu, W.; Feng, W.; Yang, X.; Zuo, D. Adsorption and deposition of micro diamond particles in preparing diamond magnetic abrasives by electroless composite plating. *Diam. Relat. Mater.* **2017**, *73*, 137–142. [CrossRef]
48. Si, C.; Tang, X.; Zhang, X.; Wang, J.; Wu, W. Characteristics of 7055Al alloy powders manufactured by gas-solid two-phase atomization: A comparison with gas atomization process. *Mater. Des.* **2017**, *118*, 66–74. [CrossRef]
49. Song, Z.; Zhao, Y.; Li, Z.; Cao, C.; Liu, G.; Liu, Q.; Zhang, X.; Dai, D.; Zheng, Z.; Zhao, C.; et al. Study on the Micro Removal Process of Inner Surface of Cobalt Chromium Alloy Cardiovascular Stent Tubes. *Micromachines* **2022**, *13*, 1374. [CrossRef]
50. Deng, Y.; Zhao, Y.; Zhao, G.; Gao, Y.; Liu, G.; Wang, K. Study on magnetic abrasive finishing of the inner surface of Ni–Ti alloy cardiovascular stents tube. *Int. J. Adv. Manuf. Technol.* **2022**, *118*, 2299–2309. [CrossRef]

micromachines

MDPI

Article

Concurrently Fabricating Precision Meso- and Microscale Cross-Scale Arrayed Metal Features and Components by Using Wire-Anode Scanning Electroforming Technique

Shicheng Li, Pingmei Ming *, Junzhong Zhang *, Yunyan Zhang and Liang Yan

School of Mechanical and Power Engineering, Henan Polytechnic University, Jiaozuo 454000, China
* Correspondence: mingpingmei@163.com (P.M.); zhangjunzhong0520@163.com (J.Z.)

Abstract: In order to improve the thickness uniformity of the electroformed metal layer and components, a new electroforming technique is proposed—wire-anode scanning electroforming (WAS-EF). WAS-EF uses an ultrafine inert anode so that the interelectrode voltage/current is superimposed upon a very narrow ribbon-shaped area at the cathode, thus ensuring better localization of the electric field. The anode of WAS-EF is in constant motion, which reduces the effect of the current edge effect. The stirring paddle of WAS-EF can affect the fluid flow in the microstructure, and improve the mass transfer effect inside the structure. The simulation results show that, when the depth-to-width ratio decreases from 1 to 0.23, the depth of fluid flow in the microstructure can increase from 30% to 100%. Experimental results show that. Compared with the traditional electroforming method, the single metal feature and arrayed metal components prepared by WAS-EF are respectively improved by 15.5% and 11.4%.

Keywords: cross-scale arrayed metal; thickness uniformity; wire-anode scanning electroforming

1. Introduction

Length scales for manufacturing processes are generally classified as nanoscale (<100 nm), microscale (100 nm to 100 μm), mesoscale (0.1 mm to 10 mm), and macroscale (>0.5 mm) [1]. It can be seen that the meso-manufacturing process is cross-scale manufacturing; it fills the gap between macro- and micromanufacturing processes and overlaps both of them. At each scale, of course, there are various available manufacturing processes based on different governing mechanisms developed for a variety of engineering materials and geometric shapes. In the miniature engineering fields, a wide variety of microscale and mesoscale metal (M^3) features and components with high accuracy and precision are highly demanded, for example, mechanical watch gears [2], small motors and bearings, mesoscale fuel cells [3], micro-/meso-scale pumps and valves [4,5], medical stents [6], mini nozzles, printing stencils for electronic packaging, and many others.

Manufacturing at the microscale and mesoscale can be accomplished by scaling down macroscale manufacturing processes or scaling up nanomanufacturing or micromanufacturing processes. The scaling down processes create the features and components by subtractively removing materials gradually; hence, they are also called subtractive manufacturing processes. Oppositely, the latter are also called additive manufacturing (AM) processes. The subtractive micro and mesoscale metal manufacturing (subtractive-M^4) processes generally produce the features and components from the given materials one by one, and include mechanical machining (milling [7], turning, drilling [8], etc.), laser beam machining [9], focused ion beam machining [10,11], electro-discharge machining [12], and chemical/electrochemical machining [13,14], etc. The additive-M^4 processes produce the objects by depositing materials typically layer by layer and include electrochemical deposition (ECD) [15], electroless plating [16,17], focused-ion beam induced deposition (FIBID) [18], laser-chemical vapor deposition (LCVD) [19], etc. The additive-M^4 processes

are increasingly attractive since they can flexibly create geometric shapes and controllably tailor the material performances synchronously.

ECD is a widely used method to prepare metal materials with different forms such as film, coating, powder, bulk, and articles in a wide range of industrial applications, and correspondingly it has different application modes including electroplating, electrolytic refining, and electroforming. Compared with other additive-M^4 processes, ECD is more competitive in cost-efficiency, machinable materials, geometric shapes, and sizes, forming accuracy and precision, material compactness, etc. More attractively, it enables the manufacture of M^3 features and components in a large volume simultaneously in the same electrochemical reaction system with the photoresist mask-based electrodeposition (mask-based ECD) processes. The TM-ECD (through-mask ECD) forms precision M3 features and components by depositing the reduced metal atoms into the accurately pre-patterned thick-photoresist mask cavities which are finally removed, and so it is generally considered as a photoresist through-mask defined process, as shown in Figure 1. Currently, the TM-ECD has been preferably employed to manufacture M^3 features and components used for various applications.

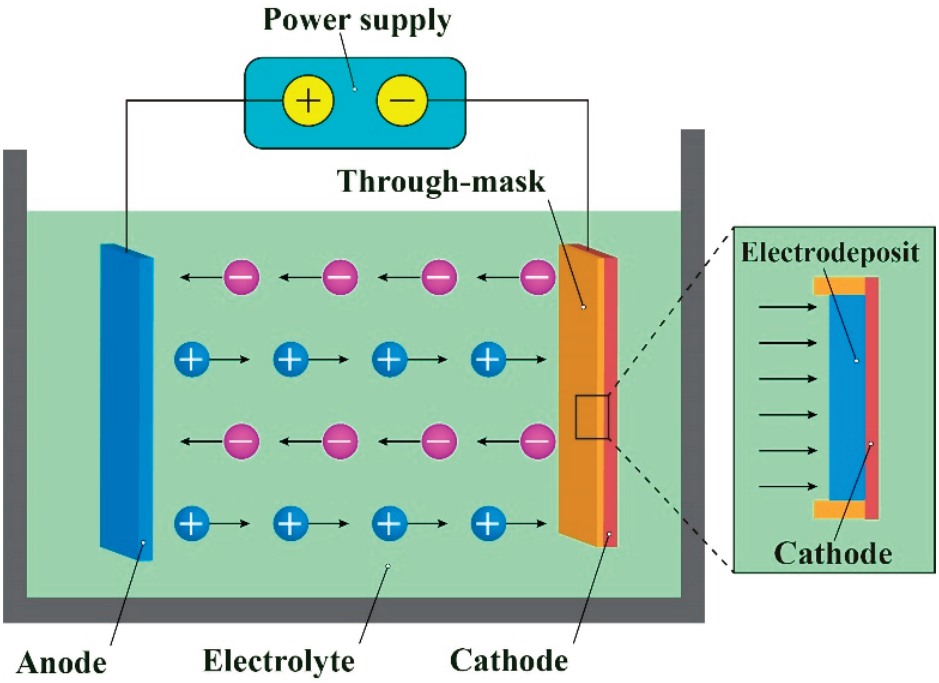

Figure 1. Working scheme and mechanism of TM-ECD.

In the traditional TM-ECD processes, electrodeposition is generally carried out by placing the cathode and anode to completely immerse in the electrolyte bath with the cathode and anode facing each other. The distance between the two electrodes is usually required to be not less than 10 cm to allow necessary mass transfer activities and related operations. Furthermore, to maintain normal dissolution of the anode, the area ratio of the cathode to the anode is generally greater than 1.5. These requirements mentioned above inevitably cause some problems, in which the uneven distribution of the deposit thickness in different through-mask cavities is the most frequently observed problem. The unevenness of the thickness distribution during the traditional TM-ECD stems from the nonuniform distribution of the current density at different electrodeposition areas, and in turn, the nonuniform electric field is mainly caused by the existence of the interelectrode gap (IEG) and through-mask patterns at the cathode as well as by the difference in the mass transportation rate at the different place. That is to say, the distribution characteristics of the mass transfer field and electric current field are the fundamental factors determining the deposit thickness distribution during TM-ECD. The uneven distribution of the deposit

thickness will result in a significantly reduced dimensional accuracy even the failure of the deposited M^3 features and components. Therefore, a number of investigators have made a variety of efforts to improve the deposit thickness distribution during TM-ECD.In the traditional maskless electrodeposition processes, assisting auxiliary electrode/thief electrode (cathode or anode) [20–24], using an electric field shield/conformal anode [25], reciprocating the cathode [26], applying modulated electric current [27,28], and adding appropriate additives [29–31] are frequently used methods to improve the deposit thickness distribution. However, these traditional methods are less effective for the TM-ECD processes, since the patterned photoresist through-masks are inherently inhomogeneous regarding the distribution of the current density and also the mass transfer rate distribution, especially when the electrodeposition is carried out via electrically filling the multiple-scale through-masks. Therefore, some investigators made a great effort to additionally explore some nontraditional methods to further homogenize the patterned deposits.

Tsai et al. [32] carried out the electroforming process in a highly pressurized bath to uniformize the deposit thickness. Zhai et al. [33] reported that appropriately applying ultrasonic or megasonic field to the bath solution can uniformize electrodeposition rate distribution during through-mask electroforming. Jie et al. [34] achieved an improved thickness uniformity by electrodepositing metals from the supercritical solution. Some researchers verified that the use of the reciprocating-paddle agitation close to the top surface of the patterned through-mask is significantly beneficial to achieve an improved deposit thickness.

This paper proposes a unique TM-ECD that is fundamentally different from the traditional TM-ECD processes in which a large surface-area ratio between the anode and cathode is used and the IEG is also very large. In the proposed TM-ECD, a linear wire-shaped ultrafine (diameter/width $\leq$ 50 μm) electrically inert anode (abbreviated as wire-anode) that is fixed on a reciprocating paddle is used, and the working gap between the anode and the top surface of the through-mask is kept below 500 μm. Here, this novel TM-ECD is especially called wire-anode scanning electroforming (WAS-EF). During WAS-EF, the stirring paddle is moving reciprocally with a constant speed. With WAS-EF, it is expected to achieve high-precision deposition of a variety of multi-scale components on the same cathode at the same time. In the following sections, verification studies will be carried out theoretically and experimentally with various evaluations including electrodeposition behaviors, surface morphology, dimensional accuracy, etc.

2. Working Scheme of Wire-Anode Scanning Electroforming

Figure 2 shows the schematic diagram of the WAS-EF. The electric potential/current from a static anode superimposes a very narrow ribbon-shaped area at the cathode, showing a Gaussian distribution characteristic. It was found in that, depending on the working gap between the anode and the top surface of the through-mask, the ribbon width is generally less than 100 times as wide as the width/diameter of the anode. The theoretical model of a static WSA-EF is shown in Figure 2b. Based on the Butler–Volmer equation, the overpotential deriving from the wire-anode at the cathode also shows a similar Gaussian distribution characteristic. The overpotential distribution function, $\eta(w)$, can be approximately expressed as follows [35],

$$\eta(w) = \frac{2\eta_0}{\pi w_0^2} \exp\left(-\frac{2w^2}{w_0^2}\right) \quad (1)$$

where w is the horizontal distance away from the anode's central line, η_0 is the overpotential value when w = 0, and w_0 is the distance away from the anode central line when $\eta(w_0) = \eta_e$ (η_e is the critical evolution overpotential of a specific metal ion).

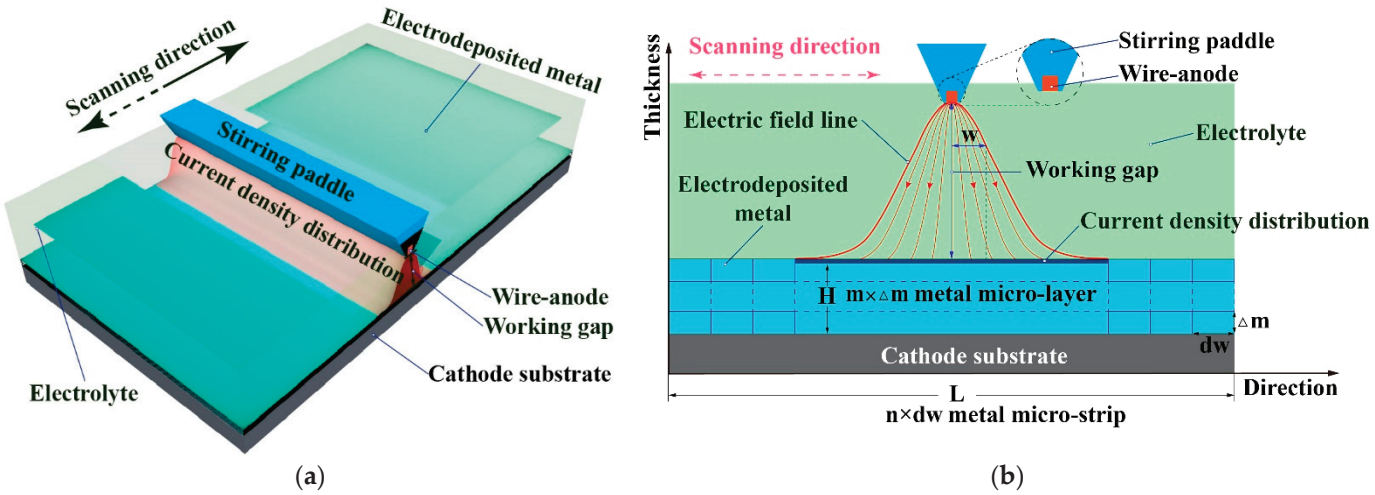

Figure 2. Schematic diagram of the WAS-EF without using through-masks and its forming mechanism. (**a**) schematic diagram of the WAS-EF; (**b**) forming mechanism of deposit during WAS-EF.

According to the metal growth mechanism during WAS-EF, the resulting electrodeposited material can be divided horizontally into m micro-layers, and each microlayer can be divided vertically into n micro-strips, as shown in Figure 2b. The length dw of the micro-strip is calculated as follows,

$$dw = \frac{L}{n} \tag{2}$$

where L is the total length of electrodeposited material along the scanning direction. The deposition time of the micro-strip can be estimated by the following formula,

$$t = (dw + |2w_0|)/v \tag{3}$$

$$\Delta m \propto t \tag{4}$$

where v is the scanning speed of the wire-anode and Δm is the height of a single micro-layer.

According to Formulas (2)–(4), the deposit thickness is majorly controlled by the scanning speed. This is significantly different from the traditional bath electroplating processes in which the deposit thickness is affected by quite a few process parameters. Therefore, a very uniform deposit can be achieved if the deposition time is deliberately selected.

Figure 3 schematically shows the working mode when the WAS-EF is used to fabricate micro/mesoscale features and components in batches with through-masks. Unlike the blank WAS-EF with a constantly homogeneous electric current field, the mask-based WAS-EF may have a varying electric field distribution changing with the location change of the scanning anode. As shown in Figure 3b, during the scanning of the wire-anode, the electric current distribution varies when the anode approaches and is right over the through-masks. This is due to the existence of dielectric material (through-masks) which locally changes the electric conductivity. It is also shown that the electric current distribution varies somewhat with the size of the through-mask's cavity during the scanning of the anode. However, these differences may be greatly reduced because the electric energy acts very locally and keeps moving, and especially, the mass transfer rate in the working gap stirred by a moving triangle-sectional paddle is little affected by the size of the cavities. It has been verified that, with the stirring of a triangular paddle moving slowly, laminar-flow convection mass transfer forms outside the mask's cavities, but diffusion mass transfer dominates within the cavities. These beneficial factors may greatly improve the current distribution and thus the thickness distribution uniformity of WAS-EF.

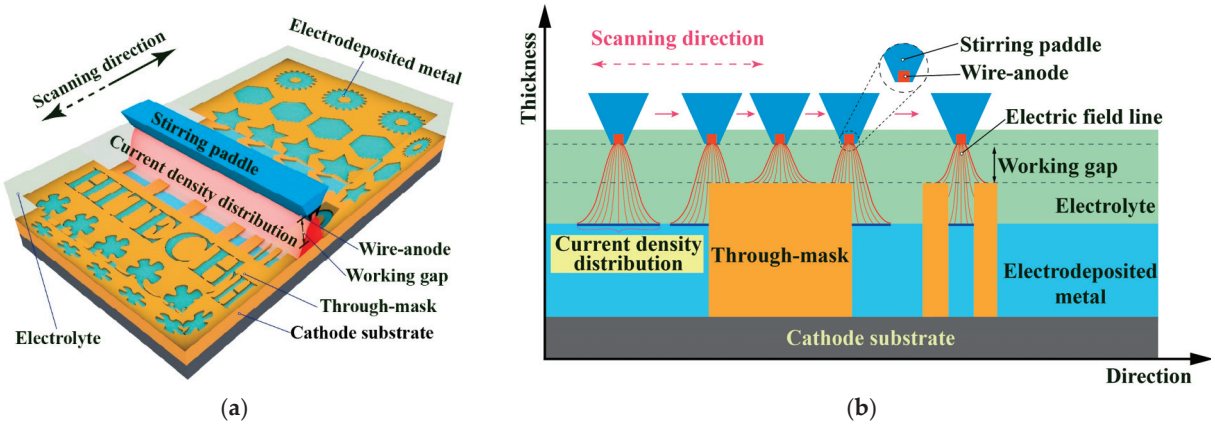

Figure 3. Schematic diagram of the WAS-EF using through-masks and its forming mechanism. (**a**) schematic diagram of the WAS-EF; (**b**) forming mechanism of deposit during WAS-EF.

3. Simulation of Electric and Flow Fields during WAS-EF

3.1. Modeling and Conditions

According to the machining principle described above, the wire-anode scanning electroforming machining is simplified into a physical model of numerical simulation, as shown in Figure 4. In the direction of calculating the length of the domain, three kinds of micro-groove structures with a thickness of 70 µm and width of 0.07 mm, 0.1 mm, 0.2 mm, and 0.3 mm were set. The wire-anode and the stirring paddle are located 100 µm above the through-mask. The COMSOL Multiphysics (5.5a) software was used to simulate the model. The secondary current distribution interface was selected in the simulation physical field, and the flow of electrolyte and the reciprocating linear motion of wire-anode were realized through the fluid-structure coupling interface. The flow field and electric field were coupled by the conductivity. To improve the convergence of simulation calculation, the mesh is automatically re-divided in the calculation. Data collection is performed during a single process of wire-anode movement. The corresponding time is as follows, S1-0.6s, S2-1.5s, S3-2.4s, S4-3.4s, S5-4.7s, S6-6.4s, S7-8.4s, S8-11s, and S9-13.7s.

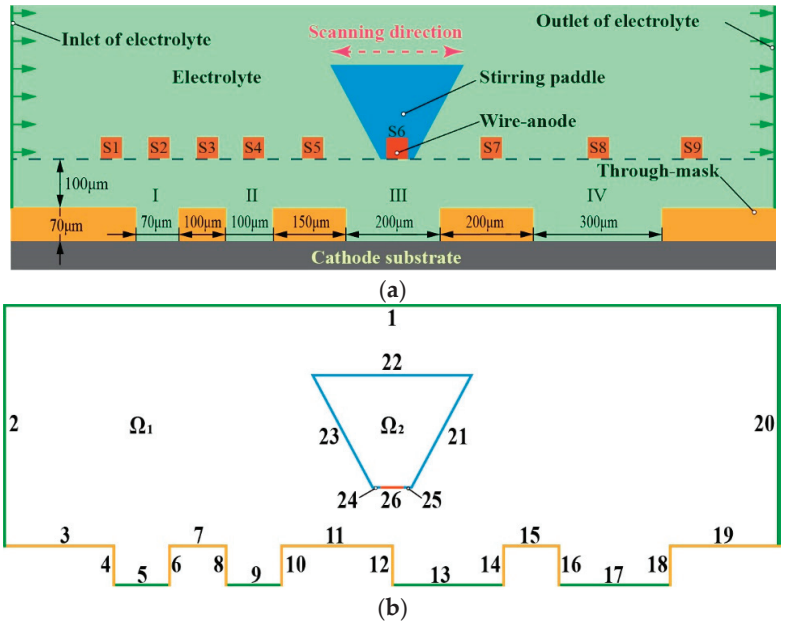

Figure 4. Schematic diagram of a simplified model of wire-anode scanning electroforming. (**a**) Diagram of the simplified geometric model. S1 to S9 are the wire-anodes located at 9 specific positions; (**b**) Diagram of domains and boundaries.

The fluid flow model adopts the flow governing equation of incompressible fluid, namely, the Navier–Stokes equation [36], and the relevant governing equation is as follows.

$$\nabla u = 0 \tag{5}$$

$$\rho(\frac{\partial u}{\partial t} + u{\cdot}\nabla u) = -\nabla p + \nabla(\mu(\nabla u + (\nabla u)^T)) + F \tag{6}$$

where ρ stands for density (kg/m^3), μ for dynamic viscosity ($N{\cdot}s/m^2$), u for velocity (m/s), p for pressure (Pa), and F for surface tension.

The secondary current density distribution was used to characterize the electrochemical kinetic reaction at the cathode interface, that is, the Bulter–Volmer equation [37] was used as the kinetic model of the electrochemical polarization reaction at the cathode.

$$i_{loc} = i_0 \left(\exp(\frac{\alpha_a F\eta}{RT}) - \exp(\frac{\alpha_c F\eta}{RT})\right) \tag{7}$$

$$\eta = \phi_s - \phi_l - E_{eq} \tag{8}$$

where i_{loc} is the local current density, i_0 is the exchange current density, α_a is the anode reaction coefficient, α_c is the cathode reaction coefficient, η is the over-potential, F is the Faraday constant with the value of 98,485 C/mol, R is the gas constant with 8.314 J/(mol·K), T is the thermodynamic temperature, ϕ_s is the electrode potential, and ϕ_l is electrolyte potential; E_{eq} is the equilibrium potential of electrodeposited metal.

As shown in Figure 4b, domain Ω_1 is the electrolyte, domain Ω_2 is the stirring paddle, boundary 2 is the electrolyte inlet, boundary 20 is the electrolyte outlet, boundary 26 is the wire-anode, boundary 3–19 is the photoresist, boundary 5, 9, 13, 17 is the cathode surface, and boundary 21 to 25 is the stirring paddle boundary. Other specific settings and parameters are shown in Table 1. Boundary conditions for numerical simulation of wire-anode scanning electroforming are shown in Table 2.

Table 1. Domain conditions of WAS-EF.

Domain Conditions	Domain	Property
Electrolyte	Ω_1	ρ_1 = 1.042 g/cm^3; $\mu_1 = 1.062 \times 10^{-3}$ Pa·s σ_1 = 10.3 S/m; T = 328.15 K
Stirring paddle	Ω_2	ρ_2 = 1.18 g/cm^3; E = 3.16 × 109 Pa nu = 0.32
Specify deformation domain	Ω_2	X = 0.00055 [m] × sin (2 × pi × t [1/s]); Y = 0

Table 2. Boundary conditions for numerical simulation of wire-anode scanning electroforming.

Boundary Conditions	Boundary	Property
Electrolyte inlet	2	U_0 = 0.1 m/s
Outlet	20	p_0 = 0 Pa
Anode	26	I_0 = 250 A/m^2
Cathode	5, 9, 13, 17	0 V
Wall	3–19	Slip

To simplify the calculation without losing generality, the following assumptions were made in terms of flow field: (1) the electrolyte is an incompressible viscous fluid, and the conductivity, temperature, density, and other parameters in the electrolyte remain unchanged and equal at each position; (2) The initial state of electrolyte is static, and the influence of electrolyte gravity is ignored; (3) The temperature does not change during the electrode reaction.

3.2. Electric Field Distribution in the Cathode Region

To better represent the current density distribution on the cathode surface in the process of wire-anode scanning electroforming, nine feature points were selected to analyze the current density distribution on the cathode surface based on a moving stroke.

As shown in Figure 5, the current density in the microstructure was the highest when the anode was directly above the microstructure (S2, S4, S6, S8), and the current density decreased as the anode moved away. The current density distribution is affected by the depth-to-width ratio. When the depth-to-width ratio is smaller, the current density per unit surface is lower, and the current distribution tends to be uniform with the increase in the aspect ratio.

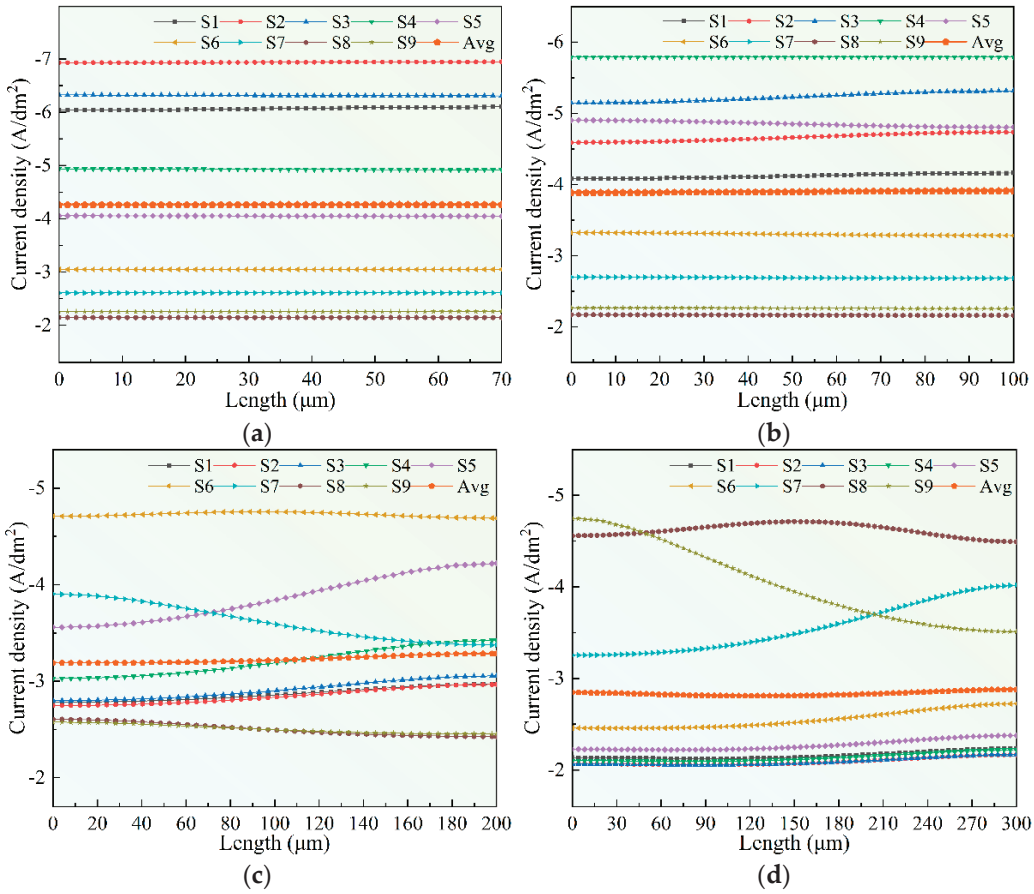

Figure 5. Diagram of current density distribution in each region when the anode is in different positions. (**a**) I; (**b**) II; (**c**) III; (**d**) IV.

Because the wire-anode is in constant motion, the current density distribution also changes in real time. Taking the microstructure IV as an example, when the wire-anode distance is far away from the microstructure IV (located at S1), the current density distribution is more uniform. When the wire-anode is in the S8 position (directly above IV), the current density distribution on the surface of microstructure IV is a Gaussian distribution, indicating that the width of the ribbon is less than the width of microstructure IV, which is consistent with what was said before. When the wire-anode is located at S7 and S9, the current density distribution on the cathode surface is reversed. In other words, the anode compensates for the current density distribution on the cathode surface during its motion. When the anode is on the left side of the area to be deposited, the high (low) current density area on the surface will be compensated when the anode is on the right side, thus achieving a dynamic equilibrium process.

The current density on the cathode surface of wire-anode scanning electroforming was superimposed (when the wire-anode was at nine characteristic points), and compared with the traditional electroforming mode, as shown in Figure 6. It can be seen that under the condition of wire-anode scanning electroforming, the current density distribution on the cathode surface is more uniform, which reduces the influence of bending electric field lines into the deposition area and improves the uniformity of the electroforming layer.

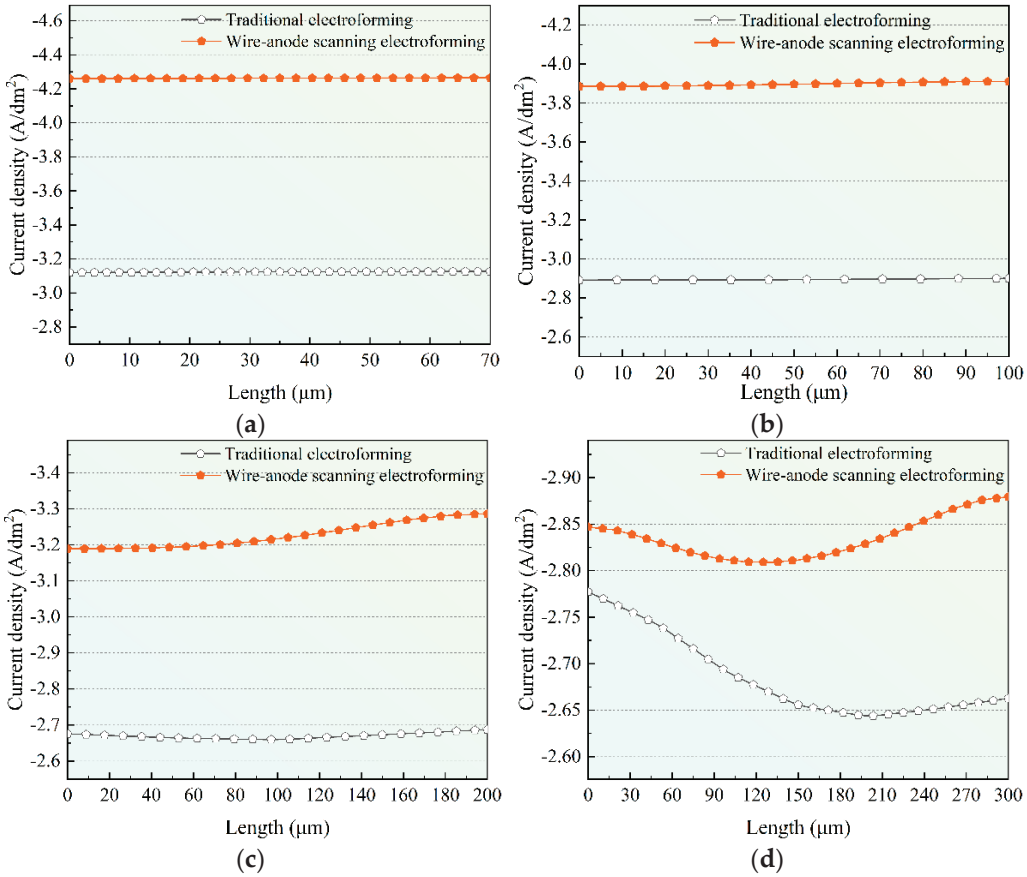

Figure 6. Schematic diagram of current density distribution in different areas under different electroforming methods. (**a**) I; (**b**) II; (**c**) III; (**d**) IV.

Therefore, compared with traditional electroforming methods, the wire-anode scanning electroforming method can improve the uniformity of electroforming current density to some extent.

3.3. Distribution of Flow Field in the Cathode Region

Figure 7 shows the influence of the stirring paddle on the cathode surface flow field when it is above the microstructure. It can be seen that the eddy generated by the stirring paddle motion will affect the fluid flow in the microstructure, which will improve the mass transfer effect inside the structure.

Figure 8a shows the flow velocity at the center of each microstructure of the stirring paddle under a static state. It can be seen that, due to the small size of the micro-structure, the internal influence of the flow field is weak. Figure 8b shows the fluid velocity in the inner central region of each microstructure when the stirring paddle is located above each structure (S2, S4, S6, S8).

It can be seen that the agitation effect of the stirring paddle on the electrolyte in the microstructure becomes more and more obvious with the decrease in the aspect ratio. When the depth-to-width ratio decreases from 1(I) to 0.23(IV), the agitation caused by the

stirring paddle can range from 20 μm to 70 μm. In this way, the mass transfer mode of electroforming is determined by diffusion and forced convection.

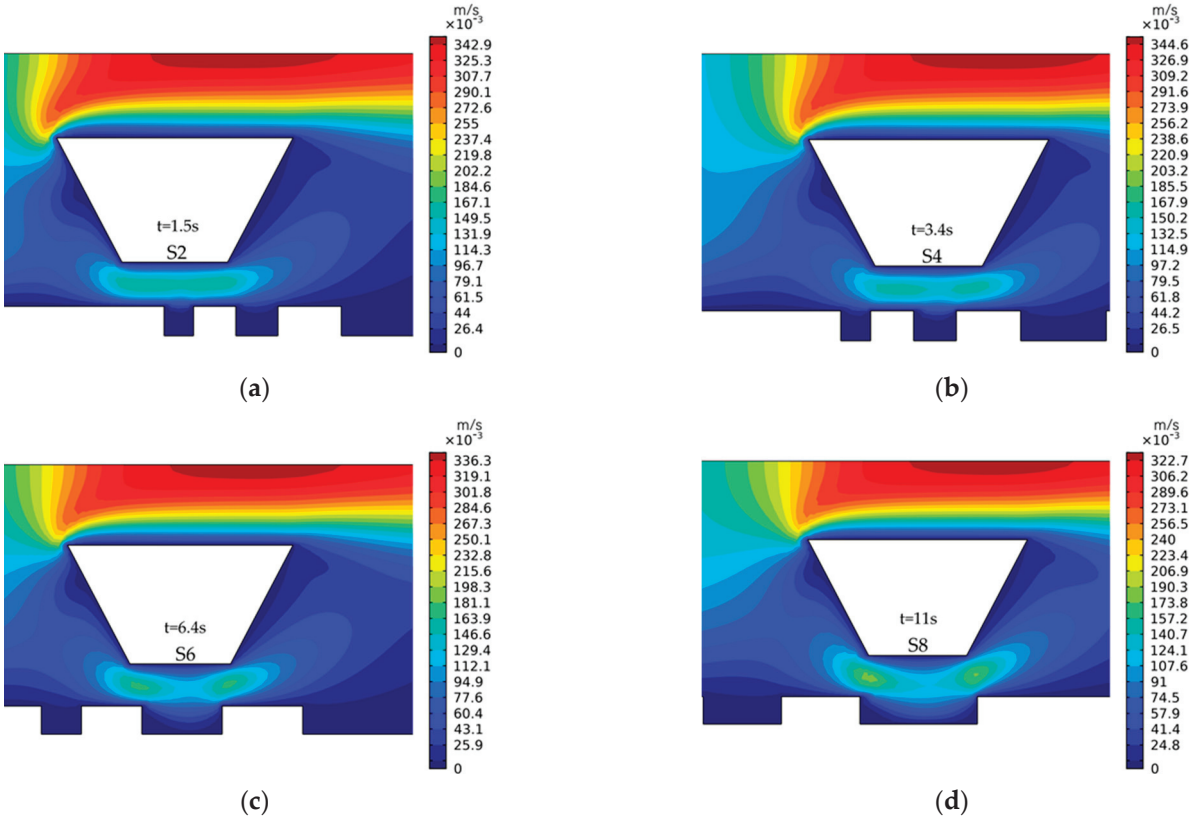

Figure 7. Diagram of flow field distribution in each region when the stirring paddle is directly above it. (**a**) I; (**b**) II; (**c**) III; (**d**) IV.

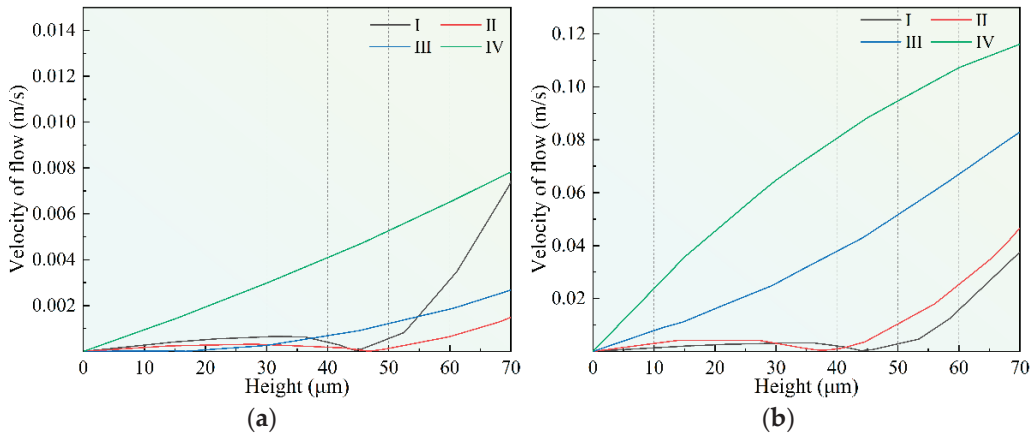

Figure 8. Diagram of the flow rate in each region of the stirring paddle under different states. (**a**) Static state; (**b**) When the stirring paddle is located directly above each area.

4. Experimental Study

4.1. Experimental Setup and Materials

The setup developed for WAS-EF is schematically shown in Figure 9. The electrolyte solution tank consists of the electroforming main tank and the electrolyte reservoir. An overflowing plate separating the electroforming tank and electrolyte reservoir was used to maintain and regulate the electrolyte height. The isosceles triangle cross-section of the used stirring paddle is 40 mm (B) and × 70 mm (S). The paddle is made of polymethyl

methacrylate polypropylene material. The anode is made of the platinum strip (99.999 wt%, 100 mm × 20 mm × 0.05 mm) which is embedded in the paddle with their bottom surfaces aligning with each other. The reciprocating scanning speed of the wire-anode is 1.0–100 mm/s. The working gap can be regulated, ranging from 10 μm to 70 μm. The wire-anode travel is 0–150 mm.

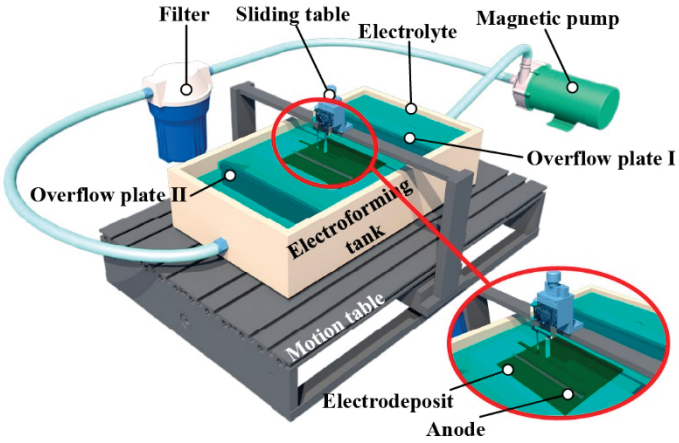

Figure 9. Schematic diagram of wire-anode scanning electroforming system.

The polished SUS304 stainless steel plate (100 mm × 100 mm × 1 mm) was used as the cathode substrate and was carefully pre-treated before its use. The photoresist through-masks were subsequentially prepared on the cathode substrates by using the standard dry photoresist film ((Dupont, Wilmington, DE, USA) lithographical processes. The thickness of the through-masks is 70 ± 1 μm, and the details of the through-masks are shown in Figure 10.

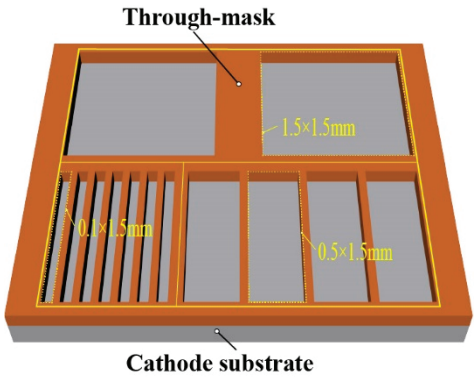

Figure 10. Schematic diagram of the designed multi-scale through-mask.

The electrolyte compositions were nickel sulfamate (500 g/L, AR, 98%) and boric acid (15 g/L, AR, 98%). Because of the use of the electrochemically inert anode, nickel chloride was not added. The electrolyte temperature was kept at 50 ± 1 °C. The pH value of the electrolyte was maintained at 4 ± 0.2 by adding sulfamate acid or nickel carbonate. A composition online testing and the auto-adding system were used to maintain compositions in the electrolyte at a designated value. A direct-current power supply (ITECH, IT6122B, China) was applied to the electroforming processes, and the working voltage was controlled at 2.6–6.0 V.

4.2. Surface Morphologies and Geometrical Dimension Accuracy Characterization

Observation of the surface morphology and topographies of the fabricated features and structures was conducted with a scanning electron microscope (Merlin Compact, Carl Zeiss NTS GmbH, GER), and laser confocal microscopes (Olympus, OLS5100, JP).

To facilitate the characterization of the thickness distribution of the samples with different scales, two parameters, θ, and η, were defined. θ was defined as the thickness distribution uniformity of the single-scale features, and η was defined as the thickness distribution uniformity of multiscale combined features, as shown in Figure 11.

$$\theta = \left(1 - \frac{D_{max} - d_{min}}{d_m}\right) \times 100\% \quad (9)$$

$$d_m = \frac{D_{max} + d_{min}}{2} \quad (10)$$

$$\eta = \left(1 - \frac{H_{max} - h_{min}}{h_m}\right) \times 100\% \quad (11)$$

$$h_m = \frac{\sum_{i=1}^{n}(H_i + h_i)}{n} \quad (12)$$

where D_{max} and d_{min}, respectively are the maximum and minimum thickness of the single part, d_m is the average thickness of the single part, H_{max} and h_{min} are the maximum and minimum thickness of i parts in the part array, h_m is the average thickness of all electroformed components using the same through-mask, and n is the number of electroformed parts using the same through-mask.

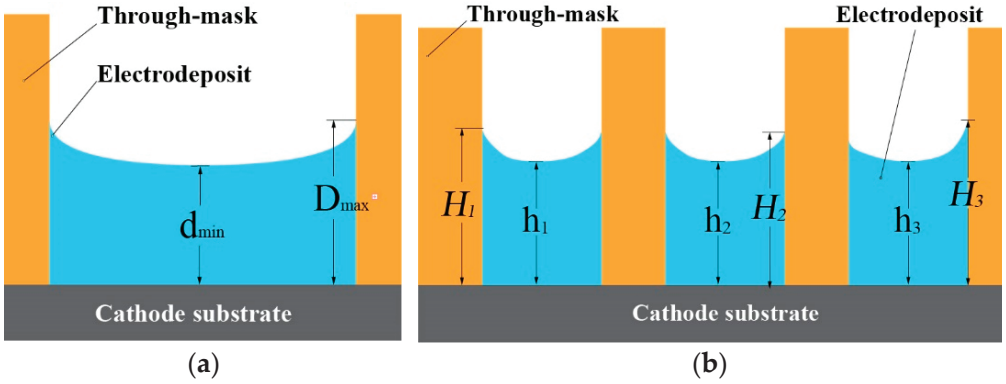

Figure 11. Schematic diagram of electroformed parts thickness evaluation. (**a**) single part; (**b**) part arrays.

5. Results and Discussion

5.1. Surface Morphology Analysis of Parts

Figure 12 shows the effect on surface quality at different machining voltages, from 2.6 to 6 V. When the electroforming voltage is low (2.6 V), the surface of the parts is not smooth, and there are local protrusions and other defects, as shown in Figure 12a. This is because under the condition of low voltage, the reaction is slow and the bubbles are generated slowly. Therefore, large bubbles cannot be quickly formed and be desorbed on the electrode surface, resulting in bubble accumulation and resulting in poor surface quality. When the machining voltage is 4 V, the surface morphology of the electrodeposited layer is smooth, as shown in Figure 12b. When the voltage is too high (6 V), there are more nodules on the surface of the parts, as shown in Figure 12c. The parts made by traditional electroforming are shown in Figure 12d; under the same conditions, the surface of the electroforming is poor, and there is insufficient deposition and other phenomena. This is because the accumulation of bubbles in the electroforming process will block the photoresist surface and thus affect the electroforming process. However, in the wire-anode scanning electroforming mode, the reciprocating movement of the stirring paddle will accelerate the desorption of bubbles from the electrode surface, thus reducing the influence of bubbles on the electroforming process.

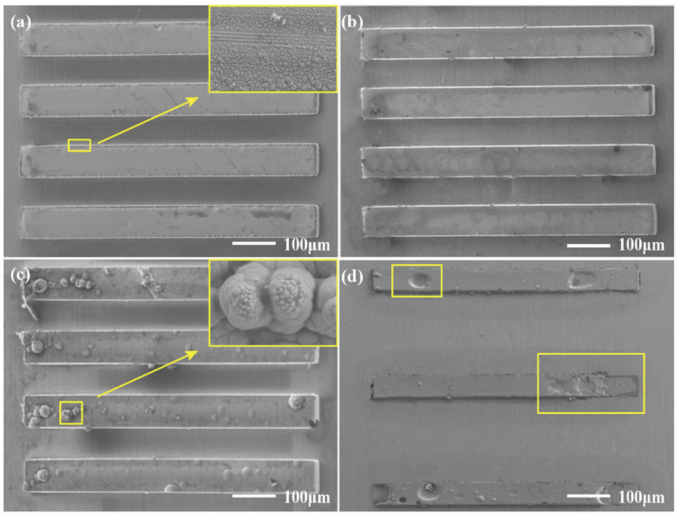

Figure 12. Surface morphologies of the electrodeposited 0.1 mm × 1.5 mm rectangular microscale features under different electroforming methods. (**a**) WAS-EF, 2.6 V; (**b**) WAS-EF, 4 V; (**c**) WAS-EF, 6 V; (**d**) Traditional electroforming.

Figure 13 shows the structural characteristics of the parts under different working gaps. As the working gap increases, the thickness uniformity of the parts decreases, which is because the parts are affected by the current edge effect. As mentioned above, the width of the current distribution at the cathode of wire-anode scanning electroforming depends on the size of the working gap. Figure 13e–h shows a schematic diagram of the current distribution in line anode scanning electroforming. When the working gap is small, the current distribution is narrow, the action area is small and hindered by the film, and the edge effect of the current is small. When the working gap is large, the action area becomes wider, when the wire-anode is located at the edge, the through-mask on the power line obstruction effect is weak, the influence of the current edge effect is larger, and the electrodeposited metal will become uneven.

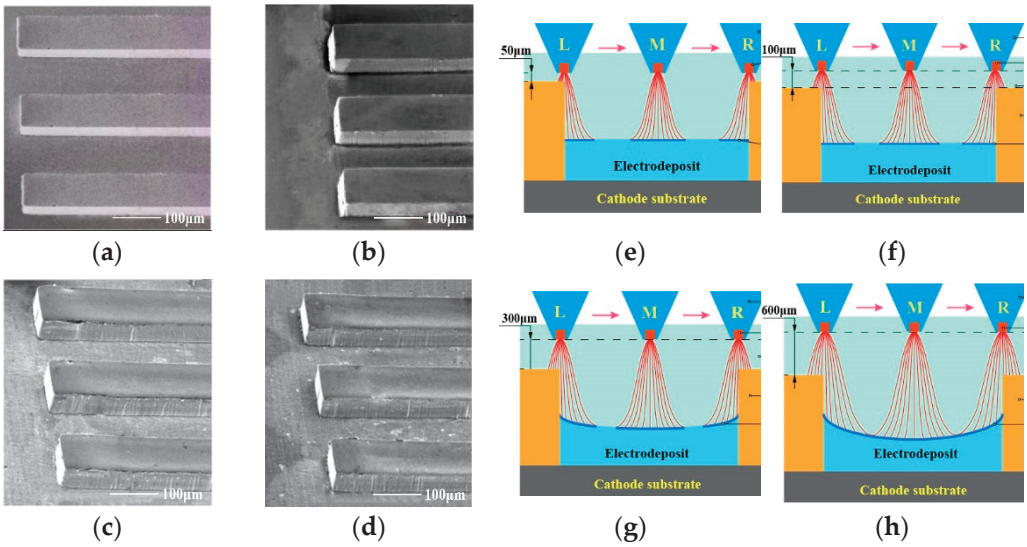

Figure 13. Profile and forming principle of wire-anode scanning electroforming with different working gaps. (**a**,**e**) 50 μm; (**b**,**f**) 100 μm; (**c**,**g**) 300 μm; (**d**,**h**) 600 μm.

5.2. Characteristic Analysis of Single Part

Figure 14a–c shows the thickness characteristics of different sizes of parts under the same electroforming condition. It can be seen that, when the processing conditions are the

same, the thickness of larger parts is significantly lower than small ones. This is because the same current density is applied to larger machining areas, and the average current density is lower, so the deposition rate is smaller and the deposition thickness is smaller; this is consistent with the current density distribution shown in Figure 5. Microcomponents with sizes of 100 µm and 1500 µm show a saddle shape with both sides high and the middle low, which is still affected by the edge effect of the current. When the microcomponent with the size of 300 µm presents a low convex shape on both sides of the middle process, this is because the mass transfer of the electrolyte on the side wall of the mask is constrained by the surface tension effect, so the electrolyte flow rate in the middle of the pit is faster than that on the side wall, and the final surface profile of the electrodeposited part is convex. In contrast, microstructures of the same size were prepared by the traditional electroforming method, as shown in Figure 14d–f. It can be seen that the influence of the current edge effect is more serious, and the thickness of the electroforming layer is more uneven.

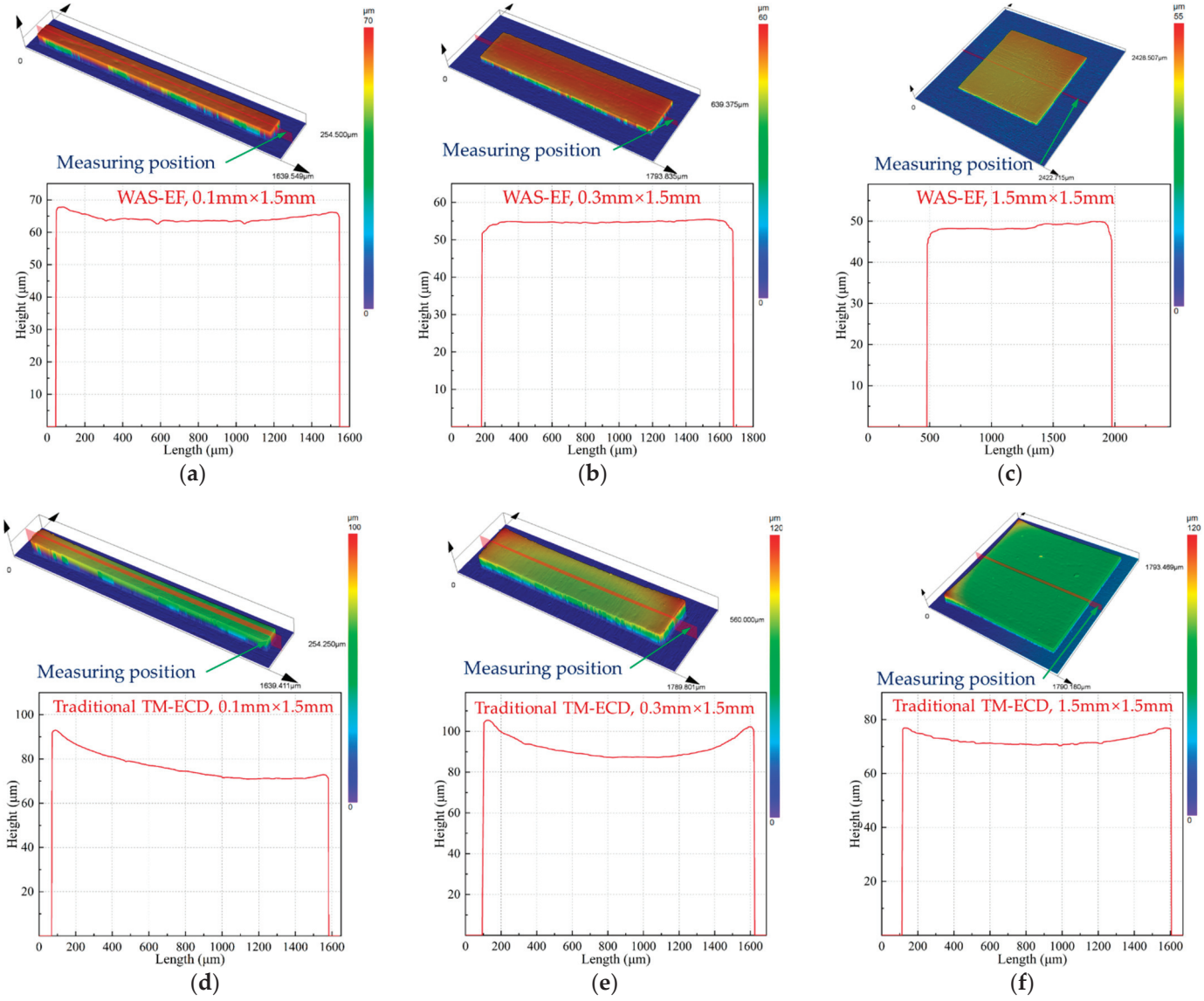

Figure 14. Geometric profile and thickness uniformity of the single part fabricated by different electroforming methods. (**a**) WAS-EF, 0.1 mm × 1.5 mm; (**b**) WAS-EF, 0.3 mm × 1.5 mm; (**c**) WAS-EF, 1.5 mm × 1.5 mm; (**d**) traditional TM-ECD, 0.1 mm × 1.5 mm; (**e**) traditional TM-ECD, 0.3 mm × 1.5 mm; (**f**) traditional TM-ECD, 1.5 mm × 1.5 mm.

5.3. Characteristic Analysis of Part Arrays

In the actual electroforming process, electroforming parts often face the problem of multi-scale/cross-scale, which is also the key factor affecting the thickness uniformity of parts at multi-scale/cross-scale. Therefore, the film containing pattern arrays were prepared on the substrate and used the optimized wire-anode scanning electroforming parameters to process

Figure 15 show the characteristics of the macro and micro parts of wire-anode scanning electroforming and traditional electroforming. It can be seen that the thickness uniformity of wire-anode scanning electroforming is better than that of traditional groove plating. However, from the aspect of scale effect characteristics (concave and convex on the surface of parts), the wire-anode scanning electroforming and traditional electroforming parts are affected by the edge effect, and their profiles cannot be completely flat. This is because of the existence of the photoresist; the substrate is divided into several conductive and non-conductive regions with different areas, and the obstruction and interference of the film on the electric field line will result in more chaotic and distorted current distribution on the cathode surface. Therefore, the current density of each part of the deposition zone is biased, so the thickness will also be affected.

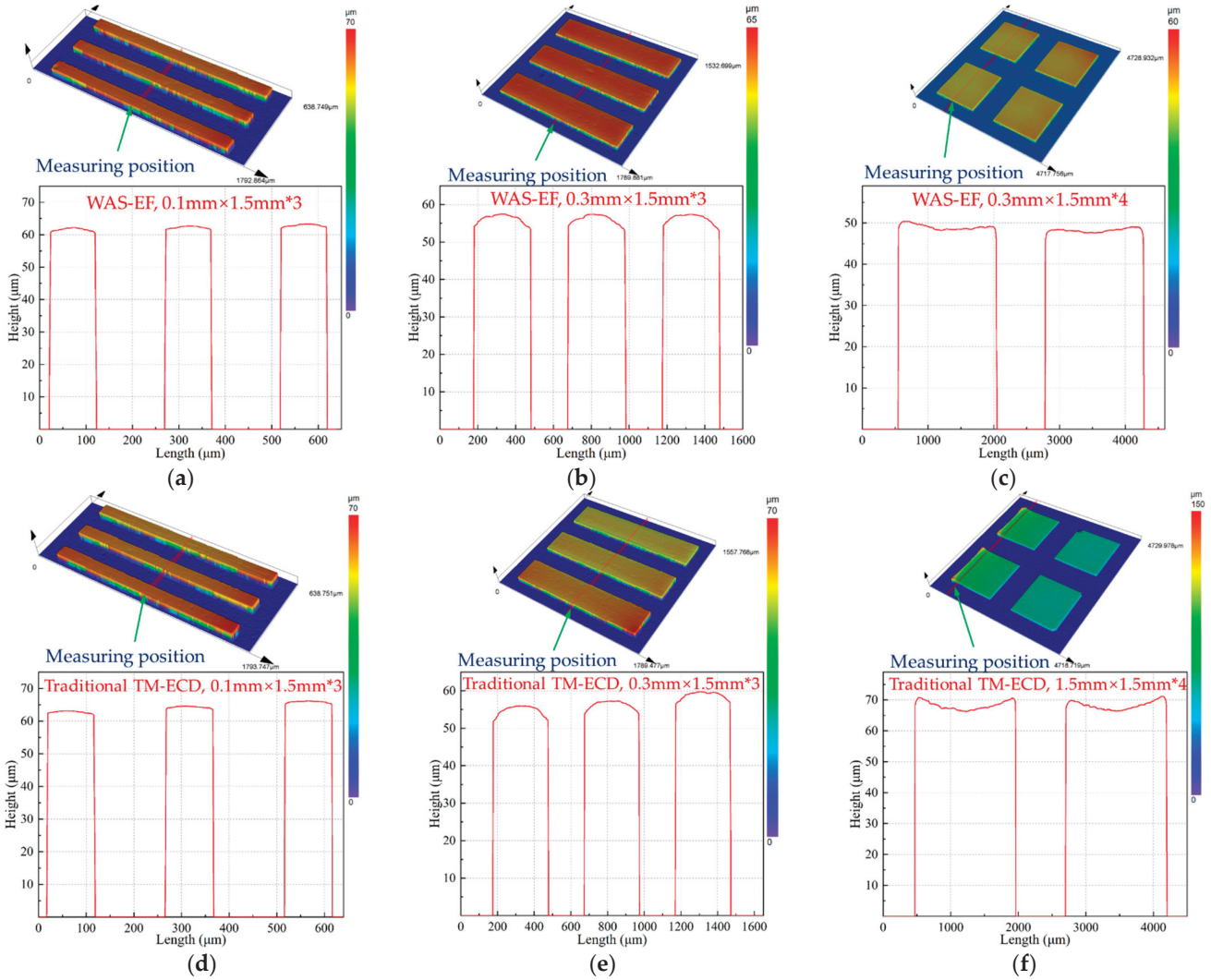

Figure 15. Geometric profile and thickness uniformity of the part arrays fabricated by different electroforming methods (**a**) WAS-EF, 0.1 mm × 1.5 mm; (**b**) WAS-EF, 0.3 mm × 1.5 mm; (**c**) WAS-EF, 1.5 mm × 1.5 mm; (**d**) traditional TM-ECD, 0.1 mm × 1.5 mm; (**e**) traditional TM-ECD, 0.3 mm × 1.5 mm; (**f**) traditional TM-ECD, 1.5 mm × 1.5 mm.

5.4. Parametric Analysis of Thickness Uniformity of Electroforming Parts

To evaluate the thickness uniformity of electroforming parts parametrically, θ and η defined above are used to evaluate them. Shown in Figure 16 are the thickness uniformity evaluation of single-size parts, and the uniformity evaluation of part arrays. Compared with the traditional electroforming method, the single metal feature and arrayed metal components prepared by WAS-EF are, respectively, improved by 15.5% and 11.4%. This shows that the effect of the current edge effect can be reduced by wire-anode scanning electroforming.

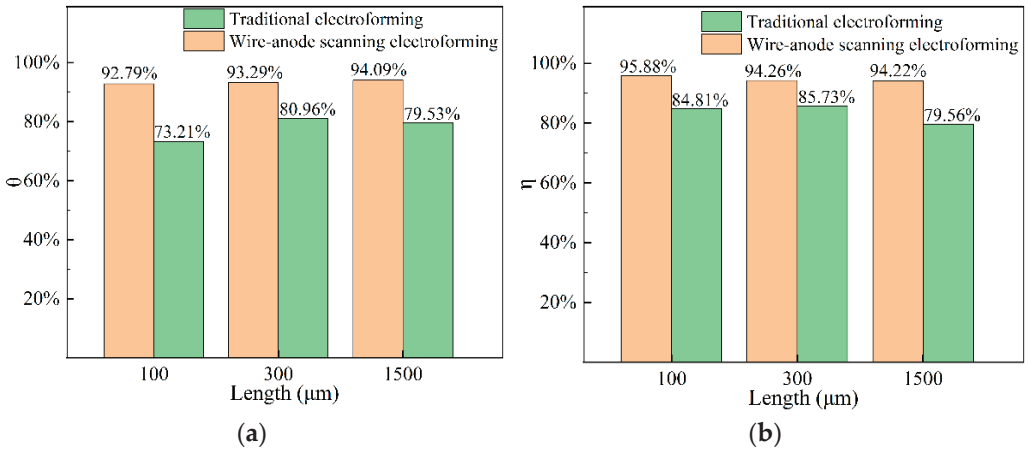

Figure 16. The value of θ and. (**a**) θ; (**b**) η.

6. Conclusions

In this paper, to prepare components with better thickness uniformity, a novel WAS-EF is proposed, in which a wire-anode is used and is kept moving to and fro over the cathode with a markedly small working gap. The simulation mode for WAS-EF was established, and the working principle was analyzed. Some conclusions are made as follows.

(1) Through numerical simulation, it can be concluded that the eddy current generated by a stirring paddle motion can affect the flow field in the micropore, resulting in a better mass transfer effect on the cathode surface. On the other hand, by stacking electric fields, it can be seen that the current density is higher and the distribution is more uniform in the mode of wire-anode scanning electroforming.

(2) The results show that the uniformity of components decreases with the increase in the working gap. When the machining voltage is high or low, the surface quality of components is not ideal. Under the optimized working gap and machining voltage, components with better uniformity can be obtained.

(3) Compared with the traditional electroforming technique, the thickness uniformity of wire-anode scanning electroforming is improved by 15.5% on average for the preparation of single-scale components, and 11.4% for the preparation of multi-scale component arrays.

Author Contributions: Conceptualization, P.M. and J.Z.; methodology, P.M.; software, S.L.; validation, P.M., J.Z. and S.L.; formal analysis, Y.Z.; investigation, L.Y.; resources, L.Y.; data curation, Y.Z.; writing—original draft preparation, S.L.; funding acquisition, P.M. All authors have read and agreed to the published version of the manuscript.

Funding: This research was funded by the National Natural Science Foundation of China, grant number 51875178, and the Scientific and Technological Key Project in Henan Province, grant number 20210221006.

Data Availability Statement: Not applicable.

Acknowledgments: This work was supported by the Fundamental Research Funds for the Universities of Henan Province grant number NSFRF210338.

Conflicts of Interest: The authors declare no conflict of interest.

References

1. Ehmann, K.F.; DeVor, R.E.; Kapoor, S.G. PL-2 Micro/Meso-Scale Mechanical Manufacturing: Opportunities and Challenges. *JSME/ASME Int. Conf. Mater. Process.* **2002**, *1*, 6–13. [CrossRef]
2. Chaubey, S.K.; Jain, N.K. State-of-Art Review of Past Research on Manufacturing of Meso and Micro Cylindrical Gears. *Precis. Eng.* **2018**, *51*, 702–728. [CrossRef]
3. Seo, H.; Kishimoto, M.; Nakagawa, T.; Iwai, H.; Yoshida, H. Mechanism of Improved Electrochemical Performance of Anode-Supported Solid Oxide Fuel Cells by Mesostructural Modification of Electrode–Electrolyte Interface. *J. Power Sources* **2021**, *506*, 230107. [CrossRef]
4. Lee, Y.-S.; Bhattacharjee, N.; Folch, A. 3D-Printed Quake-Style Microvalves and Micropumps. *Lab Chip* **2018**, *18*, 1207–1214. [CrossRef] [PubMed]
5. Im, S.B.; Uddin, M.J.; Jin, G.J.; Shim, J.S. A Disposable On-Chip Microvalve and Pump for Programmable Microfluidics. *Lab Chip* **2018**, *18*, 1310–1319. [CrossRef]
6. Van Lith, R.; Baker, E.; Ware, H.; Yang, J.; Farsheed, A.C.; Sun, C.; Ameer, G. 3D-Printing Strong High-Resolution Antioxidant Bioresorbable Vascular Stents. *Adv. Mater. Technol.* **2016**, *1*, 1600138. [CrossRef]
7. O'Toole, L.; Kang, C.-W.; Fang, F.-Z. Precision Micro-Milling Process: State of the Art. *Adv. Manuf.* **2021**, *9*, 173–205. [CrossRef]
8. Hasan, M.; Zhao, J.; Jiang, Z. A Review of Modern Advancements in Micro Drilling Techniques. *J. Manuf. Process.* **2017**, *29*, 343–375. [CrossRef]
9. Bachus, K.J.; Mats, L.; Choi, H.W.; Gibson, G.T.T.; Oleschuk, R.D. Fabrication of Patterned Superhydrophobic/Hydrophilic Substrates by Laser Micromachining for Small Volume Deposition and Droplet-Based Fluorescence. *ACS Appl. Mater. Interfaces* **2017**, *9*, 7629–7636. [CrossRef]
10. Li, P.; Chen, S.; Dai, H.; Yang, Z.; Chen, Z.; Wang, Y.; Chen, Y.; Peng, W.; Shan, W.; Duan, H. Recent Advances in Focused Ion Beam Nanofabrication for Nanostructures and Devices: Fundamentals and Applications. *Nanoscale* **2021**, *13*, 1529–1565. [CrossRef]
11. Buchnev, O.; Grant-Jacob, J.A.; Eason, R.W.; Zheludev, N.I.; Mills, B.; MacDonald, K.F. Deep-Learning-Assisted Focused Ion Beam Nanofabrication. *Nano Lett.* **2022**, *22*, 2734–2739. [CrossRef]
12. Zou, Z.; Guo, Z.; Huang, Q.; Yue, T.; Liu, J.; Chen, X. Precision EDM of Micron-Scale Diameter Hole Array Using in-Process Wire Electro-Discharge Grinding High-Aspect-Ratio Microelectrodes. *Micromachines* **2021**, *12*, 17. [CrossRef]
13. Zhan, D.; Han, L.; Zhang, J.; Shi, K.; Zhou, J.-Z.; Tian, Z.-W.; Tian, Z.-Q. Confined Chemical Etching for Electrochemical Machining with Nanoscale Accuracy. *Acc. Chem. Res.* **2016**, *49*, 2596–2604. [CrossRef]
14. Schuster, R.; Kirchner, V.; Allongue, P.; Ertl, G. Electrochemical Micromachining. *Science* **2000**, *289*, 98–101. [CrossRef]
15. Wei, W.; Pingmei, M.; Xinmin, Z.; Xinchao, L.; Yunyan, Z.; Shen, N.; Sansan, A. Additive Manufacturing of Three-Dimensional Intricate Microfeatures by Electrolyte-Column Localized Electrochemical Deposition. *Addit. Manuf.* **2022**, *50*, 102582. [CrossRef]
16. Hossain Bhuiyan, M.E.; Moreno, S.; Wang, C.; Minary-Jolandan, M. Interconnect Fabrication by Electroless Plating on 3D-Printed Electroplated Patterns. *ACS Appl. Mater. Interfaces* **2021**, *13*, 19271–19281. [CrossRef]
17. Kimura, M.; Yamagiwa, H.; Asakawa, D.; Noguchi, M.; Kurashina, T.; Fukawa, T.; Shirai, H. Site-Selective Electroless Nickel Plating on Patterned Thin Films of Macromolecular Metal Complexes. *ACS Appl. Mater. Interfaces* **2010**, *2*, 3714–3717. [CrossRef]
18. Chen, P.; van Veldhoven, E.; Sanford, C.A.; Salemink, H.W.M.; Maas, D.J.; Smith, D.A.; Rack, P.D.; Alkemade, P.F.A. Nanopillar Growth by Focused Helium Ion-Beam-Induced Deposition. *Nanotechnology* **2010**, *21*, 455302. [CrossRef]
19. Ning, B.; Xia, T.; Tong, Z.-X.; He, Y.-L. Experimental and Numerical Studies of Tungsten Line Growth in Laser Chemical Vapor Deposition. *Int. J. Heat Mass Transf.* **2019**, *140*, 564–578. [CrossRef]
20. Yang, H.; Kang, S.-W. Improvement of Thickness Uniformity in Nickel Electroforming for the LIGA Process. *Int. J. Adv. Manuf. Technol.* **2000**, *40*, 1065–1072. [CrossRef]
21. Qian, S.; Ji, F.; Qu, N.; Li, H. Improving the Localization of Surface Texture by Electrochemical Machining with Auxiliary Anode. *Mater. Manuf. Process.* **2014**, *29*, 1488–1493. [CrossRef]
22. Zhao, M.; Du, L.; Wei, Z.; Du, C.; Liu, X.; Ji, X. Fabrication of Metal Microfluidic Chip Mold with Coplanar Auxiliary Cathode in the Electroforming Process. *J. Micromech. Microeng.* **2018**, *29*, 025002. [CrossRef]
23. Ishizuka, N.; Yamada, T.; Izui, K.; Nishiwaki, S. Topology Optimization for Unifying Deposit Thickness in Electroplating Process. *Struct. Multidiscipl. Optim.* **2020**, *62*, 1767–1785. [CrossRef]
24. Xiang, J.; Chen, P.; Wang, Y.; Zeng, C.; Yang, W.; Li, J.; Xu, Y. Numerical Simulation of Optimizing Plating Uniformity of Interconnect Circuits on Printed Circuit Boards. *J. Phys. Conf. Ser.* **2021**, *1986*, 012135. [CrossRef]
25. Volgin, V.M.; Lyubimov, V.V.; Gnidina, I.V.; Kabanova, T.B.; Davydov, A.D. Effect of Anode Shape on Uniformity of Electrodeposition onto Resistive Substrates. *Electrochim. Acta* **2017**, *230*, 382–390. [CrossRef]
26. Fukukawa, M.; Tong, L. Effect of Mass Flow Induced by a Reciprocating Paddle on Electroplating. In Proceedings of the 2017 COMSOL Conference, Boston, MA, USA, 4–6 October 2017.

27. Zhao, Y.; Qian, S.; Zhang, Y.; Wan, X.; Zhang, H. Experimental Study on Uniformity of Copper Layer with Microstructure Arrays by Electroforming. *Int. J. Adv. Manuf. Technol.* **2021**, *114*, 2019–2030. [CrossRef]
28. Cao, Q.-D.; Fang, L.; Lv, J.-M.; Zhang, X.-P.; Thuy Dat, N. Effects of Pulse Reverse Electroforming Parameters on the Thickness Uniformity of Electroformed Copper Foil. *Trans. Inst. Met. Finish.* **2018**, *96*, 108–112. [CrossRef]
29. Suzuki, A.; Oue, S.; Kobayashi, S.; Nakano, H. Effects of Additives on the Surface Roughness and Throwing Power of Copper Deposited from Electrorefining Solutions. *Mater. Trans.* **2017**, *58*, 1538–1545. [CrossRef]
30. Chen, T.-C.; Tsai, Y.-L.; Hsu, C.-F.; Dow, W.-P.; Hashimoto, Y. Effects of Brighteners in a Copper Plating Bath on Throwing Power and Thermal Reliability of Plated Through Holes. *Electrochim. Acta* **2016**, *212*, 572–582. [CrossRef]
31. Chen, Y.; He, W.; Chen, X.; Wang, C.; Tao, Z.; Wang, S.; Zhou, G.; Moshrefi-Torbati, M. Plating Uniformity of Bottom-up Copper Pillars and Patterns for IC Substrates with Additive-Assisted Electrodeposition. *Electrochim. Acta* **2014**, *120*, 293–301. [CrossRef]
32. Tsai, T.-H.; Yang, H.; Chein, R. New Electroforming Technology Pressure Aid for LIGA Process. *Microsyst. Technol.* **2004**, *10*, 351–356. [CrossRef]
33. Zhai, K.; Du, L.; Wang, W.; Zhu, H.; Zhao, W.; Zhao, W. Research of Megasonic Electroforming Equipment Based on the Uniformity of Electroforming Process. *Ultrason. Sonochem.* **2018**, *42*, 368–375. [CrossRef]
34. Ke, J.; Su, W.; Howdle, S.M.; George, M.W.; Cook, D.; Perdjon-Abel, M.; Bartlett, P.N.; Zhang, W.; Cheng, F.; Levason, W.; et al. Electrodeposition of Metals from Supercritical Fluids. *Proc. Natl. Acad. Sci. USA* **2009**, *106*, 14768–14772. [CrossRef]
35. Xiao, Y.; Ming, P.; Zhang, X.; Hou, Y.; Du, L.; Li, S.; Zhang, Y.; Song, J. Ultrahigh Strength Ultrapure Nanostructured Nickel Metal Prepared via Ultrafine Anode Scanning Electrodeposition. *Mater. Des.* **2022**, *213*, 110339. [CrossRef]
36. Foias, C.; Temam, R. Gevrey Class Regularity for the Solutions of the Navier-Stokes Equations. *J. Funct. Anal.* **1989**, *87*, 359–369. [CrossRef]
37. Dickinson, E.J.F.; Wain, A.J. The Butler-Volmer Equation in Electrochemical Theory: Origins, Value, and Practical Application. *J. Electroanal. Chem.* **2020**, *872*, 114145. [CrossRef]

micromachines

MDPI

Article

An Ultraviolet-Lithography-Assisted Sintering Method for Glass Microlens Array Fabrication

Fangyuan Zuo [1,2,3], Shenghua Ma [2,3,4], Wei Zhao [1,2,3], Chenqian Yang [2,3,4], Ziyu Li [1,2,3], Chen Zhang [1,2,3,*] and Jintao Bai [1,2,3,*]

[1] State Key Laboratory of Photon-Technology in Western China Energy, Xi'an 710127, China; zuofy@stumail.nwu.edu.cn (F.Z.); zwbayern@nwu.edu.cn (W.Z.); li_ziyu@stumail.nwu.edu.cn (Z.L.)
[2] International Collaborative Center on Photoelectric Technology and Nano Functional Materials, Xi'an 710127, China; mashenghua@nwu.edu.cn (S.M.); yangchenqian@stumail.nwu.edu.cn (C.Y.)
[3] Institute of Photonics & Photon Technology, Northwest University, Xi'an 710127, China
[4] Key Laboratory of Optoelectronics Technology in Shaanxi Province, Xi'an 710127, China
* Correspondence: nwuzchen@nwu.edu.cn (C.Z.); baijt@nwu.edu.cn (J.B.)

Abstract: Glass microlens arrays (MLAs) have tremendous prospects in the fields of optical communication, sensing and high-sensitivity imaging for their excellent optical properties, high mechanical robustness and physicochemical stability. So far, glass MLAs are primarily fabricated using femtosecond laser modification assisted etching, in which the preparation procedure is time-consuming, with each concave-shaped microlens being processed using a femtosecond laser point by point. In this paper, a new method is proposed for implementing large-scale glass MLAs using glass particle sintering with the assistance of ultraviolet (UV) lithography. The glass particles are dispersed into the photoresist at first, and then immobilized as large-scaled micropillar arrays on quartz glass substrate using UV lithographing. Subsequently, the solidified photoresist is debinded and the glass particles are melted by means of sintering. By controlling the sintering conditions, the convex microlens will be self-assembled, attributed to the surface tension of the molten glass particles. Finally, MLAs with different focal lengths (0.12 to 0.2 mm) are successfully fabricated by utilizing different lithography masks. Meanwhile, we also present the optimization of the sintering parameter for eliminating the bubbles in the microlenses. The main factors that affect the focal length of the microlens and the image performance of the MLAs have been studied in detail.

Keywords: convex microlens arrays; sintering; ultraviolet lithography; glass particle

1. Introduction

Microlens arrays (MLAs) are one of the essential micro-optical components. For the merits of their light weight, small size and easy integration, MLAs have been widely applied in organic light emitting diodes, 3D displays, light field cameras, solar cells, etc. [1–5].

Generally, MLAs are made of polymers and glass. The fabrication of polymeric MLAs includes ultraviolet (UV) lithography [6,7], thermal reflow [8–10], hot imprint [11,12] and ink-jet printing [13,14]. For example, in Taniguchi's work [6], microlens arrays (MLAs) were obtained by curing a UV resin which was modified using ultrasonic vibration simultaneously. In another work, Ashraf [10] utilized the thermal reflow method to fabricate MLAs. The cured photoresist cylinder will be melted at a certain temperature and eventually turn into a hemispherical shape under the effect of surface tension. However, due to their high thermal expansion coefficient and low chemical and mechanical stability, polymer MLAs are prone to deformation and wear.

Glass MLAs have a comparatively higher transparency, chemical and mechanical stability and abrasion resistance; therefore, they can be applied in extreme and special environments. The conventional method for fabricating glass MLAs is femtosecond laser modification assisted etching [15–17]. In this method, the glass substrate is modified using

a femtosecond laser in micro-regions at first, and then the structure is etched using an ion beam or a chemical solution to obtain MLAs. For instance, based on femtosecond laser modification and ion beam etching, Liu et al. [18] produced MLAs with a surface roughness of 2.5 nm and focal length of 60 to 100 μm in fused silica. Qin et al. [19] implemented MLAs by modifying fused silica with a femtosecond laser and processing with HF etching. The depth and radius of the modified area could be adjusted flexibly by controlling the laser energy and pulse delay. At last, MLAs with a numerical aperture in the range of 0.1 to 0.65 were obtained. In the above cases, the MLAs were concave-shaped when the femtosecond-laser-modified glass was removed from the substrate. Some scholars obtained convex glass MLAs by reverse-molding the concave MLAs with softened or molten glass. Li et al. [20] fabricated a concave microlens template with femtosecond laser modification assisted HF etching first. Then, by placing thermally softened As_2Se_3 glass onto the template, they finally obtained a 1600 rectangular and hexagonal convex MLA. Liu et al. [21] reported the fabrication of over 190,000 convex MLAs using reverse molding as concave compound eye templates, which were produced in sapphire using femtosecond laser modification assisted etching, and utilizing melted K9 glass. Definitely, the femtosecond laser modification assisted etching methods were suitable for high accuracy, low surface roughness and excellent homogeneity in glass MLA fabrication. However, these methods ask for point-by-point high-energy femtosecond laser processing of the material, which results in high cost and long fabricating times in high-throughput production. In addition, Shi [22] presented a work of fabricating germanium MLAs by utilizing reactive ion etching (RIE), which is capable of fabricating glass MLAs as well. However, RIE instruments are usually large and complex, the procedure is complicated and the fabrication usually costs a lot. In recent years, 3D printing techniques have been applied to printing SiO_2-doped polymeric materials, which have shown a promising way of fabricating glass microstructures [23]. Kotz et al. [24,25] constructed a model for a microlens using SiO_2-nanoparticle-doped photo-curable resin, and then the model was thermally treated to debind the polymerized resin. The remaining SiO_2 nanoparticles in the model were sintered and eventually converted into fused silica glass. However, this kind of glass additive fabrication method has only been reported in the processing of larger-size structures. In addition, the sintering temperature reaches as high as 1300 °C, which requires high-standard sintering devices.

In this paper, we proposed a new method, namely UV-lithography-assisted sintering (UVLAS), to implement convex glass MLAs. In this method, low-melting-point micron glass particles (GPs) were doped in the photoresist (PR) and immobilized as large-scale micropillar structures via UV lithography. Subsequently, the polymerized PR in the micropillars was removed and the GPs were melted via a sintering process. Finally, convex glass MLAs with focal lengths ranging from 0.12 to 0.2 mm were obtained. This method is capable of high throughput and mass production of glass MLAs compared to femtosecond laser modification assisted etching. The fabrication system and procedure are much simpler and the MLA fabrication cost is much lower compared to techniques with large instruments such as RIE. Further, it could be applied to micrometer-scale fabrication, and is safer and cost-saving compared with the above-mentioned sintering method. Therefore, UVLAS is promising for the rapid and efficient preparation of convex glass MLAs.

2. Method and Materials

The sintering method of glass MLAs is a high-temperature version of fabricating polymer MLAs using thermal reflow, as in references [8–10]. The shaping of the MLAs mainly relies on the surface tension of the material in the liquid phase. Therefore, there are three factors to ensure the uniformity of lenses in MLAs. First, the glass particles need to be uniformly dispersed into the photoresist to ensure that each lens contains the same amount of glass particles. Second, the quartz glass substrate needs to be very clean before spin-coating the GP-doped PR, as well as after development, to avoid the morphological flaws caused by impurities. Third, the bubbles in the sintering should be well controlled by using appropriate sintering conditions.

As shown in Figure 1, the procedure of UVLAS consists of eight stages. (1) Grinding: Low-melting-point micron GPs (D255, Anywhere New Materials Co., Ltd., Guangzhou, China) with an average particle size of 5 μm were, respectively, washed with acetone, isopropanol and pure water for 30 min to remove impurities. The GPs were dried and grinded with a mortar, and then finally sieved using a 2800 mesh standard sieve (shown in Figure 1a, the scale bar refers to 10 μm). Moreover, the compositions and the corresponding weight ratios of the GPs are summarized in Table 1. (2) Stirring: The sieved GPs were dispersed into the PR (SU-8 3005, Kayaku Advanced Materials Inc., Westborough, MA, USA) with a weight ratio of 45.5 wt% and stirred for 10 h at low speed with a magnetic stirrer (shown in Figure 1b). (3) Degassing: The GP-doped PR should be put into a vacuum chamber and degassed at −82 kpa for 2 h to remove the air bubbles (shown in Figure 1c). (4) Spin coating: The degassed GP-doped PR was spin-coated (2500 rpm for 30 s) on a quartz glass substrate and the thickness of the spin coating H_1 was 13.5 μm (shown in Figure 1d). (5) Baking: The sample was placed onto a heater and baked at 95 °C for 10 min to solidify the GP-doped PR as a membrane (shown in Figure 1e). (6) UV lithography: The membrane was exposed using a UV lithography system (MDA-400LJ, Midas Systems Co., Ltd., Daejeon, Republic of Korea) 10 times (10 s for each exposure and 10 s as an interval) and the sample was baked for 10 min after exposure to sharpen the structure of the pattern after lithography (shown in Figure 1f). Then, the baked sample was processed using developer to obtain the micropillar structures. (7) Sintering: The micropillar structures were sintered in an atmosphere furnace (CQ-ZKQF18E, Luoyang Chunqing Furnace Industry Co., Ltd., Luoyang, China) (shown in Figure 1g). (8) Shaping: The microlenses were self-assembled under surface tension and then MLAs were produced (shown in Figure 1h).

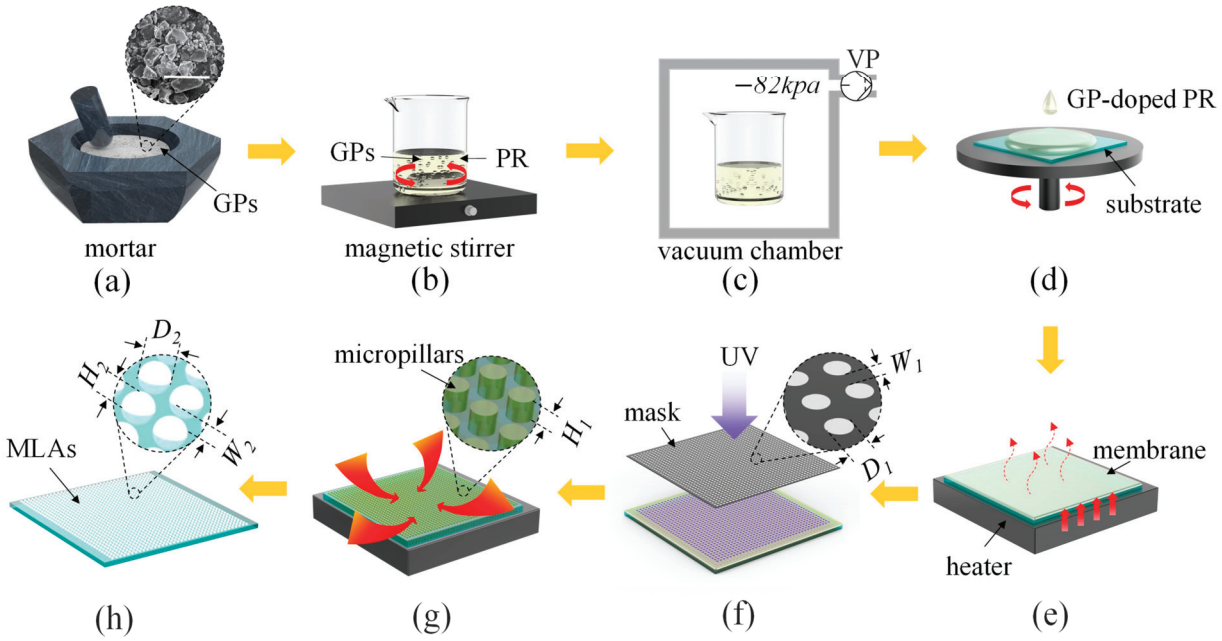

Figure 1. Schematic of fabricating MLAs using UVLAS. (**a**) Grinding; (**b**) stirring; (**c**) degassing; (**d**) spin coating; (**e**) baking; (**f**) UV lithography; (**g**) sintering; (**h**) shaping.

Table 1. Information on the composition of GPs.

Composition	Na_2O	MgO	Al_2O_3	SiO_2	CaO	BaO	KF
Weight ratio (wt%)	18.43	2.06	4.47	55.17	8.12	5.68	6.07

3. Results and Discussion

The sintering of the samples was carried out in an atmospheric furnace and the sintering process includes four stages: preheating, debinding, melting and cooling. The debinding stage focused on removing the polymerized PR from the micropillar using thermal decomposition. Since non-optimized debinding conditions can cause bubbles and cracks, which in turn affect the performance of the microlens, prolonged heating was necessary to give the polymerized PR sufficient time to decompose [26]. At the melting stage, the remaining GPs after debinding were melted and spontaneously assembled as a microlens under the effect of the surface tension of the molten glass. Herein, by applying different processing temperatures and duration times in the sintering, the effect of processing temperature and duration time on the flaws in the MLAs was investigated. Then, the optimum sintering parameters suitable for low-melting-point GPs were obtained.

As shown in Figure 2a, the four sintering stages are labeled I to IV, and the microstructure and morphology changes in the samples corresponding to each stage are shown in Figure 2(b_1–b_4). Stage I is preheating: the temperature in the furnace was raised from room temperature to the debinding temperature at a rate of 2 °C/min. The corresponding lasting time was t_1. Because the softening temperature of the GPs is 550 °C, the debinding temperature was set at 520 °C. The microstructures of the samples, i.e., the micropillars, at stage I consisted of the polymerized PR and GPs (Figure 2(b_1)). II is the debinding stage corresponding to the time period t_2. The micropillars were debound at 520 °C for 6 h. At this stage, the polymerized PR in the micropillars was removed using thermal decomposition; meanwhile, the GPs were gathered inwardly, and the space between the GPs became smaller (Figure 2(b_2)). III is the melting stage corresponding to the time period t_3. At this stage, due to the furnace structure and heating method, the outer GPs melted first and wrapped the incompletely melted GPs of the inner side, thus preventing the escape of the gas, which remained between the GPs or was produced during the melting of the GPs. These phenomena resulted in the tiny bubbles inside the sintered structure (Figure 2(b_3)). Herein, three different melting conditions (III-1, III-2, III-3) were used for comparative study. The melting temperature T_{3_1} and duration time t_{3_1} in melting condition III-1 were 650 °C and 2 h, respectively. In melting condition III-2, the melting temperature T_{3_2} was 700 °C and the duration time t_{3_2} was 2 h. The melting parameter corresponding to melting condition III-3 was 680 °C for 2 h, and then warmed up to 700 °C for 2 h. The optical images of the microlenses after cooling (stage IV) corresponding to the three sets of sintering conditions are shown in Figure 2(b_4). At the cooling stage, the microstructures slowly cooled down from the temperature of stage III to room temperature at a rate of 1 °C/min to ensure that the structures were heated uniformly and avoid the generation of cracks on the surface. From left to right in Figure 2(b_4), the illustration showing large and densely distributed bubbles in the structure corresponds to condition III-1. The microlens with fewer bubbles corresponds to the result of condition III-2, while the bubble-free microlens is obtained corresponding to III-3. The scale bars refer to 20 μm in Figure 2(b_4).

It can be seen that increasing the melting temperature can reduce the viscosity of the molten glass, which can accelerate the rising speed of the submerged bubbles in the molten glass. Furthermore, the rise rate of the bubbles is proportional to the quadratic of the bubble radius, so bubbles with larger radii will have a higher rise rate [27–29]. Therefore, when the melting condition was changed from III-1 to III-2, the rising speed of the bubbles increased as the viscosity of the molten glass reduced with a higher temperature. Finally, bubbles with larger diameters were eliminated while small-diameter bubbles were left for the insufficient processing time of III-2. In case of condition III-3, all the bubbles were eliminated as the viscosity of the molten glass was low and the corresponding phase lasted long enough. In addition, a stepwise increase in temperature was adopted, which might lower the crack risk of the quartz glass substrate. In summary, it can be concluded that reducing the viscosity of the molten glass and appropriately extending the period of low viscosity are the key factors to eliminate bubbles and control the quality of MLAs.

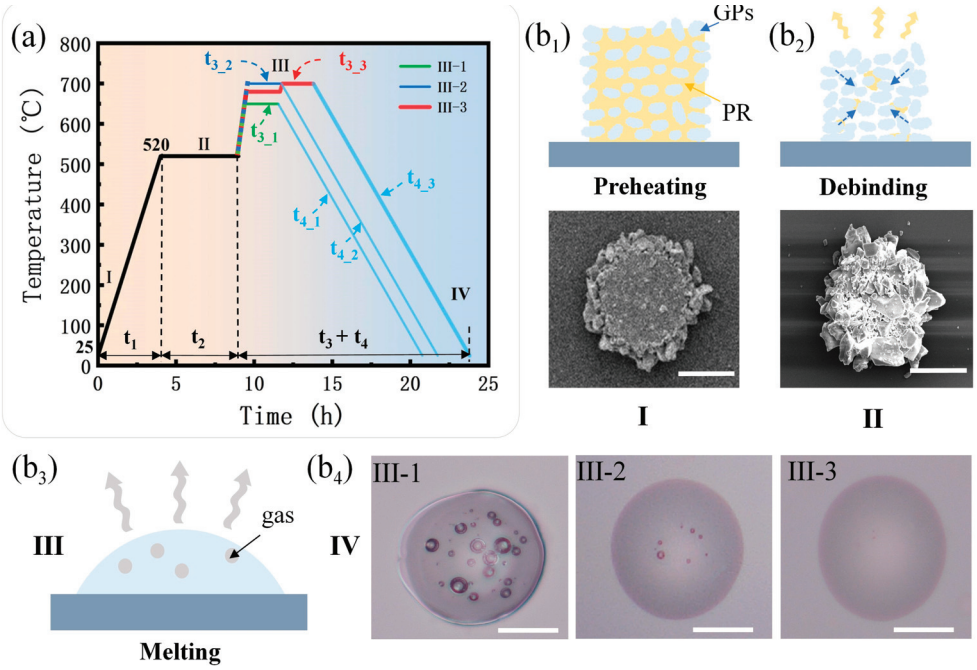

Figure 2. Sintering process of MLAs utilizing UVLAS. (**a**) Sintering scheme; (**b$_1$**–**b$_4$**) schematic diagrams of the microstructure and morphology changes in the MLAs at different stages; (**b$_1$**) preheating; (**b$_2$**) debinding; (**b$_3$**) melting; (**b$_4$**) cooling.

Based on the UVLAS method, circular lithography patterns with different diameters were applied to the fabrication of MLAs. The fabrication results are shown in Figure 3. In Figure 3a–d are the results of MLAs processed with different masks. The diameters of the circular patterns of the lithography mask, D_1, are 30, 40, 50 and 60 μm, respectively. Different spacing W_1 was adopted in these masks so the ultimate microlenses are different. It can be seen that the MLAs are uniformly round-shaped and evenly arranged. In addition, Figure 4b indicates that the error ranges of the prepared MLAs are 4.13% to 5.24% and 3.34% to 4.62% for the diameter D_2 and height H_2, respectively, which are too slight to influence the uniformity of MLAs both in shape and arrangement. Figure 3e–h show the zoomed-in images of the single microlenses, respectively, in Figure 3a–d. Let D_{min} and D_{max} be the minimum and maximum of the diameter of the microlens at the bottom contours. The ratio D_{min}/D_{max} could evaluate the morphological symmetry of the fabricated microlens. As the value of D_{min}/D_{max} is close to 1, the bottom profile of the microlens would be closer to an ideal circle. As shown in Figure 4a, the values of D_{min}/D_{max} for the microlenses obtained using the four sets of lithographing masks are all above 0.970; thus, the microlens profiles were complete and closed to an ideal circle.

Figure 3i–l show the height morphology of the above four sets of microlenses corresponding to Figure 3e–h. It can be found that the morphology of the microlenses was intact and smooth. The contact angle of the different-sized microlenses (as highlighted in Figure 3i) was measured to be 11° with a slight fluctuation (up to 0.6°) (shown in Figure 4a). This is because the contact angle is related to the properties of the molten glass and the quartz glass substrate itself. Despite the volume of the molten glass droplets, the contact angle is constant at a certain sintering temperature.

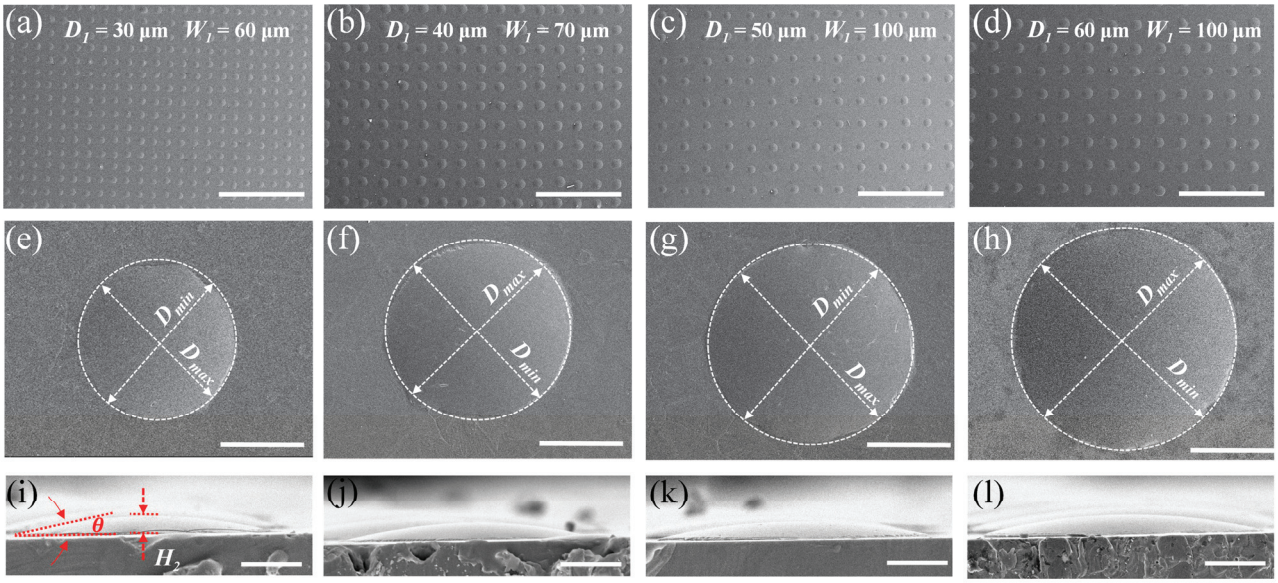

Figure 3. Fabrication results of MLAs with different lithography masks. (**a**) D_1 = 30 μm, W_1 = 60 μm; (**b**) D_1 = 40 μm, W_1 = 70 μm; (**c**) D_1 = 50 μm, W_1 = 100 μm; (**d**) D_1 = 60 μm, W_1 = 100 μm; (**e**–**h**) magnified view of individual microlenses, respectively, in (**a**–**d**); (**i**–**l**) height morphology of individual microlenses, respectively, in (**e**–**h**). The scale bars in (**a**–**d**), (**e**–**h**) and (**i**–**l**) are 500 μm, 20 μm and 10 μm, respectively.

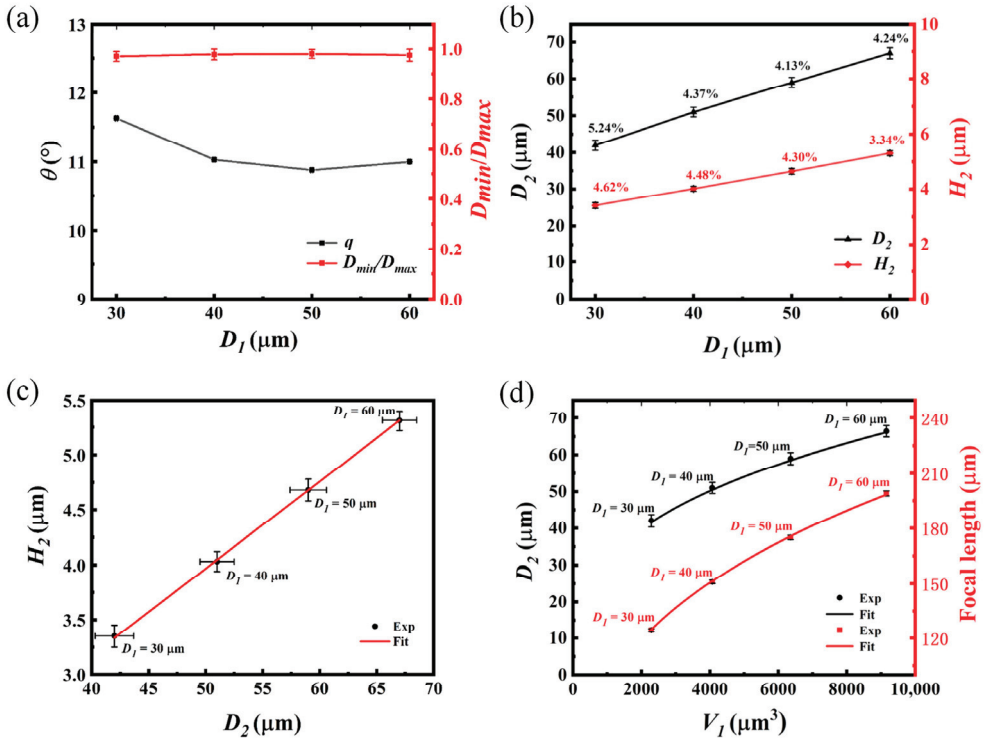

Figure 4. Analysis of MLA fabrication results based on UVLAS. (**a**) Contact angles and the morphological symmetry of MLAs fabricated with different lithography masks; (**b**) variation in microlens diameter D_2 and height H_2 with respect to D_1 (The percentage indicates the error ranges of the fabrication results); (**c**) variation in the microlens height H_2 in relation to microlens diameter D_2; (**d**) variation in D_2 in relation to D_1, and the focal length f of the MLAs in relation to volume V_1 of the GPs.

Figure 4 shows the analysis of the MLA fabrication results based on UVLAS. Let D_2 be the diameter and H_2 be the height of the fabricated microlens. The diameters D_2 of the microlenses were larger than the D_1 of the masks, and the increments were, respectively, 0.376, 0.265, 0.172 and 0.110, corresponding to D_1 = 30, 40, 50 and 60 μm. The corresponding mean values of the microlens heights H_2 were 3.30, 4.02, 4.65 and 5.31 μm, respectively. It seems abnormal that the molten glass spread wider as the lithographed capillary was smaller. However, from Figure 4b, it can be found that the diameter D_2 and the height H_2 linearly increased. Further, from Figure 4c, the ratio of D_2 and H_2 was approximate to a constant (0.079), and the tangent angle corresponding to H_2 and the radius of the MLAs was maintained around 9° (quite close to the contact angle θ). These findings indicate that the spread of the microlens on the substrate is always determined by the surface tension of the molten glass. Regardless of the volumes of the microlens, the contact angle of each microlens should be same.

Subsequently, the variation in the diameter D_2 and focal length f of the MLAs with respect to the volume V_1 of the GPs in the micropillar before sintering is plotted and shown in Figure 4d. It is seen that the diameter D_2 and the focal length f enlarged with an increase in V_1. To further understand the mechanism of the changes, the following derivation was carried out. Assume V_1 is the volume of the GPs in the micropillar structure before sintering, V_2 is the volume of the microlens after sintering and f refers to the focal length of the microlens: they have the following expressions:

$$V_1 = \alpha\pi\left(\frac{D_1}{2}\right)^2 H_{\ 1} \tag{1}$$

$$V_2 = \frac{1}{6}\pi H_2\left[3\left(\frac{D_2}{2}\right)^2 + H_2^2\right] \tag{2}$$

$$f = \frac{D_2^2 + 4H_2^2}{8H_2(n-1)} \tag{3}$$

where α in Equation (1) is the ratio of the GPs to the volume of the micropillars, which can be calculated using the weight and density of GPs and PR, and the value of α is 0.240 in this paper. n in Equation (3) is the refractive index of the GPs, n = 1.54.

In this paper, the loss of GPs in the process of sintering was very slight; thus, V_1 was approximately equal to V_2. Substituting H_2/D_2 = 0.079 into Equations (1)–(3), respectively, can derive the relationship of diameter D_2 and the focal length f to V_1. As shown in Figure 4d, the experimental results fit with the derived functions. Therefore, the diameter D_2 and focal length f of the microlens after sintering could be calculated by knowing the volume V_1 of the GPs before sintering. Similarly, this method could be applied to fabricating the MLAs with controllable diameter D_2 and focal length f by adjusting the volume V_1 when the H_2/D_2 is approximately a constant value.

Finally, an imaging system as shown in Figure 5a was built to test the imaging performance of the MLAs. The system was constructed using a wide-field light source (WL), an imaging target, an objective lens and a CMOS camera. In the system, the focal plane (FP) of the objective lens was aligned overlapping with the FP of the microlens. MLAs arranged in hexagons and obtained using a mask with D_1 = 40 μm and spacing W_1 = 70 μm were utilized in the test. As shown in Figure 5b, when the target was illuminated with WL, the target letter "F" could be clearly observed as the array of "F" using the CMOS camera (MER-2000-19U3C-L, Daheng New Epoch Technology, Inc., Beijing, China). Figure 5c is a magnified optical image of a single microlens observed using a 40× objective lens. From Figure 5c, it can be seen that the target letter "F" is clear and undeformed. In Figure 5d, there are five columns of microfocus obtained by the MLAs in Figure 5b, and it can be seen that the spots are uniformly distributed in hexagons in the FP. The scale bars in Figure 5b–d refer to 50, 15 and 50 μm, respectively. The actual focal lengths of all the microlenses in Figure 5d are listed in Figure 5e. The average focal length of the microlenses was calculated

based on Equation (3), which is 151 μm. The actual value of the lens focal length fluctuated around the mean value with a maximum error of 0.66% compared to the mean focal length. The clear and uniform images indicate that the focal planes of each microlens were essentially flush with each other. In addition, the normalized light field intensity at the focal cross-section of each column of microlenses in Figure 5d was plotted, and the results are shown in Figure 5f. The peaks of intensity were in the range of 0.982 to 1.000. The transmission spectra of the MLAs were plotted and compared with that of quartz glass in Figure 5g. The transmittance of MLAs has a bigger fluctuation in the range of 230–385 nm compared to the quartz glass substrate. The lowest transmittance (83.6%) and the maximum transmittance (92.7%) emerge at 264 nm and 890 nm, respectively. Meanwhile, the spectral transmittance of MLAs in the visible region is about 2% lower than that of quartz glass, while the spectral transmittance of the MLAs is comparable to that of quartz glass after 890 nm. At last, Raman spectra of the MLAs and quartz glass were plotted and compared in Figure 5h. It can be observed that the Raman spectrum shapes of MLAs and quartz glass are similar; the different intensity at 1380 nm can be attributed to the difference in SiO_2 content in the two testing areas.

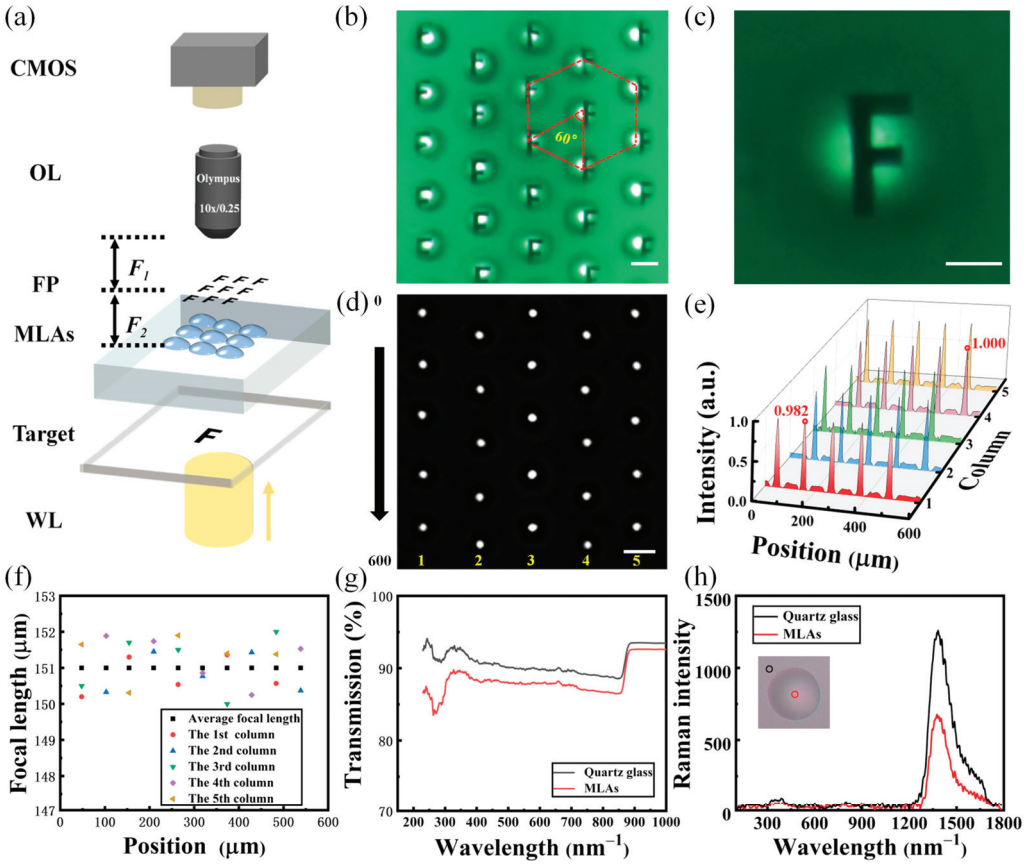

Figure 5. Imaging performance of MLAs using UVLAS. (**a**) Schematic diagram of the optical measuring system; (**b**) optical imaging utilizing MLAs; (**c**) magnified optical imaging of a single microlens; (**d**) focusing performance of MLAs; (**e**) focal length analysis of MLAs; (**f**) characterization of the normalized light intensity distribution of the MLAs; (**g**) ultraviolet–near-infrared transmission spectra of MLAs and quartz glass substrate; (**h**) Raman spectra of MLAs and quartz glass substrate. The scale bars in (**b**–**d**) refer to 50, 15 and 50 μm, respectively.

4. Conclusions

In this paper, a UV-lithography-assisted sintering method for convex glass microlens array fabrication was proposed and validated. It was found that lowering the viscosity of the molten glass and appropriately prolonging the duration of melting could eliminate bubbles in the microlenses. By utilizing four sets of different-sized masks, whose pattern diameters were, respectively, 30, 40, 50 and 60 μm, MLAs with average focal lengths of 122, 151, 175 and 201 μm were obtained successfully. The MLA morphology is symmetrically smooth, and the maximum error between the actual and theoretical focal length of the MLAs was 0.66%. It is found that both the diameter D_2 and the focal length f of the microlens after sintering have a function relationship with the volume V_1 of the GPs before sintering when the H_2/D_2 is approximately a constant value. Therefore, the size and focal length of the MLAs could be controllably adjusted by modifying the volume of the GPs. Finally, the imaging performance of the MLAs has been investigated. The results demonstrated the excellent imaging and focusing capabilities of the MLAs.

Author Contributions: Conceptualization, C.Z.; methodology, C.Z., F.Z., S.M. and W.Z.; software, F.Z. and Z.L.; validation, C.Z., F.Z. and S.M.; formal analysis, C.Z., F.Z. and S.M.; investigation, F.Z. and C.Y.; resources, F.Z. and C.Y.; data curation, F.Z.; writing—original draft preparation, F.Z.; writing—review and editing, C.Z., F.Z. and S.M.; visualization, F.Z.; supervision, C.Z.; project administration, C.Z. and J.B.; funding acquisition, J.B. All authors have read and agreed to the published version of the manuscript.

Funding: This research was funded by the National Major Scientific Research Instrument Development Project of China (grant no. 51927804); the National Natural Science Foundation of China (grant no. 62275216) and the Science and Technology Innovation Team Project of Shaanxi Province (grant nos. S2018-ZC-TD-0061 and 2023-CX-TD-06).

Data Availability Statement: Not applicable.

Conflicts of Interest: The authors declare no conflict of interest.

References

1. Kuang, D.; Zhang, X.; Gui, M.; Fang, Z.H.R. Hexagonal microlens array fabricated by direct laser writing and inductively coupled plasma etching on organic light emitting devices to enhance the outcoupling efficiency. *Appl. Opt.* **2009**, *48*, 974–978. [CrossRef] [PubMed]
2. Wang, W.; Chen, G.; Weng, Y.; Weng, X.; Zhou, X.; Wu, C.; Guo, T.; Yan, Q.; Lin, Z.; Zhang, Y. Large-scale microlens arrays on flexible substrate with improved numerical aperture for curved integral imaging 3D display. *Sci. Rep.* **2020**, *10*, 11741. [CrossRef] [PubMed]
3. Kim, K.; Jang, K.W.; Bae, S.I.; Kim, H.K.; Cha, Y.; Ryu, J.K.; Jo, Y.J.; Jeong, K.H. Ultrathin arrayed camera for high-contrast near-infrared imaging. *Opt. Express* **2021**, *29*, 1333–1339. [CrossRef]
4. Peer, A.; Biswas, R. Nanophotonic Organic Solar Cell Architecture for Advanced Light Trapping with Dual Photonic Crystals. *ACS Photonics* **2014**, *1*, 840–847. [CrossRef]
5. Liu, C.M.; Su, G.D.J. Enhanced light extraction from UV LEDs using spin-on glass microlenses. *J. Micromech. Microeng.* **2016**, *26*, 055003. [CrossRef]
6. Taniguchi, S.; Koyama, D.; Nakamura, K.; Matsukawa, M. Fabrication of an optical lens array using ultraviolet light and ultrasonication. *Ultrasonics* **2015**, *58*, 22–26. [CrossRef]
7. Chen, J.; Cheng, J.; Zhang, D.; Chen, S.C. Precision UV imprinting system for parallel fabrication of large-area micro-lens arrays on non-planar surfaces. *Precis. Eng.* **2016**, *44*, 70–74. [CrossRef]
8. Albero, J.; Perrin, S.; Bargiel, S.; Passilly, N.; Baranski, M.; Gauthier-Manuel, L.; Bernard, F.; Lullin, J.; Froehly, L.; Krauter, J.; et al. Dense arrays of millimeter-sized glass lenses fabricated at wafer-level. *Opt. Express* **2015**, *23*, 11702–11712. [CrossRef]
9. Zhang, D.; Xu, Q.; Fang, C.; Wang, K.; Wang, X.; Zhuang, S.; Dai, B. Fabrication of a Microlens Array with Controlled Curvature by Thermally Curving Photosensitive Gel Film beneath Microholes. *ACS Appl. Mater. Interfaces* **2017**, *9*, 16604–16609. [CrossRef]
10. Ashraf, M.; Gupta, C.; Chollet, F.; Springham, S.V.; Rawat, R.S. Geometrical characterization techniques for microlens made by thermal reflow of photoresist cylinder. *Opt. Laser Eng.* **2008**, *46*, 711–720. [CrossRef]
11. Chang, C.Y.; Yu, C.H. A basic experimental study of ultrasonic assisted hot embossing process for rapid fabrication of microlens arrays. *J. Micromech. Microeng.* **2015**, *25*, 025010. [CrossRef]
12. Hou, T.; Zheng, C.; Bai, S.; Ma, Q.; Bridges, D.; Hu, A.; Duley, W.W. Fabrication, characterization, and applications of microlenses. *Appl. Opt.* **2015**, *54*, 7366–7376. [CrossRef] [PubMed]

13. Vespini, V.; Coppola, S.; Todino, M.; Paturzo, M.; Bianco, V.; Grilli, S.; Ferraro, P. Forward electrohydrodynamic inkjet printing of optical microlenses on microfluidic devices. *Lab Chip* **2016**, *16*, 326–333. [CrossRef]
14. Zhang, Q.; Schambach, M.; Schlisske, S.; Jin, Q.; Mertens, A.; Rainer, C.; Hernandez-Sosa, G.; Heizmann, M.; Lemmer, U. Fabrication of Microlens Arrays with High Quality and High Fill Factor by Inkjet Printing. *Adv. Opt. Mater.* **2022**, *10*, 2200677. [CrossRef]
15. Bian, H.; Yang, Q.; Chen, F.; Liu, H.; Du, G.; Deng, Z.; Si, J.; Yun, F.; Hou, X. Scalable shape-controlled fabrication of curved microstructures using a femtosecond laser wet-etching process. *Mat. Sci. Eng. C-Mater.* **2013**, *33*, 2795–2799. [CrossRef]
16. Chen, F.; Liu, H.; Yang, Q.; Wang, X.; Hou, C.; Bian, H.; Liang, W.; Si, J.; Hou, X. Maskless fabrication of concave microlens arrays on silica glasses by a femtosecond-laser-enhanced local wet etching method. *Opt. Express* **2010**, *18*, 20334–20343. [CrossRef] [PubMed]
17. Li, M.; Yang, Q.; Yong, J.; Liang, J.; Fang, Y.; Bian, H.; Hou, X.; Chen, F. Underwater superoleophobic and anti-oil microlens array prepared by combing femtosecond laser wet etching and direct writing techniques. *Opt. Express* **2019**, *27*, 35903–35913. [CrossRef]
18. Liu, X.Q.; Yu, L.; Yang, S.N.; Chen, Q.D.; Wang, L.; Juodkazis, S.; Sun, H.B. Optical Nanofabrication of Concave Microlens Arrays. *Laser Photonics Rev.* **2019**, *13*, 1800272. [CrossRef]
19. Qin, B.; Li, X.; Yao, Z.; Huang, J.; Liu, Y.; Wang, A.; Gao, S.; Zhou, S.; Wang, Z. Fabrication of microlenses with continuously variable numerical aperture through a temporally shaped femtosecond laser. *Opt. Express* **2021**, *29*, 4596–4606. [CrossRef]
20. Li, R.; Li, C.; Yan, M.; Li, M.; Lin, C.; Dai, S.; Song, B.; Xu, T.; Zhang, P. Fabrication of chalcogenide microlens arrays by femtosecond laser writing and precision molding. *Ceram. Int.* **2023**, *49*, 15865–15873. [CrossRef]
21. Liu, X.Q.; Yang, S.N.; Yu, L.; Chen, Q.D.; Zhang, Y.L.; Sun, H.B. Rapid Engraving of Artificial Compound Eyes from Curved Sapphire Substrate. *Adv. Funct. Mater.* **2019**, *29*, 1900037. [CrossRef]
22. Shi, L.F.; Du, C.L.; Dong, X.C.; Deng, Q.L.; Luo, X.G. Effective formation method for an aspherical microlens array based on an aperiodic moving mask during exposure. *Appl. Opt.* **2007**, *46*, 8346–8350. [CrossRef]
23. Camposeo, A.; Persano, L.; Farsari, M.; Pisignano, D. Additive Manufacturing: Applications and Directions in Photonics and Optoelectronics. *Adv. Opt. Mater.* **2019**, *7*, 1800419. [CrossRef] [PubMed]
24. Kotz, F.; Arnold, K.; Bauer, W.; Schild, D.; Keller, N.; Sachsenheimer, K.; Nargang, T.M.; Richter, C.; Helmer, D.; Rapp, B.E. Three-dimensional printing of transparent fused silica glass. *Nature* **2017**, *544*, 337–339. [CrossRef] [PubMed]
25. Kotz, F.; Quick, A.S.; Risch, P.; Martin, T.; Hoose, T.; Thiel, M.; Helmer, D.; Rapp, B.E. Two-Photon Polymerization of Nanocomposites for the Fabrication of Transparent Fused Silica Glass Microstructures. *Adv. Mater.* **2021**, *33*, e2006341. [CrossRef]
26. Doualle, T.; Andre, J.C.; Gallais, L. 3D printing of silica glass through a multiphoton polymerization process. *Opt. Lett.* **2021**, *46*, 364–367. [CrossRef]
27. Ma, Q.; Li, C.; Zhang, G.; Fang, H. A novel method for accelerating bubble rising in highly viscous molten quartz. *Int. J. Heat Mass Tran.* **2019**, *138*, 1359–1367. [CrossRef]
28. Stokes, G.G. *On the Effect of the Internal Friction of Fluids on the Motion of Pendulums*; Cambridge Library Collection—Mathematics; Cambridge University Press: Cambridge, UK, 2009; pp. 1–10.
29. Moore, D.W. Drops, bubbles and solid particles. *Nature* **1979**, *279*, 267–268. [CrossRef]

micromachines

Article

Processing and Properties of Single-Crystal Copper Wire

Jun Cao *, Xuefeng Wu, Chenghao Su, Hewei Jia and Yongzhen Sun

School of Mechanical and Power Engineering, Henan Polytechnic University, Jiaozuo 454003, China; wuxuefeng@hpu.edu.cn (X.W.); sumurong666@gmail.com (C.S.); 212105020051@home.hpu.edu.cn (H.J.); syz@home.hpu.edu.cn (Y.S.)
* Correspondence: cavan@hpu.edu.cn

Abstract: The effects of drawing parameters and annealing process on the properties and microstructure of single crystal copper wire are studied using a wire-drawing machine, heat-treatment equipment, microcomputer-controlled electronic universal tester, resistance tester, and scanning electron microscope. The results show that, after drawing the single-crystal copper wire with a single-pass deformation of 14%, the grains elongate along the tensile direction, tensile strength increases from 500.83 MPa to 615.5 Mpa, and resistivity changes from 1.745×10^{-8} Ω·m to 1.732×10^{-8} Ω·m. After drawing at a drawing rate of 500 m/min, the degree of grain refinement increases and tensile strength increases from 615.5 Mpa to 660.26 Mpa. When a copper wire of Φ0.08 mm is annealed, its tensile strength decreases from 660.26 Mpa to 224.7 Mpa, and elongation increases from 1.494% to 19.87% when the annealing temperature increases to 400 °C. When the annealing temperature increases to 550 °C, the tensile strength and elongation decrease to 214.4 MPa and 12.18%, respectively.

Keywords: copper wire; multipass drawing; deformation; heat treatment

1. Introduction

Wire bonding occupies a dominant position in the field of chip packaging because of its mature technology and low cost [1–4]. Wire bonding can connect the metal cloth welding area or microelectronic packaging I/O lead to the semiconductor chip welding area, which is an important process link in the semiconductor packaging process. Its construction quality has a great influence on the functional applications of the semiconductors. Compared to gold wire, bonded copper wire has a lower production cost, good conductivity, and superior mechanical properties which facilitates its widespread use in many applications such as semiconductor packaging, integrated circuits, and light-emitting diodes [5–7]. Although pure copper has excellent electrical and thermal conductivity and corrosion resistance, its strength and hardness are low. Improving its mechanical properties without reducing the electrical conductivity is one of the key challenges in the preparation of ultrafine and high-performance copper wires [8–10].

Integrated circuits and electronic components are progressing towards miniaturization and high integration, and the demand for ultrafine, high-performance copper bonding wires with diameters less than 30 μm is increasing. Song et al. studied the variations in the mechanical properties and electrical conductivity of Φ0.02 mm Cu-1Ag alloy wire with strain. They concluded that with the increase in strain, the tensile strength of the Cu-1Ag alloy increased, whereas the electrical conductivity first decreased and then stabilized [11]. Zhu et al. prepared Φ0.04 mm Cu-4wt% Ag alloy wire by continuous directional solidification and drawing. The evolution of the microstructure and properties at each stage of the drawing was studied. The tensile strength, yield strength, and electrical conductivity of the alloy were 1048 MPa, 886 MPa, and 75.2% IACS (IACS: international annealed copper standard), respectively, after deformation at a tensile of 11.28 [12]. Gokhfel'd et al. studied the microstructure, mechanical properties, and electrical conductivity of a Cu3Pd alloy after severe cold plastic deformation following repeated stretching and annealing,

and determined the microstructure evolution of the alloy after severe deformation and subsequent annealing [13]. Fu et al. tested the strength and electrical conductivity of Ag-11.40Cu-0.66Ni-0.05Ce (wt%) alloy wire at different deformation stages and observed the microstructure during deformation. After a large deformation drawing, the room-temperature Vickers hardness of the as-cast alloy increased from HV 81.6 to HV 169.3, and the electrical conductivity increased from 74.3% to 78.6% IACS [14]. Cheng et al. studied the evolution of the microstructure, mechanical properties, and electrical properties of Cu-20wt% Ag alloy wire during the drawing process. It was concluded that when the diameter was stretched to 0.02 mm (η = 11.94), the tensile strength of the alloy was 1682 MPa and elongation was 2.0%. The relationship between the tensile strength, elongation, and diameter conformed to Allometric and Boltzmann functions, respectively [15]. Cao studied the performance and microstructure changes in Ag-4Pd alloy wire during heat treatment and determined the best heat treatment temperature for achieving excellent wire performance [16]. Cheng et al. studied the dislocation boundary of single-crystal copper wire. In the spatial distribution of a high-angle dislocation boundary, when the strain is greater than 2.77, the dislocation boundary extends from the center to the surface with the increase in strain [17]. By studying the texture evolution of single-crystal copper wire when the strain is less than 4.12, the results show that when the initial orientation of single-crystal copper is <111>, <100>, and <110>, the grains are refined during cold drawing. A mixture of <111> and <100> fiber textures is formed under high strain [18]. Li et al. studied that a single-crystal copper wire with a diameter of 1 mm was drawn into 0.2 mm and analyzed its structure and properties. The results show that fine grain strengthening and dislocation strengthening are the key factors affecting the strength and conductivity of single-crystal copper wire [19]. At present, there are many studies on most alloy wires at home and abroad but few studies on fine single-crystal copper wires, and the tensile strength of single-crystal copper wires discussed in the existing literature is low. This paper takes single-crystal copper wire as the research object, studies the deformation behavior of copper wire under different single-pass deformation and different drawing speeds, analyzes the influence of drawing parameter change on the copper wire performance, and improves the theoretical system of drawing parameter change on the copper wire drawing process. The properties and microstructure differences of copper wire under different drawing conditions and different heat treatment conditions are studied. The tensile strength of copper wire also reached 660 MPa. After annealing, the strength reaches 225 MPa and the elongation reaches 20%.

2. Original Materials and Experimental Details

2.1. Original Materials and Equipment

The original material was a single-crystal copper rod with a diameter of 8.0 mm, prepared by a thermal horizontal continuous casting equipment. The single-crystal copper rod with a diameter of 8.0 mm was drawn to a diameter of 3.0 mm by a large diameter wire drawing machine, and then multi-mode drawn by a medium diameter wire drawing machine to a diameter of 0.9 mm. Finally, the single-crystal copper wire with a diameter of 0.2 m was processed by multimode drawing of a small diameter wire drawing machine. The single-crystal copper samples were prepared on a self-made hot horizontal continuous casting equipment, which is presented in Figure 1. First, the electrolytic copper raw material with a mass fraction of 99.95% was added to the graphite crucible. The temperature of the copper liquid was 1140~1250 °C, and the smelting process was protected using an inert gas. After the raw material melted completely, the pressure bar pressed the melt in the graphite crucible downward so that the melt entered the mold through the guide tube. While pouring, the traction rod with a groove at the front end entered the mold and contacted the melt. The pouring temperature was 1080~1110 °C, the traction speed was 40 mm/min, the cooling water temperature was 20 °C, the flow rate was 25 mm/min, and the cooling distance was 10 mm. Under these conditions, the melt changed from liquid to solid, producing a single-crystal copper rod blank of 16 mm. The single-crystal copper

exhibited highly oriented longitudinal grains with a low number of grain boundaries, which reduced the hindrance to dislocation movement and significantly improved the plastic deformation ability.

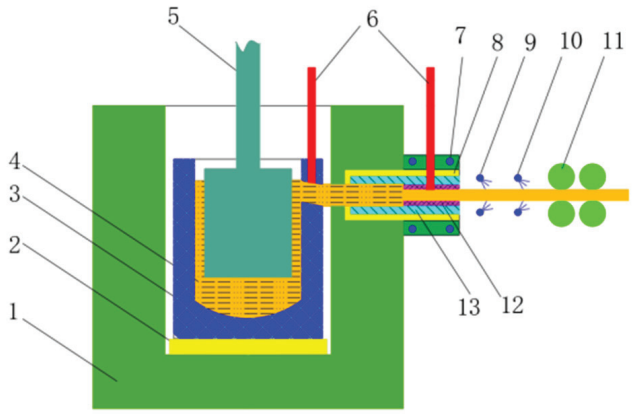

1 .Continuous casting furnace body 2.Insulation pad 3.Graphite crucible 4.Melt 5Pressure bar 6.Thermocouple 7.Water-cooled casing 8. Insulation cotton layer 9.Primary cooling device 10.Secondary cooling device 11.Traction 12.Mould 13.Globar

Figure 1. Schematic diagram of heated-mold continuous casting device.

The raw material used in the experiment was a 4 N single-crystal copper wire (single-crystal copper with purity 99.99%). The wire possessed original parameters of a tensile strength measuring 500.83 MPa, an elongation of 0.93%, and a resistivity measuring 1.745×10^{-8} Ω·m. An LH150-36-type very fine wire drawing machine was used to draw the single-crystal copper wire. A KD2-0.02-type electronic universal tester and an HS-3004A tensile tester were used to test the mechanical properties of the copper wire; the specimen length was 100 mm, and the tensile speed was 10 mm/min. The electrical properties were tested by an SB2231-type resistance tester, and the length of the specimen was 1000 mm. In the heat treatment test of the 0.08 mm single-crystal copper wire, the SD-40 continuous heat treatment equipment was utilized. The heat treatment process involved the use of electric heating as the heating mode, a quartz glass annealing tube with a length of 1200 mm, and a temperature fluctuation range of 2 °C. An angular displacement sensor was employed to control the wire tension during the heat treatment, with the tension range set between 0.01–0.10 N for various annealing rate tests. The annealing rate, which refers to the speed at which the wire passes through the annealing tube, represents the closing speed of the annealing heat treatment.

Metallographic preparation was carried out as follows, by placing the intercepted copper wire strands into the bottom of a rubber mold and pouring epoxy resin to solidify naturally. The polishing process involved the use of 600#, 800#, 1000#, 1200#, and 2000# SiC sandpaper on a polishing machine. Throughout the process, the surface of the sandpaper was continuously rinsed with water flow. To ensure a thorough sanding operation, the specimen was rotated by 90° after each stage of sanding, with each stage carried out without any remnants of the previous scratch on the surface. Following the grinding steps, the surface of the specimen exhibited no apparent scratches. Subsequently, rough polishing and fine polishing were executed using 1.0 μm and 0.5 μm diamond suspension spray, resulting in a smooth specimen surface without any visible scratches under microscope observation. The corrosion solution was a mixture of 5 g of copper chloride and 100 mL of ammonia solution, and the corrosion solution was ready for use. The corrosion time was 5–10 s; after completion of the corrosion, we used distilled water or anhydrous ethanol cleaning and blow-dried the specimen. The surface of the corrosion cleaned specimen was sprayed with gold and then put under the scanning electron microscope of JEOL JSM-6700F to analyze and observe the changes in microstructure under different conditions. Scanning electron microscope manufacturer is Nippon Electron Co. (Huizhou, China).

2.2. Test Scheme

To investigate the effects of single-pass deformation on the mechanical and electrical properties of copper wire, a multipass drawing test was conducted on the original Φ0.25 mm copper wire. Three experimental schemes were devised, as shown in Table 1, where the single-pass drawing amounts were set at 18%, 14%, and 10%, respectively. The drawing speed was maintained at 500 m/min, resulting in a final wire diameter of Φ0.135 mm. At each pass, samples were collected and tested for their tensile strength, elongation, and resistivity. Subsequently, the effects of the three different levels of single-pass deformation on the properties of the copper wire were compared and analyzed.

Table 1. Drawing test schemes with different deformation.

Scheme Number	Initial Wire Diameter (mm)	Single-Pass Surface Volume Reduction (%)	Number of Molds	Drawing Speed (m/min)	Final Wire Diameter (mm)
Scheme 1	0.25	18	7	500	0.135
Scheme 2		14	9		
Scheme 3		10	12		

Considering the influence of electrical conductivity, the Φ0.135 mm copper wire with a single-pass drawing amount of 14% (Scheme 2 of Table 1) was selected for the drawing test at three drawing rates, as shown in Table 2. The three schemes employed drawing speeds of 300, 500, and 700 m/min and deformation of a single pass of 15%, resulting in a wire with a diameter of Φ0.08 mm. The samples were tested for tensile strength, elongation, and resistivity to compare the effects of the three drawing rates on the mechanical properties of copper wire.

Table 2. Drawing test schemes with different rates.

Scheme Number	Initial Wire Diameter (mm)	Single-Pass Surface Volume Reduction (%)	Drawing Speed (m/min)	Final Wire Diameter (mm)
Scheme 1	0.135	15	300	0.08
Scheme 2			500	
Scheme 3			700	

The drawing speed was set at 500 m/min and a wire of Φ0.08 mm was annealed at 250, 300, 350, 400, 450, 500, and 550 °C. The annealing speed was 100 m/min for the heat treatment test, as shown in Table 3. The samples underwent measurements of tensile strength, elongation, and resistivity, and the changes in mechanical and electrical properties at different annealing temperatures were studied. Metallographic samples of the wires annealed at different temperatures were fabricated, and their microstructure evolution was observed using a scanning electron microscope (SEM). The evolution of the microstructure of the material under different temperature conditions was analyzed.

Table 3. Annealing test scheme.

Equipment Type	Initial Wire Diameter (mm)	Annealing Temperature (°C)	Annealing Rate (m/min)
SD-40	0.08	250–550	500
SD-40	0.08	300	20–120

The Φ0.08 mm wire rod was selected with a drawing speed of 500 m/min. As shown in Table 3, the wire rod was annealed at rates of 20, 40, 60, 80, 100, and 120 m/min. The

annealing temperature was 300 °C. The tensile strength, elongation, and resistivity of the aforementioned copper wire rod were measured, and the material properties were studied at different annealing rates.

3. Test Results and Analysis

3.1. Effect of Different Deformation on the Microstructure of Single-Crystal Copper Wire

In the drawing process of single-crystal copper, the slip phenomenon occurs first, and each grain is elongated along the drawing direction. After that, the columnar crystal inside the wire is broken. The wire changes from the single-crystal state to a polycrystalline state, and the dislocation density increases. With the increase in strain, the broken grains gradually become orderly and elongate along the drawing direction; the degree of grain refinement continues to increase, finally forming a fibrous structure. The microstructure of the single-crystal copper wire after drawing with different single-pass deformations is as follows. Figure 2 is the SEM image of the Φ0.25 mm sample. After a single pass of deformation of 18%, 14%, and 10%, the copper wires all have similar fiber structures, and there is no obvious difference.

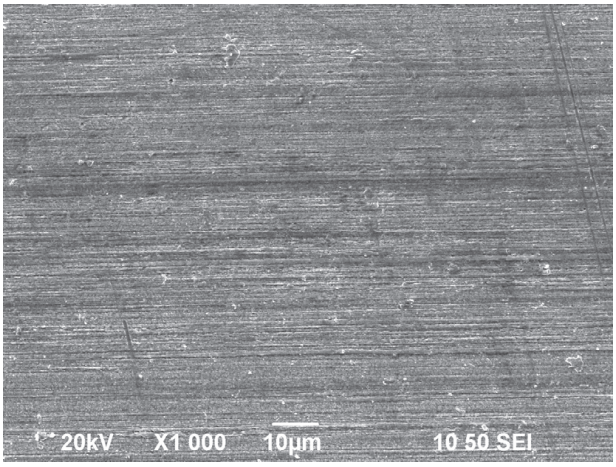

Figure 2. Microstructure of original copper wire.

3.2. Effect of Deformation on Mechanical and Electrical Properties of Single-Crystal Copper Wire

With the increase in the strain rate, the dynamic recovery process of the dislocations is inhibited, and the work-hardening effect is higher than that of dynamic recovery. Therefore, dislocations are accumulated more at high strain rates of deformation, thus improving the strength of the material. At the same time, the dynamic recovery of dislocations is a thermal activation process. High-temperature deformation can accelerate the dynamic recovery of dislocations, thus reducing the dislocation density. The low temperature and high strain rate inhibit the dynamic recovery process of dislocations so that dislocations can be further accumulated and the work-hardening rate of the material can be improved. Therefore, during the cold drawing of single-crystal copper wire, low-temperature high-strain-rate deformation is beneficial for the formation of twins. The grain boundary and twin boundary hinder the slip of dislocations simultaneously; thus, dislocations are entangled at these interfaces, which increases the strength of the material.

Figure 3a is the change curve of the tensile strength of the copper wire under three different strains. As the strain increases, the tensile strength of the wire initially rises from 500.83 MPa to 631.3 MPa, 615.5 MPa, and 637 MPa, before stabilizing. This is due to lattice distortion during deformation, which elongates and refines the grain. After grain refinement, the grain boundary area, slip effect on dislocation, and the deformation-resistance index (tensile strength, etc.) of the metal increases with the increase in the deformation degree.

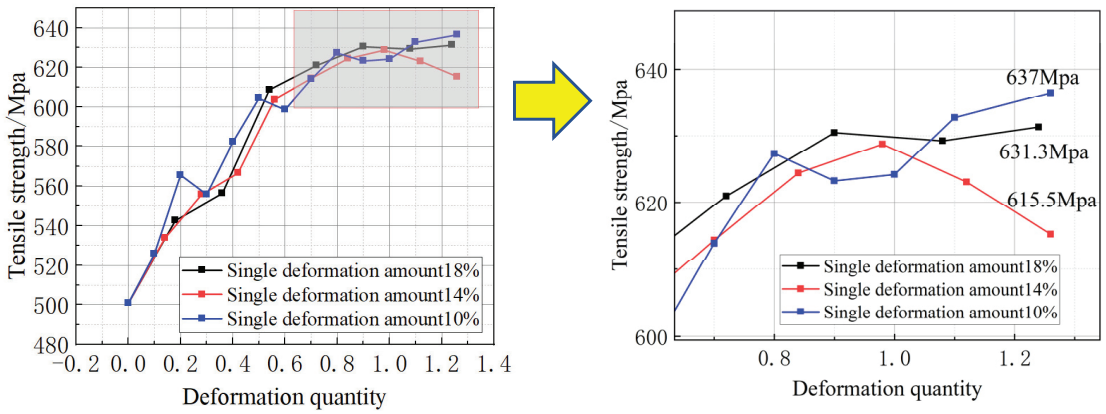

(**a**)

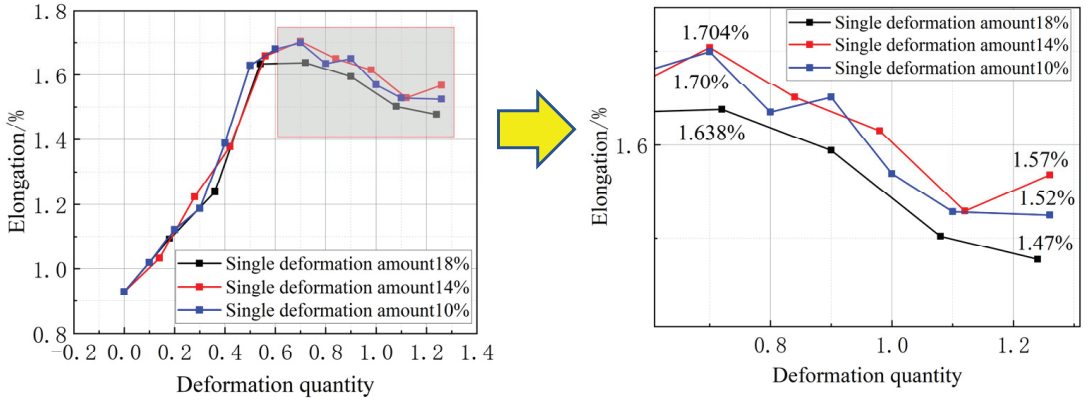

(**b**)

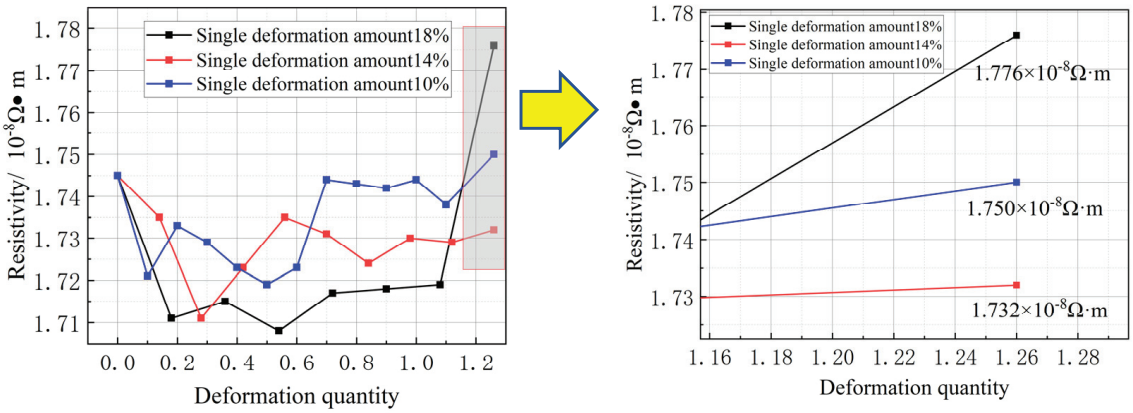

(**c**)

Figure 3. Mechanical properties and electrical conductivity of single-crystal copper wires under different deformations. (**a**) Tensile strength change in copper wire; (**b**) elongation change in copper wire; (**c**) resistivity change in copper wire.

Figure 3b is the change curve of elongation after drawing at three different deformations. The elongation increases from 0.93% to 1.47%, 1.57%, and 1.52%. When the strain is approximately 0.7, the elongation reaches the maximum value (1.638%, 1.704%, and 1.70%). Then, with the increase in the deformation degree, the elongation gradually decreases

because of the occurrence of intragranular and intergranular damage during deformation, uneven deformation, etc., which is the plastic index (elongation, etc.) of the metal.

Figure 3c shows the change curve of resistivity of the single-crystal copper wire in different deformation tests. The final result shows that the resistivity of the wire with 18% deformation is the highest at 1.776×10^{-8} Ω·m. The wire with 14% deformation has the lowest resistivity, measuring at 1.732×10^{-8} Ω·m, while the wire with 10% deformation has a resistivity of 1.750×10^{-8} Ω·m. In all three schemes, the resistivity decreases during the initial drawing phase when compared to the resistivity of the initial wire. The smaller the grain size of the metal, the more the number of internal grains and grain boundaries, and the stronger the scattering effect on electrons. Among the three different deformations, after drawing with a single-pass deformation of 14%, the internal grain size is larger, grain boundary area ratio is smaller, and electrons are less scattered when passing through the grain boundary; therefore, the resistivity is lower.

3.3. Influence of Different Drawing Rates on the Performance of Single-Crystal Copper Wire

The plastic deformation of the crystal is achieved by the continuous movement and proliferation of dislocations under stress. As the degree of deformation increases, the dislocation density in the crystal increases rapidly. The dislocations are entangled with each other, and the entangled dislocations form a dislocation wall; when many dislocation walls are surrounded by independent dislocation-free regions, dislocation cells are formed one by one. During the wire-drawing process, the grains are elongated along the drawing direction, and grain-structure fibrosis occurs, resulting in a larger interface area, greater resistance to dislocation movement, and improved tensile strength.

A Φ0.135 mm copper wire with a single-pass drawing amount of 14% was selected for the three drawing rate tests. As shown in Figure 4a, after drawing at rates of 300 m/min, 500 m/min, and 700 m/min, the tensile strength of the wire is significantly improved, compared to that of the initial wire, from 615.5 MPa to 654.9 MPa, 660.26 MPa, and 659.4 MPa, respectively. When the strain is 0.15–0.45, the tensile strength increases rapidly; when the strain is 0.45–0.9, the tensile strength tends to be stable. After drawing at 300 m/min, the elongation of the wire increases from 1.57% to 1.581%. It decreases to 1.494% and 1.39% after drawing at 500 m/min and 700 m/min, respectively. When the drawing rate is 700 m/min, it is evident that the elongation of the single-crystal copper wire decreases significantly. This decrease in elongation corresponds to a gradual increase in tensile strength and a diminishing elongation as the level of metal deformation intensifies. Figure 5b illustrates that the resistivity changes in the material under three different drawing rates are relatively minimal. Specifically, the resistivity values increase successively from 1.732×10^{-8} Ω·m to 1.770×10^{-8} Ω·m, 1.784×10^{-8} Ω·m, and 1.789×10^{-8} Ω·m, respectively. An inflection point is produced at a strain of 0.9. As the strain continues to increase, the resistivity of the material at three different drawing rates continues to increase.

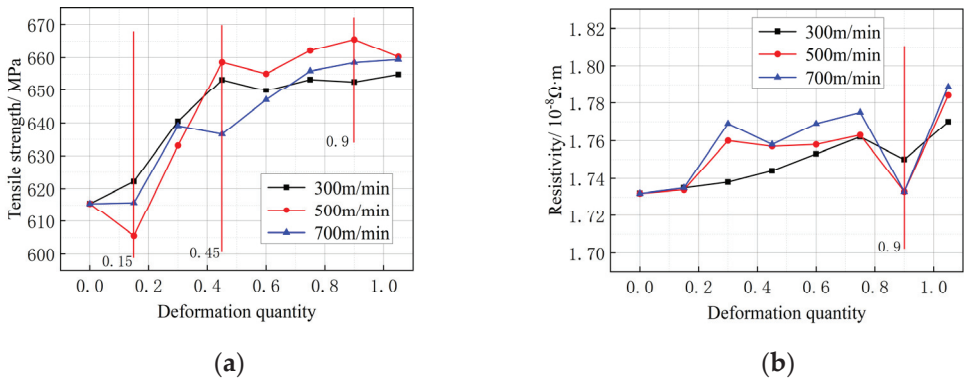

Figure 4. Mechanical properties and electrical conductivity of single-crystal copper wires at different drawing rates.(**a**) Tensile strength change in copper wire; (**b**) resistivity change in copper wire.

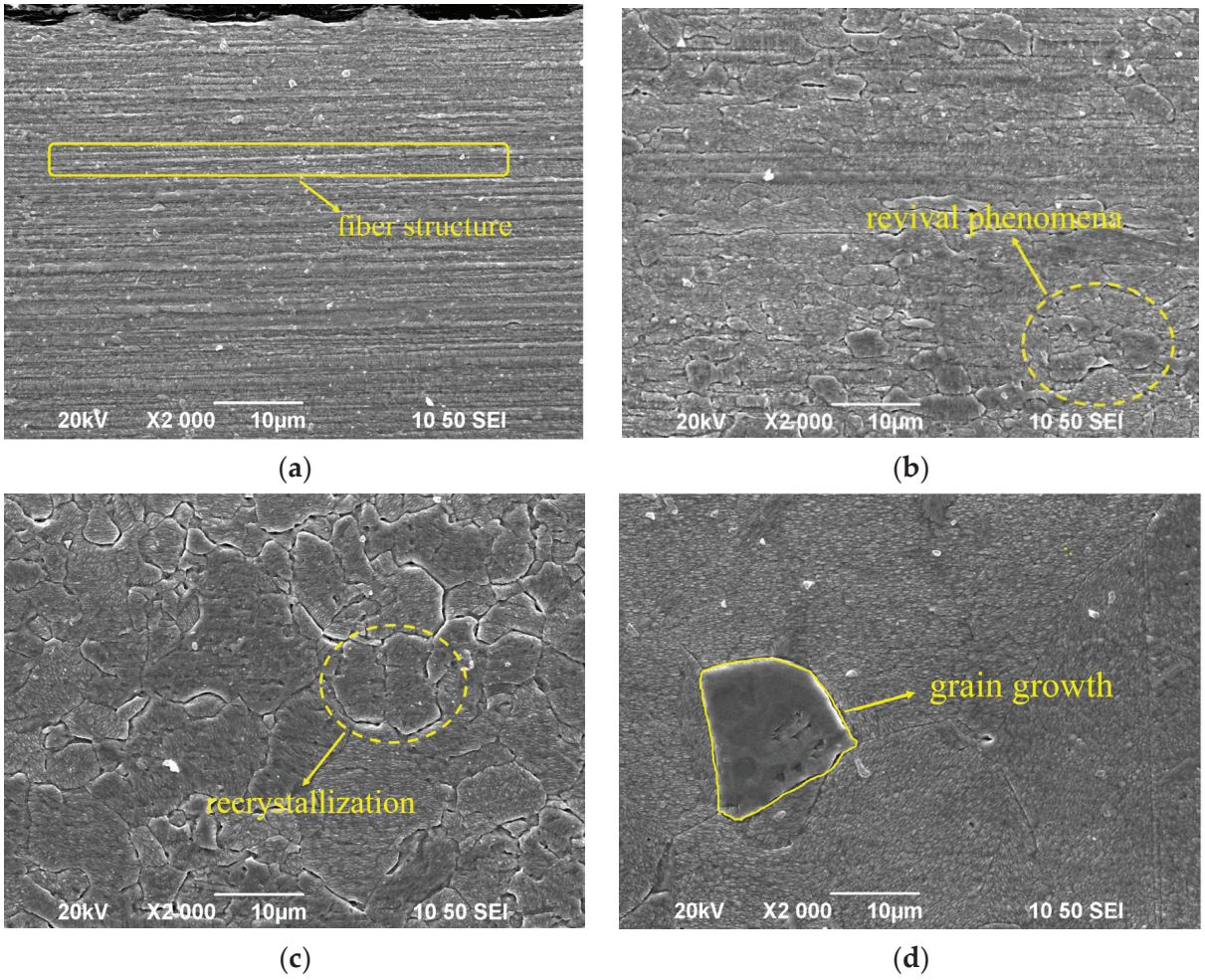

Figure 5. Microstructure of single-crystal copper wire under different annealing conditions. (**a**) Unannealed state; (**b**) annealing at 250 °C; (**c**) annealing at 350 °C; (**d**) annealing at 550 °C.

3.4. Microstructure of Single-Crystal Copper Wires under Different Heat Treatment Temperatures

The plastic deformation of the single-crystal metal is caused by crystal slip; that is, the movement of a large number of dislocations leads to the relative movement of one part of the crystal with respect to the other part along a certain crystal plane and direction. With the continuous plastic deformation of single-crystal copper wires, the changes in the internal structure of the crystal are mainly the changes in the density, distribution, and properties of the dislocations. The shear stress required to maintain the plastic deformation will also increase with the change in the shear variables. Therefore, in order to achieve further movement of dislocations, greater stress is required; that is, work hardening occurs.

After the multipass drawing of a single-crystal copper wire, serious work hardening and residual stress is created in the copper wire. Heat treatment can partially restore the mechanical properties changed by plastic deformation, reduce or eliminate residual stress, reduce resistivity, and improve the hardness and strength of the material. Copper is an active metal that is prone to oxidation during high-temperature heat treatment. The resulting oxide layer on the surface of the bonding wire can significantly reduce the reliability of the subsequent bonding process. For copper, the oxides that react with oxygen are mainly CuO and Cu_2O. H_2 is a reducing gas, which can react with CuO or Cu_2O at high temperatures, as follows:

$$CuO + H_2 = Cu + H_2O$$

$$Cu_2O + H_2 = 2Cu + H_2O$$

In the heat treatment process, if H_2 is used as the reducing gas, the products will be Cu and water vapor. Water vapor will not pollute the surface of the single-crystal copper bonding wire but will play a role in brightening heat treatment. The heat treatment temperature of the copper wire is within the range of 550 °C, and the ignition point is 572 °C, which is much lower than that of H_2. As there is no open fire source in the heat treatment tube, the mixing of H_2 and air in the furnace will not cause an explosion.

Figure 5a shows the microstructure of the unannealed Φ0.08 mm single-crystal copper wire; finer fibrous grains can clearly be observed. This is due to the slip phenomenon of single-crystal copper during wire drawing. Each grain is elongated along the drawing direction, following which the columnar crystal inside the wire is broken and the dislocation density increases. With the increase in strain, the broken grains gradually become orderly and elongate along the drawing direction. The degree of grain refinement continues to increase, finally forming a fibrous structure.

Figure 5b shows the microstructure of the single-crystal copper wire annealed at 250 °C. After annealing at 250 °C, the recovery phenomenon occurs in the copper wire. Owing to the movement and rearrangement of dislocations, the different dislocations on the same slip surface converge and are offset, and the fiber structure formed by grain elongation begins to gradually disseminate.

Figure 5c shows the microstructure of the single-crystal copper wire annealed at 350 °C. The deformed structure within the single-crystal copper wire due to drawing has disappeared, and the lattice defects, such as the point defects and dislocations, have undergone vigorous movement under the high temperature and have been absorbed and reduced by adjacent grains. The residual stress inside the copper wire is eliminated, the grain boundary characteristics are obvious, and the grains of the material begin to change. The new grains with low dislocation densities gradually replace the deformed grains with high dislocation density. The single-crystal copper wire now begins to recrystallize, with obvious grains appearing and gradually growing.

Figure 5d shows the microstructure of the single-crystal copper wire annealed at 550 °C. After the recrystallization of the wire, to reduce the large amount of stored energy remaining in the material, some grain sizes increase and others decrease by the movement of large-angle grain boundaries. Large grains annex small grains, resulting in grain growth. Compared to the samples annealed at 350 °C, several notable differences are observed in the samples annealed at higher temperatures, the grain size of the single-crystal copper wire annealed at 550 °C is larger, only a few larger grains can be observed in the same transverse direction, and the recrystallization process is completed.

After multipass drawing, serious work hardening and residual stress are observed in the copper wire rod. Heat treatment can partially restore the mechanical properties changed by deformation, reduce or eliminate the residual stress, reduce resistivity, and improve the hardness and strength. By eliminating the work-hardening phenomenon inside the material, the performance of the copper wire can be improved to meet the requirements of the high-performance copper wire.

3.5. Properties of Single-Crystal Copper Wires at Different Heat Treatment Temperatures

Figure 6a presents the change curve of the mechanical properties of the single-crystal copper wire at different annealing temperatures. The single-crystal copper wire without heat treatment has high tensile strength and low elongation. After heat treatment at 250 °C, the single-crystal copper bonding wire recovers, and the dislocation and residual stress inside the wire are partially eliminated and released. The tensile strength of the material decreases significantly to 284.3 MPa, which is 56% lower than that of the original sample. On the other hand, the elongation of the material increases from 1.49% to 12.6%. When the heat treatment temperature is increased to 300 °C, the tensile strength of the wire reduces to 242.1 MPa, which is 63.3% lower than that of the initial sample, and the elongation

increases to 19.5%. When the annealing temperature is 400 °C, the single-crystal copper bonding wire fully recovers and recrystallizes. At this time, the tensile strength of the material reaches 224.7 MPa and the elongation becomes 19.87%. With further increase in the annealing temperature, the recrystallized grains begin to grow. In the later stages, the tensile strength of the bonding wire decreases slowly, and the elongation decreases greatly. When the heat treatment temperature is 550 °C, the recrystallized grains continue to grow, and the elongation of the wire decreases greatly. When the heat treatment temperature is 300–400 °C, the tensile strength and elongation of copper wire tend to be stable and present excellent performance.

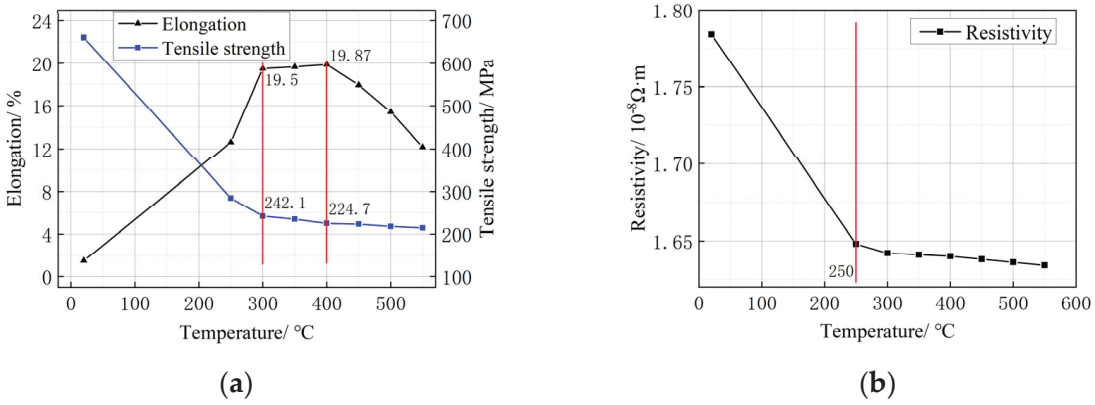

Figure 6. Properties of single-crystal copper wires at different annealing temperatures. (**a**) Change in mechanical properties of copper wire; (**b**) change in copper wire resistivity.

Figure 6b presents the change in the resistivity of the single-crystal copper wire at different heat treatment temperatures. The material exhibits high resistivity before heat treatment. When the heat treatment temperature is 250 °C, the resistivity of the material reduces significantly, 1.784×10^{-8} Ω·m to 1.648×10^{-8} Ω·m. With the further increase in the heat treatment temperature, the resistivity of the material continues to decrease. When the heat treatment temperature is 550 °C, the resistivity of the single-crystal copper wire is reduced to 1.634×10^{-8} Ω·m. The decrease in the resistivity is mainly because of the fact that heat treatment eliminates most of the defects such as dislocations and vacancies in the material, which decreases the resistance of electron motion and the degree of scattering of free electrons, thereby increasing the conductivity.

3.6. Mechanical Properties and Electrical Conductivity of Single-Crystal Copper Wires at Different Heat Treatment Rates

Figure 7a illustrates the impact of different heat treatment speeds on the mechanical properties of single-crystal copper wire at 300 °C. At an annealing rate of 20 m/min, the wire exhibits a tensile strength of 230.5 MPa and an elongation of 16.3%. As the annealing rate increases to 20–40 m/min, there is a noticeable improvement in both the tensile strength and elongation. However, further increasing the annealing rate leads to a slower increase in elongation and a slight decrease in tensile strength. At an annealing rate of 120 m/min, the wire achieves a tensile strength of 244.91 MPa and an elongation of 20.24%. Conversely, the material annealed at 20 m/min demonstrates significantly lower tensile strength and elongation compared to other annealing rates. This can be attributed to the slower annealing rate and longer annealing time, which promote a greater degree of recrystallization and grain growth within the material, resulting in a degradation of its mechanical properties.

Figure 7b depicts the resistivity change in the single-crystal copper wire at different annealing rates. Overall, the resistivity of the wire demonstrates an increasing trend as the annealing rate is increased. In the range of 20–80 m/min, the resistivity shows a slight increase from 1.598×10^{-8} Ω·m to 1.607×10^{-8} Ω·m and then from 1.607×10^{-8} Ω·m to

1.641 × 10^{-8} Ω·m. Finally, within the range of 80–120 m/min, the resistivity exhibits a slower increase from 1.641 × 10^{-8} Ω·m to 1.648 × 10^{-8} Ω·m. The annealing rate has a certain influence on the resistivity of the copper wire. When other conditions are fixed, a lower annealing rate is selected for annealing, and the copper wire exhibits better conductivity.

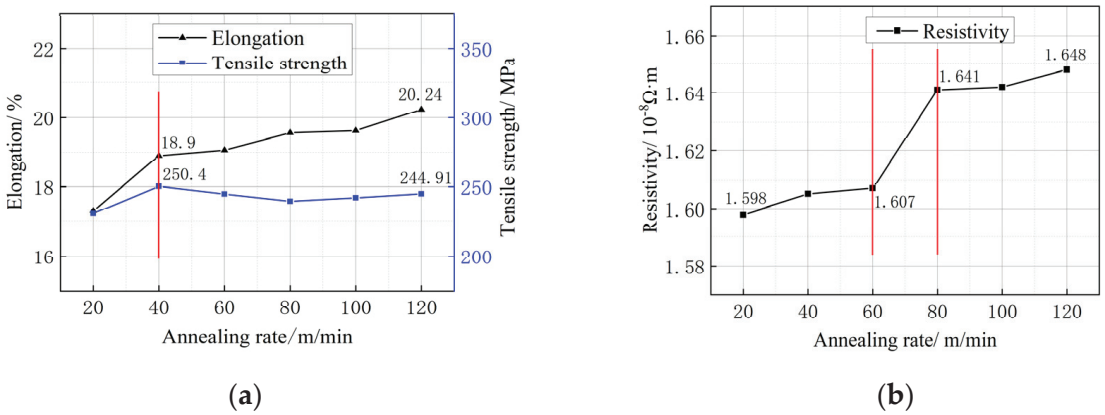

Figure 7. Mechanical and electrical properties of single-crystal copper wires at different annealing rates. (**a**) Change in mechanical properties of copper wire; (**b**) resistivity change in copper wire.

Figure 8 shows a 0.08 mm wire drawn. In this paper, the properties of copper wire under different process conditions are studied. At present, the strength and elongation of the 80μ m copper wire prepared by us are high in the same diameter wire, which is conducive to the subsequent fine drawing process and provides basic guidance for the preparation of ultrafine high-performance copper wire with a diameter less than 30 μm.

Figure 8. 0.08 mm real wire.

4. Conclusions

(1) After single-pass deformations of 18, 14, and 10%, the Φ0.25 mm copper wire rod changed to a Φ0.135 mm copper wire rod, and the tensile strength increased from 500.83 to 631.3, 615.5, and 637 MPa, respectively. The single-crystal copper wire in different schemes showed a trend of rising first and then stabilizing. The elongation of the final wire was 1.47, 1.57, and 1.52%, respectively. The resistivity of the wire changed from 1.745 × 10^{-8} to 1.776 × 10^{-8}, 1.732 × 10^{-8}, and 1.750 × 10^{-8} Ω·m, respectively. The overall performance of the wire was the best under deformation of a single pass of 14%.

(2) The experiment involved drawing a Φ0.135 mm copper wire at rates of 300, 500, and 700 m/min, after which its tensile strength and resistivity were measured. The results indicate that both the tensile strength and resistivity increased as the wire was drawn

further. Specifically, the initial tensile strength of the single-crystal copper wire was 615.5 MPa. After drawing the wire at a speed of 300 m/min, the tensile strength increased to 654.9 MPa. Subsequently, at drawing speeds of 500 and 700 m/min, the tensile strength further improved to 660.26 and 659.4 MPa, respectively. Similarly, the resistivity of the wire increased from 1.732×10^{-8} Ω·m to 1.770×10^{-8}, 1.784×10^{-8}, and 1.789×10^{-8} Ω·m.

(3) The Φ0.08 mm copper wire was annealed at a high temperature under an annealing rate of 100 m/min. After annealing at 300 °C, the resistivity of the wire decreased to 1.642×10^{-8} Ω·m. Simultaneously, the tensile strength reduced to 242.1 MPa, and the elongation increased to 19.5%. As the annealing temperature continued to increase, the tensile strength, elongation, and resistivity exhibited downward trends beyond 400 °C, and the decrease in elongation became more obvious. When the microstructure was annealed at 350 °C, the copper wire began to recrystallize. When the heat treatment temperature increased to 550 °C, the large grains swallowed up the small grains and grain growth occurred. The optimized annealing temperature of the Φ0.08 mm single-crystal copper wire was determined to be 350–400 °C.

(4) Following heat treatment of a Φ0.08 mm copper wire rod at different annealing rates, changes in tensile strength and elongation were observed. Tensile strength and elongation values were 230.5 MPa and 16.3%, respectively, at an annealing rate of 20 m/min. Meanwhile, at annealing rates ranging from 40–100 m/min, the material showed consistently high tensile strength and elongation with minor variations. At an annealing rate of 120 m/min, using single-crystal copper wire, the tensile strength was measured at 244.91 MPa, while elongation was recorded at 20.24%. However, the resistivity of this material increased from 1.598×10^{-8} Ω·m to 1.648×10^{-8} Ω·m. Overall, the single-crystal copper wire annealed within the range of 40–60 m/min exhibited excellent performance.

Author Contributions: Conceptualization, J.C.; methodology, X.W.; software, C.S.; validation, H.J.; investigation, H.J. and Y.S.; resources, J.C.; data curation, Y.S.; writing—original draft, X.W.; writing—review and editing, J.C. and X.W.; supervision, J.C. and X.W.; project ad-ministration, J.C.; funding acquisition, J.C. All authors have read and agreed to the published version of the manuscript.

Funding: This research is supported by the joint fund project of the evolution law of microstructure and properties and the regulation mechanism of bonding properties in the preparation and processing of copper-based micro-bonding wires. Project approval number: U21A2051.

Data Availability Statement: The data presented in this study are available on request from the corresponding author. The data are not publicly available due to the partner needs to keep the original data confidential, it cannot be shared.

Conflicts of Interest: The authors declare no conflict of interest.

References

1. Wang, L. *Design and Simulation of Ultrasonic Lead Bonding Tool for Microelectronic Packaging*; College of Mechanical and Electrical Engineering, Qingdao University: Qingdao, China, 2021.
2. Long, Y.; Arndt, M.; Dencker, F.; Wurz, M.; Twiefel, J.; Wallaschek, J. Impact of surface texture on ultrasonic wire bonding process. *J. Mater. Res. Technol.* **2022**, *20*, 1828–1838. [CrossRef]
3. Chiu, J.-E.; Wang, C.-S.; Lu, S.-W. Multi-response optimization of IC wire bonding for large probe marks by the RSM and desirability function approach. *Int. J. Adv. Manuf. Technol.* **2022**, *123*, 2719–2731. [CrossRef]
4. Ahn, B. Emerging Interconnection Technology and Pb-Free Solder Materials for Advanced Microelectronic Packaging. *Metals* **2021**, *11*, 1941. [CrossRef]
5. Alam, L.; Kehtarnavaz, N. A Survey of Detection Methods for Die Attachment and Wire Bonding Defects in Integrated Circuit Manufacturing. *IEEE Access* **2022**, *10*, 83826–83840. [CrossRef]
6. Mi, X.; Lou, H.; Xie, H.; Mo, Y.; Zhang, W.; Xiang, C. Development Strategy for Advanced Copper-Based Materials in China. *Chin. J. Eng. Sci.* **2023**, *25*, 96. [CrossRef]
7. Alim, A.; Abdullah, M.; Aziz, M.A.; Kamarudin, R. Die attachment, wire bonding, and encapsulation process in LED packaging: A review. *Sens. Actuators A Phys.* **2021**, *329*, 112817. [CrossRef]

8. Yang, F.; Zhang, X.; Fang, F. Microstructure and properties of cold-drawn Cu and Cu-Fe alloy wires. *IOP Conf. Series Mater. Sci. Eng.* **2022**, *1249*, 012057. [CrossRef]
9. Jiang, Y.-B.; Li, Y.-S.; Lei, Y.; Xie, J.-X. Cross-sectional structure, microstructure and mechanical property evolutions of brass cladding pure copper stranded wire composite during drawing. *Trans. Nonferr. Met. Soc. China* **2020**, *30*, 1857–1872. [CrossRef]
10. Zhou, H.; Zhang, Y.; Cao, J.; Su, C.; Li, C.; Chang, A.; An, B. Research Progress on Bonding Wire for Microelectronic Packaging. *Micromachines* **2023**, *14*, 432. [CrossRef]
11. Feng, J.; Song, K.; He, J.; Cheng, C.; Zhang, C.; Zhou, Y.; Cao, J.; Huang, T.; Zhang, X. Study on Microstructure and Properties of Cu-1Ag Alloy Microwire in Multi-pass Drawing. *Foundry Technol.* **2020**, *41*, 1020–1023.
12. Zhu, X.; Xiao, Z.; An, J.; Jiang, H.; Jiang, Y.; Li, Z. Microstructure and properties of Cu-Ag alloy prepared by continuously directional solidification. *J. Alloys Compd.* **2021**, *883*, 160769. [CrossRef]
13. Gokhfel'd, N.V.; Buinova, L.N.; Pushin, A.V.; Pushin, V.G. High Strength Nanocrystalline Ordered Cu3Pd Alloy Produced by Severe Cold-Drawing and Annealing. *Russ. Phys. J.* **2020**, *62*, 2288–2295. [CrossRef]
14. He, X.; Fu, H.; Xie, J. Microstructure and properties evolution of in-situ fiber-reinforced Ag−Cu−Ni−Ce alloy during deformation and heat treatment. *Int. J. Miner. Met. Mater.* **2022**, *29*, 2000–2011. [CrossRef]
15. Cheng, C.; Song, K.; Mi, X.; Wu, B.; Xiao, Z.; Xie, H.; Zhou, Y.; Guo, X.; Liu, H.; Chen, D.; et al. Microstructural evolution and properties of Cu–20 wt% Ag alloy wire by multi-pass continuous drawing. *Nanotechnol. Rev.* **2020**, *9*, 1359–1367. [CrossRef]
16. Cao, J.; Wu, W.; Zhang, C.; Hua, H.; Xu, X. Effects of heat treatment temperature on properties and microstructure of Ag-4Pd alloy bonding wire. *Trans. Mater. Heat Treat.* **2018**, *39*, 44–48. [CrossRef]
17. Chen, J.; Yan, W.; Ding, R.G.; Fan, X.H. Dislocation boundaries in drawn single crystal copper wires produced by Ohno continuous casting. *J. Mater. Sci.* **2009**, *44*, 1909–1917. [CrossRef]
18. Chen, J.; Yan, W.; Liu, C.; Ding, R.; Fan, X. Dependence of texture evolution on initial orientation in drawn single crystal copper. *Mater. Charact.* **2011**, *62*, 237–242. [CrossRef]
19. Li, X.; Zhou, Y.; Liu, Y.; Li, S.; Song, K.; Feng, C.; Wu, B.; Zhang, P.; Wu, H.; Gu, J.; et al. Microstructure evolution of high-strength and ultra-high-conductivity microfilament wire prepared by continuous deformation of single-crystal copper. *J. Mater. Sci.* **2022**, *57*, 20895–20908. [CrossRef]

micromachines

Article

Fabricating Ultra-Narrow Precision Slit Structures with Periodically Reducing Current Over-Growth Electroforming

Xiaohong Yang [1,2,3], Xinmin Zhang [1,*], Pingmei Ming [1,*], Yuntao Li [1], Wei Wang [1], Yunyan Zhang [1], Zongbin Li [1], Lunxu Li [1], Youping Xiao [1], Xiaoyi Guo [1] and Zheng Yang [1]

[1] School of Mechanical and Power Engineering, Henan Polytechnic University, Jiaozuo 454003, China; yangxiaohong@hpu.edu.cn (X.Y.); 15230636967@163.com (Y.L.); wangwei119230@163.com (W.W.); yun9404@163.com (Y.Z.); 18503843886@163.com (Z.L.); lilunxu1998@gmail.com (L.L.); 15215287591@163.com (Y.X.); tearsofsun@163.com (X.G.); yzheng1013@126.com (Z.Y.)
[2] School of Engineering and Technology, Henan University of Technology, Hebi 458030, China
[3] School of Mechanical and Electronic Engineering, Hebi Polytechnic, Hebi 458030, China
* Correspondence: xmzhang@hpu.edu.cn (X.Z.); mpm@hpu.edu.cn (P.M.)

Abstract: An ultra-narrow precision slit with a width of less than ten micrometers is the key structure of some optical components, but the fabrication of these structures is still very difficult to accomplish. To fabricate these slits, this paper proposed a periodically reducing current over-growth electroforming process. In the periodically reducing current over-growth electroforming, the electric current applied to the electrodeposition process is periodically stepped down rather than being constant. Simulations and experimentation studies were carried out to verify the feasibility of the proposed process, and further optimization of process parameters was implemented experimentally to achieve the desired ultra-narrow precision slits. The current values were: $I_1 = I_{initial}$, $I_2 = 0.75I_{initial}$ *at* $Q_c = 0.5Q_t$, $I_3 = 0.5I_{initial}$ *at* $Q_c = 0.75Q_t$, respectively. It was shown that, compared with conventional constant current over-growth electroforming, the proposed process can significantly improve the surface quality and geometrical accuracy of the fabricated slits and can markedly enhance the achievement of the formed ultra-narrow slits. With the proposed process, slits with a width of down to 5 ± 0.1 μm and a surface roughness of less than 62.8 nm can be easily achieved. This can improve the determination sensitivity and linear range of the calibration curves of spectral imagers and food and chemical analysis instruments. Periodically reducing current over-growth electroforming is effective and advantageous in fabricating ultra-narrow precision slits.

Keywords: periodically reducing current; over-growth electroforming; ultra-narrow precision slit structure

1. Introduction

A micro-scale slit structure is used as the primary component with the function of light filtering, collimation, and diffraction [1–4], and the slit width directly affects the sensitivity and resolution in the field of spectrometry [5–7]. The slits for optical applications are often several micrometers in width and tens of millimeters in length. Generally, the narrower the width, the higher resolution and sensitivity the slits have. Correspondingly, the ultra-narrow slits with widths of less than 10 μm are required to have an extremely high geometrical accuracy including a very small dimensional tolerance and a very small surface roughness of slit walls. However, such ultra-narrow precision metal slits are significantly harder to fabricate.

To fabricate the ultra-narrow precision metal slits, several methods including conventional machining methods and nontraditional machining methods have been employed. They mainly involve mechanical micro-milling [8–11], laser beam machining [12–18], electro-discharge micromachining (Micro-EDM) [19,20], electron beam machining [21], electrochemical micromachining (Micro-ECM) [22], chemical milling [23,24], micro-electroforming (Micro-

EF) [25–27], etc. For example, Xia et al. [28] utilized laser-induced oxidation-assisted micro-milling to fabricate high aspect ratio micro-slits on Ti6Al4V with a width of 0.5 mm and an aspect ratio of 5.4. Chow H M et al. [29] developed a modified rotating disk electrode (RDE) for the fabrication of micro-slit machining using EDM and obtained a 42 μm wide micro-slit on the Ti-6Al-4V workpiece. The above methods generate micro-slits by removing materials from the bulk workpiece based on the principles of mechanical shearing or thermal melting. These methods unavoidably leave debris on the slit wall and/or cause the machined thin-thickness slit to deform, so they are seldom used for ultra-narrow slits. Kim B H et al. [30] proposed an ultrashort ECM to fabricate slit microstructures but only achieved a tapered micro-slit whose upper width was 60 μm and lower width was 40 μm. Bing Zhu et al. [31] proposed an innovative micro-ECM process, i.e., wire-ECM, and successfully fabricated a 30-aspect-ratio 0.16 mm-wide slit. Although the micro-ECM processes based on an anodic dissolution mechanism do not cause debris or deformation defects, they are hard to generate high-accuracy ultra-narrow slits with due to the inherent stray corrosive effect. This indicates that an electrochemical process can provide a relatively desirable mechanism to generate micro-scale structures. Unlike ECM, which is a subtractive manufacturing process, micro-electroforming (micro-EF), which is also based on the electrochemical reaction process, uses the material additive process to create microstructures and micro-components atom by atom and layer upon layer. These unique machining mechanisms and forming processes enable micro-EF to extremely accurately fabricate or replicate the structures and articles. According to the mask used, micro-EF has two fabrication manners: maskless EF and mask EF. Among them, mask EF has a considerably higher formation accuracy, and so it is used more widely. Mask EF can be further divided into two categories: through-mask electroforming (TM-EF) and over-growth electroforming (over-growth EF). TM-EF forms microstructures and micro-components by filling the reduced atoms into the predefined through-mask cavities (molds), which are geometrically accurate, finally achieving the replicates of the through-mask molds. However, this kind of EF is hard to create ultra-narrow slits with because the corresponding ultrathin convex photoresist molds are hard to make. Unlike TM-EF, over-growth EF is mostly used to generate tapered hollow microfeatures such as micro-sized conical orifices and tapered slits due to its different formation manner. The total procedure of over-growth EF involves two phases. In the first phase, the deposited materials are gradually filled into the photoresist mold cavities, as in TM-EF, until the cavities are completely filled up, and then the second phase starts. In the second phase, the deposited materials not only continue to grow along the direction of the thickness but also expand freely along the horizontal direction on the top surface of the photoresist masks, thus gradually forming the narrowing hollow structures by the expanding deposited materials and finally giving a tapered hollow structure—lower big and upper small. With this nontraditional EF, some micro-scale precision hollow structured components have been created. Yunyan Zhang et al. [32] used this technique to fabricate a 3 μm-diameter micro-hole plate for a precision medical atomizer. The fabricated micro-holes have a favorable dimensional tolerance, which is within $\pm$0.1 μm. However, ultra-narrow slits with a width of less than ten micrometers are significantly difficult to fabricate when the standard over-growth EF is used. This is probably because the mass transportation conditions become poorer and poorer with the narrowing of the forming slits or holes, generating more defects. To overcome these drawbacks, a modified over-growth EF process was proposed. In the modified over-growth EF, a gradually reducing interelectrode (between the anode and cathode) electric current rather than a constant electric current was used during the electrodeposition, so it was called periodically reducing current over-growth electroforming (PRC over-growth EF). With PRC over-growth EF, ultra-narrow precision slits with widths of several micrometers are expected to be fabricated. In the following sections, PRC over-growth EF is modeled via a numerical simulation based on the tertiary current distribution and validated experimentally and further attempts are made to fabricate the components with ultra-narrow slits.

2. Principle and Simulation Analysis of PRC Over-Growth EF

2.1. Principle of PRC Over-Growth EF

The schematic diagram of PRC over-growth EF for fabricating slit structures is shown in Figure 1. In PRC over-growth EF, the interelectrode electric current, I, applied to the electrodeposition process is periodically reduced according to some criterion rather than kept constant. For example, I is reduced two times according to the increase in Coulombic quantity consumed, i.e., $I_1 = I_{initial}$, $I_2 = 0.75I_{initial}$ *at* $Q_c = 0.5Q_t$, $I_3 = 0.5I_{initial}$ *at* $Q_c = 0.75Q_t$. Hereto, $I_{initial}$ is the initial value of the interelectrode electric current applied to the process, Q_t is the theoretical value of the total Coulomb volume of the whole electroforming process. The main reason for periodically reducing current during electrodeposition is to reduce the possibility of mass transportation limitation because the depositing space where the electrochemical reactions are taking place increasingly narrows with deposition time.

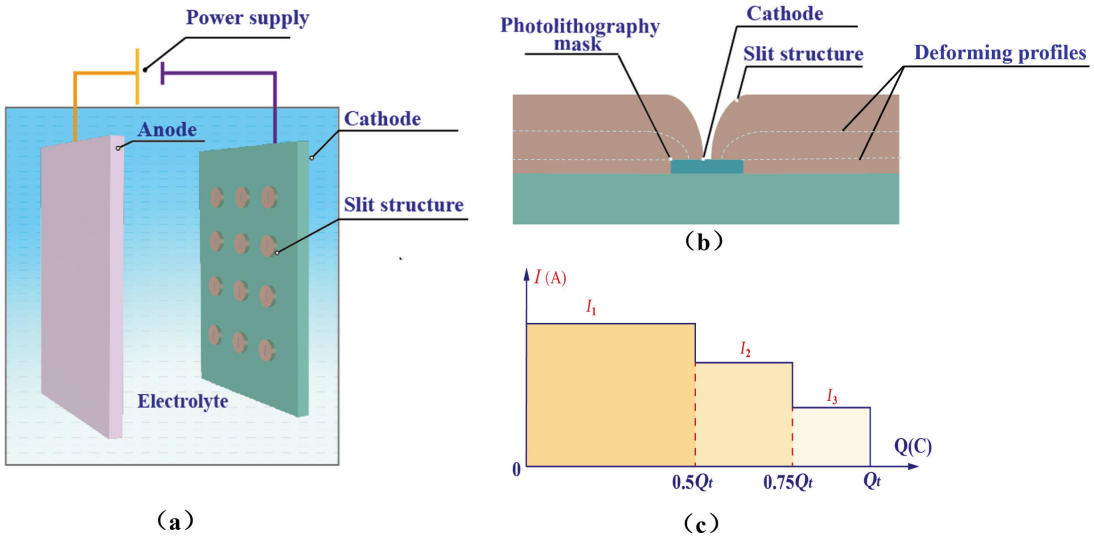

Figure 1. Schematic diagram of the periodically reducing current over-growth electroforming for fabricating slit structures. (**a**) Technical approach. (**b**) Process of over-growth EF. (**c**) Periodically reducing current.

2.2. Simulation Analysis

2.2.1. Simulations

In order to understand the variation in electrolyte flow rate, cathode current density, and cation concentration with electrodeposition time while forming ultra-narrow slits with PRC over-growth EF, a two-dimensional simulation model based on the tertiary current distribution was developed, as shown in Figure 2. The upper boundary denotes the anode, Γ_1, and the lower boundary denotes the cathode, Γ_3. The cathode is covered with well-defined photoresist mask patterns, which are denoted by Γ_4. The left boundary of the model is defined as the electrolyte inlet and the right boundary is defined as the electrolyte outlet, denoted by Γ_2 and Γ_5, respectively.

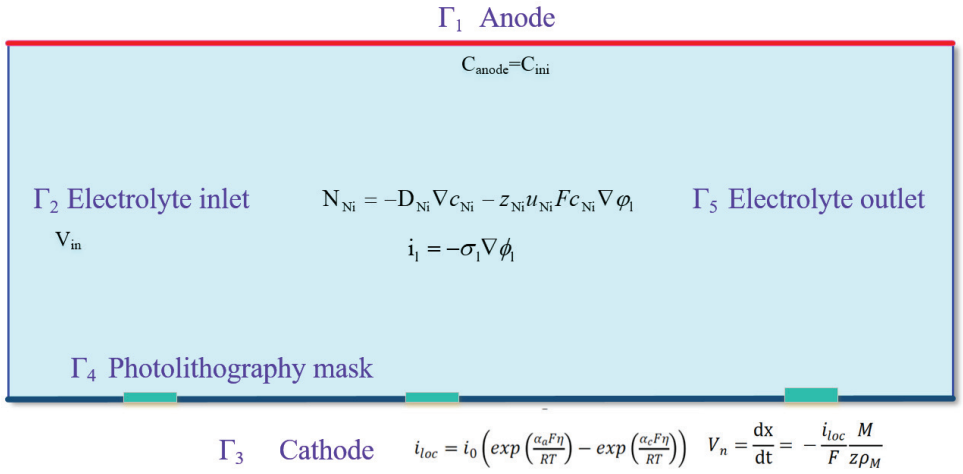

Figure 2. Two-dimensional model established to simulate PRC over-growth EF.

Since the electroforming process involves multiphysics fields including an electrochemical reaction field, an electric current field, a mass transfer rate field, an ion concentration field, etc. [33], multiple field theories are theoretically needed to simulate such a process. However, this is extremely difficult. Usually, a simplified electric field and flow field coupled multiphysics field are used to facilitate the simulation. For this, some assumptions were made as follows.

(1) Boundary effects are neglected and the potentials at each electrode surface are equal.
(2) The electrolyte is isotropic and its conductivity is constant over the confined area.
(3) Concentration polarization is not considered, and only the mass transport of nickel cations associated with electrodeposition is considered in the simulations. The anode boundary is set as an invariant boundary, while the cathode boundary is a geometric deformation boundary.

In the numerical model, the mass transportation of nickel flux in the electrolyte is expressed as follows:

$$N_{\mathrm{Ni}} = -D_{\mathrm{Ni}}\nabla c_{\mathrm{Ni}} - z_{\mathrm{Ni}}u_{\mathrm{Ni}}Fc_{\mathrm{Ni}}\nabla\phi_l \quad (1)$$

$$\frac{\partial c_{Ni}}{\partial t} + \nabla\cdot N_{Ni} = 0 \quad (2)$$

where N_{Ni} denotes the transport vector (mol/(m^2·s)), c_{Ni} is the nickel concentration in the electrolyte (mol/m^3), z_{Ni} is the charge of the nickel ion, u_{Ni} is the mobility of the nickel ion (m^2/(s·J·mol)), F is Faraday's constant (C/mol), and ϕ_l is the electrolyte potential (V).

The current density is obtained by solving the above equations with the electrolyte conductivity σ_l and the electrolyte potential ϕ_l. At the cathode–electrolyte interface, the local current density i_{loc} is given by the Butler–Volmer equation.

$$i_l = -\sigma_l\nabla\,\phi_l \quad (3)$$

$$i_{loc} = i_0\left(exp\left(\frac{\alpha_a F\eta}{RT}\right) - exp\left(\frac{\alpha_c F\eta}{RT}\right)\right) \quad (4)$$

where α_a is the anodic transfer coefficient, α_c is the cathode transfer coefficient, i_0 is the exchange current density, η is the overpotential, R is the gas constant, and T is the Kelvin temperature.

The deformation caused by electrodeposition was controlled by the local current density and nickel icon transportation, and the equation was established using Faraday's law:

$$N_{Ni} = -\frac{i_{loc}}{2F} \quad (5)$$

$$V_n = -\frac{i_{loc}}{F}\frac{M}{z\rho_M} \tag{6}$$

where V_n is the deformation rate, M is the mean molar mass, ρ is the nickel density, and n is the number of participating electrons.

The same model was employed to simulate the slit formation under different current modes, i.e., the constant current mode and the periodically reducing current mode, in which the total charge on the anode was kept constant while different current densities were applied at the anode boundary. In the constant current mode, the current was maintained at the level of I = 1 A. Specifically, the periodically reducing current mode was divided into three phases, as shown in Figure 1c. The definition and boundary conditions of the simulation model are listed in Table 1.

Table 1. Definition and boundary conditions of the simulation model.

Notation	Description	Property
Γ_1	Anode	Ion concentration Canode $= 500$ mol/m^3 Constant current mode : $I = 1$ A Periodically reducing current mode : $Q_c = (0\text{–}0.5)Q_t$, $I_1 = 1$ A $Q_c = (0.5\text{–}0.75)Q_t$, $I_2 = 0.75$ A Q_c= (0.75–1)Q_t, I_3 = 0.5 A
Γ_2	Electrolyte inlet	V_{in} = 0.2 m/s
Γ_3	Cathode	Set as the equipotential boundary with 0 V and the geometrical deformation rate depicted as V_n
Γ_4	Photolithography mask	No flux
Γ_5	Electrolyte outlet	-

2.2.2. Results and Discussion

(1) Flow field distribution

The velocity variation during the over-growth EF simulation for the slit formation process is shown in Figure 3. It was found that the simulated geometric deformation was mainly concentrated above the photolithography mask, as the deposition height increased from 21 μm to 48 μm while the slit width decreased from 50 μm to 5 μm, as shown in Figure 3b. Correspondingly, the velocity distribution near the slit shifted with the raised contour profiles. At the same time, the electrolyte filled into the slit was slowed down to less than 0.005 m/s, which can be considered stagnant. The formation of ultra-narrow slits resulted in an extremely low electrolyte flow within the narrowing slit. The space for metallic ion transportation became increasingly restricted. Despite attempts to increase the electrolyte flow rate over the cathode, the convective mass transfer efficiency within the extremely narrow slits was not significantly improved.

(2) Cathodic current density distribution

The cathodic current density distribution under the modes of the constant current and the PRC over-growth EF current is shown with contours ranging from 0 to 120 A/m^2 in Figure 4. The same slit-forming shapes were found as the slit shrunk. However, the distribution of current density changed more significantly according to the slit's structural formation as the slit width changed from 50 μm to 5 μm. The formation caused the concentrated cathodic current density on the tapered slit wall. Specifically, in the constant current mode, the maximum current density at the surface of the slit structure reached 162 A/m^2 when the slit width was 5 μm, and the current density at the bottom of the slit was almost negligible, while the flat sides had a constant current density of 100 A/m^2. On the contrary, the maximum current density at the slit decreased to 65 A/m^2 in the PRC mode. Compared with the constant current mode, the periodically reducing current mode can significantly improve the current density concentration on the cathode surface, which is favorable for obtaining high-quality slit structures.

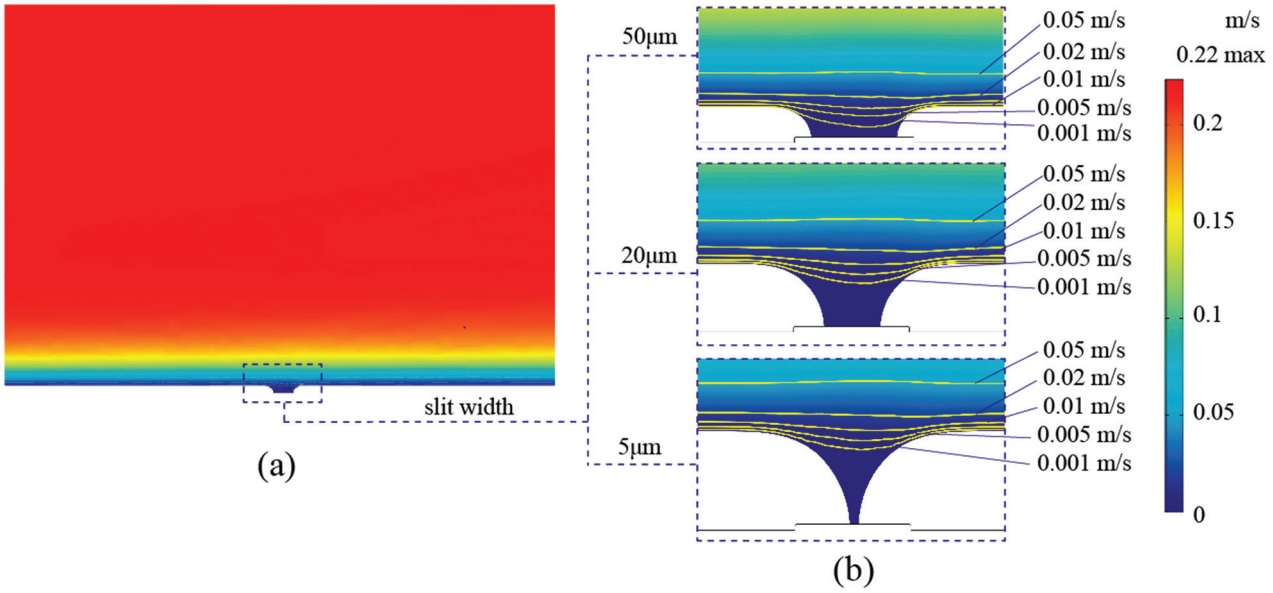

Figure 3. Velocity variation during the over-growth EF simulation. (**a**) The velocity distribution between the anode and cathode. (**b**) Local flow distribution with velocity contours as the slit width decreased from 50 μm to 5 μm.

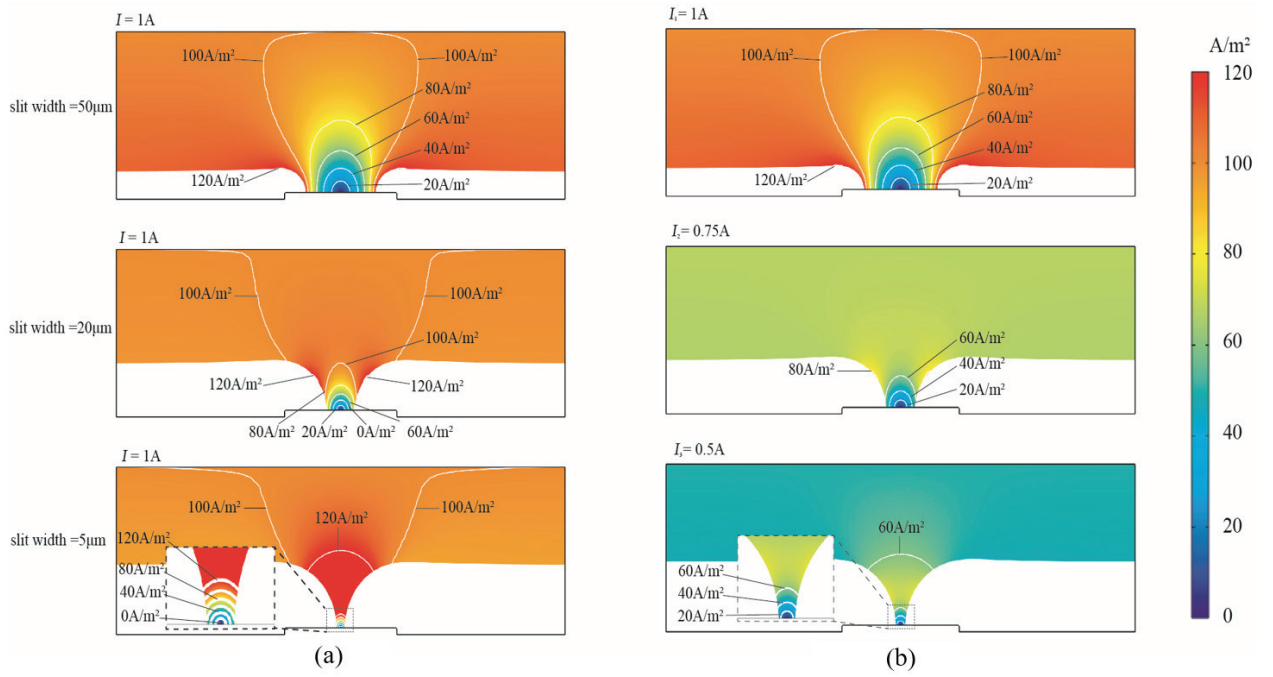

Figure 4. Cathodic current density distribution of over-growth EF. (**a**) Constant current mode. (**b**) Periodically reducing current mode.

(3) Ion concentration distribution

The ion concentration distributions of the over-grown EF with constant current and periodically reduced current modes are shown in Figure 5. When the slit width was reduced from 50 μm to 5 μm using the constant current mode, the ion concentration at the slit decreased significantly. At a slit width of 5 μm, the lowest ion concentration was 224 mol/m^3, which was less than half of the electrolyte bulk concentration. The lowest ion concentration was 440 mol/m^3 at a slit width of 5 μm when using the PRC current mode. The simulation result has shown that the PRC current contributed to the improved

ion concentration at the bottom, which was beneficial for the geometrical accuracy of the ultra-narrow slit structure under poor mass transportation conditions.

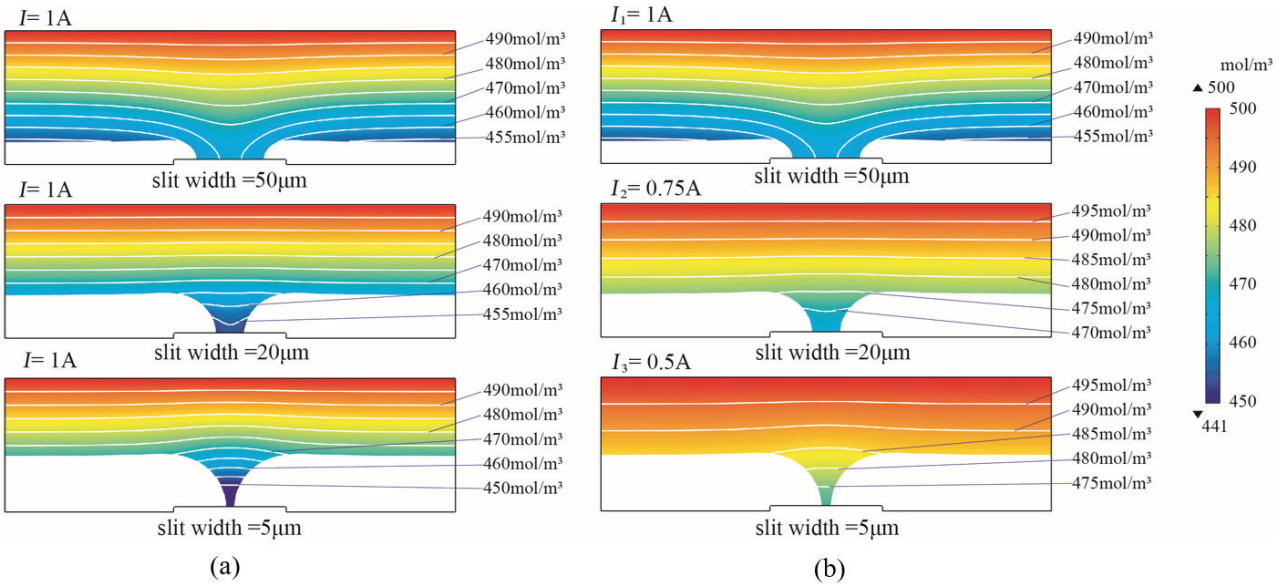

Figure 5. Ion concentration distribution of over-growth EF. (**a**) Constant current mode. (**b**) Periodically reducing current mode.

The simulation results show that the mass transfer behavior of metal cations from the electrolyte to the cathode surface during the slit formation using the over-growth electroforming electrodeposition technique deteriorates as the slit width decreases, as shown in Figure 6. The process is categorized into three phases including a phase of good mass transfer (Figure 6a), near the phase where mass transfer is limited (Figure 6b), and a mass transfer limitation phase. In the good mass transfer phase, the slit size is wide and the migration of cations is not restricted. However, at the stage where mass transfer is limited, the decrease in slit width hinders cation migration into the slit structure, resulting in a lower cation concentration in the region with a narrower slit width. In addition, the cathode undergoes a hydrogen reaction to produce bubbles, which can affect the electrodeposition quality. A periodically reducing current model using over-growth EF can enhance mass transfer in the fabrication of ultra-narrow slit structures. This is because the input current is periodically lowered, resulting in a subsequent decrease in cationic demand at the cathode, which improves the ion-deficient state of the slit region under mass-transfer-limited conditions.

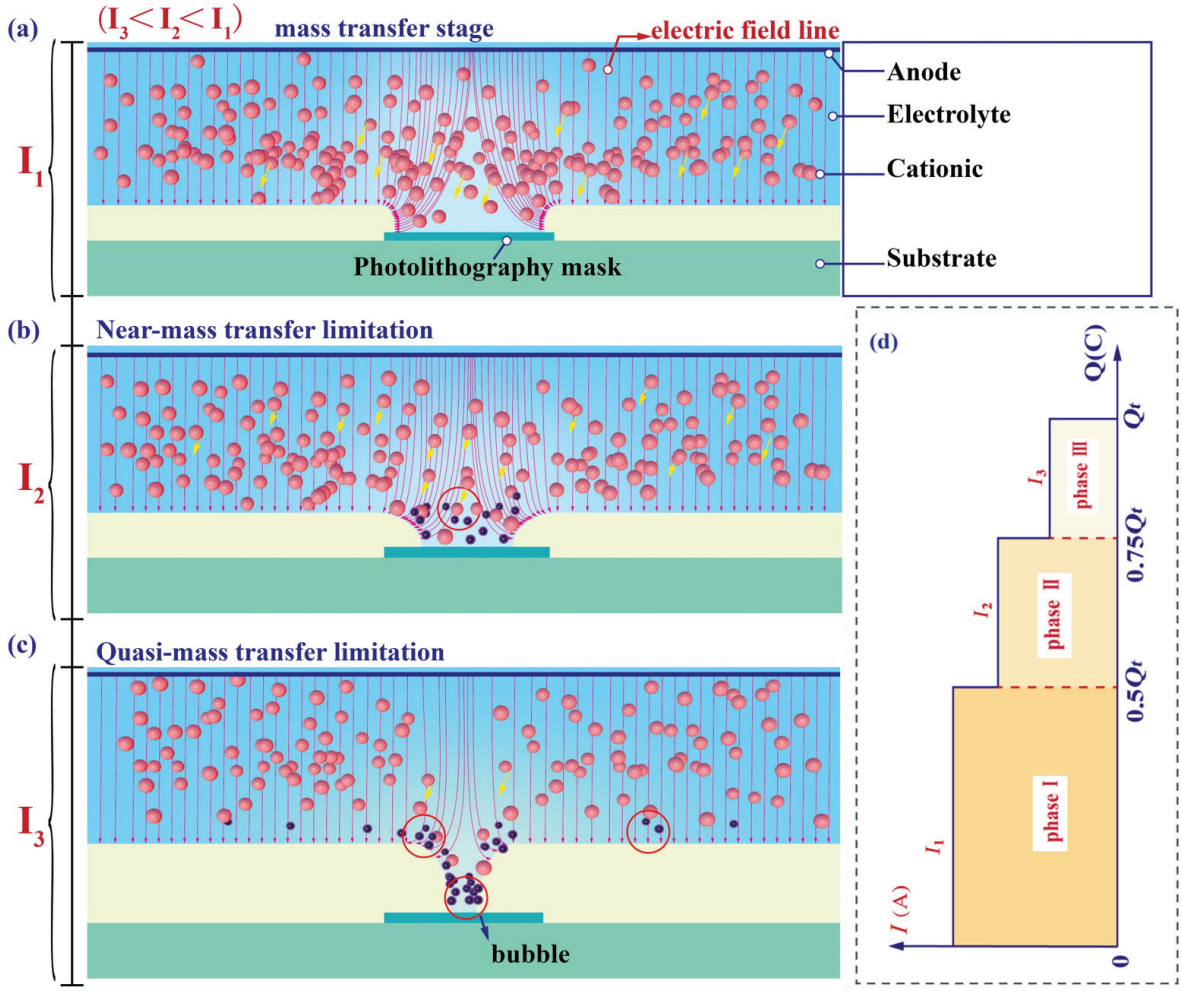

Figure 6. Schematic diagram of mass transfer during over-growth EF. (**a**) Phase of good mass transfer. (**b**) Near the phase where mass transfer is limited. (**c**) Phase in which mass transfer is limited. (**d**) Phase of periodically reducing currents corresponding to electrodeposition charge.

3. Experimental Study

3.1. Materials and Methods

A 304 stainless steel plate with a thickness of 1 mm was selected as the substrate. The cathode substrate was covered by the photolithography mask array with a thickness of 3 μm, a width of 80 μm, and a length of 3 mm. The experiments used the nickel sulfamate system, electrolyte ratio, and experimental process parameters shown in Table 2. The surface morphology detection equipment used is FEI-F50 Nova450 field emission scanning electron microscope (SEM, Beijing, China), the surface roughness detection equipment is the confocal laser scanning microscope (CLSM) type IX83-FV3000 (Olympus, Tokyo, Japan), and the geometrical accuracy detection was performed using the AM600CNC imaging instrument (Dongguan, China).

Table 2. Electrolyte composition and experimental process parameters.

Items (Unit)	Value
Nickel sulfamate ($Ni(SO_3NH_2)_2{\cdot}4H_2O$)/(g/L)	500
Nickel chloride ($NiCl_2{\cdot}6H_2O$)/(g/L)	6–10
boric acid (H_3BO_3)/(g/L)	30–40
Temperature (°C)	50–55
pH	3.8–4

In order to compare and analyze the quality of the slit structure, two modes were used: the constant current mode and the periodically reducing current mode over-growth EF. Combining the electrodeposition efficiency and molding quality, a constant current model with an interpolar current of 1 A and a periodic reduced current mode with interpolar currents of 1 A, 0.75 A, and 0.5 A were used. According to the theoretical total Coulomb amount Q_t required to fabricate the slit structure and the molding characteristics, the whole fabrication process was divided into three stages according to the Coulomb variation and the molding characteristics, and the interpolar current was constant at each stage. The detailed stages of changing the interpolar current are when the Coulomb quantity increases from 0 to 0.5 Q_t, the interpolar current is 1 A; when the Coulomb quantity increases from 0.5 Q_t to 0.75 Q_t, the interpolar current is 0.75 A; and when the Coulomb quantity increases from 0.75 Q_t to Q_t, the interpolar current is 0.5 A.

3.2. Results and Analysis

3.2.1. Morphology and Surface Quality

The ultra-narrow slit structure prepared by PRC over-growth EF is shown in Figure 7. The component array layout and single slit structure are shown in Figure 7a,b, respectively. The camera photograph is shown in Figure 7. The dimensions shown in the figures are the feature dimensions of the slit component.

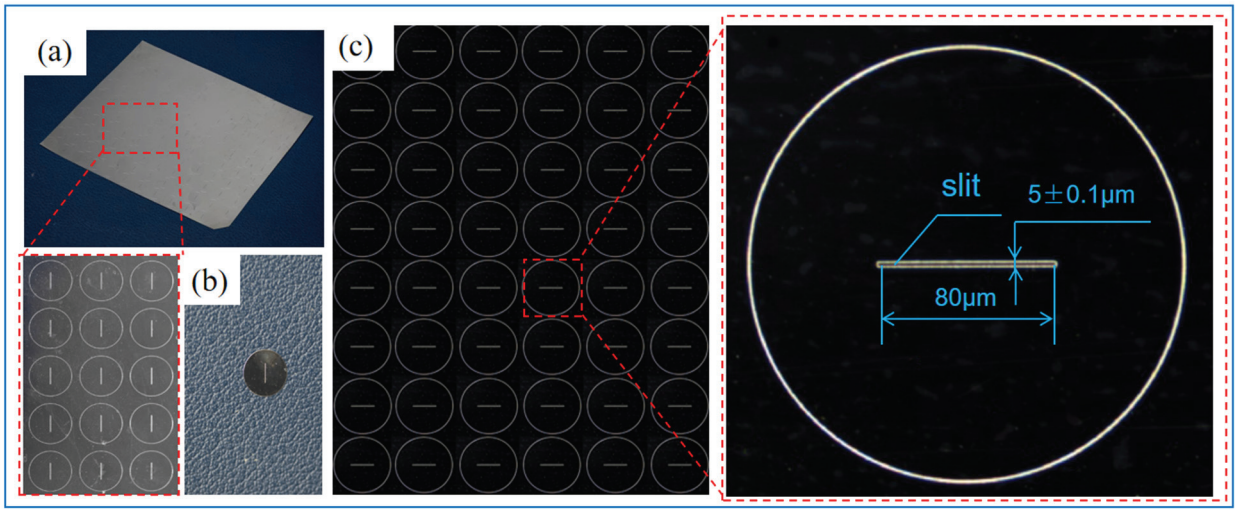

Figure 7. Total view of the ultra-narrow slit structure prepared by PRC over-growth EF. (**a**) The total view of the component with slit array. (**b**) Partial view of the slit array. (**c**) The dimensions and accuracy of the formed slit.

The SEM image of the slit is shown in Figure 8. In the over-growth EF process, as the slit width decreases, the mass transfer limitation at the slit becomes more and more serious. At this time, if the current input value at the stage of good mass transfer continues to be used, i.e., the magnitude of the current input value remains unchanged, the metal cations generated at the anode will not be able to reach all the way to the cathode due to the mass transfer limitation, and the phenomenon of metal cation excess will occur in the solution. When using PRC over-growth EF, as the slit width is gradually smaller, the current input value is gradually reduced according to the mass transfer limitation. At this time, the number of metal cations supplied by the anode in the unit time is reduced, which is exactly matched with the number of cations that can reach the cathode and undergo the electrodeposition reaction, and there will be no excess cations in the solution so that the phenomenon of nodules due to the deposition of metal cations in the rest of the slit is avoided. The phenomenon of nodulation due to the deposition of metal cations in other parts of the slit will be avoided.

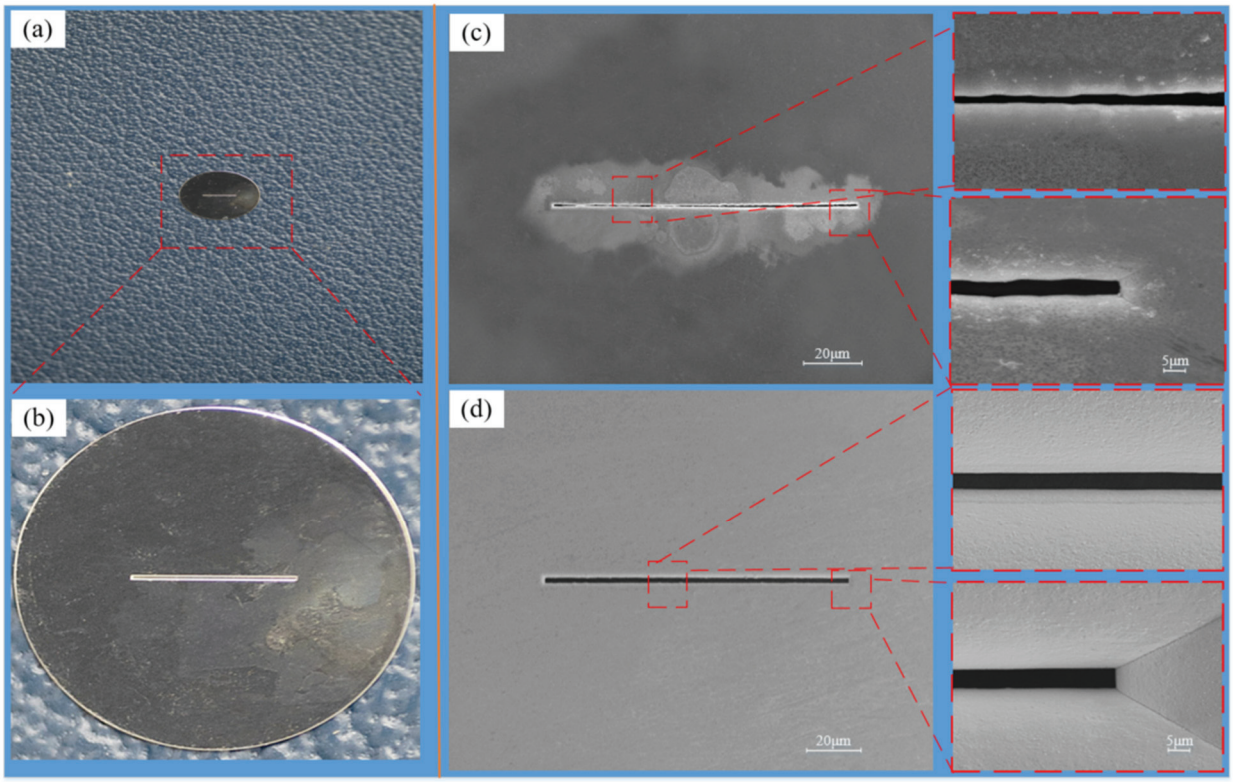

Figure 8. The component with the slit structure and the SEM image of the slit structure. (**a**) Photographs of individual slit parts. (**b**) Enlarged view of a single slit part. (**c**) Constant current mode. (**d**) Periodically reducing current mode.

The surface roughness test results are shown in Figure 9. It was found that the surface roughness value of the PRC over-growth EF slit structure (62.8 nm) was lower than those formed by constant current over-growth EF (72.6 nm).

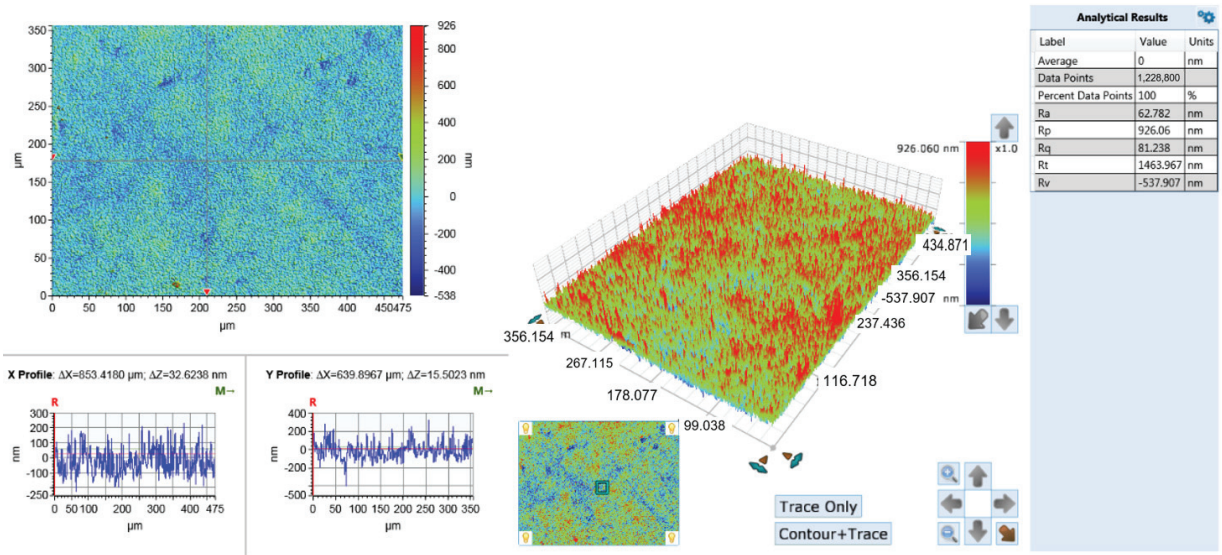

Figure 9. Characterization of slit surface roughness in PRC over-growth EF mode.

3.2.2. Geometrical Accuracy

The AM600CNC imaging instrument (Dongguan, China) is used to observe the slit structure. The slit parts are placed horizontally on the imaging instrument table, the

intensity of the light source above and below the lens of the imaging instrument is adjusted, and the part that transmits light, which is the slit part, is in a bright state, and the part that does not transmits light is the outer edge of the slit, and the slit part is the outer edge of the slit. As shown in Figure 10a, the two edge lines of the slit made using the constant current mode are uneven and jagged, showing a sawtooth shape, and there are more nodules. The two edge lines of the slit utilizing PRC over-growth EF are straight, with a complete shape and uniform growth, as shown in Figure 10b. The results show that the poor quality of the slit molding is due to the uneven mass transfer of the electrolyte during electroforming when the constant current mode is used, and as the slit width becomes narrower, the mass transfer becomes worse, resulting in uneven growth of the slit edges and the formation of jagged edges. As shown in Figure 10a, the two edge lines of the incision using PRC over-growth EF were straight, with a complete shape and uniform growth, and the accuracy of the slit width ranged from ± 0.1 μm. The two edge lines of the slit fabricated using the constant current mode were uneven, with more nodules, and the slit widths were uneven with a wide range of variations, as shown in Figure 10b. The main reason for this is the same as the effect of the current mode on the surface morphology.

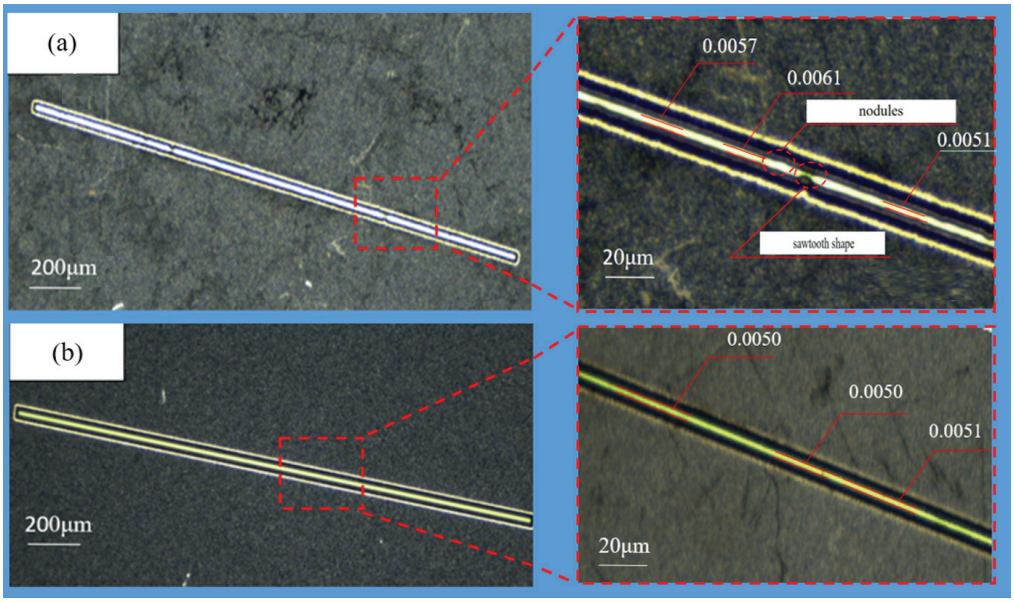

Figure 10. The enlarged photo view of a single slit's structure. (**a**) Constant current mode. (**b**) Periodically reducing current mode.

In order to characterize the straightness and parallelism of the slit, a reference coordinate system was established with the length of the slit parallel to the *x*-axis, as shown in Figure 11a. The distances from both edges of the slit to the *x*-axis were measured: y_s for the distance from the upper edge to the *x*-axis, and y_x for the distance from the lower edge to the *x*-axis. Fifty points on both edges were measured and plotted as scatter plots, as shown in Figure 11b,c. As shown in Figure 11b, the points with a distance of 5 μm between the slits were neatly arranged in a straight line, which indicates that the parallelism of the two slits is good, while in Figure 11c, it is shown that the points at the wall of the slits deviate from the straight line, which indicates that the parallelism of the slits is poor. By observing these scatter plots, it is clear that both edges of the slit exhibit high straightness while maintaining high parallelism under the mode of PRC over-growth EF.

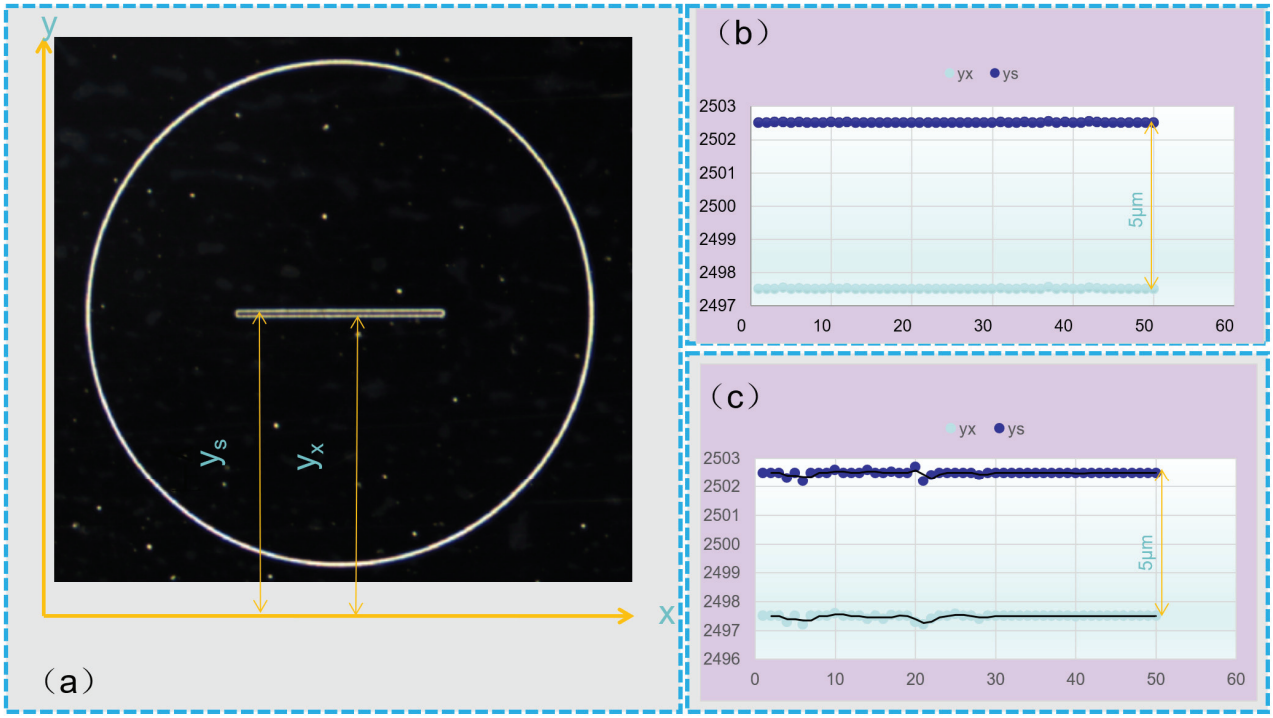

Figure 11. Characterization of the straightness and parallelism of slits. (**a**) Coordinate systems for evaluating edge accuracy. (**b**) Periodically reducing current mode. (**c**) Constant current mode.

In the above, two electrochemical deposition modes (constant current mode and periodically decreasing current mode) were used to prepare slit structures with a slit width of 5 μm, and the surface quality, surface morphology, and geometrical accuracy of the slit structures were characterized. Compared with the constant-current mode, slits with a small range of slit size variation, uniform size, and which are flat can be obtained by using the periodic decreasing current mode. The dimensions varied between 0.0049 and 0.0051 mm and the slits were free from defects such as nodules and sawtooth shapes. It shows that the surface roughness value at the slit is even smaller and can reach 62.8 nm with good surface quality. For the above phenomenon, the paper reveals the forming principle of periodic decreasing current mode over electroforming from the principle of electrodeposition slits, i.e., as the width of the slit decreases, the amount of metal cations provided by the anode to the cathode is limited, and a state of cation excess occurs. During the deposition process, if the state of excess metal cations can be avoided by matching the amount of metal ions supplied by the anode to the amount of metal ions deposited, there will be no excess metal ions and the nodule phenomenon can be avoided. Finally, it was found that PRC over-growth EF significantly improved the surface topography, surface quality, and geometrical accuracy of the slit structure.

4. Conclusions

To fabricate ultraprecision micro-slit structures using the electroforming process, specially ultra-narrow slits, in order to improve the resolution and sensitivity in filtering, collimation, and diffraction, a modified PRC over-growth EF technique was proposed. Numerical simulations and experimental studies were carried out to verify its feasibility and practicability. Some conclusions are made as follows.

(1) PRC over-growth EF is significantly effective and advantageous for fabricating ultra-narrow precision slits, since it can maintain a constantly favorable condition for the total electrodeposition process.
(2) With PRC over-growth EF, slits with a width of down to 5 ± 0.1 μm and a surface roughness of less than 62.8 nm can be easily achieved.

(3) With PRC over-growth EF, the reduction in the current is carried out preferentially in terms of the consumed Coulomb quantity.

Author Contributions: Methodology, X.Y. and P.M.; Software (COMSOL6.0), Y.Z.; Validation, X.Z.; Formal analysis, Z.L.; Investigation, L.L. and Z.Y.; Resources, W.W.; Data curation, Y.L., Y.X. and X.G. All authors have read and agreed to the published version of the manuscript.

Funding: This work was supported by the National Natural Science Foundation of China (Grant number 51875178), the Scientific and Technological Key Project in Henan Province (Grant number 232102221023 and 232102220042), and the Fundamental Research Funds for the Universities of Henan Province (NSFRF210338).

Data Availability Statement: Data available on request from the authors. The data that support the findings of this study are available from the corresponding author, [P.M.], upon reasonable request.

Conflicts of Interest: The authors declare that they have no known competing financial interests or personal relationships.

References

1. Esmaeili, S.; Talebi, M.; Pourdeilami, A.; Farsangi, E.N. Innovative cost-effective pendulum tiltmeter based on the moiré technique. *Opt. Eng.* **2023**, *62*, 054101. [CrossRef]
2. Sidoli, M.; Magnani, G.; Fornasini, L.; Scaravonati, S.; Morenghi, A.; Vezzoni, V.; Bersani, D.; Bertoni, G.; Gaboardi, M.; Riccò, M.; et al. Defective graphene decorated with TiO_2 nanoparticles as negative electrode in Li-ion batteries. *J. Alloys Compd.* **2023**, *958*, 170420. [CrossRef]
3. Richard, B.; Thomas, S.A.; Reddy, M.A.; Pallavolu, M.R.; Cherusseri, J. Minireview on Fluid Manipulation Techniques for the Synthesis and Energy Applications of Two-Dimensional MXenes: Advances, Challenges, and Perspectives. *Energy Fuels* **2023**, *37*, 6999–7013. [CrossRef]
4. Karagoz, E.; Altaf, C.T.; Yaman, E.; Yildirim, I.D.; Erdem, E.; Celebi, C.; Fidan, M.; Sankir, M.; Sankir, N.D. Flexible Metal/Semiconductor/Metal Type Photodetectors Based on Manganese Doped ZnO Nanorods. *J. Alloys Compd.* **2023**, *959*, 170474. [CrossRef]
5. Moyo, D.S.; van der Merwe, E.M.; Rademeyer, M.; Malan, F.P.; Atanasova, M.T.; Mapossa, A.B.; Focke, W.W. Characterizing the thermal phase behaviour of fipronil polymorphs. *J. Therm. Anal. Calorim.* **2023**, *148*, 6761–6777. [CrossRef]
6. Qin, L.; Huang, T.; Cui, H.; Cheng, M.; Wei, G.; Liao, F.; Xiong, W.; Jiang, H.; Zhang, J.; Fan, H. A fluorescence-electrochemiluminescence dual-mode sensor based on a" switch" system for highly selective and sensitive K-ras gene detection. *Biosens. Bioelectron.* **2023**, *235*, 115385. [CrossRef] [PubMed]
7. Morais, A.T.D.B.; Morais, S.T.; Feitor, J.F.; Santos, W.G.; Gomes da Silva Catunda, L.; Walkling-Ribeiro, M.; Ahrne, L.; Cardoso, D.R. Impact of Physicochemical Modifications in Casein Promoted by UV-C on the Peptide Profile of Gastric Digestion and the Transepithelial Transport of Peptides. *J. Agric. Food Chem.* **2023**, *71*, 7495–7507. [CrossRef] [PubMed]
8. Hanson, N.N.; Wurster, C.M.; EIMF; Todd, C.D. Comparison of secondary ion mass spectrometry and micromilling/continuous flow isotope ratio mass spectrometry techniques used to acquire intra-otolith δ18O values of wild Atlantic salmon (Salmo salar). *Rapid Commun. Mass Spectrom.* **2010**, *24*, 2491–2498. [CrossRef]
9. Lu, X.; Cong, C.; Hou, P.; Xv, K.; Liang, S.Y. Improved Cutting Force Modelling in Micro-Milling Aluminum Alloy LF 21 Considering Tool Wear. *Appl. Sci.* **2022**, *12*, 5357. [CrossRef]
10. Vladisavljević, G.T.; Khalid, N.; Neves, M.A.; Kuroiwa, T.; Nakajima, M.; Uemura, K.; Ichikawa, S.; Kobayashi, I. Industrial lab-on-a-chip: Design, applications and scale-up for drug discovery and delivery. *Adv. Drug Deliv. Rev.* **2013**, *65*, 1626–1663. [CrossRef]
11. Chern, G.-L.; Wu, Y.-J.E.; Cheng, J.-C.; Yao, J.-C. Study on burr formation in micro-machining using micro-tools fabricated by micro-EDM. *Precis. Eng.* **2007**, *31*, 122–129. [CrossRef]
12. Campanelli, S.L.; Casalino, G.; Ludovico, A.D.; Bonserio, C. An artificial neural network approach for the control of the laser milling process. *Int. J. Adv. Manuf. Technol.* **2013**, *66*, 1777–1784. [CrossRef]
13. Parandoush, P.; Hossain, A. A review of modeling and simulation of laser beam machining. *Int. J. Mach. Tools Manuf.* **2014**, *85*, 135–145. [CrossRef]
14. Kravchenko, K.; Feuchtgruber, H.; Riccardi, A. A new versatile infrared facility at the VLT. *Nat. Astron.* **2023**, *7*, 504. [CrossRef]
15. Chen, L.; Cai, L.; Huang, E.; Zhou, Y.; Yue, T.; Cao, X. A notch-mask and dual-prism system for snapshot spectral imaging. *Opt. Lasers Eng.* **2023**, *165*, 107544. [CrossRef]
16. Kaur, A.; Ribton, C.; Balachandaran, W. Electron beam characterisation methods and devices for welding equipment. *J. Mater. Process. Technol.* **2015**, *221*, 225–232. [CrossRef]
17. Qu, N.S.; Xu, K.; Zeng, Y.B.; Yu, Q. Enhancement of the homogeneity of micro slits prepared by wire electrochemical micromachining. *Int. J. Electrochem. Sci.* **2013**, *8*, 12163–12171. [CrossRef]

18. Wang, J.; Liu, Q.; Sun, P.; Ning, Z.; Wang, L. Study on Model and Experimental of Laser Scribing Parameter of Maskant in Chemical Milling for Aerospace Applications. *Appl. Sci.* **2022**, *12*, 2914. [CrossRef]
19. Chow, H.M.; Yan, B.H.; Huang, F.Y.; Hung, J.C. Study of added powder in kerosene for the micro-slit machining of titanium alloy using electro-discharge machining. *J. Mater. Process. Technol.* **2000**, *101*, 95–103. [CrossRef]
20. Yang, C.Z.; Guo, W.; Wang, Y.F.; Hu, L.H.; Wang, J.; Luo, J.M.; Yao, X.H.; Liu, S.; Tao, L.T.; Sun, L.L.; et al. Reduction in gefitinib resistance mediated by Yi-Fei San-Jie pill in non-small cell lung cancer through regulation of tyrosine metabolism, cell cycle, and the MET/EGFR signaling pathway. *J. Ethnopharmacol.* **2023**, *314*, 116566. [CrossRef]
21. Kobayashi, Y.; Yokoi, A.; Hashimura, M.; Oguri, Y.; Konno, R.; Matsumoto, T.; Tochimoto, M.; Nakagawa, M.; Ishibashi, Y.; Ito, T.; et al. Nucleobindin-2 mediates TGF-β1-driven phenotypes in ZEB1-high uterine carcinosarcoma. *Am. J. Pathol.* **2023**, *193*, 1116–1128. [CrossRef] [PubMed]
22. de Souza Niero, A.L.; Possolli, N.M.; da Silva, D.F.; Demétrio, K.B.; Zocche, J.J.; de Souza, G.M.S.; Dias, J.F.; Vieira, J.L.; Barbosa, J.D.V.; Soares, M.B.P.; et al. Composite beads of alginate and biological hydroxyapatite from poultry and mariculture for hard tissue repair. *Ceram. Int.* **2023**, *49*, 25319–25332. [CrossRef]
23. Aramini, A.; Bianchini, G.; Lillini, S.; Tomassetti, M.; Pacchiarotti, N.; Canestrari, D.; Cocchiaro, P.; Novelli, R.; Dragani, M.C.; Palmerio, F.; et al. Ketoprofen, lysine and gabapentin co-crystal magnifies synergistic efficacy and tolerability of the constituent drugs: Pre-clinical evidences towards an innovative therapeutic approach for neuroinflammatory pain. *Biomed. Pharmacother.* **2023**, *163*, 114845. [CrossRef] [PubMed]
24. Raj, A.; Kumar, A. Recent advances in assessment methods and mechanism of microbe-mediated chlorpyrifos remediation. *Environ. Res.* **2022**, *214*, 114011. [CrossRef] [PubMed]
25. Venkitakrishnan, P.; Philip, J.; Krishnamurthy, R. An assessment of stresses in thin walled welded tubes through hole drilling and sectioning methods. *J. Mater. Process. Technol.* **2007**, *185*, 228–232. [CrossRef]
26. Hülsenberg, D.; Harnisch, A.; Bismarck, A. Joining Methods for Glass Based Microdevices. In *Microstructuring of Glasses*; Springer: Berlin/Heidelberg, Germany, 2008; pp. 263–278.
27. Huang, J.T.; Lee, K.Y.; Wu, C.S.; Lin, C.Y.; Shih, S.H. Using Micro-Electroforming and Micro-Assembly Technology to Fabricate Vertical Probe Card. In Proceedings of the 2006 International Conference on Electronic Materials and Packaging, Kowloon, China, 11–14 December 2006; IEEE: Piscataway, NJ, USA, 2006; pp. 1–5.
28. Xia, H.; Zhao, G.; Li, L.; Hu, M.; He, N.; Ochengo, D. Fabrication of high aspect ratio microgroove on Ti6Al4V by laser-induced oxidation assisted micro milling. *J. Manuf. Process.* **2019**, *45*, 419–428. [CrossRef]
29. Chow, H.M.; Yan, B.H.; Huang, F.Y. Micro slit machining using electro-discharge machining with a modified rotary disk electrode (RDE). *J. Mater. Process. Technol.* **1999**, *91*, 161–166. [CrossRef]
30. Kim, B.H.; Ryu, S.H.; Choi, D.K.; Chu, C.N. Micro electrochemical milling. *J. Micromech. Microeng.* **2004**, *15*, 124. [CrossRef]
31. Zhu, B.; Zhu, D.; Zeng, Y.; Wang, S. Pilot study on electrolytic wire cutting processing technology. *China Mech. Eng.* **2010**, *21*, 963–967.
32. Zhang, Y.; Ming, P.; Li, R.; Qin, G.; Zhang, X.; Yan, L.; Li, X.; Zheng, X. Numerical analysis and experimental study on fabrication of high aspect ratio tapered ultrafine holes by over-growth electroforming process. *Micromachines* **2019**, *10*, 824. [CrossRef]
33. Zhang, J.; Ming, P.; Zhang, X.; Qin, G.; Yan, L.; Zhao, X.; Zheng, X. Facile Fabrication of Highly Perforated Hollow Metallic Cylinder with Changeable Micro-Orifices by Electroforming-Extrusion molding Hybrid Process. *Micromachines* **2020**, *11*, 70. [CrossRef] [PubMed]

micromachines

MDPI

Article

Fabricating Precise and Smooth Microgroove Structures on Zr-Based Metallic Glass Using Jet-ECM

Dongdong Li, Pingmei Ming *, Shen Niu, Guangbin Yang and Kuaile Cheng

School of Mechanical and Power Engineering, Henan Polytechnic University, Jiaozuo 454003, China; li863964931@163.com (D.L.); ns2019@hpu.edu.cn (S.N.)
* Correspondence: mpm@hpu.edu.cn

Abstract: Zr-based metallic glasses (MGs) are promising materials for mold manufacturing due to their unique mechanical and chemical properties. However, the high hardness of metallic glasses and their tendency to crystallize at high temperatures make it challenging to fabricate precise and smooth microscale structures on metallic glasses. This limitation hampers the development of metallic glasses as molds. Jet electrochemical machining (jet-ECM) is a non-contact subtractive manufacturing technology that utilizes a high-speed electrolyte to partially remove material from workpieces, making it highly suitable for processing difficult-to-machine materials. Nevertheless, few studies have explored microgroove structures on Zr-based MGs using sodium nitrate electrolytes by jet-ECM. Therefore, this paper advocates the utilization of the jet-ECM technique to fabricate precise and smooth microgroove structures using a sodium nitrate electrolyte. The electrochemical characteristics were studied in sodium nitrate solution. Then, the effects of the applied voltages and nozzle travel rates on machining performance were investigated. Finally, micro-helical and micro-S structures with high geometric dimensional consistency and low surface roughness were successfully fabricated, with widths and depths measuring 433.7 ± 2.4 μm and 101.4 ± 1.6 μm, respectively. Their surface roughness was determined to be 0.118 ± 0.002 μm. Compared to non-aqueous-based methods for jet-ECM of Zr-based MGs, the depth of the microgrooves was increased from 20 μm to 101 μm. Furthermore, the processed microstructures had no uneven edges in the peripheral areas and no visible flow marks on the bottom.

Keywords: Zr-based metallic glasses (MGs); jet-ECM; precise and smooth microgroove structures; sodium nitrate electrolyte

1. Introduction

The dependable large-scale manufacturing of components with micro-/nanoscale features is crucial for the rapid advancement of microelectromechanical systems (MEMS) [1]. Polymers are the most commonly used substrate materials in microelectromechanical systems (MEMS) due to their low cost, chemical corrosion resistance, and the availability of fabrication processes [2]. Polymer surface microstructures are obtained by replicating mold structures. Currently, a variety of materials are employed as molds, including electroformed nickel [3], silicon [4], and stainless steel [5]. However, these materials have the disadvantages of poor precision and short service life. Metallic glasses have outstanding mechanical properties, such as high strength and corrosion resistance, which allow them to be used as mold materials [6–8]. Nevertheless, the fabrication of surface microstructures on metallic glass molds presents a significant challenge.

At present, thermoplastic forming has been demonstrated as a prevalent technique for microstructures based on metallic glasses [9]. However, the method requires precise control of temperature and duration to prevent crystallization and oxidation [10]. Micro-subtractive manufacturing exhibits a clear advantage in terms of processing precision and repeatability for fabricating microstructures in metallic glasses. This primarily includes

techniques such as cutting, electrical discharge machining, laser processing, etc. [11–14]. In the cutting process, the high hardness and toughness of amorphous alloys can lead to significant tool wear, consequently diminishing the operational lifespan of the tool [15]. In addition, electrical discharge machining and laser machining are regarded as thermal processing techniques. During the machining process, certain defects may arise, such as recast layers, heat-affected zones, and microcracking [16–18].

Electrochemical machining (ECM) removes material through anodic dissolution via electrochemical reactions without generating cutting forces or heat-affected zones during the machining process. Koza et al. [19] employed microtool electrodes for the electrochemical machining of Zr-based bulk metallic glass and confirmed that $NaNO_3$ aqueous solution is not suitable for electrochemical machining of Zr-based MG due to the formation of corrosion products. Furthermore, they found that using a methanol–$HClO_4$ solution could reduce the precipitation of corrosion products. However, methanol–$HClO_4$ solutions cannot be widely used due to their toxicity. Similarly, Geber et al. [20] asserted the impracticality of using standard water-based salt electrolytes for the electrochemical machining of Zr-based metallic glass. Cole et al. [21] discovered that the corrosion products and the dense oxides generated in water-based electrolytes hindered the electrochemical machining (ECM) of Zr-based MG. To address this issue, they adopted a method of increasing the bias voltage to reduce the adhesion of corrosion products to the machined surface. Subsequently, Guo et al. [22–24] proposed the utilization of non-aqueous-based methods for pulse electrochemical machining of microstructures on Zr-based bulk metallic glass. However, the machined microstructures exhibited uneven edges in the peripheral regions and pronounced flow marks on the bottom. Additionally, electrochemical machining of Zr-Based MGs using organic solvent electrolytes results in low material removal rates, limiting fabrication to shallow microstructures. In the past decade, Zeng et al. [25–27] proposed the utilization of WECMM technology to manufacture high-precision and -quality microstructures in metallic glasses using water-based electrolytes. However, wire electrochemical micromachining faces difficulties in machining blind holes, grooves, and cavities, as well as three-dimensional complex structures and parts.

Jet electrochemical machining is a technology that uses a hollow metal nozzle as the cathode, enabling the electrolyte to be sprayed directly onto the workpiece surface from within the metal nozzle. This technology utilizes the electrochemical anodic dissolution principle to achieve material removal from specific locations on the workpiece [28]. In comparison to alternative ECM techniques, jet-ECM employs high-speed electrolyte flushing to address the adhesion issues of electrolytic products encountered in electrochemical machining. Jet-ECM has shown significant promise as a shaping method. Hackert-Oschatzchen et al. [29] fabricated complex microstructures on stainless steel surfaces using tubular electrodes with an inner diameter of 0.1 mm to mill microgrooves measuring 200 μm in width and 60 μm in depth. Liu et al. [30] investigated the influence of process parameters on the surface groove structure of a titanium alloy through jet electrochemical machining. Ultimately, they utilized optimal process parameters to fabricate an S-shaped groove structure.

To the best of our knowledge, there have been no reports on the study of precise and smooth microgroove structures on Zr-based metallic glass produced using sodium nitrate electrolytes by jet electrochemical machining thus far. Therefore, this paper assesses the feasibility of jet electrochemical machining for fabricating precise, smooth microgroove structures on Zr-based MG. Firstly, the electrochemical characteristics of the Zr-based MG in $NaNO_3$ solution are discussed. Then, the effects of the applied voltage and the nozzle travel rate on the machining quality of microgrooves on the Zr-based MG were investigated. Finally, micro-helical and micro-S structures with high geometric consistency and low surface roughness were successfully fabricated, featuring widths and depths of 433.7 ± 2.4 μm and 101.4 ± 1.6 μm, respectively. Their surface roughness measures were 0.118 ± 0.002 μm.

2. Materials and Methods

2.1. Sample Preparation

The Zr-based metallic glass (MG) was obtained through copper mold suction casting. The Zr-based metallic glass ($Zr_{41.2}Ti_{13.8}Cu_{12.5}Ni_{10.0}Be_{22.5}$) is named Vit1. The major metal component is Zr, with a mass fraction of 41.2%, and the secondary metal elements are Be and Ti, with mass fractions of 22.5% and 13.8%, respectively. Additionally, 10.0% nickel and 12.5% copper were added to the Zr-based MG. The material properties of the Zr-based MG are presented in Table 1. The workpiece materials (20 mm (W) × 20 mm (L) × 2 mm (T)) were used in jet-ECM. The surfaces were polished with waterproof abrasive paper and ultrasonically cleaned with deionized water and ethanol before the experiments.

Table 1. Properties of the Zr-based MG.

Parameters	Value
Specific conductance (Ms/m)	0.52–0.53
Young's modulus (GPa)	94.9
Poisson ratio	0.30
Hardness (HV)	568–619

2.2. Electrochemical Measurement Setup

The electrochemical characteristics were measured in a three-electrode system using an electrochemical workstation (CHI604E, CH Instruments, Shanghai, China), as shown in Figure 1. A platinum plate was used as a counter electrode (CE). The reference electrode (RE) employed was Hg/Hg_2Cl_2, which was in contact with the electrolyte via a salt bridge to reduce the liquid junction potential. The Vit1 (10 mm (W) × 10 mm (L) × 2 mm (T)) was insulated with epoxy resin as the working electrode (WE), and only 1 cm^2 of surface area was exposed to the electrolyte. The open circuit potential (OCP) was monitored in $NaNO_3$ solution until a stable surface state was reached before the electrochemical measurements.

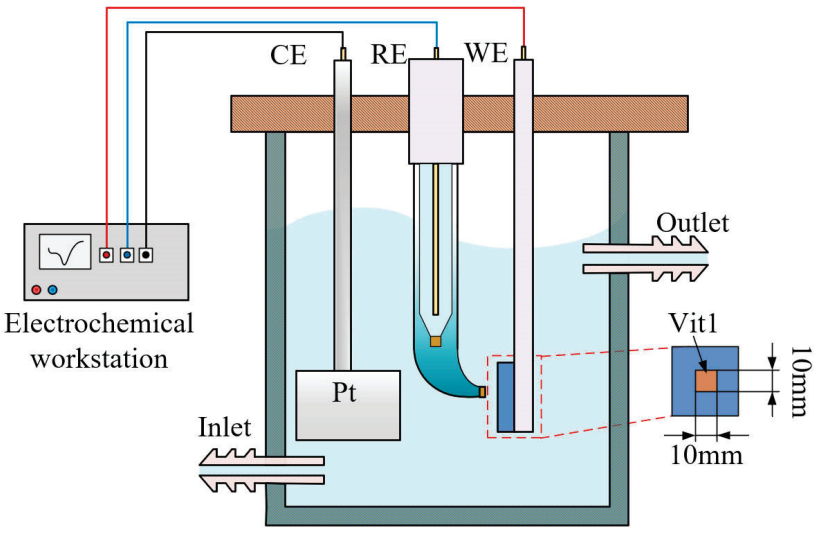

Figure 1. Electrochemical measurement setup.

Polarization tests were conducted with a scan rate of 10 mV s^{-1}. The potential range was −1 V to 3 V vs. Hg/Hg_2Cl_2. To obtain details of the interface structure of the passive film on the Vit1 in $NaNO_3$ solution under different corrosion states, electrochemical impedance spectroscopy (EIS) was employed over a frequency range of 100 kHz to 0.1 Hz with a disturbance amplitude set to 5 mV. The EIS fitting data for the Zr-based MG were determined using ZView2 software.

2.3. Experimental System for Jet-ECM

The experimental setup was conducted in $NaNO_3$ solutions using a homemade experimental system, as depicted in Figure 2. The system included a 3D XYZ stage, a power supply, an electrolyte circulation unit, and a motion control unit. The anode workpiece was the Vit1, and a hollow SUS304 nozzle was chosen as the cathode. The hollow nozzle and anode workpiece were installed on the Z-stage and XY-stage, respectively. The electrolyte was ejected from the nozzle at a relatively constant high speed by a pump. The positioning and movement operations between the anode and the cathodic substrate were precisely controlled by a computer numerical control system. A groove was machined on the surface of the Vit1 through electrochemical milling. All experiments were carried out under the conditions listed in Table 2.

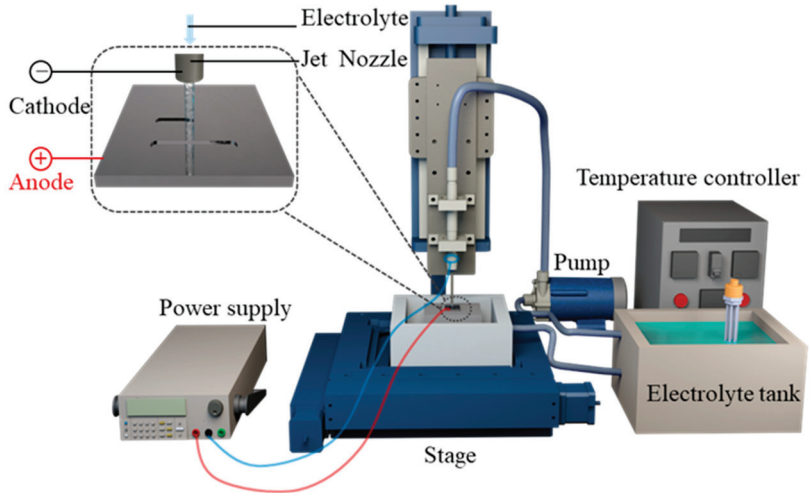

Figure 2. The experimental setup for processing the Vit1 by jet-ECM.

Table 2. Processing conditions for jet-ECM.

Parameters	Value
Material	$Zr_{41.2}Ti_{13.8}Cu_{12.5}Ni_{10.0}Be_{22.5}$
Tool electrode	SUS 304 nozzle
Inner diameter of nozzle	220 ± 2 μm
Outer diameter of nozzle	450 ± 3 μm
Electrolyte composition	10 wt% $NaNO_3$
Machining gap (μm)	200
Electrolyte pressure (MPa)	1
Machining voltage (V)	10, 15, 20, 25,
Nozzle travel rate (μm/s)	100, 200, 300, 400
Temperature of electrolyte (°C)	25 ± 5

2.4. Test Equipment

A field emission scanning electron microscope (Merlin Compact, Carl Zeiss NTS GmbH, Jena, Germany) was used to analyze the topography of the sample. The surface morphology and the surface roughness were measured by a confocal laser scanning microscope (OLS5100, Olympus, Tokyo, Japan). A photograph of the microstructure as obtained using a camera (Z5, Nikon, Tokyo, Japan).

The performance evaluation criteria for machining in the experiment included width, depth, aspect ratio, surface roughness, and stray corrosion, as shown in Figure 3. The aspect ratio is defined as the ratio of depth to width. Figure 3a exhibits an SEM picture of the groove profile machined by jet-ECM with an applied voltage of 20 V and a nozzle travel rate of 100 μm/s. Stray corrosion is defined in Figure 3a.

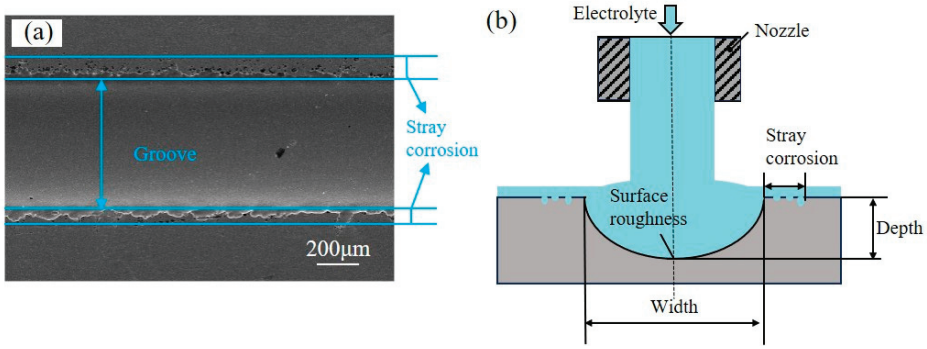

Figure 3. Profile of the machined groove: (**a**) SEM picture of the detailed stray corrosion; (**b**) schematic of performance evaluation indices.

3. Results and Discussion

3.1. Electrochemical Characteristic Analysis of the Vit1

3.1.1. Anodic Polarization Curves

The anodic electrochemical characteristics of the Vit1 in a 10 wt% $NaNO_3$ solution at a temperature of 25 °C were investigated after the surface stabilized. A linear sweep voltammetry (LSV) curve is shown in Figure 4a. When the voltage is below 2.15 V, the passive film remains intact, and the current density does not change with increasing potential, forming a passive region. When the voltage exceeds the breakdown potential (2.15 V), the curve exhibits an ohmic (R_{oh}) behavior [31]. The current increases with voltage, which indicates that the electrochemical dissolution enters the transpassive region. At this stage, the passive film ruptures, leading to pitting corrosion. As illustrated in Figure 4c, pits are distributed on the sample surface, resulting in a uniform and rough surface morphology.

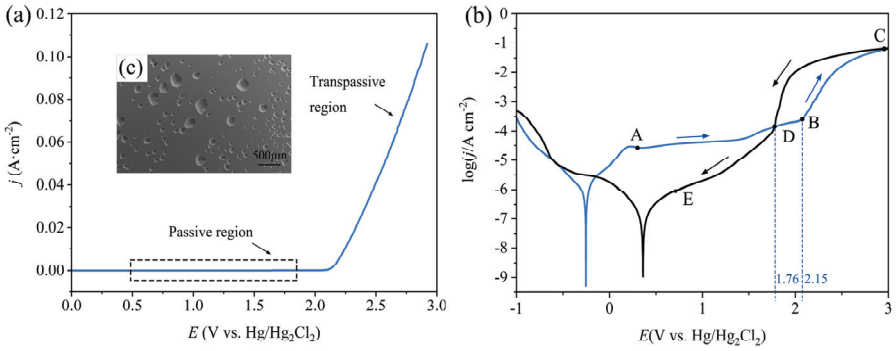

Figure 4. Polarization curve of the Vit1 in $NaNO_3$ solution: (**a**) linear sweep voltammetry curve; (**b**) cyclic voltammetry curve; (**c**) SEM image of the transpassive region.

E_{corr} and E_{trans} are the corrosion potential and the transpassivation potential, respectively. As shown in Figure 4b, the corrosion potential is E_{corr} (−0.27 V), corresponding to the minimum value of the polarization curve, which is conducive to the formation of passive film in the air. When the potential exceeds −0.27 V, the corrosion current density of the Vit1 increases rapidly, reaching 31.7 μA cm^{-2} at 0.13 V. When the polarization potential is between 0.13 and 1.48 V, the current density remains nearly constant, and a passive film forms on the sample surface, hindering the anodic reaction. As the potential is increased from 1.48 V to 2.15 V, the current density increases from 50.6 to 363.5 μA cm^{-2}. When the potential exceeds E_{trans} (2.15 V), pitting corrosion starts to appear on the surface of the anodic specimen. Weak points in the passivation film can be penetrated. Therefore, the resistance of the passivation film decreases, leading to an increase in current.

A reverse scan was conducted to investigate the re-passivation performance of the Vit1 in $NaNO_3$ solution. Upon reaching a potential of 3 V during the reverse scan (regions C and D), the current density rapidly decreases as the voltage descends. In the pitting area,

the passive film is re-established. In the phase D–E, the deceleration in the rate of current decrease is attributed to the increase in resistance. Point D in the cyclic voltammetry curve is the intersection of the forward voltage scan and the reverse voltage scan. The presence of point D indicates that the pitting generated during the forward voltage scan is filled during the reverse scan [32].

3.1.2. Electrochemical Impedance Spectroscopy (EIS)

In the $NaNO_3$ electrolyte, electrochemical impedance spectroscopy (EIS) tests were performed on three typical DC potentials in the polarization curve: 0.1 V (Tafel region), 1 V (passive region), and 2.1 V (near pitting onset) vs. Hg/Hg_2Cl_2.

Table 3 displays the EIS data and fitting results for the Vit1. The equivalent circuit is proposed, mainly consisting of the solution resistance (R_1), charge transfer resistance (R_2), constant phase element (CPE), and inductance element (L_1). R_1 is related to the dissolution resistance of the workpiece material. Z_{CPE} represents the capacitance of the passivation film, which is defined as follows [33]:

$$Z_{CPE} = [Q(jw)^n]^{-1} \quad (1)$$

where Q is the constant of the CPE, j is the imaginary number ($j^2 = -1$), w is the angular frequency, and n is the deviation parameter, which is used to gauge surface heterogeneity. The closer n is to 1, the more uniform the surface [34,35]. The EIS data (scatter plot) and the fitting data (straight line) are shown in Figure 5. The fitted values for all the variables are listed in Table 3. At a potential of 0.1 V, the initial surface forms a monolayer of passive film, typically exhibiting a relatively dense structure. R_2 exhibits the highest value, and the value of n_1 is equal to 0.91, indicating the presence of pores within the typically dense internal structure of the passive film. A Nyquist plot of the polarization process at 1 V is illustrated in Figure 5b. The appearance of a semicircle is attributed to the oxidation of the base metal during the electrochemical dissolution process. As depicted in Figure 5c, increasing the polarization potential to 2.1 V leads to an evident reduction in the impedance modulus and the appearance of an inductive loop. The charge transfer resistance (R_2) decreases to 44.18 $\Omega \cdot cm^2$, indicating that the material begins to dissolve in the solution.

Table 3. Fitting results of the Vit1.

Potential (V)	R_1 (Ω cm^{-2})	$Q_1 \times 10^{-6}$ ($s^n \Omega^{-1}$ cm^{-2})	n_1	R_2 (Ω cm^{-2})	R_3 (Ω cm^{-2})	L_1 (H cm^{-2})
0.1	16.36	17.96	0.91	182,770	-	-
1	8.49	8.13	0.93	78,989	-	-
2.1	6.55	10.21	0.93	44.18	15.06	0.064

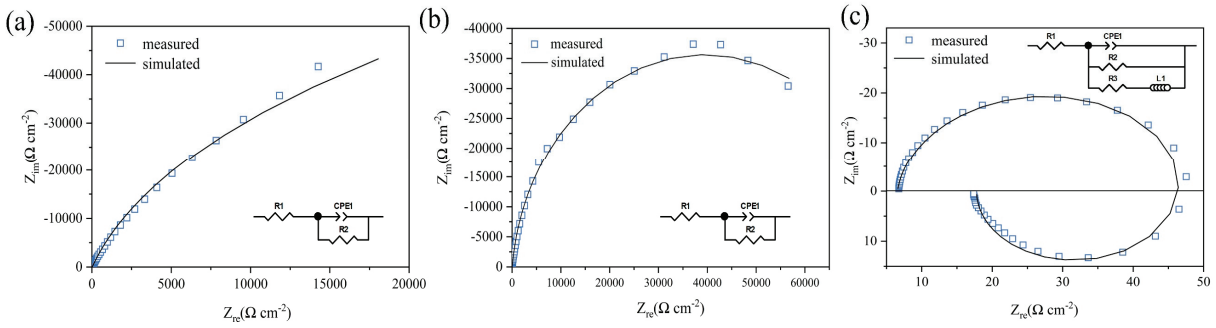

Figure 5. EIS results during polarization at different potentials: (**a**) 0.1 V; (**b**) 1 V; (**c**) 2.1 V.

3.1.3. Discussion of the Material Removal Region in Jet-ECM

Jet-ECM processing uses a nozzle as the cathode, and an electrolyte is sprayed out from the cathode of the nozzle. The electrolyte is dispersed radially around the center

of the nozzle, forming a thin layer of electrolyte of a certain thickness around the nozzle. The distribution of the electric field determines the magnitude of the current density. Low electric field intensities and current densities are distributed in regions far from the electrode center. In the high-current-density region, the passive film ruptures or reaches a dynamic equilibrium stage of transpassivation, leading to the workpiece material being rapidly removed. The passive film is regenerated in the low-current-density region [36]. The passive film prevents the material from contacting the electrolyte and thus plays a protective role.

3.2. Parametric Effects of Microgroove Fabrication by Jet-ECM

3.2.1. Effects of Applied Voltage

Applied voltage plays a crucial role in determining the precision, surface quality, and morphology characteristics in electrolytic processing. In order to investigate the effect of applied voltage on microstructural morphological changes and geometric contours, jet-ECM was carried out with the following processing parameters: a $NaNO_3$ electrolyte concentration of 10 wt%, an initial gap of 200 μm, a nozzle travel rate of 100 μm/s, and an applied voltage of 10 to 25 V.

Figure 6 shows the microgroove morphology and cross-sectional profiles at different applied voltages. When the voltage was 10 V and 15 V, the microgroove structure contour was not clear, the width of the microgroove was only 392.4 μm and 437.5 μm, and the depth was only 47.5 μm and 78.1 μm. When the applied voltage was increased to 20 V, the material dissolution increased and the width and depth of the microgroove were 465.8 μm and 109.6 μm, respectively. When the voltage was 25 V, the width and depth of the microgroove were 475.9 μm and 119.8 μm, with less stray corrosion at the edges and a smoother bottom. The main reasons for this phenomenon are as follows: When the applied voltage is low, the passive film on the surface of the sample cannot be dissolved constantly, the amount of material removed is less, and the microgroove contour is shallower.

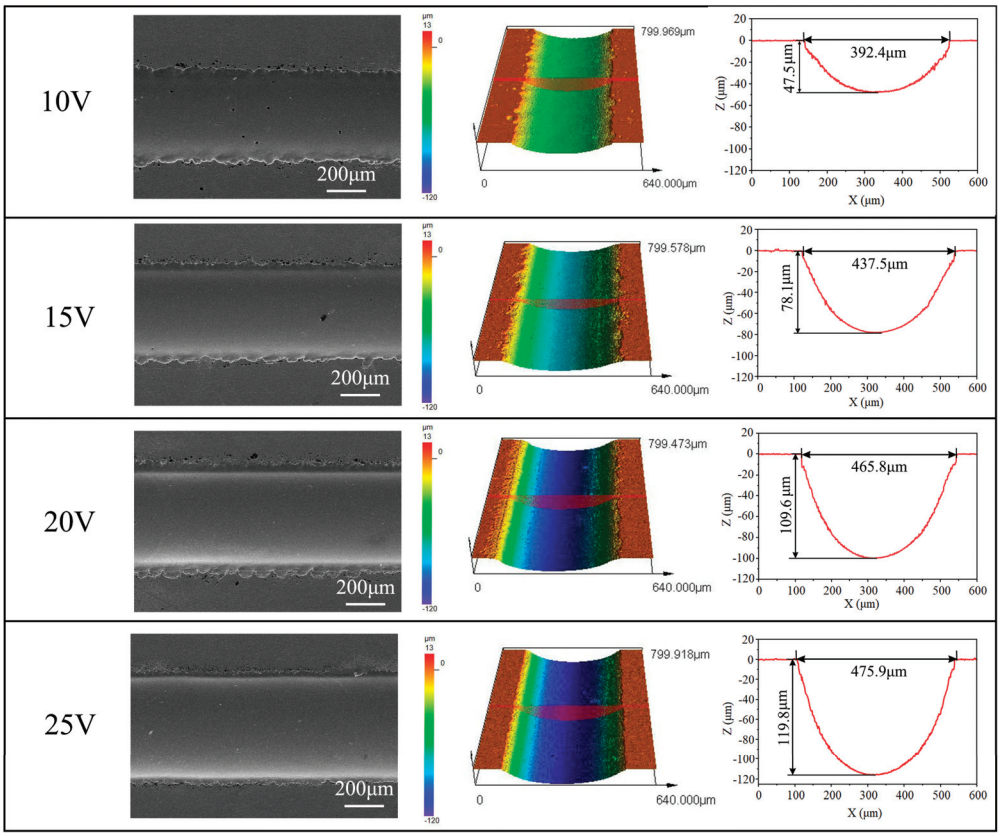

Figure 6. Morphology and profiles of microgrooves at different applied voltages.

As shown in Figure 7, when the applied voltages were 10, 15, 20, and 25 V, the Ras were 0.211, 0.146, 0.135, and 0.129 μm, respectively. The surface roughness of Vit1 produced in the $NaNO_3$ electrolyte is mainly dependent on the voltage applied to the machined surface, with smoother surfaces obtained at higher applied voltages. The surface roughness and stray corrosion show a decreasing trend. However, the aspect ratio gradually increases. With an increase in applied voltage from 10 V to 25 V, the aspect ratio increased from 0.121 to 0.252, the stray corrosion was reduced from 38.21 μm to 29.54 μm, and the surface roughness was changed from 0.211 μm to 0.129 μm. According to the results of studies, higher applied voltages can decrease stray corrosion and surface roughness. Consequently, 25 V was used as the applied voltage for jet-ECM of microgrooves.

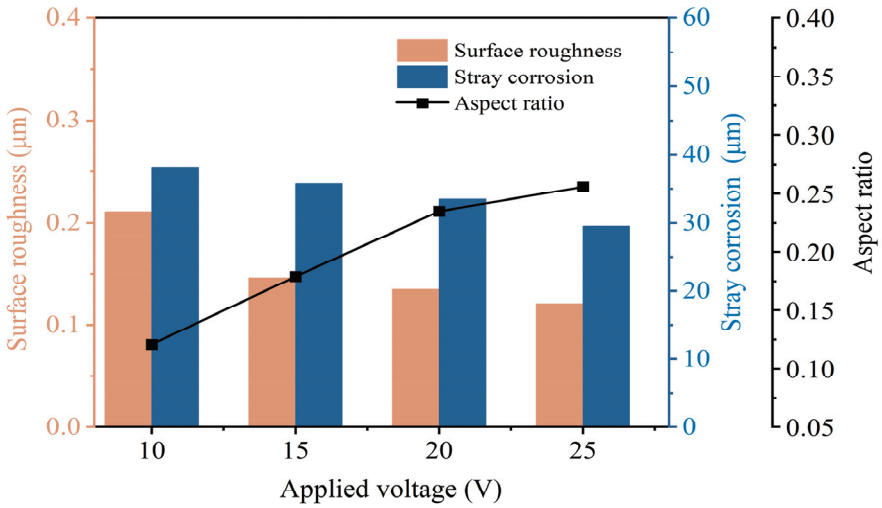

Figure 7. Influence of applied voltage on machining performance.

3.2.2. Effects of Nozzle Travel Rate

Unlike stationary microdimples, microgrooves remove material through relative motion between the tool electrode and the workpiece. The tool electrode moves at a relatively fast rate, leading to significant changes in the electric field. However, the relative motion between the tool electrode and the workpiece is too slow and there may be excessive accumulations of products which cannot be discharged in time. Therefore, the nozzle travel rate has a significant impact on the surface quality of the machining. Jet-ECM was performed with the following machining parameters: a $NaNO_3$ electrolyte concentration of 10 wt%, an initial gap of 200 μm, an applied voltage of 25 V, and a nozzle travel rate of 100 to 400 μm/s.

Figure 8 exhibits the machining parameters of the grooves obtained using different nozzle travel rates (100, 200, 300, and 400 μm/s). At a nozzle travel rate of 100 μm/s, the bottoms of the microgrooves exhibited relatively smooth surfaces, characterized by distinct boundaries and minimal stray corrosion. At this point, the width and depth of the microgrooves were 432.9 μm and 112.4 μm, respectively. With the increase in the nozzle travel rate, the depth of the microgrooves had a tendency to decrease gradually, and the edge contours became less clear. When the nozzle moving speed reached 400 μm/s, the fast movement caused a drastic change in the current density distribution, resulting in minimal anode material removal. Consequently, the width and depth of the microgrooves were only 454.6 μm and 44.6 μm, respectively.

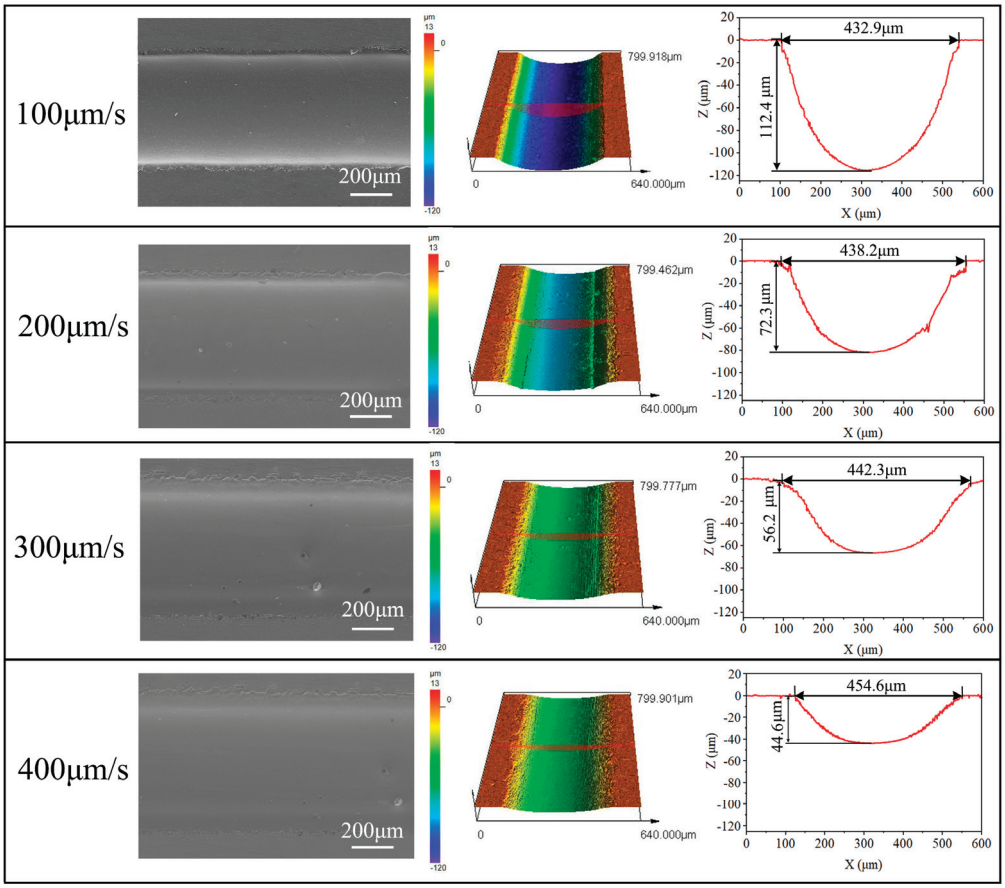

Figure 8. Morphology and profiles of microgrooves at different nozzle travel rates.

The main machining quality indicators (aspect ratio, stray corrosion, and surface roughness) measured at different nozzle travel rates are shown in Figure 9. The aspect ratio decreases from 0.259 to 0.098 as the nozzle travel rate increases. Additionally, the stray corrosion range increases from 29.54 μm to 48.70 μm. Surface roughness tends to decrease from 0.128 μm to 0.120 μm. Due to the high-speed scouring of the electrolyte, the product can easily be eliminated, resulting in a smoother surface. Considering both machining efficiency and precision, better machining results are achieved at a nozzle travel rate of 100 μm/s.

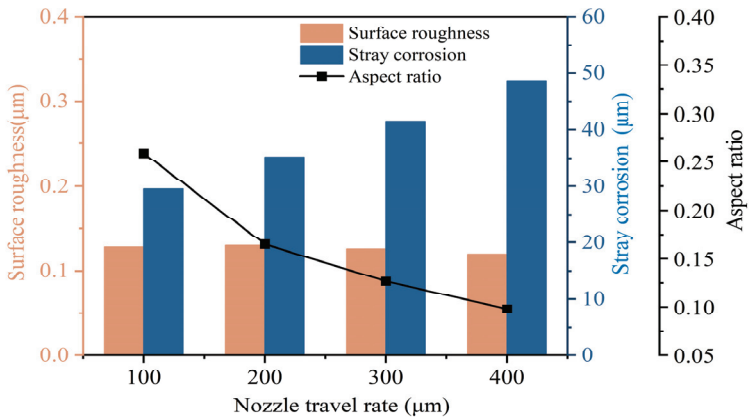

Figure 9. Influence of nozzle travel rate on machining performance.

3.2.3. The Dissolution Mechanism of the Zr-based MG in $NaNO_3$

Figure 10 illustrates a possible dissolution mechanism of the Vit1 in a 10 wt% $NaNO_3$ solution. Based on the preceding discussion of polarization properties, the Vit1 exhibited behaviors of passivation, transpassivation, and re-passivation in $NaNO_3$ solution.

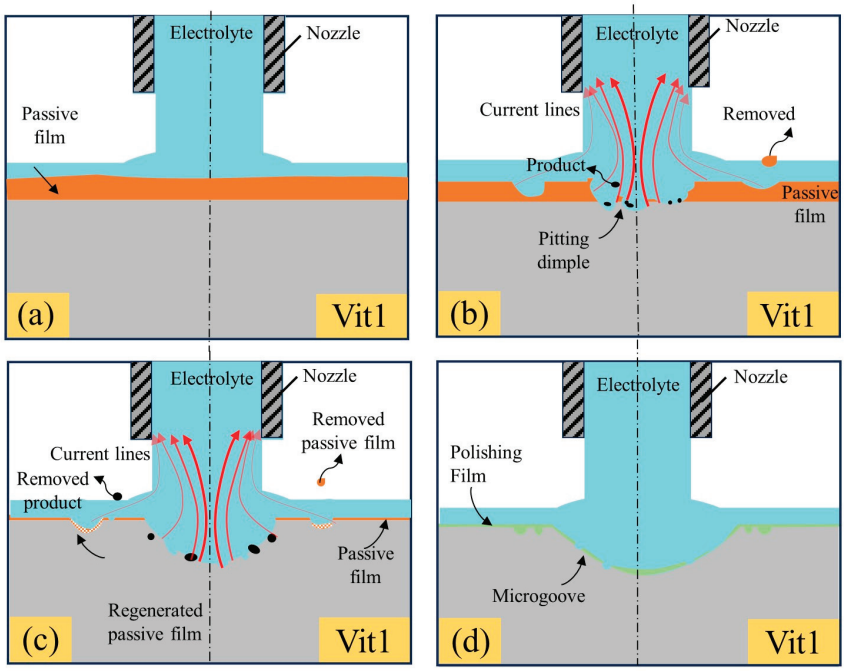

Figure 10. (**a**–**d**) Schematic of the dissolution mechanism of the Vit1 in 10 wt% $NaNO_3$ solution.

As shown in Figure 10a, the passive film is generated on the surface of Vit1 and the thickness is uneven at the initial stage. As shown in Figure 10b, the scouring action of the fast-flowing electrolyte causes rupture of the film layer, leading to local dissolution and thinning of the passive film by jet electrochemical machining [37]. In the high-current-density region, pitting occurs on the surface of the anode material and dissolution of the material occurs. In the low-current-density region, partial rupture of the passive film occurs [36].

With an increase in both the number and dimensions of pits, the localized corrosion region expands as it intersects with neighboring minor pits, ultimately leading to the removal of the passive film covering the entire anodic surface and the stable dissolution of the anode material, as shown in Figure 10c. Due to the oxidation by NO_3^- ions in the passive electrolyte $NaNO_3$. In the low-current-density region, the passivation film is regenerated, which is similar to that observed during reverse scanning for cyclic voltammetry [30]. As shown in Figure 10d, the anodic surface is covered with a layer of supersaturated nitrate film, which works as a polishing film and levels the anodic surface [38].

3.3. Fabrication of Precise and Smooth Microgroove Structures

Jet-ECM can selectively remove material with the multidimensional movement of the cathode nozzle [39]. This characteristic of jet-ECM renders it a highly flexible machining technique suitable for fabricating complex microstructures. A series of experiments were conducted using the following machining parameters: an applied voltage of 25 V, an initial gap of 200μm, a nozzle travel rate of 100 μm/s, and a $NaNO_3$ electrolyte concentration of 10 wt%.

The complex microstructures fabricated on the Vit1 are depicted in Figure 11. As depicted in Figure 11a, both SEM and photographic images of the microhelical spiral are presented. The manufactured helical spiral structure exhibits clear edge contours and a smooth bottom. Figure 11b shows magnified SEM images of two regions with surface

roughness values of 0.118 μm and 0.120 μm, respectively. Figure 11c displays the cross-sectional profiles of the groove bottoms in the two distinct regions. From measurements of the profiles in the cross-sections AB and CD, the results indicate microgroove widths of 431.2 μm and 432.8 μm and depths of 102.3 μm and 102.4 μm.

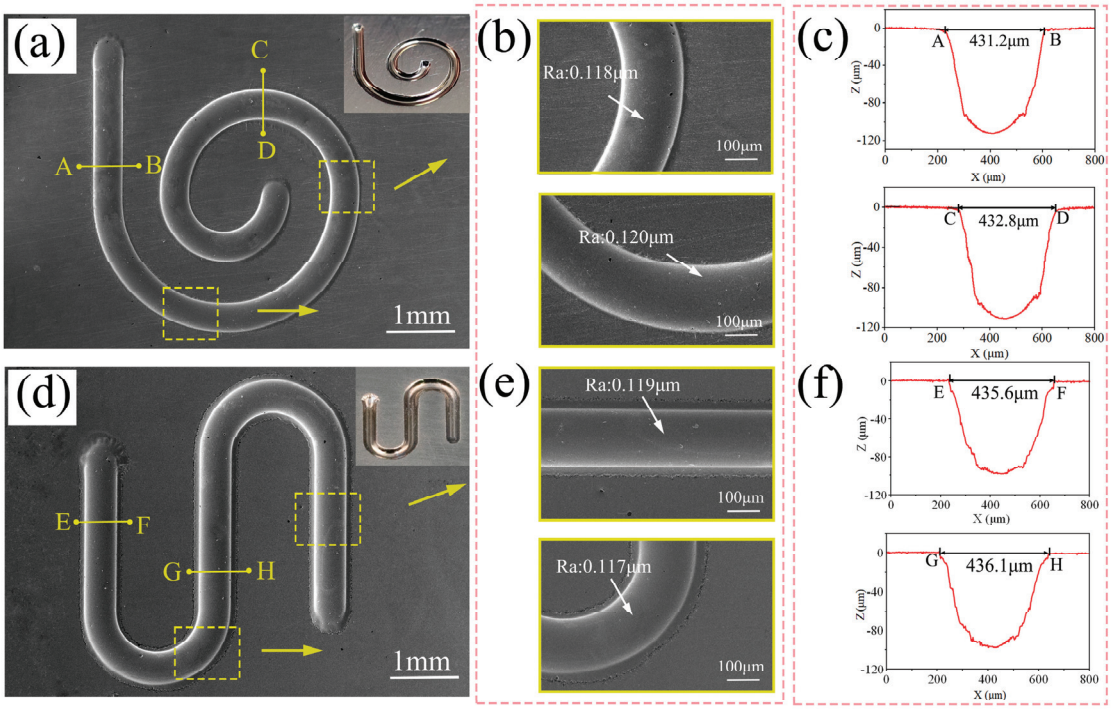

Figure 11. (**a**–**f**) Complex microstructures fabricated on the Vit1 by jet-ECM.

In Figure 11d, both SEM and photographic images of the micro-S structure are presented. Figure 11e displays magnified SEM images of two regions exhibiting surface roughness values of 0.119 μm and 0.117 μm. Figure 11f shows the cross-sectional profiles of the groove bottoms in the two distinct regions. Measurements of the profiles in the cross-sections EF and GH indicate microgroove widths of 435.6 μm and 436.1 μm, with depths of 101.1 μm and 99.8 μm. Additionally, the widths, depths, and surface roughness values of the microstructures were calculated to be 433.7 ± 2.4 μm, 101.4 ± 1.6 μm, and 0.118 ± 0.002 μm, which indicates the consistency of the contour dimensions of the fabricated microstructures. Therefore, jet electrochemical machining can manufacture precise and smooth microgroove structures on the Zr-based MG by using sodium nitrate solution.

4. Discussion

In this study, the electrochemical properties of Zr-based MG in $NaNO_3$ solution and the feasibility of manufacturing precise and smooth microgrooves using jet-ECM were investigated. The main conclusions are summarized as follows:

1. Electrochemical characteristics indicate that Zr-based MG exhibited passive, transpassive, and re-passive performances. An applied voltage higher than the transpassivation potential is required for jet electrochemical machining of Zr-based MG.
2. Jet-ECM can attain precise and smooth microgroove structures on the Zr-based metallic glass using a sodium nitrate electrolyte, with processing parameters including an applied voltage of 25 V, a nozzle travel rate of 100 μm/s, and a $NaNO_3$ electrolyte concentration of 10 wt%.
3. High geometric dimensional consistency and low surface roughness microhelical and micro-S structures can be fabricated, and their widths and depths are 433.7 ± 2.4 μm and 101.4 ± 1.6 μm, respectively. Their surface roughness is 0.118 ± 0.002 μm, which

represents a significant improvement over the structures obtained by non-aqueous-based ECM processes reported earlier.

Author Contributions: Data curation, D.L., P.M., S.N., G.Y. and K.C.; funding acquisition, P.M. and S.N.; investigation, D.L. and P.M.; methodology, D.L. and P.M.; project administration, P.M.; supervision, P.M.; validation, D.L., P.M., S.N., G.Y. and K.C.; writing—original draft, D.L. and P.M.; writing—review and editing, D.L. and P.M. All authors have read and agreed to the published version of the manuscript.

Funding: This research was funded by the Scientific and Technological Innovation Leaders in Central Plains of Henan Province, grant number 214200510018; the China Postdoctoral Science Foundation, grant number 2020M682289; the Key Research and Development and Promotion Program of Henan Province, grant number 222102220001; and the Fundamental Research Funds for the Universities of Henan Province, grant number NSFRF210338.

Data Availability Statement: Data are contained within the article.

Conflicts of Interest: The authors declare no conflicts of interest.

References

1. Zhang, N.; Chu, J.S.; Byrne, C.J.; Browne, D.J.; Gilchrist, M.D. Replication of Micro/Nano-Scale Features by Micro Injection Molding with a Bulk Metallic Glass Mold Insert. *J. Micromech. Microeng.* **2012**, *22*, 065019. [CrossRef]
2. Becker, H.; Gärtner, C. Polymer Microfabrication Technologies for Microfluidic Systems. *Anal. Bioanal. Chem.* **2008**, *390*, 89–111. [CrossRef] [PubMed]
3. Kukharenka, E.; Farooqui, M.M.; Grigore, L.; Kraft, M.; Hollinshead, N. Electroplating Moulds Using Dry Film Thick Negative Photoresist. *J. Micromech. Microeng.* **2003**, *13*, S67. [CrossRef]
4. Bourne, G.R.; Bardt, J.; Sawyer, W.G.; Ziegert, J.; Zeenberg, D.; Schmitz, T. Closed Channel Fabrication Using Micromolding of Metallic Glass. *J. Mater. Process. Technol.* **2009**, *209*, 4765–4768. [CrossRef]
5. Hupert, M.L.; Guy, W.J.; Llopis, S.D.; Shadpour, H.; Rani, S.; Nikitopoulos, D.E.; Soper, S.A. Evaluation of Micromilled Metal Mold Masters for the Replication of Microchip Electrophoresis Devices. *Microfluid. Nanofluid* **2006**, *3*, 1–11. [CrossRef]
6. Saotome, Y.; Imai, K.; Shioda, S.; Shimizu, S.; Zhang, T.; Inoue, A. The Micro-Nanoformability of Pt-Based Metallic Glass and the Nanoforming of Three-Dimensional Structures. *Intermetallics* **2002**, *10*, 1241–1247. [CrossRef]
7. Gong, Y.D.; Liu, Y.; Sun, Y.; Wen, X.L.; Li, Q.; Qu, S.S.; Cai, M. Experimental and Emulational Investigations into Grinding Characteristics of Zr-Based Bulk Metallic Glass (BMG) Using Microgrinding. *Int. J. Adv. Manuf. Technol.* **2018**, *97*, 3431–3451.
8. Inoue, A. Stabilization of Metallic Supercooled Liquid and Bulk Amorphous Alloys. *Acta Materialia* **2000**, *48*, 279–306. [CrossRef]
9. Wei, Z.; Miao, H.T.; Li, Y.H.; Chang, C.T.; Xie, G.Q.; Jia, X.J. Glass-Forming Ability and Thermoplastic Formability of Ferromagnetic (Fe, Co, Ni)75P10C10B5 Metallic Glasses. *J. Alloys Compd.* **2017**, *707*, 57–62.
10. Bakkal, M.; Shih, A.J.; McSpadden, S.B.; Scattergood, R.O. Thrust Force, Torque, and Tool Wear in Drilling the Bulk Metallic Glass. *Int. J. Mach. Tools Manuf.* **2005**, *45*, 863–872. [CrossRef]
11. Bakkal, M.; Shih, A.J.; McSpadden, S.B.; Liu, C.T.; Scattergood, R.O. Light Emission, Chip Morphology, and Burr Formation in Drilling the Bulk Metallic Glass. *Int. J. Mach. Tools Manuf.* **2005**, *45*, 741–752. [CrossRef]
12. Williams, E.; Lavery, N. Laser Processing of Bulk Metallic Glass: A Review. *J. Mater. Process. Technol.* **2017**, *247*, 73–91. [CrossRef]
13. Pradana, Y.; Ferara, A.; Aminnudin, A.; Wahono, W.; Jang, S.C. The Effect of Discharge Current and Pulse-On Time on Biocompatible Zr-Based BMG Sinking-EDM. *Open Engineering* **2020**, *10*, 401–407. [CrossRef]
14. Ding, F.; Wang, C.Y.; Zhang, T.; Zheng, L.J.; Zhu, X.G. High Performance Cutting of Zr-Based Bulk Metallic Glass: A Review of Chip Formation. *Procedia CIRP* **2018**, *77*, 421–424. [CrossRef]
15. Schuster, R.; Kirchner, V.; Allongue, P.; Ertl, G. Electrochemical Micromachining. *Science* **2000**, *289*, 98–101. [CrossRef] [PubMed]
16. Hsieh, S.F.; Chen, S.L.; Lin, M.H.; Ou, S.F.; Lin, W.T.; Huang, M.-S. Crystallization and Carbonization of an Electrical Discharge Machined Zr-Based Bulk Metallic Glass Alloy. *J. Mater. Res.* **2013**, *28*, 3177–3184. [CrossRef]
17. Huang, H.; Yan, J.W. Microstructural Changes of Zr-Based Metallic Glass during Micro-Electrical Discharge Machining and Grinding by a Sintered Diamond Tool. *J. Alloys Compd.* **2016**, *688*, 14–21. [CrossRef]
18. Huang, H.; Yan, J.W. On the Surface Characteristics of a Zr-Based Bulk Metallic Glass Processed by Microelectrical Discharge Machining. *Appl. Surf. Sci.* **2015**, *355*, 1306–1315. [CrossRef]
19. Koza, J.A.; Sueptitz, R.; Uhlemann, M.; Schultz, L.; Gebert, A. Electrochemical Micromachining of a Zr-Based Bulk Metallic Glass Using a Micro-Tool Electrode Technique. *Intermetallics* **2011**, *19*, 437–444. [CrossRef]
20. Gebert, A.; Gostin, P.F.; Sueptitz, R.; Oswald, S.; Abdi, S.; Uhlemann, M.; Eckert, J. Polarization Studies of Zr-Based Bulk Metallic Glasses for Electrochemical Machining. *J. Electrochem. Soc.* **2014**, *161*, E66. [CrossRef]
21. Cole, K.M.; Kirk, D.W.; Singh, C.V.; Thorpe, S.J. Optimizing Electrochemical Micromachining Parameters for Zr-Based Bulk Metallic Glass. *J. Manuf. Process.* **2017**, *25*, 227–234. [CrossRef]

22. Guo, C.; Wu, B.; Xu, B.; Wu, S.; Shen, J.; Wu, X. Investigation of Pulse Electrochemical Machining of Zr-Based Bulk Metallic Glasses in NaNO3 -Ethylene Glycol Electrolyte. *J. Electrochem. Soc.* **2021**, *168*, 071502. [CrossRef]
23. Guo, C.; He, J.; Zhuang, W.; Li, K.; Li, D. Fabrication of Dimples by Jet-ECM of Zr-Based Bulk Metallic Glasses with NaCl-Ethylene Glycol Electrolyte. *Micromachines* **2023**, *14*, 2196. [CrossRef] [PubMed]
24. Guo, C.; Zhou, A.; He, J.; Xiao, H.; Li, D. An Investigation in Sub-Millimeter Channel Fabrication by the Non-Aqueous Electrolyte Jet Machining of Zr-Based Bulk Metallic Glasses. *Micromachines* **2023**, *14*, 2232. [CrossRef] [PubMed]
25. Hang, Y.S.; Zeng, Y.B.; Yang, T.; Meng, L.C. The Dissolution Characteristics and Wire Electrochemical Micromachining of Metallic Glass Ni82Cr7Si5Fe3B3. *J. Manuf. Process.* **2020**, *58*, 884–893. [CrossRef]
26. Zhu, D.; Zeng, Y.B.; Xu, Z.Y.; Zhang, X.Y. Precision Machining of Small Holes by the Hybrid Process of Electrochemical Removal and Grinding. *CIRP Annals* **2011**, *60*, 247–250. [CrossRef]
27. Meng, L.C.; Zeng, Y.B.; Zhu, D. Investigation on Wire Electrochemical Micro Machining of Ni-Based Metallic Glass. *Electrochim. Acta* **2017**, *233*, 274–283. [CrossRef]
28. Yang, T.; Li, Y.L.; Xu, Z.Y.; Zeng, Y.B. Electrochemical Cutting with Inner-Jet Electrolyte Flushing for Titanium Alloy (Ti-6Al-4V). *Int. J. Adv. Manuf. Technol.* **2021**, *112*, 2583–2592. [CrossRef]
29. Hackert-Oschätzchen, M.; Meichsner, G.; Zinecker, M.; Martin, A.; Schubert, A. Micro Machining with Continuous Electrolytic Free Jet. *Precis. Eng.* **2012**, *36*, 612–619. [CrossRef]
30. Liu, W.D.; Ao, S.S.; Li, Y.; Liu, Z.M.; Zhang, H.; Manladan, S.M.; Luo, Z.; Wang, Z.P. Effect of Anodic Behavior on Electrochemical Machining of TB6 Titanium Alloy. *Electrochim. Acta* **2017**, *233*, 190–200. [CrossRef]
31. Wang, D.Y.; Zhu, Z.W.; Wang, N.F.; Zhu, D.; Wang, H.R. Investigation of the Electrochemical Dissolution Behavior of Inconel 718 and 304 Stainless Steel at Low Current Density in $NaNO_3$ Solution. *Electrochim. Acta* **2015**, *156*, 301–307. [CrossRef]
32. Liu, Y.; Qu, N.S. Electrochemical Milling of TB6 Titanium Alloy in $NaNO_3$ Solution. *J. Electrochem. Soc.* **2019**, *166*, E35–E49. [CrossRef]
33. Bolzoni, F.M.; Diamanti, M.V.; Ormellese, M.; Pedeferri, M.P.; Pérez-Rosales, E. Characterisation of Titanium Oxide Films By Potentiodynamic Polarization And Electrochemical Impedance Spectroscopy. *Corros. Eng. Sci. Technol.* **2010**, *45*, 428–434.
34. Wang, J.T.; Xu, Z.Y.; Wang, J.; Zhu, D. Anodic Dissolution Characteristics of Inconel 718 in $C_6H_5K_3O_7$ and $NaNO_3$ Solutions by Pulse Electrochemical Machining. *Corros. Sci.* **2021**, *183*, 109335. [CrossRef]
35. Herraiz-Cardona, I.; Ortega, E.; Antón, J.G.; Pérez-Herranz, V. Assessment of the Roughness Factor Effect and the Intrinsic Catalytic Activity for Hydrogen Evolution Reaction on Ni-Based Electrodeposits. *Int. J. Hydrogen Energy* **2011**, *36*, 9428–9438. [CrossRef]
36. Liu, G.D.; Tong, H.; Li, Y.; Tan, Q.F.; Zhu, Y.L. Passivation Behavior of S136H Steel in Neutral Electrolytes Composed of $NaClO_3$ and $NaNO_3$ and Its Influence on Micro Electrochemical Machining Performance. *Mater. Today Commun.* **2021**, *29*, 102762. [CrossRef]
37. Schultze, J.W.; Lohrengel, M.M. Stability, Reactivity and Breakdown of Passive Films. Problems of Recent and Future Research. *Electrochim. Acta* **2000**, *45*, 2499–2513. [CrossRef]
38. Rosenkranz, C.; Lohrengel, M.M.; Schultze, J.W. The Surface Structure during Pulsed ECM of Iron in NaNO3. *Electrochim. Acta* **2005**, *50*, 2009–2016. [CrossRef]
39. Liu, W.D.; Luo, Z.; Li, Y.; Liu, Z.M.; Li, K.B.; Xu, J.X.; Ao, S.S. Investigation on Parametric Effects on Groove Profile Generated on Ti1023 Titanium Alloy by Jet Electrochemical Machining. *Int. J. Adv. Manuf. Technol.* **2019**, *100*, 2357–2370. [CrossRef]

micromachines

MDPI

Article

Jet Electroforming of High-Aspect-Ratio Microcomponents by Periodically Lifting a Necked-Entrance Through-Mask

Yasai Zhang, Pingmei Ming *, Xinmin Zhang, Xinchao Li, Lunxu Li and Zheng Yang

School of Mechanical and Power Engineering, Henan Polytechnic University, Jiaozuo 454000, China
* Correspondence: mpm@hpu.edu.cn

Abstract: High-aspect-ratio micro- and mesoscale metallic components (HAR-MMMCs) can play some unique roles in quite a few application fields, but their cost-efficient fabrication is significantly difficult to accomplish. To address this issue, this study proposes a necked-entrance through-mask (NTM) periodically lifting electroforming technology with an impinging jet electrolyte supply. The effects of the size of the necked entrance of the through-mask and the jet speed of the electrolyte on electrodeposition behaviors, including the thickness distribution of the growing top surface, deposition defect formation, geometrical accuracy, and electrodeposition rate, are investigated numerically and experimentally. Ensuring an appropriate size of the necked entrance can effectively improve the uniformity of deposition thickness, while higher electrolyte flow velocities help enhance the density of the components under higher current densities, reducing the formation of deposition defects. It was shown that several precision HAR-MMMCs with an AR of 3.65 and a surface roughness (Ra) of down to 36 nm can be achieved simultaneously with a relatively high deposition rate of 3.6 μm/min and thickness variation as low as 1.4%. Due to the high current density and excellent mass transfer effects in the electroforming conditions, the successful electroforming of components with a Vickers microhardness of up to 520.5 HV was achieved. Mesoscale precision columns with circular and Y-shaped cross-sections were fabricated by using this modified through-mask movable electroforming process. The proposed NTM periodic lifting electroforming method is promisingly advantageous in fabricating precision HAR-MMMCs cost-efficiently.

Keywords: electroforming; high aspect ratio; electrodeposition; necked-entrance through-mask; jet electroforming

1. Introduction

High-aspect-ratio micro- and mesoscale metallic components (HAR-MMMCs) can play some unique roles in quite a few application fields [1]. For instance, microcoils with aspect ratios (ARs) of more than 5 have enhanced the attraction of electromagnetic actuators and a reduced current and power consumption [2], tapered micropillars with ARs of 7 can provide efficient microfluidic device performance [3], and microelectrodes with ARs of 200 can minimize damage possibility in neural tissue penetration operations [4]. Therefore, the fabrication of HAR-MMMCs has always been one of the hottest research topics in the micromanufacturing field. To date, several micromanufacturing methods have been developed to produce HAR-MMMCs, and each of them has its own nature and advantages. These methods include electric discharge machining [5], mechanical microdrilling and micromilling [6], laser beam machining [7], electron beam machining [8], metal additive micromanufacturing processes [9], etc. However, the abovementioned methods either have great difficulty producing HAR-MMMCs in a large volume mode or have significant difficulty achieving the desired machining accuracy and material properties simultaneously.

Unlike the above HAR manufacturing methods, electroforming (EF) has a distinctive fabrication mode and possesses some unique potentials in manufacturing HAR-MMMCs [10–12]. EF forms metal materials by depositing metallic atoms layer upon

layer, which are reduced from the metallic ions in an electrolyte driven by external electrical power. In such a way, the metal material is grown and thickened continually in a relatively low-temperature environment until the end metal article is achieved. In other words, EF manufactures metal articles in an additive manufacturing manner. Thereby, EF can form compact materials which can be easily tailored, and can fabricate low-stiffness precision microscale articles due to the very moderate material generation conditions and a low process temperature. According to whether a mask is used or not, electroforming can generally be divided into maskless electroforming (maskless EF) and through-mask electroforming (TM-EF). Maskless EF can theoretically fabricate HAR-MMMCs with a limitless height by continuously moving the anode or cathode during electrodeposition. For example, jet electroforming, a kind of typical maskless EF process [13–15], adopts an anodized high-speed jet electrolyte against the cathode as a tool to induce metal electrodeposition and the control material growth process. It has been verified that jet electroforming can form microcolumn structures at a considerably high current density (normally 100 A/dm^2 or above), which means that the electrodeposition rate is very high, owing to the existence of high-speed jet electrolytes. Wang et al. used jet electroforming technology to obtain columnar microcomponents with an AR as high as 30 under the growth rate of 42 μm/min [13]. However, due to the unconstrained nature of the jet during electrodeposition, which induces serious stray current electrodeposition, the forming accuracy of jet electroforming is significantly low, making it very hard to manufacture precision articles [16]. Different from the maskless EF process, TM-EF has a much higher forming accuracy because it generates articles by filling well-defined through-mask cavities (i.e., mandrels) with the deposited material layer upon layer, and is generally dramatically accurate, since mandrels are normally created by short-wavelength lithography technology [17]. In theory, TM-EF can perfectly inversely replicate the cross-sectional shapes of mandrels. LIGA (Lithographie, Galvanoformung, Abformung) is a special TM-EF technique developed especially for fabricating precision HAR-MMMCs. It was reported that the AR of microcomponents manufactured by LIGA technology can be as high as more than 100 [18]. However, LIGA needs an expensive high-energy X-ray source and special photomask to prepare thick through-masks, limiting its wide commercial applications to a great extent. On the other hand, electroforming such HAR through-mask microcavities generally takes a very long time, even several weeks, because the mass transportation limitations inside HAR microcavities is seriously significant, greatly reducing the applied maximum current density [19–21]. In most industrial practices, the current densities applied to the LIGA electroforming process are below 2 A/dm^2. To overcome these limitations, some lower-cost modified LIGA-like techniques such as UV-LIGA [22,23], Laser-LIGA [24], and ICP-RIE LIGA [25] have been developed by using conventional light sources or other methods, and photoresists to fabricate the masks. However, compared to LIGA technology, LIGA-like techniques cannot directly achieve HAR-MMMCs in a single step because the ARs of the through-masks they use are much lower. Although some researchers made some attempts to achieve HAR-MMMCs using multiple electroforming steps with a series of low-thickness through-masks, the electroforms fabricated have greatly reduced geometrical accuracy due to the unavoidable misalignment of the operations [22].

To more cost-efficiently electroform HAR-MMMCs, Zeng et al. [26] proposed a movable through-mask electroforming technology (movable TM-EF). Different from the conventional TM-EF technology, the through-mask in the movable TM-EF is lifted upwards constantly or periodically rather than being statically fixed on the cathode. This proposed process makes the manufacturing of HAR-MMMCs much easier, even when using lower-AR through-masks. In theory, it can fabricate micro- and meso-sized articles with a limitless AR. With this process, Zeng et al. successfully fabricated several HAR ($\geq$3) structures, including E-shaped structures, columnar structures, and Y-shaped structures. However, this proposed movable TM-EF is inefficient in the electrodeposition rate, with an applied current density of 2 A/dm^2 corresponding to a relatively low rate. Additionally, it does not show acceptable forming accuracy. The main reasons for these issues are likely

poor mass transfer conditions and nonuniform current density distribution within the electrodeposition space [27–30]. Insulation shielding adjusts the electric field distribution between the anode and cathode by adding structures such as shielding plates outside the deposition area, thereby improving the uniformity of current density distribution on the cathode surface [28]. This study innovatively adopted this concept by installing a necked-entrance at the entrance of each through-mask cavity. This design reduces the edge effects of the electric field, enhancing the uniformity of current density distribution throughout the continuous deposition process. Therefore, this study proposes a modified movable TM-EF, specifically the periodically lifting necked-entrance TM-EF (NTM-EF). In the periodically lifting NTM-EF, the high-speed jet electrolyte transports the electrolyte into the cavities. In the following sections, verification studies will be conducted theoretically and experimentally, evaluating electrodeposition behaviors, surface morphology, dimensional accuracy, etc.

2. Simulation Analysis

2.1. Principle of Periodically Lifting NTM-EF

Figure 1a schematically shows the periodically lifting NTM-EF technology proposed in this study. Unlike the existing movable TM-EF shown in Figure 1b, this technology features a necked structure at the inlet entrance of each through-mask cavity to improve current density distribution within the cavities being filled, as shown in Figure 1c,d. Additionally, the proposed technology adopts a jet electrolyte against the through-mask cavity to accelerate the mass transport during electrodeposition. With these modifications, this study expects to achieve significantly enhanced deposition rate and forming accuracy of HAR-MMMCs using the periodic lifting NTM-EF [19,28,31].

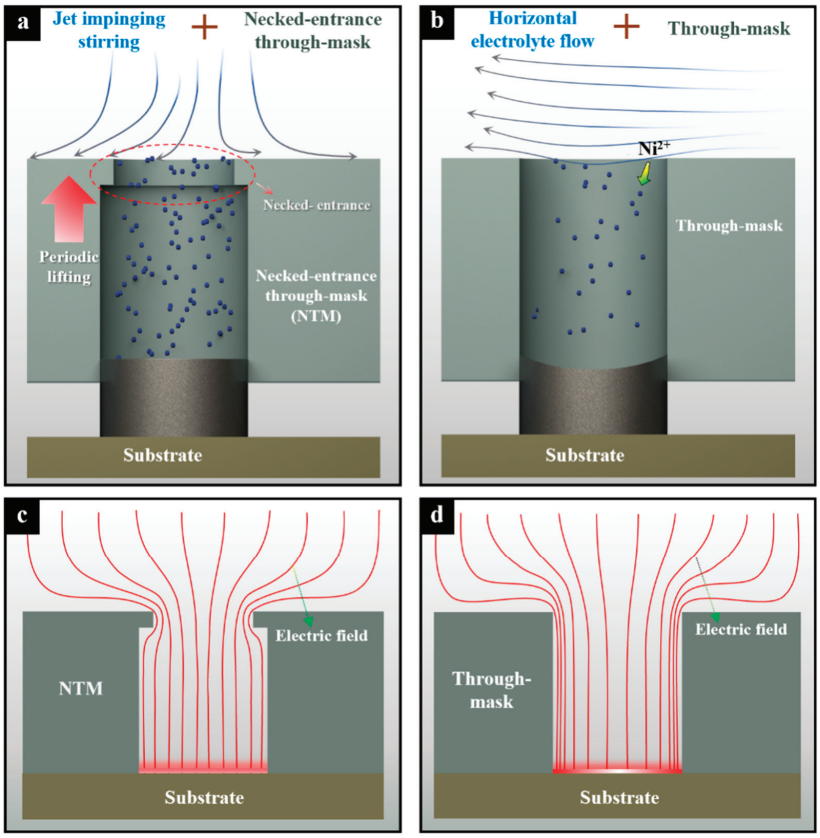

Figure 1. Schematical diagram of the two TM-EF technologies. (**a**) The periodically lifting NTM-EF with jet electrolyte; (**b**) The conventional movable TM-EF with horizontal electrolyte flow; (**c**) Current density distribution of NTM; (**d**) Current density distribution of conventional TM.

Figure 2 schematically shows the workflows of periodically lifting NTM-EF for fabricating the HAR-MMMCs. In this study, the growing surface is maintained at a relatively unchanged position inside the through-mask cavity. The aspect ratio (AR), defined as the ratio of the depth (H) to the diameter (L) of the through-mask cavity, is kept at approximately 1 by periodically lifting the NTM by a height of Δh during deposition. In the initial stage of deposition, the bottom surface of the NTM is in close contact with the cathode substrate surface, with no relative movement between them. As the deposition process proceeds, metallic atoms are deposited inside the through-mask cavities. When the deposited metal grows to a thickness of h_0, the NTM is lifted for the first time by a height of Δh. When the deposited metal increases by another thickness of Δh, the NTM is lifted again by Δh. Thereafter, the NTM will be periodically lifted by Δh whenever the deposited metal grows by Δh. When the total thickness or height of the deposited article reaches the designed value, the deposition process stops. The parameter h_0 is set to guide the deposited segment during the subsequent lifting process, ensuring proper alignment and stability. The small step size Δh helps maintain stability during the lifting process, minimizing disruptions to the deposition and ensuring consistent quality. These parameters are critical for achieving uniform deposition and preventing detachment or misalignment of the deposited segment.

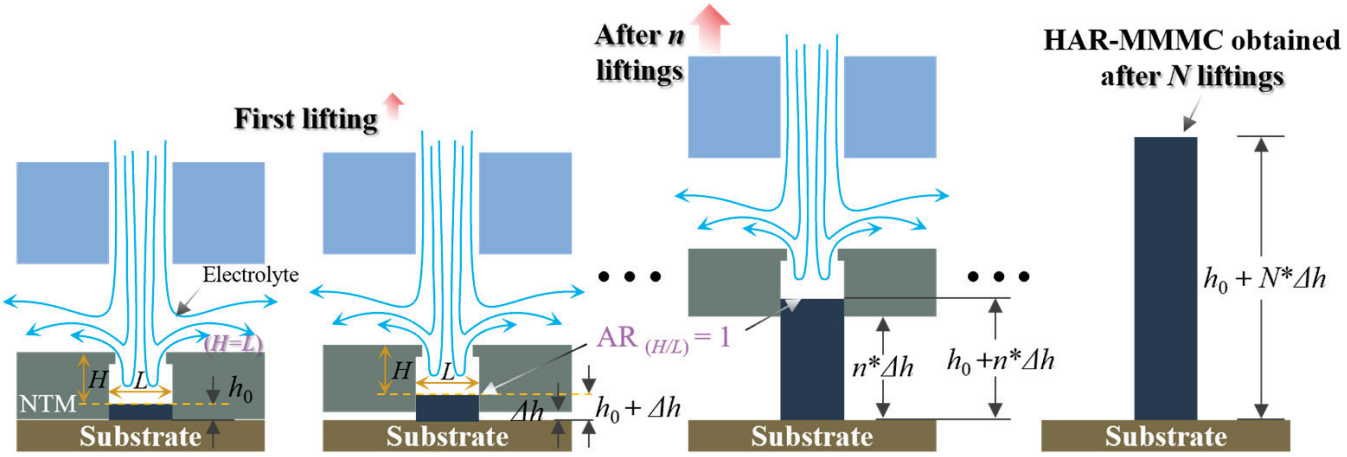

Figure 2. Workflows of the periodically lifting NTM-EF.

2.2. Simulation

2.2.1. Models

To understand and optimize the distribution characteristics of mass transfer and current density, which determine the geometrical profile and growth rate of the deposits, numerical simulations were carried out. Figure 3 shows the core working components of the actual periodically lifting NTM-EF. Electrolyte is jetted against the entrance area of the through-mask from a circular hollow channel. It then flows out from the outlets located in the middle-upper part of a cylindrical tank after passing through the cavity. In this configuration, an electrically inert anode is fixed inside the hollow channel, located along the central line of the cylindrical tank. To assess the effectiveness of electroforming using a through-mask with a necked-entrance under jet conditions, a simulation model was established with a single mask cavity. Since the core working configuration is symmetrical, a two-dimensional physical model describing half of the configuration was developed to simplify the calculations, as shown in Figure 4.

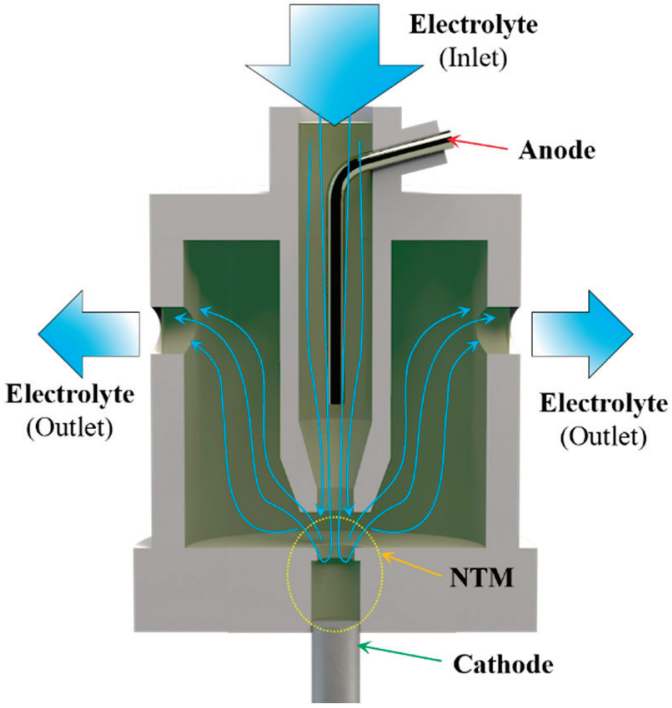

Figure 3. Schematic diagram of the core working components.

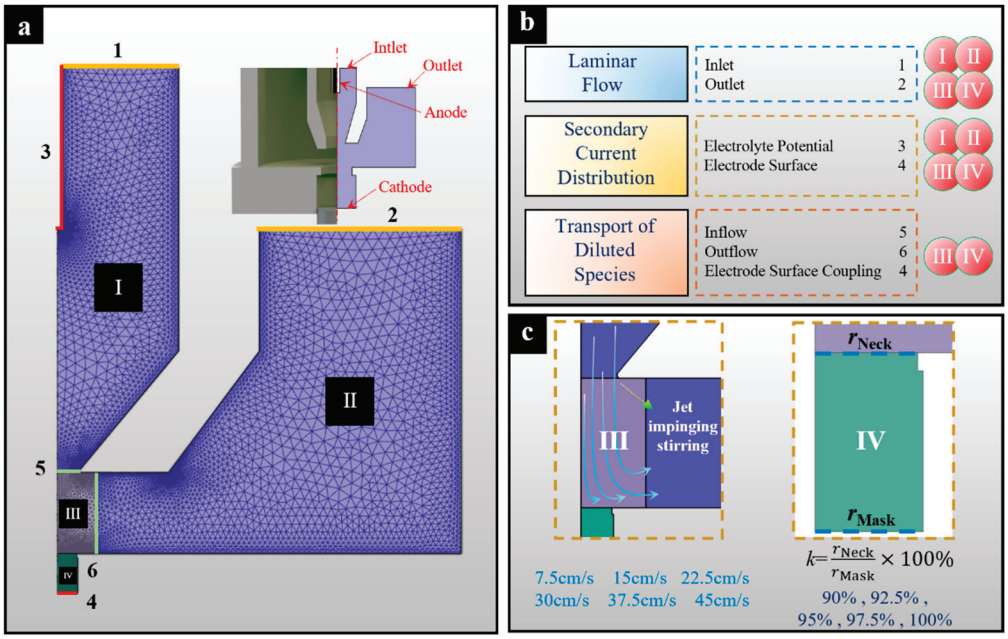

Figure 4. Numerical simulation model and its parameters definition. (**a**) Two-dimensional model; (**b**) Definition of boundaries of the model.; (**c**) Key initial condition parameters and the introduced factor.

2.2.2. Simulations

The following assumptions are made for simulations to simplify the calculation without losing generality.

(1) The electrolyte is a continuous incompressible viscous fluid.
(2) The anode reaction is ignored, and the electrolyte potential is used as the anode boundary condition.

(3) The cathode reaction is nickel electrodeposition, ignoring cathode side reactions, and obeys Faraday's law. The primary objective of the numerical simulations in this study is to investigate the effects of different necked-entrance parameters. These parameters affect the distribution of current density on the cathode surface and the mass transfer within the through-mask cavities. This study does not focus on the deposition efficiency of metal ions. Therefore, disregarding the cathodic side reactions is appropriate to meet the research objectives.
(4) The deposition surface of the microcomponent is at a stable position with an aspect ratio of the through-mask cavity of 1.

Since the electrochemical deposition process involves flow dynamics and electrochemistry, governing equations are required to solve the simplified model. The flow behavior of the electrolyte solution, as an incompressible continuous liquid, is governed by the Navier–Stokes equations, as shown below [32].

$$\nabla u = 0 \tag{1}$$

$$\rho\left(\frac{\partial u}{\partial t} + u \cdot \nabla u\right) = -\nabla p + \nabla\left(\mu\left(\nabla u + (\nabla u)^T\right)\right) + F \tag{2}$$

where ρ stands for density, μ for dynamic viscosity, u for velocity, p for pressure, and F for surface tension.

The ion transport during the electrodeposition process involves changes in the solution's composition, and its governing equations are as follows [33].

$$\frac{\partial c}{\partial t} + \nabla \cdot J + u \cdot \nabla c = R \tag{3}$$

$$J = -D\nabla c - zu_m Fc\nabla\varphi \tag{4}$$

where c stands for transported ion concentration, t for thermodynamic temperature, ∇ for gradient, J for material flux, u for velocity of the flowing fluid, R for nickel ion concentration sink, D for diffusion coefficient, F for Faraday constant, and $\nabla\varphi$ for potential gradient.

The electrical characteristics at the electrode interface are influenced by the action of ions in the solution, and their governing equations are as follows [28].

$$j_{loc} = j_0\left(C_R exp\left(\frac{\alpha_a F\eta}{RT}\right) - C_O exp\left(\frac{\alpha_c F\eta}{RT}\right)\right) \tag{5}$$

$$\eta = \phi_s - \phi_l - E_{eq} \tag{6}$$

where j_{loc} stands for local current density, j_0 for exchange current density, α_a for anodic transfer coefficient, α_c for cathodic transfer coefficient [28], C_R for reduction expression, C_O for oxidation expression, F for Faraday constant, R for gas constant, T for thermodynamic temperature, Φ_s for electrode potential, Φ_l for electrolyte potential, and E_{eq} for equilibrium potential of the electrodeposited metal.

A parameter, k, was introduced to numerically characterize the necking degree of the inlet of NTM:

$$k = \frac{r_{Neck}}{r_{Mask}} \times 100\% \tag{7}$$

where r_{Neck} stands for the radius of the necked-entrance, and r_{Mask} for the radius of the normal NTM cavity.

To simplify the numerical simulation, a single through-mask cavity was selected, and its two-dimensional model is shown in Figure 4. The COMSOL Multiphysics (6.0) software was used to solve this model. The model is divided into four regions (I, II, III, and IV). Figure 4b shows the definitions of each region and boundary in the numerical simulation.

In this simulation model, the secondary current distribution and laminar flow physics field are applied to Regions I, II, III, and IV. The transport of dilute species physics field is only applied to Regions III and IV. To improve the calculation accuracy, Regions III and IV were finely meshed because they operate on a microscale. The main data used for the numerical simulation model are listed in Table 1. Some key initial parameters and definitions are also presented in Figure 4b,c. In the simulations, the distribution of Ni^{2+} concentration in the deposition area under different inlet flow velocity conditions (v) was first analyzed. Then, the electric field distribution within the NTM cavity with different necked-entrance size was analyzed.

Table 1. The data used for simulations.

Parameter	Nomenclature	Value
Electrolyte temperature (°C)	T	55
Anodic charge transfer coefficient	α_a	1.5
Cathodic charge transfer coefficient	α_c	0.5
Cathodic current density (A/dm^2)	j	20
Electrolyte conductivity (S/m)	σ	10
Concentration of Ni^{2+} (mol/m^3)	c	1548
Electrolyte flow (cm/s)	v	7.5, 15, 22.5, 30, 37.5, 45
Electrolyte viscosity (Pa·s)	μ	1.2×10^{-4}
Electrolyte density (kg/m^3)	ρ	1400
Radius of through-mask cavity (μm)	r_{Mask}	1000
$r_{Neck}/r_{Mask} \times 100\%$	k	90%, 92.5%, 95%, 97.5%, 100%

2.3. Simulation Results and Discussion

2.3.1. Effect of Mass Transfer

In this study, k is an important characteristic parameter that affects the size of the mass exchange passage, determining the diffusion layer thickness and electrolyte flow velocity near the cathode surface. As shown in Figure 5a, the diffusion layer thickness remains almost constant at approximately 20 μm, despite changes in k. This means that the k value has little influence on the diffusion layer thickness. However, the k value significantly impacts the flow field distribution at a distance of 20 μm from the cathode surface along various distances from the NTM cavity axis, as shown in Figure 5b. Under the condition of electrolyte impingement, the flow field within the cavity fluctuates significantly. Generally, the flow velocity is smaller in the central region and near the cavity wall surface, but highest in the regions between the central part and the cavity wall. However, there are some differences when k is changed. When the necked-entrance is too large (i.e., k = 100%) or too small (i.e., k = 90%), the inflow and outflow of the electrolyte through the NTM cavity are significantly restricted. This leads to the generation of high-velocity regions and results in an extremely uneven flow field distribution within the cavity. However, when the necked-entrance size is appropriate (i.e., k = 95%), it greatly improves the uniformity of the flow field. This means that when k is selected to be 95%, the flow field distribution within the cavity is beneficial for the electroforming process.

Apart from k, the effect of the inlet flow velocity v on the mass transfer inside the cavity was also analyzed under the conditions of k = 95% and j_{AVG} = 20 A/dm^2 (see Figure 6). It is shown that the velocity of the impinging electrolyte jet has a considerable impact on the flow field and mass transportation rate within the cavity. Generally, the higher the velocity v, the faster the electrolyte flows in the vicinity of the cathode surface, and the larger the mass transfer rate, as shown in Figure 6a. In addition, a higher jet-impinging velocity leads to faster electrolyte flow close to the cavity's wall and a thinner diffusion layer. This results in a homogeneous Ni^{2+} concentration distribution, as shown in Figure 6b. These factors help enhance and homogenize the electrodeposition rate. Therefore, v = 45 cm/s is selected in this study.

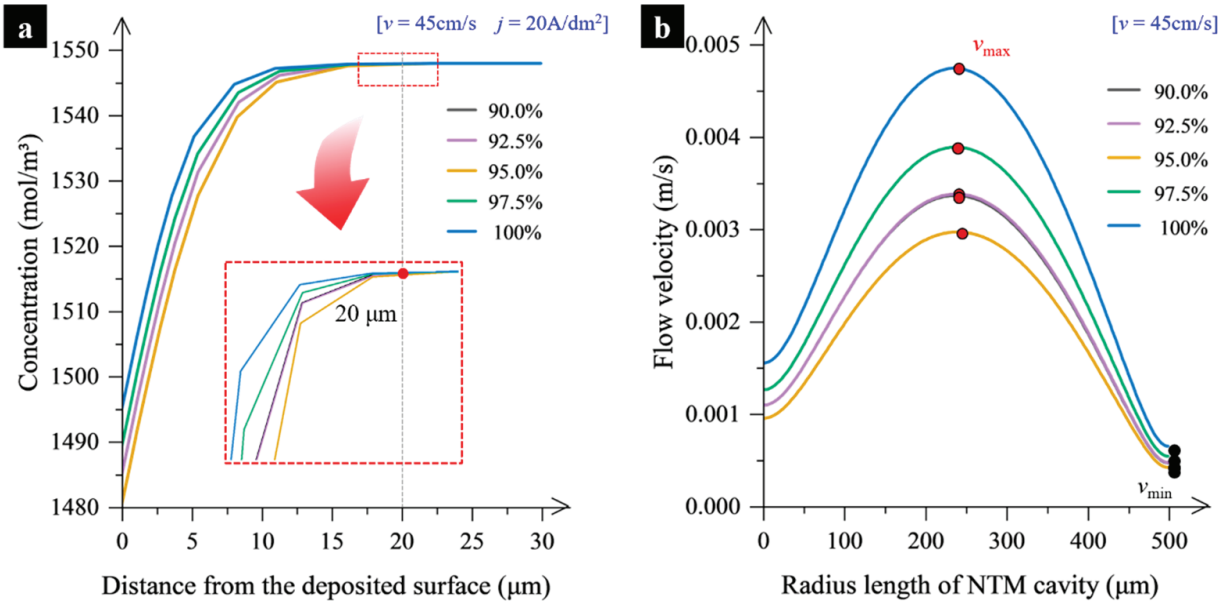

Figure 5. Change of the concentration distribution in the vicinity of the cathode surface and of the flow velocity distribution within the cavity. (**a**) Distribution of Ni^{2+} concentration within the electrolyte layer close to the cathode surface; (**b**) Distribution of the flow velocity along the radius of the NTM cavity at a distance of 20 μm away from the cathode surface.

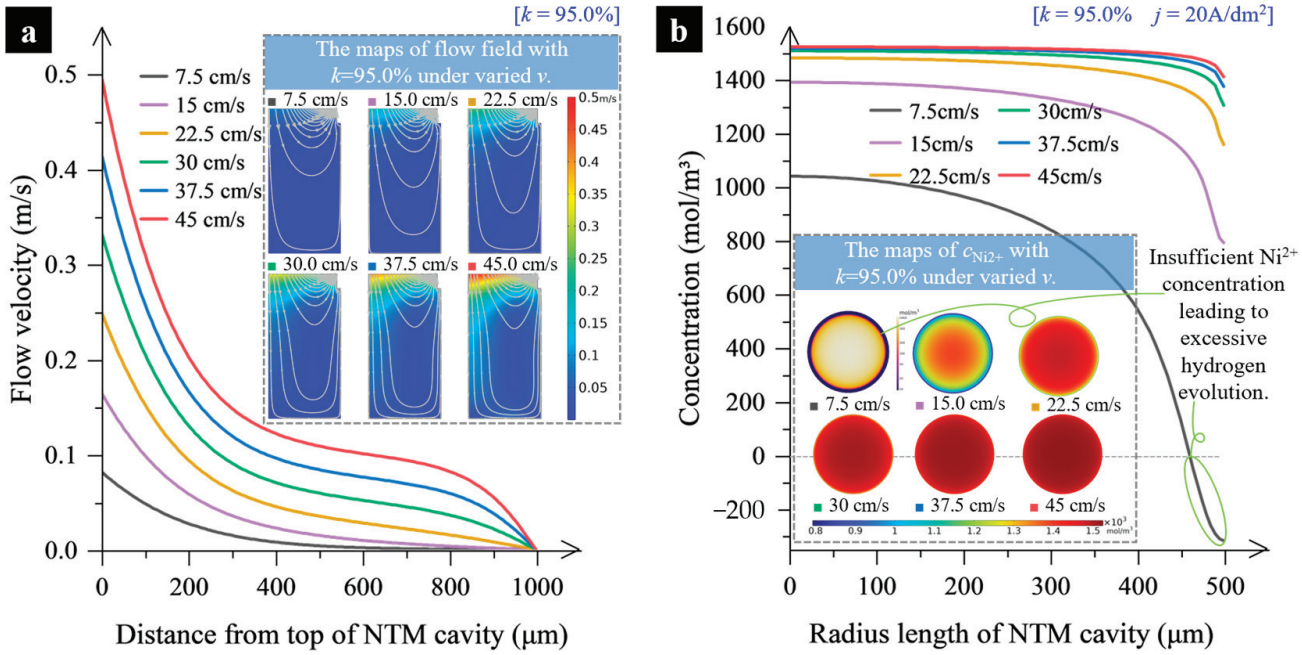

Figure 6. Change of the electrolyte flow velocity and the Ni^{2+} concentration distribution. (**a**) Distribution of the electrolyte flow velocity along the centerline of the NTM cavity; (**b**) Distribution of Ni^{2+} concentration within the electrolyte layer near the cathode surface.

2.3.2. Electric Current Density Distribution

The magnitude and distribution of the current density on the cathode surface are crucial factors determining the deposition speed and deposit thickness distribution uniformity. This study specifically analyzes the impact of changing the necked-entrance size on the current density distribution across the cavity's cross-sections, as shown in Figure 7. These results were conducted with j_{AVG} = 20 A/dm^2 and v = 45 cm/s.

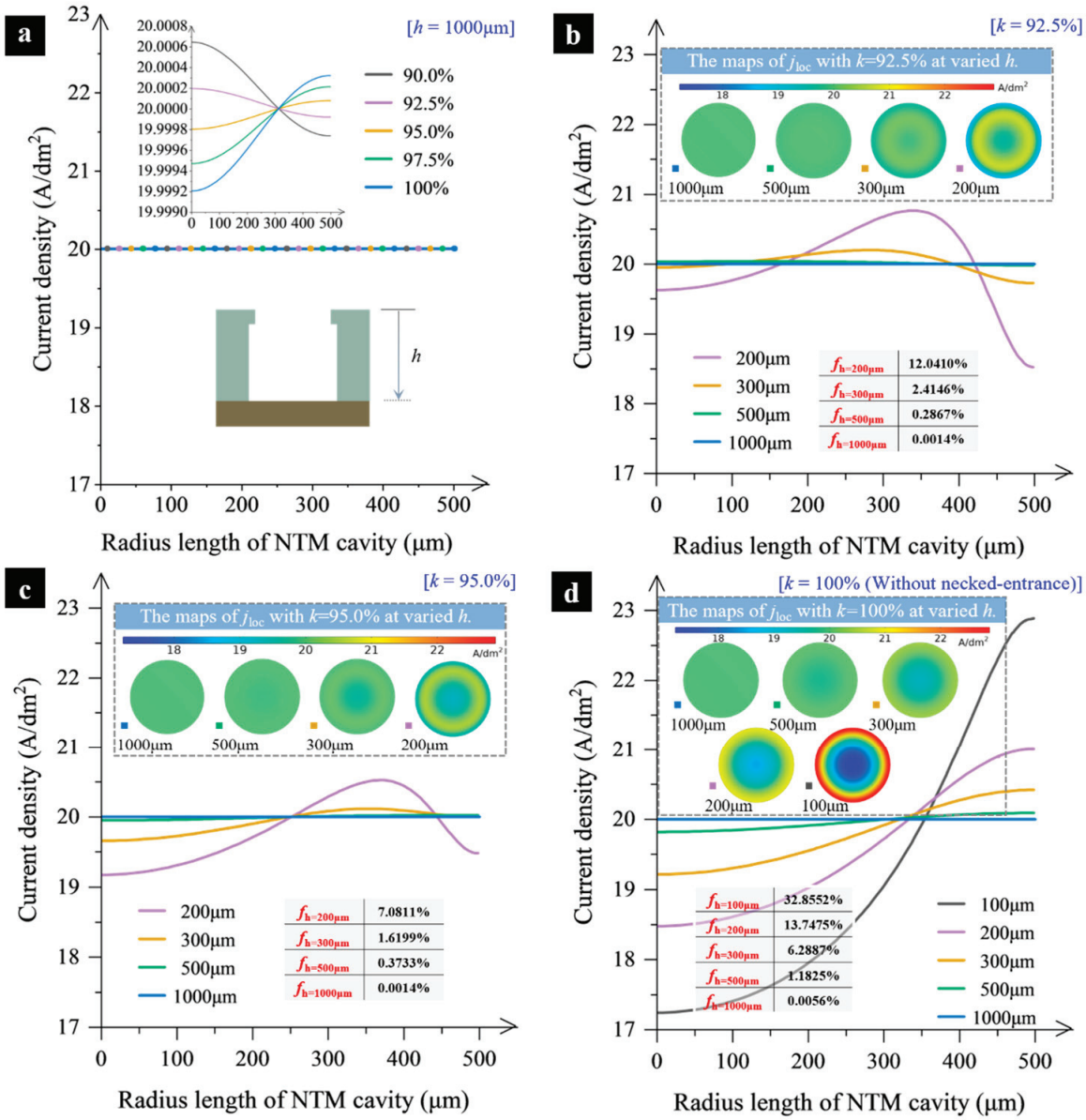

Figure 7. Change of current density distribution. (**a**) Current density distribution at the cross-section surface at the depth of h = 1000 μm; (**b**) Current density distribution with k = 92.5%; (**c**) Current density distribution with k = 95%; (**d**) Current density distribution with k = 100%.

Figure 7a indicates that current density distribution changes little in areas far from the NTM inlet. For example, at the cross-section of h = 1000 μm (depth measured from the top surface of the NTM), the change is minimal when the entrance size reduction is less than 10%. Further research shows that when the necked-entrance is 92.5% or 95% of the original size, the current density distribution is almost equal over the entire deposition surface. Based on this, the current density distribution at different distances h from the NTM top surface is further analyzed for k = 92.5%, 95%, and 100%, as shown in Figure 7b–d. The results show that when k = 92.5% and 95%, there are still some differences in the current density distribution at the cross-section close to the NTM cavity inlet. Compared with the scheme without necked-entrance, when k = 92.5% and 95%, the current density distribution at h = 500 μm still shows a high degree of uniformity. A deviation coefficient, f, is introduced to assess current density distribution uniformity, calculated using the formula $f = (j_{max} - j_{min})/j_{min} \times 100\%$ [17,34]. Comparing the deviation coefficients for different k values shows that the proper necked-entrance size helps homogenize the current density

distribution in the deposition area. k = 95% appears to be more effective in enhancing uniformity compared to k = 100% and 92.5%.

3. Experimental Study

3.1. Materials and Methods

Figure 8 shows the experimental setup specially developed for the NTM-EF technology. This setup mainly includes a mobile platform, an electrolyte supply system, a DC supply, a monitoring system, and a control system. The electrolyte compositions used were nickel sulfamate (500 g/L, AR, 98%), boric acid (30 g/L, AR, 98%), and wetting agent (0.15 g/L). The electrolyte temperature was maintained at 55 ± 1 °C. The pH of the electrolyte was maintained at 4 ± 0.2 by adding sulfamate acid or nickel carbonate. The electrolyte volume used in this study was relatively large, totaling 5 L. Due to the small amount of microcomponent deposition per experimental cycle, the inert anode minimally impacts the electrolyte pH. The pH was maintained at 4 ± 0.2 by adding nickel carbonate as needed after each experimental cycle. The electrodeposition lifting procedure was conducted using a self-built electroforming mobile platform. The power source employed for electrodeposition was a direct current (DC) power supply (ITECH, IT6122, Nanjing, China), while the monitoring system used was a charge-coupled device (CCD) microscope camera (ZQ, 616, Shanghai, China). Microhardness measurements of the components were carried out by a Vickers Hardness Tester (HV-1000, JITAI KEY, Beijing, China). Platinum was used as the anode material. To facilitate monitoring, both the nozzle and NTM shown in the enlarged view within the purple circle in Figure 8 are made from transparent organic glass. During the lifting process, strong adhesion between the deposited structure and the substrate is crucial to overcome frictional forces between the deposited segment and the mask cavity. This study used copper as the substrate material due to its strong adhesion to nickel, providing sufficient bonding strength for the deposition process.

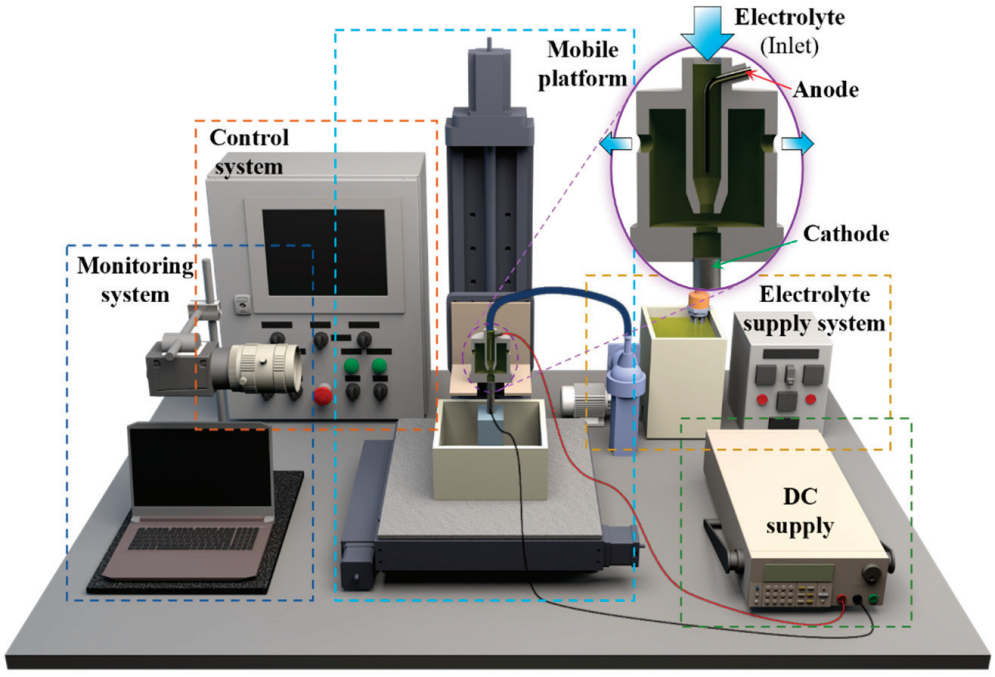

Figure 8. Schematic diagram of NTM-EF system.

In the experimentation, the parameter h_0 represents the height of the deposited component within the through-mask cavity. If h_0 is too large, it can result in excessive friction between the deposited component and the sidewalls of the through-mask cavity, hindering the lifting process. Conversely, if h_0 is too small or if the fitting segment structure is not established, the alignment between the deposited section and the through-mask cavity

will be insufficient. This inadequate alignment can cause the deposited section to detach from the through-mask cavity during the lifting process, leading to deposition failure. Therefore, $h_0/L = 0.2$ is chosen as the fitting height. Additionally, if Δh is too large, it can negatively impact the stability of the deposition process. Based on the specific conditions of the experimental setup, Δh is selected to be 25 μm.

The deposited components were examined using a scanning electron microscope (Merlin Compact, Zeiss, Jena, Germany), a laser confocal microscope (Olympus, OLS5100, Tokyo, Japan) and a fully automatic image measuring instrument (COBEK, AM600CNC, Dongguan, China). Four hardness values were obtained from different samples to calculate the average value. The surface roughness and geometric dimensions were the averages of three measurements. The error bars shown in the figures represent the mean and standard deviation of multiple measurements.

3.2. Experimental Results and Discussion

As shown in Figure 9, the NTM has a small batch of mask cavities arranged on it, and the area corresponding to the nozzle aligns with these batch-arranged mask cavities. In subsequent experiments, five evenly spaced points along the white arrow pointing outward from the center of the jet region on the component were detected to evaluate the deposition effects. This was performed according to the layout shown in Figure 9.

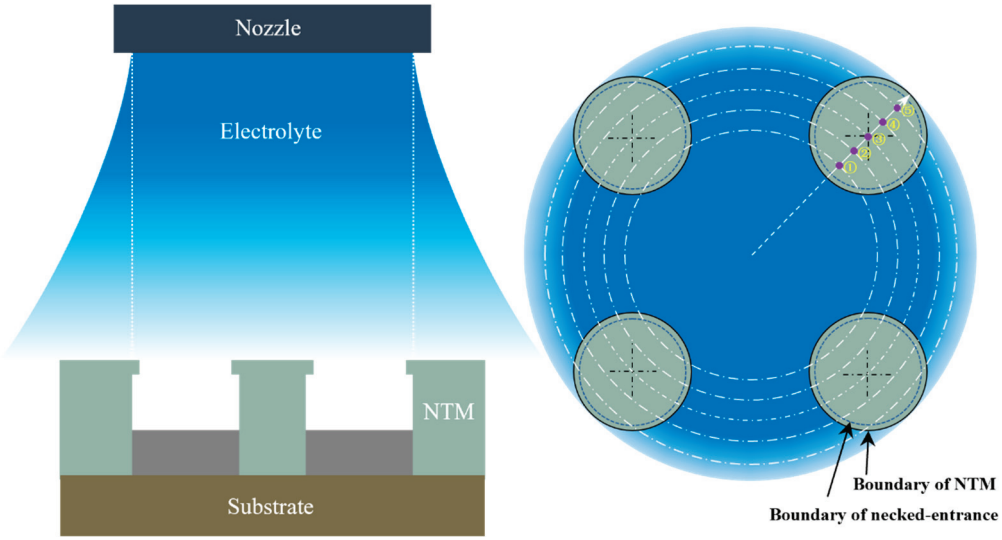

Figure 9. Schematic diagram of NTM-EF configuration.

A study on the electroforming of columnar components with a feature size of 1000 μm was conducted with the mask stationary to verify the actual effect of the NTM in the electroforming process. Figure 10 shows images of the columnar components electroformed under five different conditions, all with the same deposition time (150 min) at $j_{AVG} = 20$ A/dm^2. The top surface of the components fabricated with NTMs (with a necking degree of $k = 95\%$) is smooth with few defects, regardless of the flow velocity. As the flow velocity increases, the top surface becomes smoother, more even, and has higher Vickers microhardness, as shown in Figure 10. For instance, at $v = 45$ cm/s, the top surface roughness at the center point position ③ of the deposited component is only 0.036 μm. At the same time, the Vickers microhardness at the same point of the component reached an impressive 520.5 HV. In comparison to the hardness range of nickel components obtained through conventional electrodeposition (266 HV–360 HV), this represents an increase ranging from 44.6% to 95.7%. There is a significant consistency in the quality of the deposition surface and Vickers microhardness under different flow velocities. In general, high current density can achieve smaller grain sizes, thereby enhancing the hardness of the deposited layer [35]. In this study, the current was kept constant while the electrolyte flow rate was varied. Typically,

improving mass transfer, which increases the ion concentration level in the deposition area, can promote grain growth, which is generally unfavorable for enhancing microhardness. However, a significant increase in the density of the deposited layer was observed with higher electrolyte flow rates. Therefore, the changes in the performance of the deposited layer might be more related to the reduction in porosity and defects within the layer.

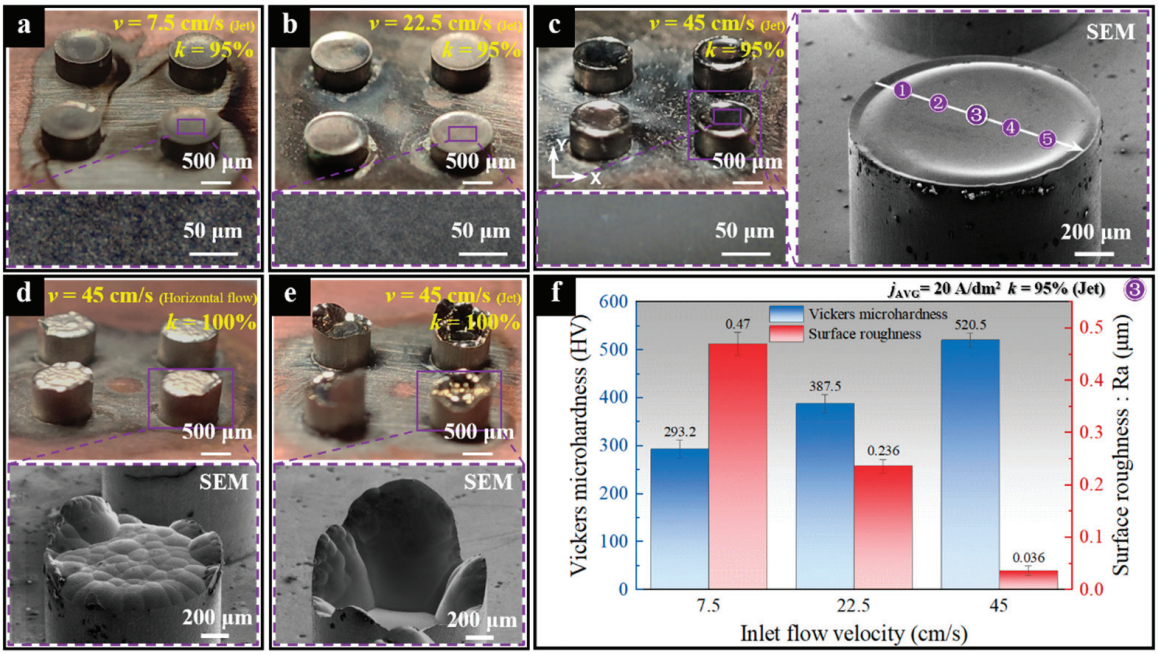

Figure 10. Electroforming effects of the columnar HAR-MMMCs under different conditions. (**a**) v = 7.5 cm/s (jet electrolyte), k = 95%; (**b**) v = 22.5 cm/s (jet electrolyte), k = 95%; (**c**) v = 45 cm/s (jet electrolyte), k = 95%; (**d**) v = 45 cm/s (horizontal electrolyte flow), k = 100%; (**e**) v = 45 cm/s (jet electrolyte), k = 100%; (**f**) Variation trend of Vickers microhardness and surface roughness of the components formed under different inlet flow velocities.

As shown in Figure 10d,e, when a through-mask without a necked-entrance is used for manufacturing, the surface of the component appears uneven, regardless of whether horizontal flow or jet flow is applied. These findings experimentally verified that an appropriate necked-entrance in the through-mask cavities improves formation accuracy and surface quality.

In this study, the electroforming effects at the center point position ③ of the component were analyzed and compared under conditions of j_{AVG} = 20 A/dm^2 and k = 95% for different inlet flow velocities. As shown in Figure 10f, components electroformed at lower flow velocities exhibit lower microhardness and higher surface roughness. In contrast, components electroformed at higher flow velocities display higher microhardness and smaller surface roughness. A comparison reveals that at v = 7.5 cm/s, the component surfaces exhibit numerous pitting defects, while at v = 45 cm/s, the components appear dense with a mirror-like surface effect. According to previous studies [28], this trend may be attributed to poor mass transfer effects at lower electrolyte flow velocities. This leads to excessive hydrogen evolution in the deposition area, resulting in the formation of numerous pores within the components and adversely affecting microhardness. Conversely, higher electrolyte flow velocities provide more efficient mass transfer, reducing hydrogen evolution and resulting in denser components. Additionally, the use of higher current density promotes the formation of smaller grains, thereby enhancing the microhardness of the components.

As shown in Figure 11a, when using an NTM with k = 95% under the experimental conditions of v = 45 cm/s jet flow, the thickness variation between the components manu-

factured in small batches is only 1.4%, ensuring stability in subsequent periodically lifting electroforming of components in small batches. In small-batch electroforming, considering the thickness distribution of an individual component along the direction of the white arrow, the thickness variation is 5.05%. Compared with the results reported in [26], the thickness variation is reduced by approximately 5% to 6%. Under this condition, the deposition rate of the components reached 3.6 μm/min ($(H - \Delta H/2)/150$ min).

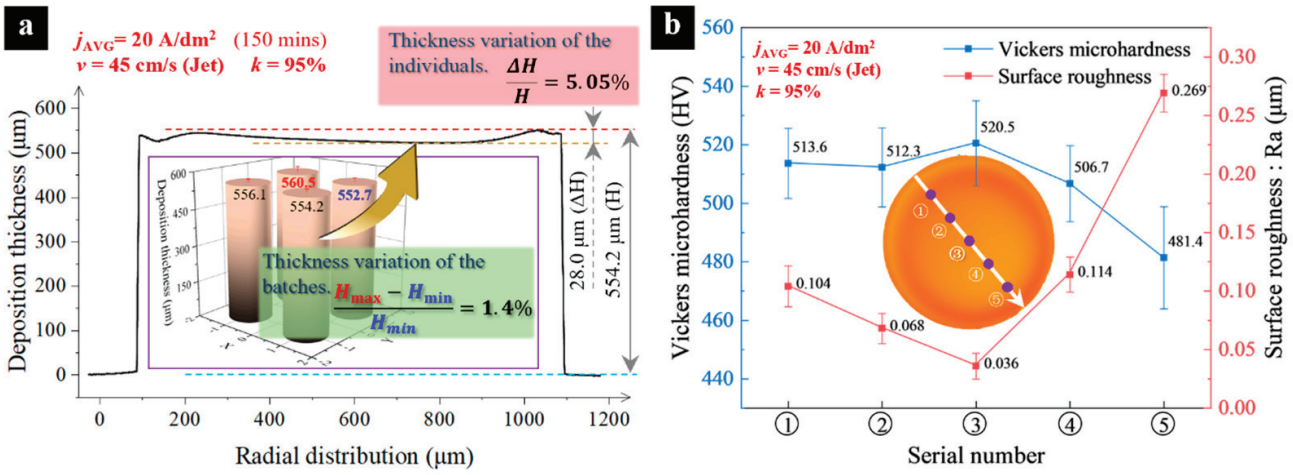

Figure 11. Electroforming effects of the components. (**a**) Height of the components; (**b**) Variation trend of Vickers microhardness and surface roughness of the components along the white arrow.

Figure 11b illustrates the distribution of Vickers microhardness and surface roughness at five evenly distributed points along the white arrow on the surface of the component. It can be observed that, from the center to the outer side of the jet, there is little difference in Vickers microhardness on the component's surface. The microhardness at the outermost part of the component is slightly lower but still reaches 481.4 HV. Meanwhile, differences in surface roughness can be noted at different locations, with the minimum roughness at the center of the component and the maximum roughness at the outermost part, albeit only at 0.269 μm. Overall, the components manufactured using NTM-EF exhibit excellent performance.

To achieve higher micro- and mesoscale components, periodically lifting TMs were used during electroforming with the necked-entrance cavity molds. Figure 12a–c sequentially display HAR-MMMCs after planarization obtained through electroforming, each exhibiting varying dimensions and cross-sectional shapes. In these cases, highly precise structures, including those with complex cross-sections such as Y-shaped, can be successfully fabricated, as shown in Figure 12c. Additionally, Y-shaped components with complex cross-sections were produced, featuring straight sidewalls and clear boundaries. Upon inspection, their relative errors (the ratio of the absolute error to the standard design value) are within the desired range. Particularly noteworthy is the Y-shaped components with sharp boundary structures, achieving an aspect ratio of 3.65.

Figure 12d shows the analysis of feature dimensions at five uniformly sampled measurement points (I/II/III/IV/V) on the deposition height of components of different scales, revealing high forming precision in all three scales of components. Specifically, for the columnar component with a feature size of 1000 μm, the size difference is only 1.10%, while for the Y-shaped component with the AR of 3.65, the size difference is also merely 1.89%. This result demonstrates the significant potential of NTM-EF technology in achieving high-precision manufacturing of HAR-MMMCs.

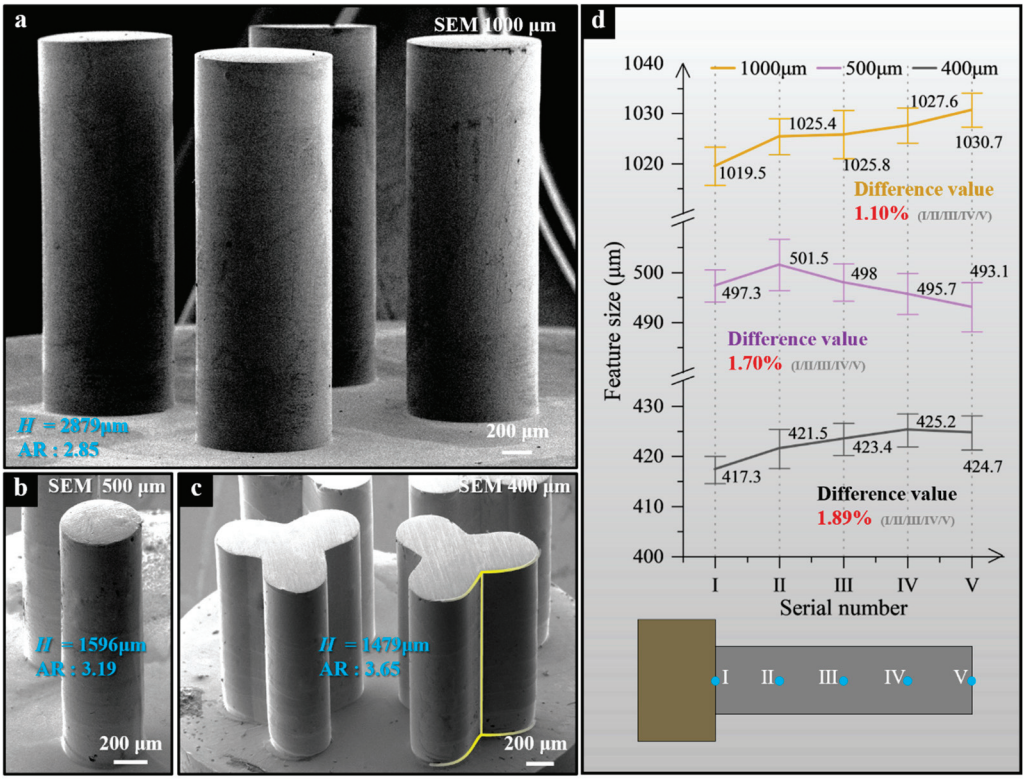

Figure 12. HAR-MMMCs after planarization. (**a**) Columnar HAR-MMMCs (designed diameter of 1000 μm); (**b**) Columnar HAR-MMMCs (designed diameter of 500 μm); (**c**) HAR-MMMCs with Y-shaped (designed line width of 400 μm); (**d**) The feature size variation of three scales of components.

4. Conclusions

To achieve high-speed and high-precision manufacturing of the high-aspect-ratio micro- and mesoscale metallic components (HAR-MMMCs), a periodically lifting necked-entrance through-mask electroforming (NTM-EF) process was proposed. The feasibility of the NTM-EF was examined numerically and experimentally. The following conclusions were drawn from the study.

(1) The periodically lifting NTM-EF process is feasible and effective for fabricating the precision HAR-MMMCs with a relatively high deposition rate.
(2) In the periodically lifting NTM-EF, the necking size of the through-mask cavity mold is crucial to achieve an evenly-distributed thickness of top-growing surface, and, generally, a slight necking of less than 10% is preferable.
(3) In the periodically lifting NTM-EF, a relatively higher speed of vertical impinging jet supply is necessary to quicken and homogenize mass transfer within the TM mold cavities.

Author Contributions: Y.Z. performed the experiment, analyzed the experiment, and wrote the manuscript. P.M. contributed significantly to the conception of the study and revised the manuscript. X.Z., X.L., L.L. and Z.Y. helped perform the analysis with constructive discussions. All authors have read and agreed to the published version of the manuscript.

Funding: This work was supported by the Fundamental Research Funds for the Universities of Henan Province (grant number NSFRF210338), and Key scientific and technological projects of Henan Province (grant number 212102210054).

Data Availability Statement: The original contributions presented in the study are included in the article, further inquiries can be directed to the corresponding author.

Conflicts of Interest: The authors declare no conflicts of interest.

References

1. Gu, Q.; Lv, J.; Mo, X.; Jiang, X. High Aspect Ratio Metamaterials and Their Applications. *Sens. Actuator A-Phys.* **2022**, *335*, 113376. [CrossRef]
2. Noda, D.; Hattori, T. Fabrication of Microcoils with Narrow and High Aspect Ratio Coil Line. *Adv. Robot.* **2010**, *24*, 1461–1470. [CrossRef]
3. Park, J.M.; Kim, J.H.; Han, J.S.; Shin, D.S.; Park, S.C.; Son, S.H.; Park, S.J. Fabrication of Tapered Micropillars with High Aspect-Ratio Based on Deep X-Ray Lithography. *Materials* **2019**, *12*, 2056. [CrossRef] [PubMed]
4. Kamaraj, A.B.; Sundaram, M.M.; Mathew, R. Ultra High Aspect Ratio Penetrating Metal Microelectrodes for Biomedical Applications. *Microsyst. Technol.* **2013**, *19*, 179–186. [CrossRef]
5. Chen, S. Fabrication of High-Density Micro Holes by Upward Batch Micro EDM. *J. Micromech. Microeng.* **2008**, *18*, 085002. [CrossRef]
6. Chang, D.-Y.; Lin, C.-H. High-Aspect Ratio Mechanical Microdrilling Process for a Microhole Array of Nitride Ceramics. *Int. J. Adv. Manuf. Technol.* **2019**, *100*, 2867–2883. [CrossRef]
7. Yadroitsev, I.; Shishkovsky, I.; Bertrand, P.; Smurov, I. Manufacturing of Fine-Structured 3D Porous Filter Elements by Selective Laser Melting. *Appl. Surf. Sci.* **2009**, *255*, 5523–5527. [CrossRef]
8. Guo, C.; Ge, W.; Lin, F. Effects of Scanning Parameters on Material Deposition during Electron Beam Selective Melting of Ti-6Al-4V Powder. *J. Mater. Process. Technol.* **2015**, *217*, 148–157. [CrossRef]
9. Khademzadeh, S.; Zanini, F.; Bariani, P.F.; Carmignato, S. Precision Additive Manufacturing of NiTi Parts Using Micro Direct Metal Deposition. *Int. J. Adv. Manuf. Technol.* **2018**, *96*, 3729–3736. [CrossRef]
10. Li, X.; Ming, P.; Ao, S.; Wang, W. Review of Additive Electrochemical Micro-Manufacturing Technology. *Int. J. Mach. Tools Manuf.* **2022**, *173*, 103848. [CrossRef]
11. Davydov, A.D.; Volgin, V.M. Template Electrodeposition of Metals. Review. *Russ. J. Electrochem.* **2016**, *52*, 806–831. [CrossRef]
12. Zhang, H.; Zhang, N.; Gilchrist, M.; Fang, F. Advances in Precision Micro/Nano-Electroforming: A State-of-the-Art Review. *J. Micromech. Microeng.* **2020**, *30*, 103002. [CrossRef]
13. Wang, W.; Ming, P.; Zhang, X.; Li, X.; Zhang, Y.; Niu, S.; Ao, S. Additive Manufacturing of Three-Dimensional Intricate Microfeatures by Electrolyte-Column Localized Electrochemical Deposition. *Addit. Manuf.* **2022**, *50*, 102582. [CrossRef]
14. Kim, H.; Kim, J.G.; Park, J.W.; Chu, C.N. Selective Copper Metallization of Nonconductive Materials Using Jet-Circulating Electrodeposition. *Precis. Eng.* **2018**, *51*, 153–159. [CrossRef]
15. Volgin, V.M.; Kabanova, T.B.; Davydov, A.D. Modeling of Local Maskless Electrochemical Deposition of Metal Microcolumns. *Chem. Eng. Sci.* **2018**, *183*, 123–135. [CrossRef]
16. Li, X.; Ming, P.; Zhang, X.; Wang, W.; Zhang, Y.; Qin, G.; Zheng, X.; Niu, S. Compressed Air-Film Encircling Jet Electrodeposition with High Deposition Accuracy. *J. Electrochem. Soc.* **2020**, *167*, 102502. [CrossRef]
17. Li, S.; Ming, P.; Zhang, J.; Zhang, Y.; Yan, L. Concurrently Fabricating Precision Meso- and Microscale Cross-Scale Arrayed Metal Features and Components by Using Wire-Anode Scanning Electroforming Technique. *Micromachines* **2023**, *14*, 979. [CrossRef] [PubMed]
18. Becker, E.W.; Ehrfeld, W.; Hagmann, P.; Maner, A.; Münchmeyer, D. Fabrication of Microstructures with High Aspect Ratios and Great Structural Heights by Synchrotron Radiation Lithography, Galvanoforming, and Plastic Moulding (LIGA Process). *Microelectron. Eng.* **1986**, *4*, 35–56. [CrossRef]
19. Weng, C.; Zhou, M.; Jiang, B.; Lv, H. Improvement on Replication Quality of Electroformed Nickel Mold Inserts with Micro/Nano-Structures. *Int. Commun. Heat Mass Transf.* **2016**, *75*, 92–99. [CrossRef]
20. Zhang, H.; Zhang, N.; Fang, F. Study of Ion Transportation and Electrodeposition under Hybrid Agitation for Electroforming of Variable Aspect Ratios Micro Structures. *Precis. Eng.* **2021**, *72*, 122–143. [CrossRef]
21. Zhang, H.; Zhang, N.; Fang, F. Investigation of Mass Transfer inside Micro Structures and Its Effect on Replication Accuracy in Precision Micro Electroforming. *Int. J. Mach. Tools Manuf.* **2021**, *165*, 103717. [CrossRef]
22. Du, L.; Yuan, B.; Guo, B.; Wang, S.; Cai, X. Fabrication of High-Aspect-Ratio Stepped Cu Microcolumn Array Using UV-LIGA Technology. *Microsyst. Technol.* **2023**, *29*, 999–1014. [CrossRef]
23. Miao, Z.-W.; Liu, Z.; Hao, Z.-C.; Zeng, Y.; Zhu, D.; Zhao, J.-H.; Ding, C.-Y.; Cheng, L.; Zhao, L.; Hong, W. A 1.0-THz High-Gain Metal-Only Transmit-Array Antenna Based on High-Precision UV-LIGA Microfabrication Technology. *IEEE Trans. Terahertz Sci. Technol.* **2024**, *14*, 269–282. [CrossRef]
24. Chung, C.K.; Syu, Y.J.; Wang, H.Y.; Cheng, C.C.; Lin, S.L.; Tu, K.Z. Fabrication of Flexible Light Guide Plate Using CO_2 Laser LIGA-like Technology. *Microsyst. Technol.* **2013**, *19*, 439–443. [CrossRef]
25. Rasmussen, K.H.; Keller, S.S.; Jensen, F.; Jorgensen, A.M.; Hansen, O. SU-8 Etching in Inductively Coupled Oxygen Plasma. *Microelectron. Eng.* **2013**, *112*, 35–40. [CrossRef]
26. Zhu, D.; Zeng, Y.B. Micro Electroforming of High-Aspect-Ratio Metallic Microstructures by Using a Movable Mask. *CIRP Ann.* **2008**, *57*, 227–230. [CrossRef]
27. Yang, G.; Deng, D.; Zhang, Y.; Zhu, Q.; Cai, J. Numerical Optimization of Electrodeposition Thickness Uniformity with Respect to the Layout of Anode and Cathode. *Electrocatalysis* **2021**, *12*, 478–488. [CrossRef]
28. Zhang, H.; Zhang, N.; Fang, F. Study on Controllable Thickness and Flatness of Wafer-Scale Nickel Shim in Precision Electroforming Process: Simulation and Validation. *J. Manuf. Sci. Eng.* **2021**, *143*, 111005. [CrossRef]

29. Yao, Y.; Rodriguez, J.; Cui, J.; Lennon, A.; Wenham, S. Uniform Plating of Thin Nickel Layers for Silicon Solar Cells. *Energy Procedia* **2013**, *38*, 807–815. [CrossRef]
30. Flott, L.W. The Challenge of Thickness Variation in Plating and Anodizing. *Met. Finish.* **2012**, *110*, 33–35. [CrossRef]
31. Li, B.; Mei, T.; Chu, H.; Wang, J.; Du, S.; Miao, Y.; Zhang, W. Ultrasonic-Assisted Electrodeposition of Ni/Diamond Composite Coatings and Its Structure and Electrochemical Properties. *Ultrason. Eonothem.* **2021**, *73*, 105475. [CrossRef]
32. Foias, C.; Temam, R. Gevrey Class Regularity for the Solutions of the Navier-Stokes Equations. *J. Funct. Anal.* **1989**, *87*, 359–369. [CrossRef]
33. Grande, W.C.; Talbot, J.B. Electrodeposition of Thin Films of Nickel-Iron: II. Modeling. *J. Electrochem. Soc.* **1993**, *140*, 675. [CrossRef]
34. Wang, H.; Xie, J.; Fan, T.; Sun, D.; Li, C. Improving the Thickness Uniformity of Micro Gear by Multi-Step, Self-Aligned Lithography and Electroforming. *Micromachines* **2023**, *14*, 775. [CrossRef] [PubMed]
35. Xiao, Y.; Ming, P.; Zhang, X.; Hou, Y.; Du, L.; Li, S.; Zhang, Y.; Song, J. Ultrahigh Strength Ultrapure Nanostructured Nickel Metal Prepared via Ultrafine Anode Scanning Electrodeposition. *Mater. Des.* **2022**, *213*, 110339. [CrossRef]

micromachines

MDPI

Article

A Scalable Digital Light Processing 3D Printing Method

Junjie Huang [1,*], Jiangkun Cai [1], Chenhao Huangfu [1], Shikai Li [1], Guoqiang Chen [1], Hao Yun [1] and Junfeng Xiao [2,3]

[1] School of Mechanical and Power Engineering, Henan Polytechnic University, Jiaozuo 454003, China
[2] Shenzhen Institute for Advanced Study, University of Electronic Science and Technology of China, Shenzhen 518000, China
[3] ShenSi Shape (Shenzhen) Technology Co., Ltd., Shenzhen 518000, China
* Correspondence: anny@hpu.edu.cn

Abstract: The 3D printing method based on digital light processing (DLP) technology can transform liquid resin materials into complex 3D models. However, due to the limitations of digital micromirror device (DMD) specifications, the normal DLP 3D printing method (NDPM) cannot simultaneously process large-size and small-feature parts. Therefore, a scalable DLP 3D printing method (SDPM) was proposed. Different printing resolutions for a part were designed by changing the distance between the projector and the molding liquid level. A scalable DLP printer was built to realize the printing resolution requirements at different sizes. A series of experiments were performed. Firstly, the orthogonal experimental method was used, and the minimum and maximum projection distances were obtained as 20.5 cm and 30.5 cm, respectively. Accordingly, the layer thickness, exposure time, and waiting leveling time were 0.08 mm, 3 s, and 6 s and 0.08 mm, 7 s, and 10 s. Secondly, single-layer column feature printing was finished, which was shown to have two minimum printing resolutions of 101 μm and 157 μm at a projection distance of 20.5 cm and 30.5 cm. Thirdly, a shape accuracy test was conducted by using the SDPM. Compared with the NDPM, the shape accuracy of the small-feature round, diamond, and square parts was improved by 49%, 42%, and 2%, respectively. This study verified that the SDPM can build models with features demonstrating high local shape accuracy.

Keywords: 3D printing resolution; 3D printer; digital light processing; scalable printing; shape accuracy

1. Introduction

Three-dimensional printing, also known as the additive manufacturing technology, differs from traditional processing methods, performing solid manufacturing by stacking materials layer by layer. Various 3D printing techniques, such as fused deposition modeling [1,2], direct ink writing [3,4], selective laser melting [5,6], and stereolithography [7,8], have been widely used in the automotive [9], aerospace [10,11], bioprinting [12], and construction [13] fields, among others. Stereolithography is the typical 3D printing technique that allows complex parts to be manufactured directly from liquid photosensitive resins. Digital light processing (DLP) based on 3D printing technology is a type of stereolithography. The DLP 3D printing method selectively cures liquid resin layer by layer based on the pattern projected onto the photosensitive resin surface, which is different from other types of 3D printing methods of stereolithography that use dots or lines to form a two-dimensional layer. Therefore, DLP 3D printing technology usually possesses high efficiency in processing large-volume and complex 3D model structures [14], and it has the advantages of rapid speed, high resolution, and good surface quality [15]. Currently, DLP 3D printing technology is widely used in microfluidics [16,17], metamaterials [18], biomedicine [19], and 4D printing [20].

Despite the above-mentioned advantages, however, DLP printing also suffers from some limitations concerning accuracy and size. Figure 1 illustrates the basic principle of the DLP 3D printing method. The DMD chip, which consists of millions of micromirrors, is

the key component for the DLP projection system. Each micromirror can be independently controlled to rotate. The digital micromirrors on the DMD chip selectively reflect incident UV light to form a projection pattern and cure resin layer by layer so that the model can be manufactured. In the projection system, the number of micromirrors of the DMD chip determines the resolution of the projection pattern, and the size of the projection format depends on the lens specifications. In addition, each micromirror represents a pixel, so increasing the print format will lead to low accuracy. Therefore, it is worth investigating how to balance size and accuracy requirements in the DLP 3D printing process.

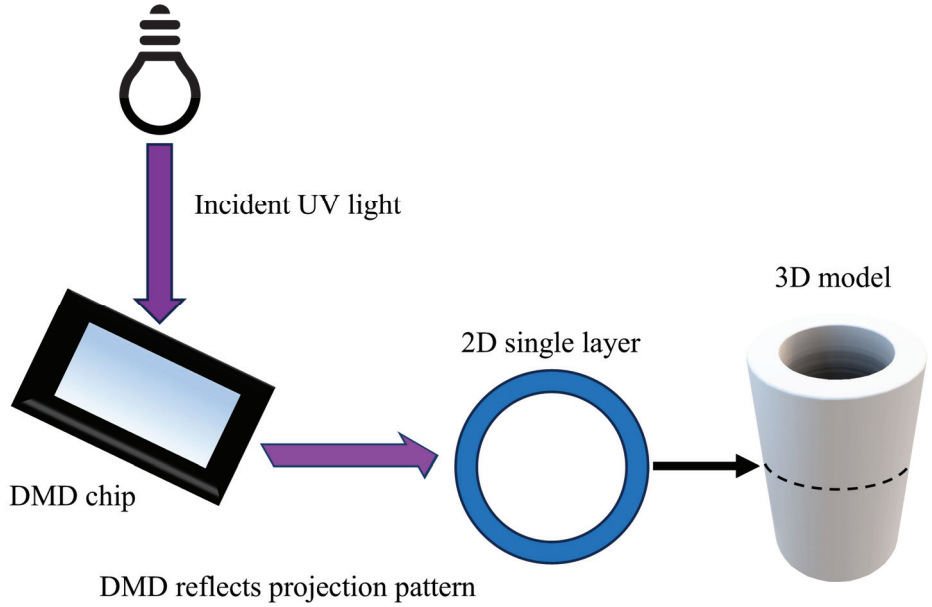

Figure 1. DLP 3D printing process.

Research on the printing size and accuracy of DLP 3D printing can be divided into two main types. One approach is to improve the accuracy but maintain the size. Specifically, Zhou et al. [21] proposed a subpixel shifting method, which improved the printing accuracy and resolution without sacrificing efficiency; Montgomery et al. [22] developed a pixel-level grayscale control method to create circular features from sharp pixels by using pixel-level grayscale control beyond the typical resolution of a given projector; and Zhou et al. [23] introduced a hybrid exposure concept. This consists of vector scanning and mask image projection subsystems, where the vector scanning system forms the boundary, and the mask projection system forms the inside area. The second approach is to maintain molding accuracy and expand molding size. He et al. [24] implemented a dynamic projection scanning method for large-part printing. This creates large parts with high resolution by moving the projector so that the projection image can be dynamically and continuously exposed on the resin surface. Xu et al. [25] presented a method that continuously moves the projector via rotation with a galvo mirror. This process is able to build 3D macroscale objects with microscale features. Wu et al. [26] designed a multi-projector DLP 3D printing scheme with energy homogenization. This effectively expands the printing size, but the scheme with multiple projectors increases the development costs. Yi et al. [27] first applied a Delta 3-DoF parallel mechanism to DLP 3D printing, where the forming platform with a parallel mechanism can be moved horizontally to print large models. However, due to the limitations of the mechanical structure, its motion control is complicated. Furthermore, there have been other attempts to solve the conflict between molding size and accuracy. Wang et al. [28] mounted a set of optical lenses at the front of the projector and made changes to the dimensions of the projection pattern by moving the convex lens to achieve different printing sizes and resolutions. Moreover, Wang et al. [29] printed the large-size objects and high-accuracy features by using double projectors with the exact resolution.

In the actual DLP 3D printing, it is not necessary for all the features within a given model to attain the same degree of accuracy. In light of this, a scalable DLP 3D printing method (SDPM) is proposed. In this study, a self-designed scalable printer is employed. The fabrication of the large-size part is initiated, followed by the movement of the projector to adjust the projection distance, thus enabling the fabrication of the small-feature part. The print format and the print pixel size of the different parts in one model are varied, thus realizing the requirements of printing accuracy under different molding sizes.

2. System and Methods

2.1. Printing Principle

Figure 2 illustrates the molding principle of the SDPM when the large-size and the small-feature parts are printed. Each grid in the molding format represents a projection pixel. It can be seen from Figure 2 that the difference between the dimensions of large-size and small-feature molding formats is obvious, even if the number of pixels is the same. The red triangle pattern exhibits identical molding sizes in both printing formats. However, the small-feature printing format exhibits a higher pixel density and a better fit to the actual model. The projector, as the core device of the DLP 3D printing system, determines the size of the molding format and molding pixel, which is defined by the projection ratio:

$$T = D/W \tag{1}$$

where T is the projection ratio, D is the projection distance, and W is the width of the molding format on the liquid resin surface. The smaller the D, the smaller the W, and the smaller the pixel size obtained, which results in the higher accuracy of the projection pattern. For a model with a large overall dimension and several small features distributed over it, the projection distance can increase to obtain a larger molding format for printing the large-size part. Subsequently, the projector moves to reduce the projection distance to obtain a smaller size of molding pixels for small-feature printing. The parameters of the DLP projector selected for this paper are listed in Table 1.

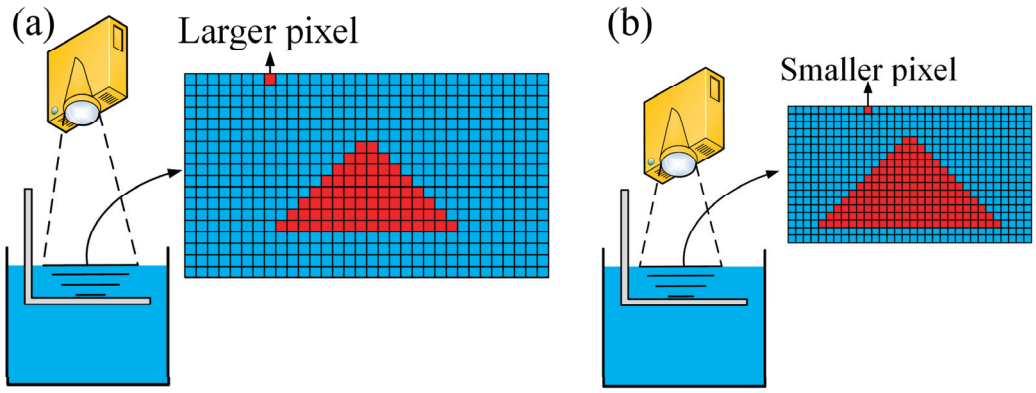

Figure 2. Schematic diagram of scalable DLP molding: (**a**) large-size printing; (**b**) small-feature printing.

Table 1. Projector parameters.

DMD Model	Wavelength of Light Source	Resolution	Aspect Ratio	Projection Ratio	Contrast
DLP 3010	405 nm	1280 × 720	16:9	1.66	1000:1

According to the structural characteristic of the model, the projector is moved to change the projection distance so that it can be flexibly adapted to the printing size and accuracy requirements for a model.

2.2. Printing Device and Procedure

To realize the SDPM, a self-developed scalable DLP printer is used [30], as shown in Figure 3. The printing device consists of a frame, a parallel mechanism, three linear motion modules, a projection module (projector with 405 nm light source), a resin tank, and a molding platform. The parallel mechanism consists of three branch chains (PRRR), each of which contains one prismatic pair (P) and three rotating pairs (R). One end of the branch chain is connected to a linear motion module, and the other end is connected to the projection module. The three linear motion modules are arranged along the X/Y/Z axial direction, and they are orthogonally set on the frame. The projector is mounted inside the projection module and uses a top-down approach to expose images. The resin tank is placed below the projection module, and the linear motion module drives the molding platform individually.

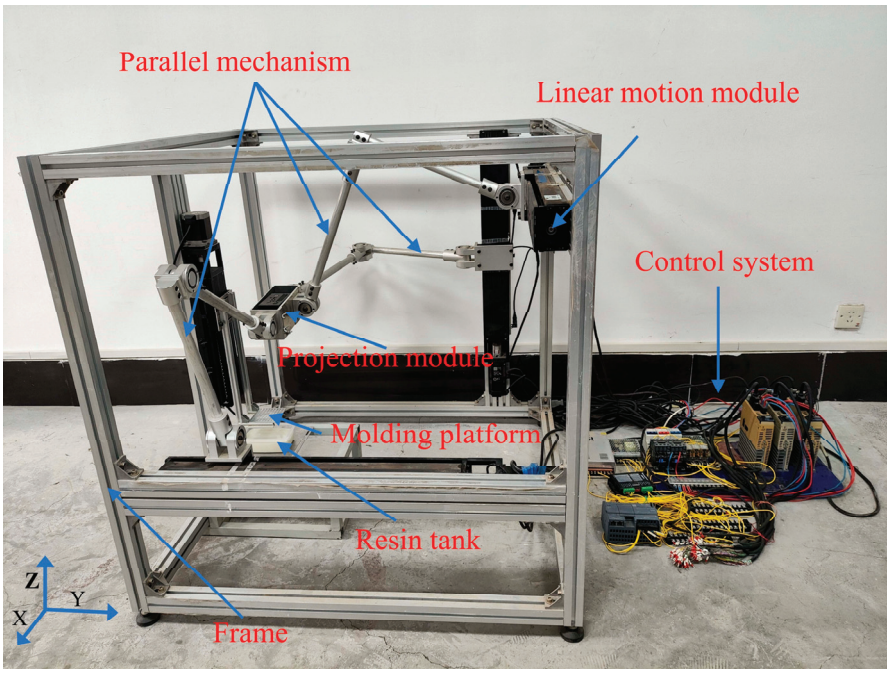

Figure 3. Scalable DLP printer.

During the printing process, the parallel mechanism drives the projection module to transform position in 3D space, so that the projection distance can be adjusted by the movement of the projection module.

For the model with the large-size part and the small features, different accuracy is required for completion. Accordingly, the SDPM printing procedure is as follows: first, the 3D model is divided into a large-size part and several small-feature parts according to the characteristic of the model, and the projection images are generated; second, the projector is moved to the origin position to fabricate the large-size part. Then, the parallel mechanism moves the projection module, which makes the projector shift to the corresponding position of small features. Finally, the small features are built. The specific printing procedure is illustrated in Figure 4.

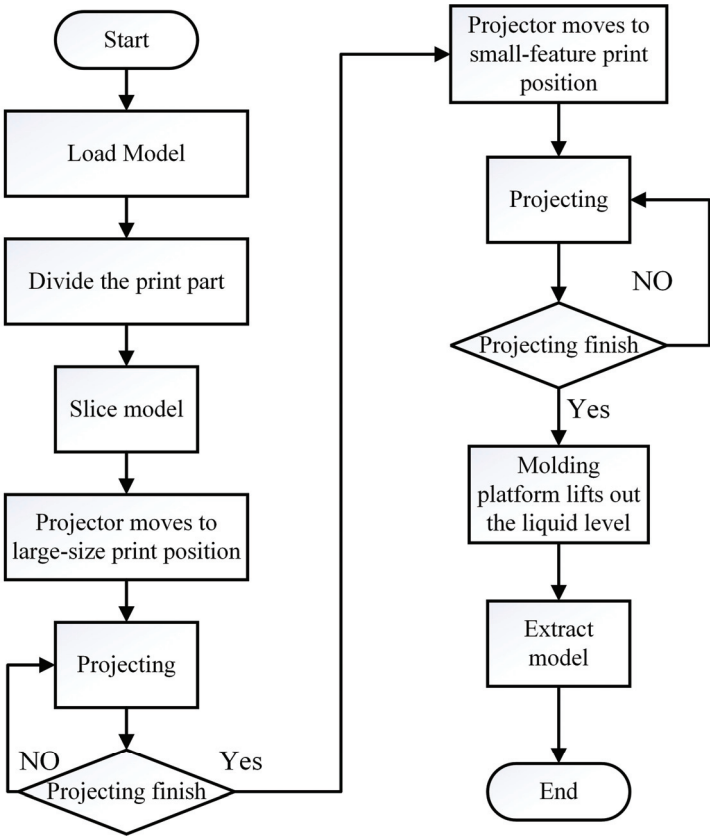

Figure 4. Printing procedure.

3. Experiments and Discussion

In this section, three groups of tests, including the determination of printing parameters, printing resolution, and shape accuracy, are designed and conducted to evaluate the scalable DLP 3D printer, and then the scalable printing is performed. To ensure the flatness of the liquid surface for each printed layer, the distance that the molding platform moves down must be greater than the thickness of each layer at a time, followed by lifting and waiting for the resin to level out. This approach allows the resin to cover the molding platform quickly and avoids uneven resin coverage due to thin layer thickness. The properties of the photosensitive resin used are shown in Table 2. The resin viscosity is low and the liquid flow rate is fast, which is conducive to the stability of the liquid reflux. In addition, the cleaning method is water washing, which is easy to operate.

Table 2. Material properties of photosensitive resin.

Supplier	Viscosity	Density	Wavelength Ranges	Color
Anycubic	150–250 mPa.s	1.15–1.2 g/cm^3	365–405 nm	White

3.1. Determination of Printing Parameters

In the scalable printer, the printing effect and capability depend on the layer thickness, exposure time, and waiting leveling time. An orthogonal experimental method is used for the above printing parameters. The three factors set for the test are the layer thickness (A), exposure time (B), and waiting leveling time (C). The minimum projection distance of the projector is set as 20.5 cm. The orthogonal test is conducted on the printing parameters at a projection distance of 20.5 cm, and three levels are considered for each factor. The values of each factor are initially selected as shown in Table 3.

Table 3. Factors level data.

Level	Factors		
	A (mm)	**B (s)**	**C (s)**
1	0.08	2.5	6
2	0.1	3	8
3	0.12	3.5	10

Nine sets of tests are presented using the $L_9(3^4)$ orthogonal table. The test sample is a rectangular block of 15 mm (X) × 20 mm (Y) × 3 mm (Z). A vernier caliper (Harbin Measuring & Cutting Tool Group CO., LTD, Harbin, China) is used to measure the dimensions of the printed samples in the X, Y, and Z directions, and five measurements are taken for each sample to obtain the average value. Using the relative size error (RSE) to represent the dimensional accuracy of the test sample,

$$RSE = |A0 - A1| / A1 \times 100\%, \quad (2)$$

where $A0$ is the measured value and $A1$ is the theoretical value. The *RSE* of each direction is denoted by ΔX, ΔY, and ΔZ, respectively. The results of nine sets of orthogonal tests are shown in Table 4.

Table 4. Orthogonal test results.

Number	A (mm)	B (s)	C (s)	ΔX (%)	ΔY (%)	ΔZ (%)
1	0.08	2.5	6	1.21	1.35	2.13
2	0.08	3	8	0.91	1.87	1.72
3	0.08	3.5	10	1.78	2.16	2.38
4	0.1	2.5	8	2.03	1.58	2.93
5	0.1	3	10	1.56	1.62	2.66
6	0.1	3.5	6	2.15	2.87	3.01
7	0.12	2.5	10	1.83	2.43	3.62
8	0.12	3	6	1.22	1.52	2.71
9	0.12	3.5	8	2.37	2.44	3.47

The measured data demonstrate that the sample has the most extensive *RSE* range in the Z direction (1.9%), so the *RSE* of the Z direction is selected as the representation for dimensional accuracy. The range analysis results are given in Table 5.

Table 5. Range analysis of RSE in Z direction (%).

Data [1]	A	B	C
K_1	2.08	2.89	2.62
K_2	2.87	2.36	2.71
K_3	3.27	2.95	2.89
R	1.19	0.59	0.27

[1] K_i (i = 1, 2, 3) is the mean at level i.

The parameter with the higher range R has a more significant influence on dimensional accuracy. Analyzed from the range results, the three parameters affecting the printing effect are A > B > C. They are in the order of layer thickness, exposure time, and waiting leveling time. The smaller the value of K, the smaller the RSE, and the optimal combination is $A_1B_2C_1$. Therefore, the printing parameters are a layer thickness of 0.08 mm, exposure time of 3 s, and waiting leveling time of 6 s. Considering that the printing parameters will change with the projection distance, orthogonal tests were carried out at intervals of 2.5 cm to determine the printing parameters and to measure the dimensional accuracy of the samples, as shown in Figure 5.

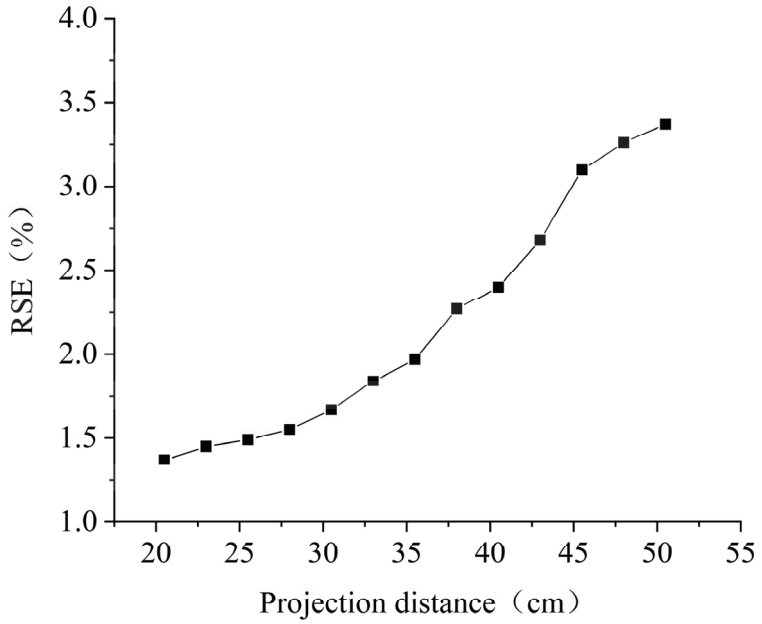

Figure 5. Plot of dimensional accuracy versus projection distance.

As can be seen from Figure 5, the RSE of the printed model is not linearly related to the projection distance. As the projection distance increases, the RSE of the printed model will also increase, and the rate of increase will be accelerated. This is because the light intensity and uniformity are reduced as the molding format width increases in the constant light power. Enlarging the printing size by continuously increasing the projection distance is impossible. The increase in RSE is 0.3%, 0.73%, and 0.97% for the projection distance range of 20.5–30.5 cm, 30.5–40.5 cm, and 40.5–50.5 cm, respectively. In order to ensure the printing accuracy of the model as much as possible, the projection distance is set to vary within 20.5–30.5 cm, 20.5 cm is set to be the small-feature printing distance, and 30.5 cm is set to be the large-size printing distance. The parameters under a large-size printing distance are a layer thickness of 0.08 mm, exposure time of 7 s, and waiting leveling time of 10 s. The molding format sizes and pixel widths at the two distances are shown in Table 6.

Table 6. Molding formats of large-size and small-feature printing distances.

Projection Distance	Molding Format	Molding Pixel Width
30.5 cm	18.37 cm × 10.34 cm	143.5 μm
20.5 cm	12.35 cm × 6.95 cm	96.5 μm

3.2. Printing Resolution Test

The single-layer printing resolution of the scalable printer determines the minimum feature size that the SDPM can achieve, which affects the printing accuracy of the model. A single-layer printing resolution test is designed to make the smallest features. The several pixels are arranged to form the column pattern as the projection image, as shown in Figure 6, and the distance between these columns is 7 pixels.

The projection image is transferred from the computer to the projector for printing, and ten layers are first printed as the base layer. Then, the single-layer columns of the pixels are exposed and cured at the large-size projection distance of 30.5 cm and the small-feature projection distance of 20.5 cm. An industrial microscope BC3630 (Bocheng Electronics, Dongguan, China) was used to observe and measure the size of the cured structure, as shown in Figure 7.

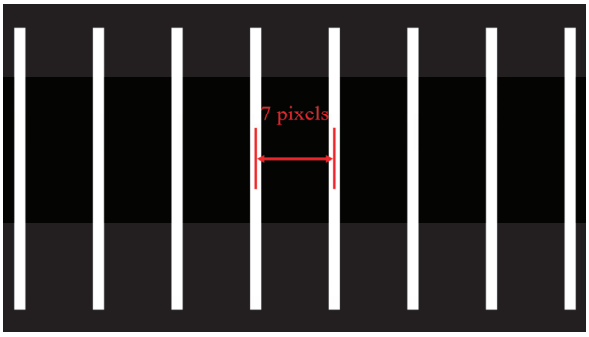

Figure 6. Column pixels pattern.

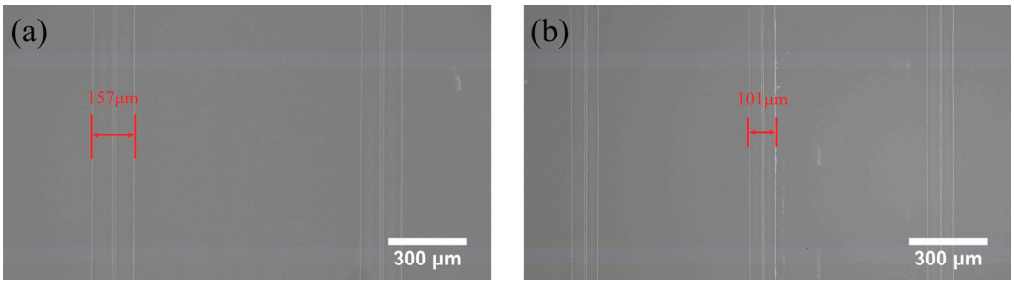

Figure 7. Minimum feature size: (**a**) 30.5 cm projection distance; (**b**) 20.5 cm projection distance.

The results in Figure 7 show that the average width of the pixel at large-size and small-feature projection distances is 157 μm and 101 μm, representing the highest printing resolution. It can also be seen that the column pixel feature sizes of both large-size and small-feature printing distances are larger than their theoretical projection pixel sizes, with errors of 13.5 μm and 4.5 μm, respectively. The reason is that the photosensitive resin outside the boundary of the projection column pixel can be cured because of the light diffraction and chemical diffusion of DLP light, resulting in lower resolution. Thus, the minimum feature size of the actual printed column pixel is slightly larger than the theoretical one.

3.3. Shape Accuracy

The scalable printing method allows for fabricating features with higher shape accuracy because it has small-size pixels to fit the feature shape better. The models (a), (b), and (c) in Figure 8 are designed for the shape accuracy test. The three models are called double-round, double-diamond, and double-square. Each model consists of the external large-size and the central small-feature part. The large-size part is at the bottom of the model. The small-feature part is convex and located in the geometric center. The printing sizes are 5 mm for all small-feature parts and 90 mm for all large-size parts. The shapes of the small-feature parts are round, diamond, and square, characterized by circular arcs, bevels, and straight-line edges, respectively. The three edges are the essential elements that make up a variety of graphics. The effect of pixel size on the shape accuracy is representative.

The 2D digital patterns with the white cured area in the BMP format (Figure 9a–f) are the projection images of small-feature parts. As can be seen from the projection images, the projection images of square features for NDPM (seen in Figure 9c) and SDPM (seen in Figure 9f) have the same shape accuracy. However, the projection images of round and diamond features for NDPM (see Figure 9a,b) have a lower shape accuracy than those for SDPM (see Figure 9d,e). This is because the projection images of small-feature round and diamonds have circular arcs and bevels, respectively. Due to the square shape of the DMD micromirror, the shape of the square patterns can be fitted by pixel perfectly with big or small sizes. However, square pixels cannot entirely match the round and diamond patterns. Moreover, the accuracy will decrease with the increase in the pixel size.

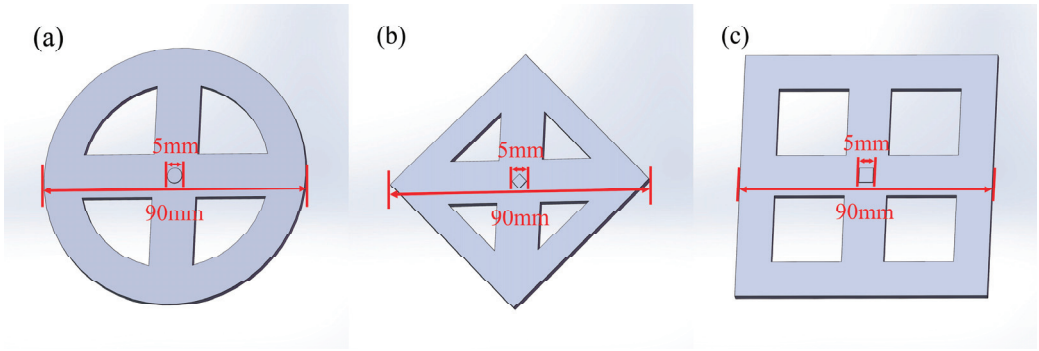

Figure 8. Shape accuracy test models: (**a**) double-round model; (**b**) double-diamond model; (**c**) double-square model.

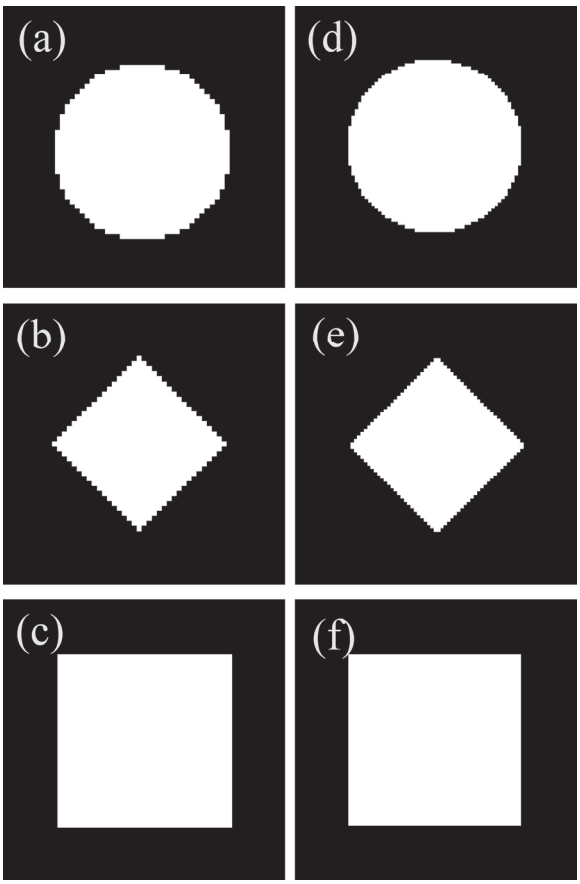

Figure 9. Projection images of small-feature parts: (**a**–**c**) projection images of small-feature parts for NDPM; (**d**–**f**) projection images of small-feature parts for SDPM.

When printing using the SDPM, the scalable printer prints the large-size part first at a projection distance of 30.5 cm, followed by the small-feature part at 20.5 cm. Compared with the SDPM, both the large-size part and the small-feature part were printed at a projection distance of 30.5 cm when using the NDPM. The layer thickness is set to 0.08 mm, with 30 layers for large-size parts and 10 for small-feature parts. Each model is printed five times under NDPM and SDPM, respectively. Then, the small-feature parts are magnified and photographed by an industrial microscope BC3630 (Bocheng Electronics, Dongguan, China), as shown in Figure 10. Using the industrial microscope software's (S-EYE_Setup-1.4.3.479-YW) circular and straight-line measurement tools, we can extract the circular and straight-line boundaries of the small-feature parts from Figure 10 and measure the shape accuracies. The measured results are shown in Table 7.

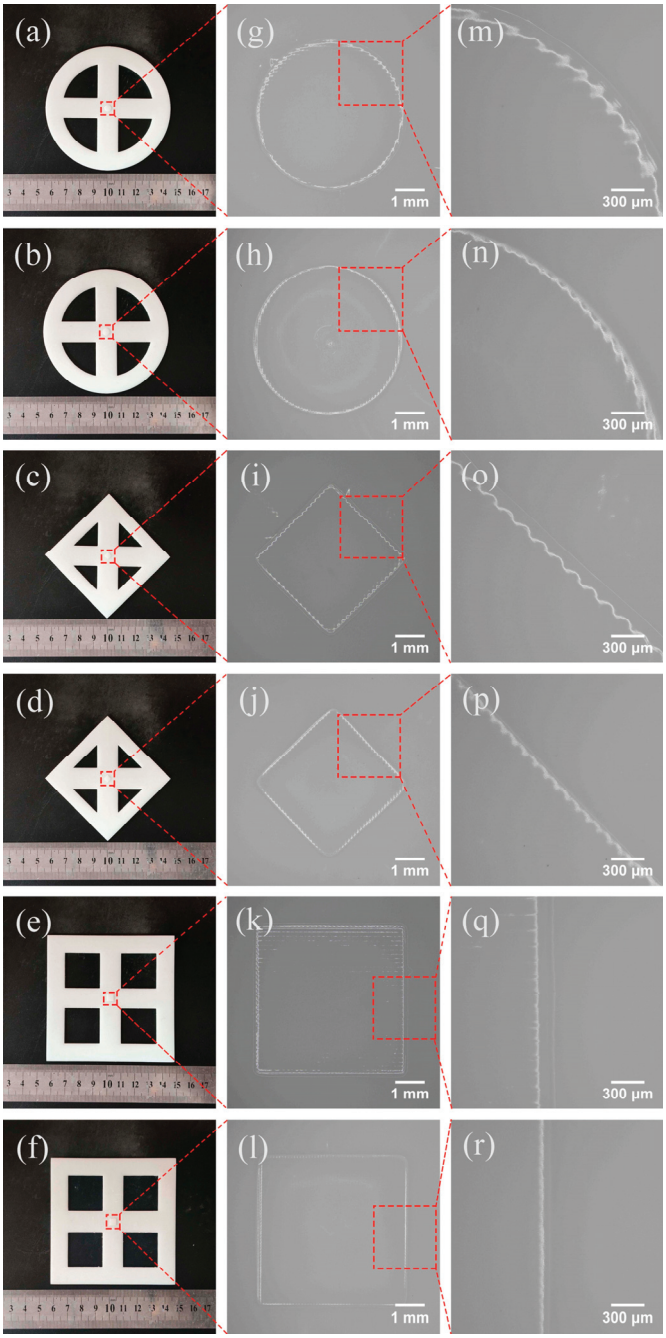

Figure 10. Shape accuracy test: (**a**,**c**,**e**) printed models of NDPM; (**b**,**d**,**f**) printed models of SDPM; (**g**–**l**) microscope shots of small-feature parts; (**m**–**r**) local edges of small-feature parts.

Table 7. Shape accuracy data.

Shape	Accuracy	Method	Number of Tests				
			1	2	3	4	5
Round	Roundness (μm)	NDPM	85	77	86	88	79
		SDPM	43	46	45	38	38
Diamond	Straightness (μm)	NDPM	67	71	65	69	72
		SDPM	39	41	35	38	45
Square	Straightness (μm)	NDPM	23	18	16	19	16
		SDPM	21	14	18	17	20

Figure 10 shows the models built using both NDPM and SDPM. The models show that obvious jagged edges occurred on both the round and diamond. This is attributed to the fact that the projection image consists of a series of discrete pixels, and each of the pixels is derived by a separate DMD micromirror. The DMD micromirror is square, and the projection image does not fit the original pattern perfectly, which causes the distortion of the image information and jagged edges. The jagged edges are reflected in the actual printed models. The edges of the models are not smooth. In addition, the edges of the small-feature parts are not strictly jagged, and the degree of jaggedness is softer than that of the theoretical edges. The reason is that the light intensity of each DMD pixel is not uniform, and its energy obeys a Gaussian distribution, where the light energy is attenuated from the center of the pixel to the edges. Therefore, the actual printed edge shape is unable to match the theoretical edge shape.

The accuracy measuring results show that the average roundness of the round decreases from 83 μm to 42 μm and the average straightness of the diamond reduced from 68.8 μm to 39.6 μm in NDPM and SDPM. Regarding the shape accuracy of the square, the average straightness of NDPM is 18.4 μm, which is close to that of SDPM (18 μm). The improvement of shape accuracy in the square feature is 2%, much smaller than that of round and diamond samples (49%, 42%). This is because the projection images of the square features for both NDPM and SDPM have the same shape accuracy, and the shape accuracies of the projection images of the round and diamond features for SDPM are higher than those for NDPM. The 2% change in shape accuracy in squares originated from measurement error. The above proves that SDPM can build the models with a high local shape accuracy of the parts.

4. Conclusions

In this work, the scalable DLP printing method was developed to realize the printing of parts with a global large size and local small features. Moreover, the feature has a high accuracy. In the equipment, the range of the effective projection distance was determined at 20.5–30.5 cm through orthogonal tests. Accordingly, the printing formats are 12.35 cm × 6.95 cm and 18.37 cm × 10.34 cm. The smallest pixel feature was printed under the formats, and two types of molding resolutions, 101 μm and 157 μm, were realized on this basis. The shape accuracy contrast test was carried out on the printer, and the samples for NDPM and SDPM were fabricated. The shape accuracy of the small-feature parts was significantly improved. In particular, the average roundness decreased by 49%, and the average straightness of the diamonds declined by 42%.

The building size is influenced by the dimensions of the three linear modules in the mechanical structure and the hardware performance of the projector. In the present work, the length of the three linear modules is 60 cm, and the projection distance is 52 cm. In addition, the short-focus lens can be used to enlarge the building size. The printing accuracy can be enhanced by the error compensation of the mechanism or by using a high-resolution DMD chip.

Author Contributions: Conceptualization, J.H., J.X. and G.C.; methodology, J.H. and J.C.; software (S-EYE_Setup-1.4.3.479-YW), J.C. and S.L.; validation, J.H. and J.C.; investigation, C.H. and J.C.; resources, J.H.; data curation, J.C. and H.Y.; writing—original draft preparation, J.C.; writing—review and editing, J.H., J.X., J.C. and G.C.; visualization, C.H., S.L. and H.Y.; supervision, J.H.; project administration, J.H.; funding acquisition, J.H. All authors have read and agreed to the published version of the manuscript.

Funding: This research was funded by the Key Research and Development & Transformation Project of Qinghai Province, Grant No. 2024-QY-211, Henan Province Scientific and Technological Research Plan, Grant No. 242102221050, Fundamental Research Funds for the Universities of Henan Province, Grant No. NSFRF210339, and Key Discipline of Mechanical Engineering in Henan Polytechnic University and the University Doctoral Fund, Grant No. B2016-24.

Data Availability Statement: The original contributions presented in this study are included in the article.

Conflicts of Interest: Junfeng Xiao is affiliated with ShenSi Shape (Shenzhen) Technology Co., Ltd. The remaining authors declare no conflict of interest.

References

1. Salentijn, G.I.J.; Oomen, P.E.; Grajewski, M.; Verpoorte, E. Fused Deposition Modeling 3D Printing for (Bio)analytical Device Fabrication: Procedures, Materials, and Applications. *Anal. Chem.* **2017**, *89*, 7053–7061. [CrossRef] [PubMed]
2. Zaki, R.M.; Strutynski, C.; Kaser, S.; Bernard, D.; Hauss, G.; Faessel, M.; Sabatier, J.; Canioni, L.; Messaddeq, Y.; Danto, S.; et al. Direct 3D-printing of phosphate glass by fused deposition modeling. *Mater. Des.* **2020**, *194*, 108957. [CrossRef]
3. Chu, T.Y.; Zhang, Z.Y.; Dadvand, A.; Py, C.; Lang, S.; Tao, Y. Direct writing of inkjet-printed short channel organic thin film transistors. *Org. Electron.* **2017**, *51*, 485–489. [CrossRef]
4. Saadi, M.; Maguire, A.; Pottackal, N.T.; Thakur, M.S.H.; Ikram, M.M.; Hart, A.J.; Ajayan, P.M.; Rahman, M.M. Direct Ink Writing: A 3D Printing Technology for Diverse Materials. *Adv. Mater.* **2022**, *34*, 57. [CrossRef] [PubMed]
5. Mizuta, K.; Hijikata, Y.; Fujii, T.; Gokan, K.; Kakehi, K. Characterization of Ti-48Al-2Cr-2Nb built by selective laser melting. *Scr. Mater.* **2021**, *203*, 114107. [CrossRef]
6. Zhou, T.; Huang, W.; Chen, C.Y. A Real-Time Monitoring Method for Selective Laser Melting of TA1 Materials Based on Radiation Detection of a Molten Pool. *Micromachines* **2024**, *15*, 570. [CrossRef]
7. Khatri, B.; Frey, M.; Raouf-Fahmy, A.; Scharla, M.V.; Hanemann, T. Development of a Multi-Material Stereolithography 3D Printing Device. *Micromachines* **2020**, *11*, 532. [CrossRef]
8. Huang, J.G.; Qin, Q.; Wang, J. A Review of Stereolithography: Processes and Systems. *Processes* **2020**, *8*, 1138. [CrossRef]
9. Giubilini, A.; Minetola, P. Multimaterial 3D printing of auxetic jounce bumpers for automotive suspensions. *Rapid Prototyp. J.* **2023**, *29*, 131–142. [CrossRef]
10. Acanfora, V.; Sellitto, A.; Russo, A.; Zarrelli, M.; Riccio, A. Experimental investigation on 3D printed lightweight sandwich structures for energy absorption aerospace applications. *Aerosp. Sci. Technol.* **2023**, *137*, 108276. [CrossRef]
11. Zhu, W.J.; Zhang, X.Y.; Li, D.C. Flexible all-plastic aircraft models built by additive manufacturing for transonic wind tunnel tests. *Aerosp. Sci. Technol.* **2019**, *84*, 237–244. [CrossRef]
12. Sun, J.R.; Gong, Y.P.; Xu, M.L.; Chen, H.P.; Shao, H.F.; Zhou, R.G. Coaxial 3D Bioprinting Process Research and Performance Tests on Vascular Scaffolds. *Micromachines* **2024**, *15*, 463. [CrossRef] [PubMed]
13. Hassan, H.; Rodriguez-Ubinas, E.; Al Tamimi, A.; Trepci, E.; Mansouri, A.; Almehairbi, K. Towards innovative and sustainable buildings: A comprehensive review of 3D printing in construction. *Autom. Constr.* **2024**, *163*, 105417. [CrossRef]
14. Kowsari, K.; Akbari, S.; Wang, D.; Fang, N.X.; Ge, Q. High-Efficiency High-Resolution Multimaterial Fabrication for Digital Light Processing-Based Three-Dimensional Printing. *3D Print. Addit. Manuf.* **2018**, *5*, 185–193. [CrossRef]
15. Wang, X.H.; Liu, J.H.; Zhang, Y.; Kristiansen, P.M.; Islam, A.; Gilchrist, M.; Zhang, N. Advances in precision microfabrication through digital light processing: System development, material and applications. *Virtual Phys. Prototyp.* **2023**, *18*, e2248101. [CrossRef]
16. Kang, J.W.; Jeon, J.; Lee, J.Y.; Jeon, J.H.; Hong, J.W. Surface-Wetting Characteristics of DLP-Based 3D Printing Outcomes under Various Printing Conditions for Microfluidic Device Fabrication. *Micromachines* **2024**, *15*, 61. [CrossRef]
17. Luo, Z.M.; Zhang, H.Y.; Chen, R.Z.; Li, H.T.; Cheng, F.; Zhang, L.J.; Liu, J.; Kong, T.T.; Zhang, Y.; Wang, H.N. Digital light processing 3D printing for microfluidic chips with enhanced resolution via dosing- and zoning-controlled vat photopolymerization. *Microsyst. Nanoeng.* **2023**, *9*, 103. [CrossRef]
18. Zhou, R.; Wang, Y.S.; Liu, Z.Y.; Pang, Y.Q.; Chen, J.X.; Kong, J. Digital Light Processing 3D-Printed Ceramic Metamaterials for Electromagnetic Wave Absorption. *Nano-Micro Lett.* **2022**, *14*, 122. [CrossRef]
19. Song, P.; Li, M.X.; Zhang, B.Q.; Gui, X.Y.; Han, Y.L.; Wang, L.; Zhou, W.Z.; Guo, L.K.; Zhang, Z.Y.; Li, Z.Y.; et al. DLP fabricating of precision GelMA/HAp porous composite scaffold for bone tissue engineering application. *Compos. Pt. B Eng.* **2022**, *244*, 110163. [CrossRef]
20. Mainik, P.; Hsu, L.Y.; Zimmer, C.W.; Fauser, D.; Steeb, H.; Blasco, E. DLP 4D Printing of Multi-Responsive Bilayered Structures. *Adv. Mater. Technol.* **2023**, *8*, 8. [CrossRef]
21. Zhou, C.; Xu, H.; Chen, Y. Spatiotemporal Projection-Based Additive Manufacturing: A Data-Driven Image Planning Method for Subpixel Shifting in a Split Second. *Adv. Intell. Syst.* **2021**, *3*, 15. [CrossRef]
22. Montgomery, S.M.; Demoly, F.; Zhou, K.; Qi, H.J. Pixel-Level Grayscale Manipulation to Improve Accuracy in Digital Light Processing 3D Printing. *Adv. Funct. Mater.* **2023**, *33*, 11. [CrossRef]
23. Zhou, C.; Ye, H.; Zhang, F. A Novel Low-Cost Stereolithography Process Based on Vector Scanning and Mask Projection for High-Accuracy, High-Speed, High-Throughput, and Large-Area Fabrication. *J. Comput. Inf. Sci. Eng.* **2015**, *15*, 011003. [CrossRef]
24. He, R.; Landowne, J.; Currie, J.; Amoah, J.; Shi, W.T.; Yunus, D.; Liu, Y.L. Three-dimensional printing of large objects with high resolution by scanning lithography. *Int. J. Adv. Manuf. Technol.* **2019**, *105*, 4147–4157. [CrossRef]
25. Xu, Y.; Mao, H.C.; Liu, C.Y.; Du, Z.Y.; Yan, W.J.; Yang, Z.Y.; Partanen, J.; Chen, Y. Hopping Light Vat Photopolymerization for Multiscale Fabrication. *Small* **2023**, *19*, 13. [CrossRef] [PubMed]

26. Wu, L.F.; Zhao, L.D.; Jian, M.; Mao, Y.X.; Yu, M.; Guo, X.H. EHMP-DLP: Multi-projector DLP with energy homogenization for large-size 3D printing. *Rapid Prototyp. J.* **2018**, *24*, 1500–1510. [CrossRef]
27. Yi, R.; Wu, C.M.; Liu, Y.J.; He, Y.; Wang, C.C.L. Delta DLP 3-D Printing of Large Models. *IEEE Trans. Autom. Sci. Eng.* **2018**, *15*, 1193–1204. [CrossRef]
28. Wang, Y.; Wang, Y.C.; Mei, D.Q. Scalable Printing of Bionic Multiscale Channel Networks Through Digital Light Processing-Based Three-Dimensional Printing Process. *3D Print. Addit. Manuf.* **2020**, *7*, 115–125. [CrossRef]
29. Wang, Y.N.; Chen, R.M.; Liu, Y.X. A double mask projection exposure method for stereolithography. *Sens. Actuator A-Phys.* **2020**, *314*, 112228. [CrossRef]
30. Huang, J.J.; Zhang, B.W.; Xiao, J.F.; Zhang, Q.L. An Approach to Improve the Resolution of DLP 3D Printing by Parallel Mechanism. *Appl. Sci.* **2022**, *12*, 12905. [CrossRef]

MDPI AG
Grosspeteranlage 5
4052 Basel
Switzerland
Tel.: +41 61 683 77 34

Micromachines Editorial Office
E-mail: micromachines@mdpi.com
www.mdpi.com/journal/micromachines

Academic Open
Access Publishing

mdpi.com

ISBN 978-3-7258-5188-1